Synthesis, Characterization and Coordination Chemistry of Pincer Ligands Based on (Benzannulated) Pyridines: An Investigation into Their Electronic Structure and Applications

by

Jason Braun

A Thesis submitted to the Faculty of Graduate Studies of

The University of Manitoba

in partial fulfilment of the requirements of the degree of

Doctor of Philosophy

Department of Chemistry

University of Manitoba

Winnipeg, MB, Canada

To my family

Abstract.

The idea of 'non-innocent' ligands is that the site of chemical or redox activity on a coordination complex may not be solely limited to the central atom. Ligands may participate either by themselves or in cooperation with a central atom to facilitate electron-transfer and/or chemical reactivity in a more active fashion than in a typical coordination complex. Each of the projects explored in this thesis include the common theme of pyridine-based pincer-type ligands, their coordination to late transition metals and main group elements, and how the reactivity and properties of these complexes involves both the ligand and the ligated element. To do so, a comprehensive investigation of the electronic structure of complexes supported by pincer-type, 'NNN' ligands is also described.

Diiminepyridine ligands tend to actively participate in the chemistry of their complexes. Taking advantage of these non-innocent ligands has allowed for the stabilization of unusual oxidation states of transition metal complexes as well as the facilitation of chemical transformations with metals unable to do so using spectator ligands. Pseudo-octahedral iron complexes of these ligands exhibit multiple reversible reductions and are shown to be viable candidates as anolytes for redox flow battery applications. In synthesizing these, a synthetic scheme to prepare these ligands with electron withdrawing groups on the flanking aryl groups was developed, opening up the chemical space for these new ligands in the already well-established field of diiminepyridine ligand chemistry. In addition, bulky analogues engender stabilization of phosphorus complexes in the +1 and +3 oxidations states, not seen before with traditional diiminepyridine ligands.

The synthetic route to diarlyamido ligands comprised of flanking quinoline (2,3-benzopyridine) and phenanthridine (3,4-benzoquinoline) donors has also been developed and the

coordination of these monoanionic ligands to a variety of late transition metals and main group elements was explored. Several aspects of this ligand can be deemed non-innocent and will be highlighted throughout the course of this thesis. We see an unusual electronic environment of pseudo-octahedral iron complexes of these ligands that exhibit record length charge-transfer excited states and panchromatic absorption. Exchanging the central metal can bring about mixed-valent species upon oxidation evidenced by strong absorption in the near infrared region of the electromagnetic spectrum that significantly depends on metal-ligand orbital overlap.

Acknowledgements.

First and foremost, I would like to express my sincerest gratitude to the boss, Dr. David Herbert. I have learned so much over the past few years. He has taught me how to stay curious and ask lots of questions. I have learned about good science and how to effectively communicate it with others. And last but not least, the key to keeping a productive and efficient lab – always change the pump oil! I'd like to acknowledge Dr. Jamie Ritch for being my first mentor. The skills that you taught me allowed me to start my graduate studies with a sense of preparedness. To my committee members – Dr. Viktor Nemykin, Dr. Georg Schreckenbach, Dr. Peter Budzelaar and Dr. Frank Hawthorne for always pushing me to be the best scientist that I can be, and for all of their valuable feedback. I would also like to express my gratefulness to the staff here at the U of M – specifically to Dr. Davidson for his NMR expertise.

To my colleagues – group members, collaborators and fellow graduate students, undergraduate students and postdocs: I appreciate all of the time spent, whether it be in collaboration or conversation. I am thankful for all I have learned from each of you, and most of all, the friendships that I have built. I wish each of you the best of luck in your future endeavors.

Last but not least – my family. To my parents, my brother and Brittany. I am grateful for the never-ending support, patience and encouragement you have shown me. Thank you.

Table of Contents.

List of Figures.

List of Schemes.

List of Tables.

List of Abbreviations and Terms.

MCC: Metal coordination complex

Tetrahydrofuran: THF

Acetylacetonate ion: $acac^-$

2,2'-Bipyridine: bpy

Denticity: κ

Cyclopentadiene: Cp

Hapticity: η

Spectator ligand: L_n

Hard and soft (Lewis) acids and bases: HSAB

1,3,5-trimethylbenzene: Mes

Valence-shell electron-pair repulsion: VSEPR

Pyridine: py

Charge-transfer: CT

Metal-to-ligand charge-transfer: MLCT

Ligand-to-metal charge-transfer: LMCT

Ligand-to-ligand charge-transfer: LLCT

Millilitre: mL

Milligram: mg

Gram: g

Nanometer: nm

Centimeter: cm

2,6-diimine(pyridine): DIP

Organic light-emitting diode: OLED

Highest occupied molecular orbital: HOMO

Lowest unoccupied molecular orbital: LUMO

Singly occupied molecular orbital: SOMO

Near-infrared: NIR

Redox flow battery: RFB

(bipyridylimino)isoindoline: BPI

Dichloromethane: DCM

X-ray diffraction: XRD

Cyclic voltammetry: CV

Differential pulse voltammetry: DPV

Coulombic efficiency: % CE

Trifluromethanesulfonate: OTf

N-heterocyclic carbene: NHC

Diethyl ether: Et_2O

Megahertz: MGz

Parts per million: ppm

High resolution mass spectrometry: HRMS

Chapter 1: Introduction

1.1 Introduction to Organometallic and Coordination Chemistry

Organometallic chemistry, as the name suggests, originates in the amalgamation of organic chemistry and inorganic chemistry. As a result of the incorporation of metals into organic chemistry, new molecules can be constructed that exhibit profound characteristics and properties, much different than from either fragments alone.[1] Early examples of such compounds include organolithium[2] and organomagnesium[3] reagents that have been utilized extensively in chemistry labs over the past century. The continued study of organometallic chemistry created the need to further classify compounds based on their bonding characteristics. The organic fragment, termed 'ligand', that is bound to a metal can be bonded through a variety of elements, and although all metal-ligand complexes are termed coordination complexes, compounds containing metal-carbon bonds are further classified as organometallic complexes. In cases where the ligand is only bound through elements other than carbon (i.e. N, O, P, S, etc.), a coordination complex is a more accurate description, though the increased overlap seen in multidentate ligands somewhat blurs the line.[1] Further development of these types of molecules enabled their use in wide variety of fields such as small molecule activation and catalysis, as well as technological and medicinal applications.[4]

The vast array of applications that utilize coordination complexes is only increasing, in great part thanks to clever ligand design. The development of new ligands can open up new reactivity and properties unique to its metal coordination complexes (MCCs) and has therefore been critical to the advance of transition metal and coordination chemistry.[5]

1.2 Ligand Classification

1.2.1 Denticity and Hapticity

Ligands are often described using several terms that define their coordination to a central element. Of these descriptors, denticity and hapticity are common as they provide insight into the bonding arrangement of a ligand. Denticity refers to the number of donor atoms through which a ligand is coordinated to a central atom and is denoted by (κ).[6] For example, monodentate ligands bind through one atom, bidentate through two atoms (κ^2), tridentate through three atoms (κ^3), and so on. Table 1.1 provides examples of these bonding modes.

Table 1.1 Names and structures of selected ligands. Adapted from reference[6]

Name of Ligand	Denticity	Structure
Water	Monodentate (κ^1)	
Ammonia	Monodentate (κ^1)	
Tetrahydrofuran (THF)	Monodentate (κ^1)	
Pyridine	Monodentate (κ^1)	
1,2-Ethanediamine	Bidentate (κ^2)	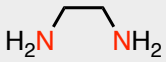
Acetylacetonate ion ($acac^-$)	Bidentate (κ^2)	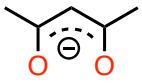
2,2'-Bipyridine (bpy)	Bidentate (κ^2)	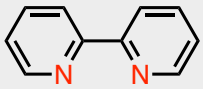
1,4,6-Triazaheptane	Tridentate (κ^3)	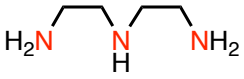

In contrast, hapticity refers to the number of contiguous atoms that directly interact with the central element and is represented by (η).[6] The typical example used in organometallic chemistry to illustrate hapticity is that of the cyclopentadienyl (Cp^-) ligand. Figure 1.1 illustrates the different bonding modes of Cp^- to a metal (M).

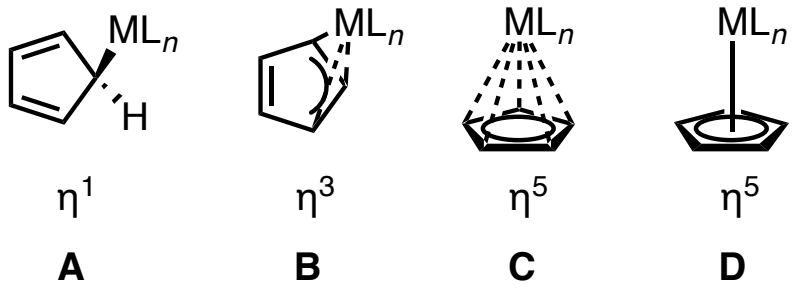

Figure 1.1 Bonding modes of the Cp ligand

The different bonding modes of the Cp^- make it a very versatile ligand that is often incorporated in complexes of both transition metals main group elements.[7] By far the most common mode of bonding for complexes of d and f block elements is η^5, with equal bonding contributions from each carbon (Figure 1.1, **C**) and is often represented by the structure of Figure 1.1, **D**. In contrast, Cp^- complexes p-block elements often exhibit η^1 (Figure 1.1, **A**) binding,[8] though η^5 examples are becoming more common[7]

1.2.2 X, L and Z – Type Ligands

In addition to the connectivity descriptors described above, ligands can be further sorted by their bonding nature. In most examples, ligands act as Lewis bases by donating electron density towards the metal or Lewis acid element centre.[5] Green and Parkin developed the Covalent Bond Classification method that allows us to classify the type and number of interactions between a metal and ligand (Figure 1.2).[9]

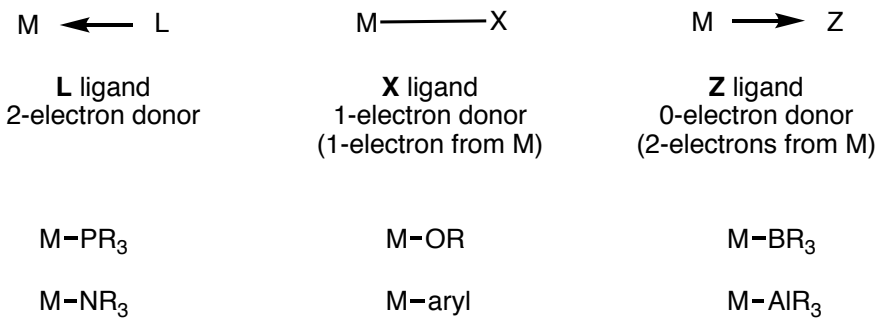

Figure 1.2 Classification and examples of X, L and Z type ligands according to the Covalent Bond Classification method[5]

Ligands that donate two electrons to the metal are considered L-type ligands with the bonding interaction described as dative. Common examples are phosphines and amines that donate through their lone pair. These types of ligands do not affect the formal oxidation state of the central metal. In contrast, ligands that are single electron donors by this method, are considered X-type ligands where bonds are comprised of one electron from both the ligand and the metal. This increases the formal oxidation state of the metal by one unit. In addition to the examples highlighted in Figure 1.2, halides and alkyl groups are also common. Finally, the less common Z-type ligand is comparable to the L-type, but in reverse. In this case, the ligand accepts two electrons from the metal. The most common examples are shown above.

1.2.3 Hard and Soft Acids and Bases

To help understand bonding strength between Lewis acids and bases, Ralph Pearson introduced the concept of 'hard and soft (Lewis) acids and bases' (HSAB) in the 1960s.[10–12] This concept empirically identifies trends in stabilities of compounds that form between acids and bases[13] and can help identify compatibility between metal centres and donor atoms within a ligand. Both acids and bases can be divided into two groups: hard and soft. In short, the theory states that

hard acids will prefer to bind with hard bases and soft acids will prefer to bind with soft bases. For example, Li^+ and F^- form a very strong adduct LiF, whereas the interaction between Li^+ and I^- to form LiI is much less favourable. Acids and bases were divided into these categories initially by work done with equilibrium constants,[10] however, a more general approach to their classification is often used and is based on their tendencies and properties.[11] A summary of these are highlighted in Table 1.2 followed by examples in Table 1.3.

Table 1.2 Summary of the properties of Lewis acids and bases[11]

Property	Hard acids and bases	Soft acids and bases
Atomic/ionic radius	Small	Large
Oxidation state	High	Low or zero
Polarizability	Low	High
Electronegativity (bases)	High	Low

Table 1.3 Classification of Lewis acids and bases[13]

Hard	Borderline	Soft
Acids	Fe^{2+}, Co^{2+}, Ni^{2+}	Cu^+, Au^+, Ag^+, Tl^+
H^+, Li^+, Na^+, K^+	Cu^{2+}, Zn^{2+}, Pb^{2+}	Pd^{2+}, Cd^{2+}, Pt^{2+}, Hg^{2+}
Be^{2+}, Mg^{2+}, Ca^{2+}	SO_2, BBr_3	BH_3
Cr^{2+}, Cr^{3+}, Al^{3+}		
SO_3, BF_3		

Bases	NO_2^-, SO_3^{2-}, Br^-	H^-, R^-, $\underline{C}N^-$, CO, I^-
F^-, OH^-, H_2O, NH_3	N_3^-, N_2	$\underline{S}CN^-$, R_3P, C_6H_5
CO_3^{2-}, NO_3^-, O^{2-}	C_6H_5N, $SC\underline{N}^-$	R_2S
SO_4^{2-}, PO_4^{3-}, ClO_4^-		

* Underlined element is the site of attachment

Using this concept, researchers have been able to design and synthesize complexes comprised of both hard and soft ligand donors and multidentate ligands that feature a combination of hard and soft base donors. Figure 1, **A** for example, highlights a Re complex of a tridentate ligand featuring relatively hard nitrogen donors along with the very hard terminal oxo donor ligand.[14] The total bonding interaction between the ligands allows for the isolation of this very sensitive complex. In Figure 1, **B**, a relatively hard phenoxide ligand is derivatized to incorporate a soft phosphine donor, enabling complexes of Ti, Zr and Hf to be synthesized that offer impressive activities as olefin polymerization catalysts.[15] Incorporating multiple donor atoms on a multidentate ligand allows for complexes to be formed that may have mismatched Lewis acid and Lewis base interactions, enabling the investigation of a limitless number of complexes.

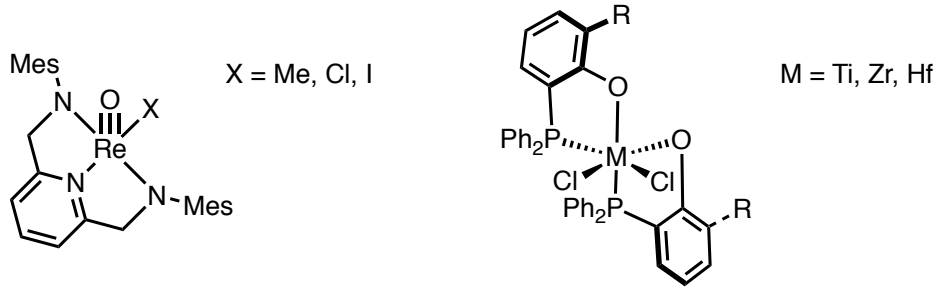

Figure 1.3 Examples of complexes featuring a combination of hard and soft ligands

1.3 Coordination Geometry

Molecules containing a central atom adopt a variety of different geometries depending on how many atoms or ligands are coordinated to it. The classic VSEPR (valence-shell electron-pair repulsion) model is commonly used to accurately predict the geometry of simple p-block molecules.[6] This model takes into account electronic arguments where the geometry is predicted by minimizing electronic repulsions. This model, however, does not take into account any steric arguments and therefore does not work as well for coordination complexes of bulkier ligands that enforce certain geometries, often seen in transition metal chemistry.

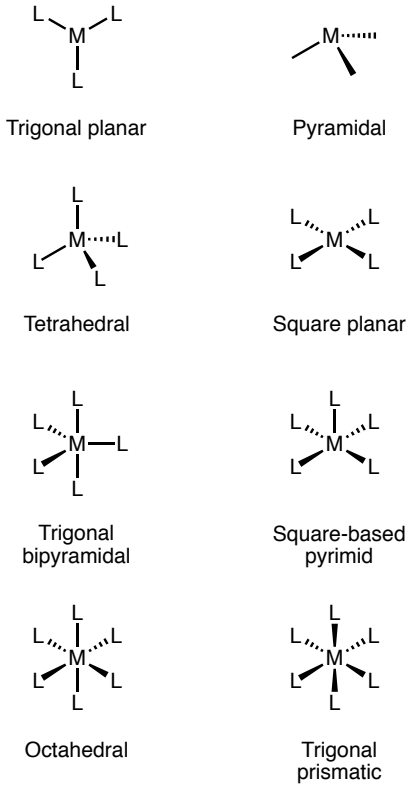

Figure 1.4 Common geometry of coordination complexes[16]

Typical coordination environments range from 3-coordinate to 6-coordinate with exceptions at both ends. For example, many Ag(I) complexes of carbene ligands occupy a linear geometry with a coordination number of two.[17]

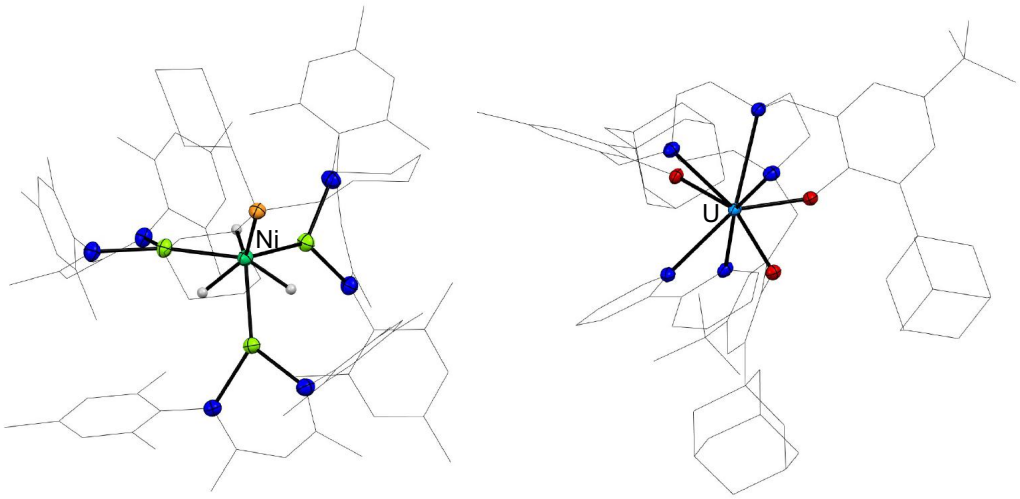

Figure 1.5 Crystal structures of coordination complexes exhibiting unusual geometries[18,19]

On the other hand, complexes may also exhibit geometries that exceed a coordination number of six. Some recent examples are highlighted above in Figure 1.5. On the left, a Ni complex with three hydride ligands (grey), three Mg(acac) (yellow) ligands and a phosphine (orange) produce a seven-coordinate geometry around the Ni metal centre.[18] As central metal atoms increase in size, higher coordination numbers can often be generated.[6] Shown above (right), a coordination complex of uranium featuring a bpy ligand exhibits 8-coordinate geometry,[19] and many examples of larger coordination numbers have been observed in f-block complexes with smaller ligands.[6]

With the development of multidentate ligands, not only the steric arrangement of the ligand influences neighboring ligands, but its rigidity can often enforce a geometry that deviates from what would be predicted with the VSEPR model.[20] These deviations from ideal geometry can often significantly influence the overall stability and reactivity of a molecule. This is something that chemists often look to exploit to induce desired properties of a molecule.

1.4 Description of Bonding in Coordination Complexes

1.4.1 Crystal and Ligand Field Theory

One of the approaches to describe metal-ligand interactions within a coordination complex is through crystal field theory.[6] This concept was first introduced nearly a century ago by Bethe[21] and Van Vleck[22] and provides an electrostatic model that illustrates the breaking of orbital degeneracy due to a ligand produced electric field around the central atom. In this simplistic model, ligands are treated as negative point charges that are electrostatically attracted to a central metal ion.[6] There is simultaneously an opposing electronic repulsion between electrons in metal and ligand orbitals that would raise the energy of the valence orbitals uniformly. However, the non-spherical nature of the valence orbitals (typically d or f) generate inequivalent interactions with the point charges, resulting in the loss of orbital degeneracy. For example, if we consider an octahedral ligand field of a transition metal with no electrostatic interactions, the d-orbital energy is degenerate as seen in Figure 1.6, **A**. If we consider a spherical electrostatic field, the d-orbital energy would be raised equally for each orbital (Figure 1.6, **B**).

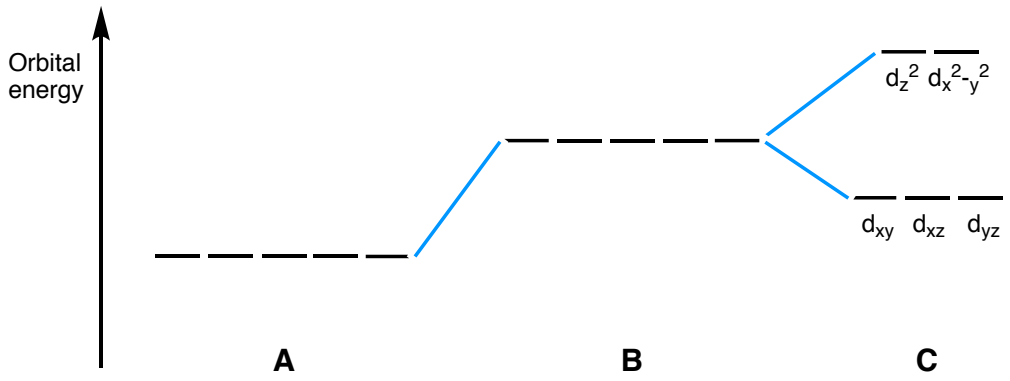

Figure 1.6 d-orbitals and orbital splitting in an octahedral crystal field[6]

In octahedral geometry, the d_z^2 and d_x^2-$_y^2$ orbitals point directly at the point charges in contrast to the d_{xy}, d_{xz} and d_{yz}. This repulsive interaction is therefore significantly destabilized and results in two sets of degenerate orbitals (Figure 1.6, **C**). Similarly, other geometries induce orbital splitting that can be explained by crystal field theory. Some of the common geometries along with their d-orbital splitting are shown below.

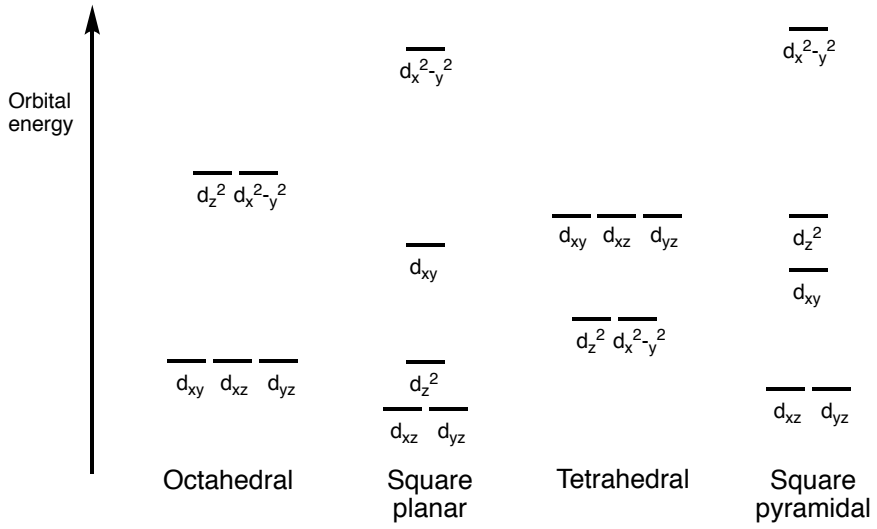

Figure 1.7 Possible energy diagrams for common geometries[6]

One drawback of crystal field theory is that it does not take into account any metal-ligand covalent interactions and therefore does not attempt to describe bonding. Using the already established crystal field theory, a more thorough approach towards bonding was proposed as ligand field theory by Griffith and Orgel.[23] This theory applies the concepts of molecular orbital theory to explain how different ligands can interact with a metal centre, and how the nature of the ligands can induce changes in the energy of a given metals d-orbitals.

1.4.2 High and Low Spin

As seen in Figure 1.7, the geometry of a complex induces a certain d-orbital splitting. Depending on the metal and its oxidation state, the orbitals can range from completely unoccupied to completely occupied with two electrons in each. Between these two extremes, there exists opportunities for electrons to occupy orbitals at different energies for a given d-electron count. For example, a d^6 octahedral complex (e.g. Fe^{2+}, Co^{3+}) would have two possible electronic configurations. The low spin configuration exhibits diamagnetism where all electrons are paired in the lower-energy orbitals (formally called t_{2g} for an octahedral complex), whereas in the high spin state, all orbitals are singly populated before they begin to pair leaving a paramagnetic species.

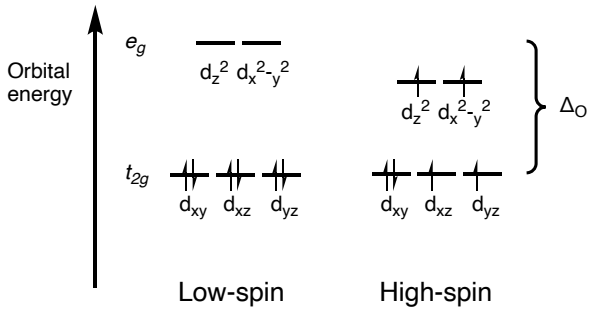

Figure 1.8 Possible electron configuration in a d^6 octahedral complex

The two major factors that contribute to the electronic configuration of a given complex are the pairing energy (P), and in the case of an octahedral ligand field, the difference in energy between the t_{2g} and e_g orbital set termed Δ_O. The pairing energy is the energy required to convert electrons of the same spin in different degenerate orbitals into spin-paired electrons within the same orbital.[6] If $\Delta_O > P$, the complex will exhibit a low-spin configuration, and if $\Delta_O < P$, high-spin. Δ_O is significantly influenced by the nature of the metal and increases down the periodic table as illustrated in Figure 1.9, using examples of low-spin group 9 d^6 octahedral ammonia complexes.

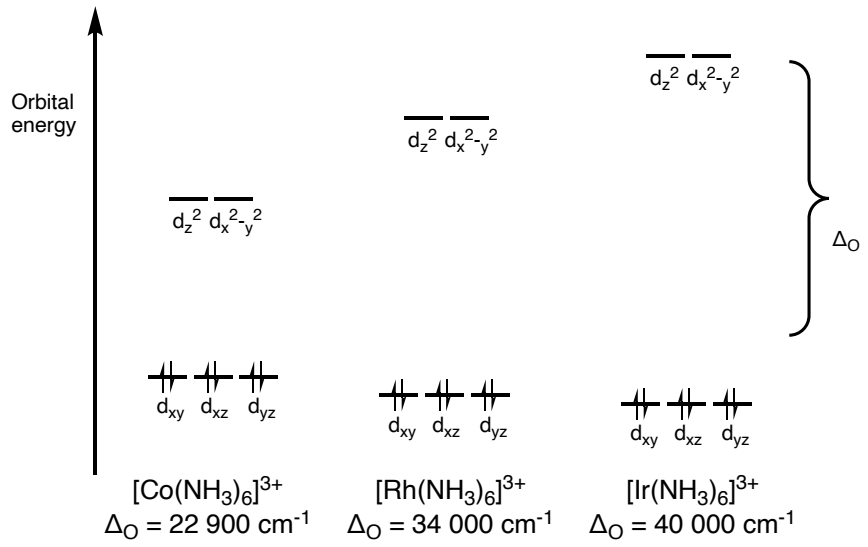

Figure 1.9 Increased Δ_O down group 9 octahedral complexes[24] - *not to scale

It is important to use the same ligand set for the comparison of the d-orbital energies among metals in the same group because the nature of the ligand can also have a significant influence on Δ_O. The influence that the ligand has on the Δ_O of a complex is a function of its electron donor and acceptor abilities, where the stronger the interaction is with the metal, the larger the Δ_O will be. Ligands that induce a large Δ_O are classified as strong-field ligands, and ligands that induce a smaller Δ_O are considered weak-field ligands. For example, large halides (i.e. I^-, Br^-) are considered weak-field ligands as they do not exhibit any π-accepting character, but rather π-donating, consequently raising the t_{2g} orbitals closer to the e_g orbitals and decreasing Δ_O.[13] In contrast, π-accepting ligands such as CN^- and CO can participate in π-backbonding, thus strengthening the metal-ligand interaction and increasing Δ_O. Ligands were first ranked according to their strength nearly a century ago based on the absorption spectra of ligated Co complexes.[25] The colour, and therefore the lowest energy absorption band correlates with the lowest-energy electronic transition

within a complex which most often represents Δ_O. Figure 1.10 highlights the spectrochemical series.[13]

$$I^- < Br^- < Cl^- < N\underline{O}_2^- < F^- < OH^- < H_2O < CH_3CN < py < NH_3 < bpy < \underline{N}O_2^- < PPH_3 < CN^- < CO$$

Weak-field Strong-field

Figure 1.10 Spectrochemical series of ligands arranged in order of increasing energy of the lowest energy transition when in a complex[13]

From this series, it can be interpreted that the strong-field ligands induce ligand field splitting parameters that are much larger than the pairing energy, and therefore often enforce a low-spin electronic configuration. In contrast, weak-field ligands generally enforce a high-spin configuration, at least with first-row transition metals. By controlling the metal and ligands, complexes with desired electronic structures can be constructed, which is critical for the engineering of complexes for certain applications.

1.5 'Non-innocent' Ligands and Their Complexes

The use of rare metals in chemistry is attractive due their unique properties,[26] however, their continued use will result in ever-increasing extraction and re-production costs that are not sustainable (Figure 1.11).[27] The introduction of 'non-innocent' ligands, initially proposed over 50 years ago by Jørgensen,[28] may alleviate these costs by imparting desirable properties on complexes of abundant metals. In the initial study, Jørgensen reported that non-innocent ligands often impart unusual properties and ambiguity in the central metal oxidation state of a coordination complex.[28] Since then, the study of non-innocent ligands has been attractive to organometallic chemists for many reasons that will be highlighted in the following sections. Most importantly, the development

of non-innocent ligands aims to improve efficiencies of chemical transformations and additionally, facilitate the development of technology based on sustainable materials.[29]

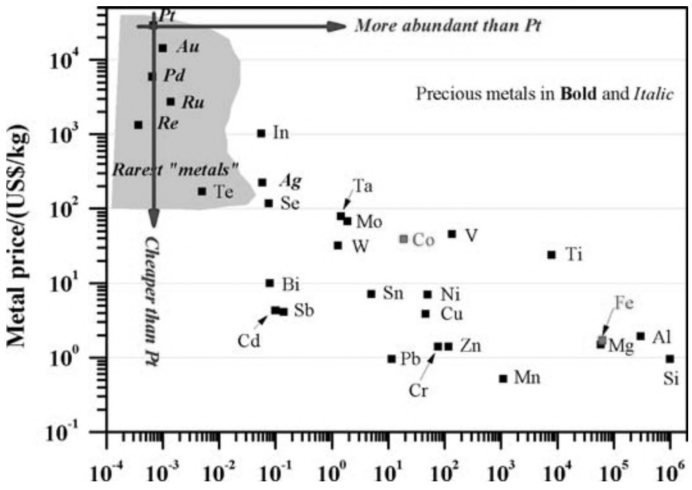

Figure 1.11 Molar abundance (relative to Si) and cost of selected metals[27]

The continued study of non-innocent ligands created the need to divide them into two distinct categories of "chemically non-innocent" and "redox non-innocent". This classification was made to help explain type of metal-ligand cooperation that is observed within MCCs.

1.5.1 Chemical Non-Innocence

Classically, the site of reactivity of a coordination complex is the central metal, whether it be in small molecule activation or catalysis, the ability of metals to form stable complexes in multiple oxidation states generally allows for the facilitation of these transformations. The development of more complex ligands has led to reactivity that is not solely metal based, but rather involves the cooperation between both the metal and the ligand. For example, Milstein has shown

several examples of a dearomatization/aromatization pathway exhibited by complexes supported by pyridine-based P^N^P and P^N^N ligands (Scheme 1.1).[30]

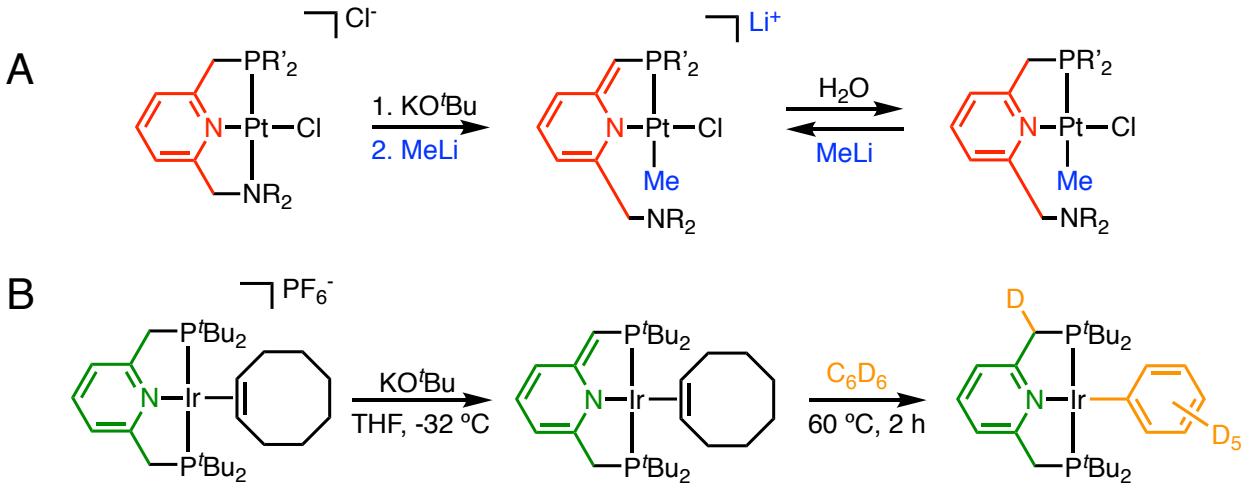

Scheme 1.1 Examples of chemical non-innocence

Reaction of [(P^N^P)PtCl]Cl$^-$ with an alkoxide base and subsequent addition of MeLi affords an anionic Pt complex (Scheme 1.1, **A**) where X-ray crystallography suggests dearomatization of the pyridine moiety and C=C double bond character on the phosphorus donor arm. In addition, the nitrogen donor arm dissociates allowing for coordination of the incoming methyl group. Hydrolysis of this complex results in the rearomatized neutral Pt complex.[31] Another example features a cationic Ir complex of a similar P^N^P ligand (Scheme 1.1, **B**) that undergoes the analogous dearomatization reaction pathway, however, addition of C_6D_6 results in C-D activation where a deuterium atom migrates to a phosphorus donor ligand arm.[32] In this case, the stronger phosphine donor does not dissociate like its nitrogen congener. In both of these examples, these ligands demonstrate chemical non-innocence whereby the ligand participates in the

complexes reactivity and allows for the metal oxidation state to remain unchained through each step. This cooperation allows for the facilitation of chemical transformations that may not be possible with other Pt or Ir complexes.

1.5.2 Redox Non-Innocence and Redox-Active Ligands

In contrast to chemical non-innocence, a more common mode of non-innocent ligand behaviour is redox non-innocence. As alluded to earlier, the ambiguity in central atom oxidation state is a key marker of complexes of non-innocent ligands, more specifically, redox non-innocent ligands.[28] Recently, the term redox-active ligands was introduced to describe ligands that act as an electron source or sink, and where the metal centre oxidation state can still be unambiguously defined by experimental techniques.[33] Although these terms are often used synonymously[34] and both participate in redox chemistry, redox-active ligands do not agree with Jørgensen's initial definition of non-innocent ligands and the distinction between the two is becoming more apparent in the literature.[33] Universal examples of ligands that confer unique electronic environments of their complexes are those of extended π-systems that take on π-radical character upon oxidation or reduction of their associated complex, delocalizing charge over multiple atoms.[35] In these cases, ligands often introduce vacant or filled orbitals that intercede the d-orbital manifold as illustrated in Figure 1.12.

In addition to chemical oxidation or reduction of a complex, excitation of a molecule may result in electron transfer (charge transfer (CT)) from the ligand to another part of the molecule (i.e. metal) or vice versa (Figure 1.12, **A**). Transitions involving relocation of an electron from a metal to ligand are termed metal-to-ligand charge-transfer (MLCT) and the opposite direction, ligand-to-metal charge-transfer (LMCT). For example, photoinduced excitation of $[Ru(bpy)_3]^{2+}$

with 375 nm light promotes an electron from the t_{2g} orbital to a low-lying π* ligand-based orbital (Figure 1.12, **B**).[36] This MLCT excited state has a distinct lifetime before it decays back down to the ground state and can harvested for use in applications such as photocatalysis[36] and photosensitization.[37]

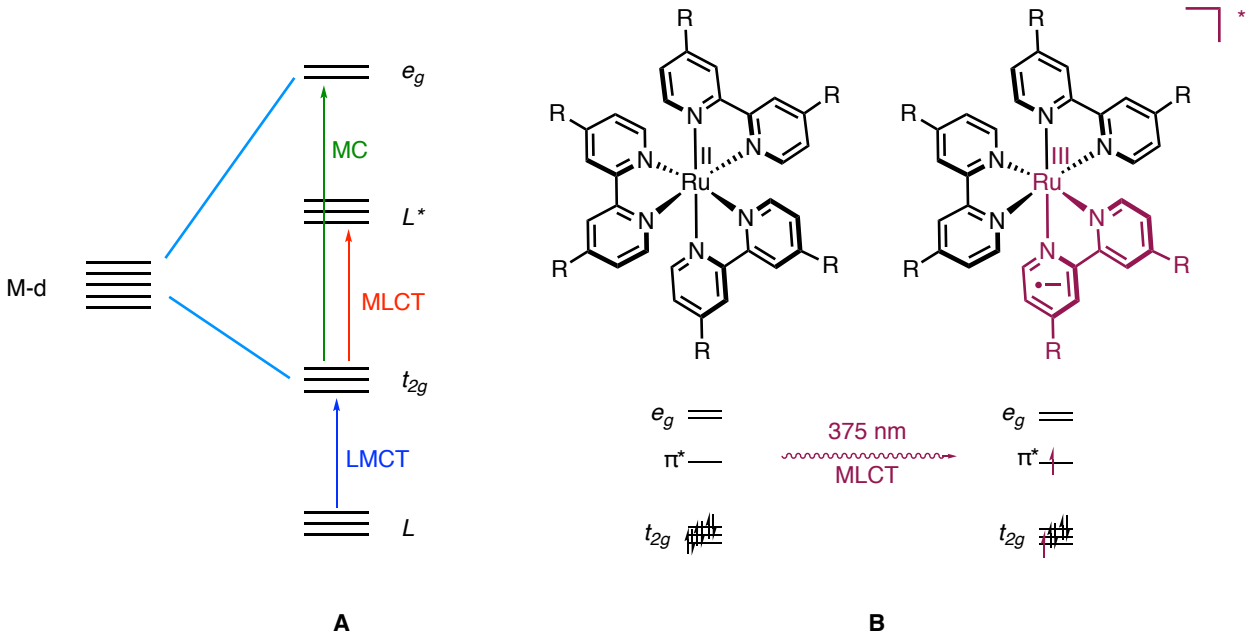

Figure 1.12 (**A**) Schematic of an electronic structure diagram[38] and (**B**) MLCT excitation of $[(Ru(bpy)_3]^{2+}$

Redox-active ligands have also proven to be useful in catalysis.[39,40] Their ability to modify the Lewis acidic nature of the metal often facilitates chemical transformations that complexes of innocent ligands would not.[39] For example, the catalytic cycle of the oxidation of dihydrogen by an Ir complex is initiated by complex oxidation by $AgBF_4$ that forms ligand-based radical on the N^O chelating bidentate ligand (Scheme 1.2).[41] The increased Lewis acidity felt by Ir brought on by this oxidation allows for the binding and formation of an H_2 complex that does not form prior to this oxidation.[41] The catalytic cycle is then completed by additional deprotonation and oxidation steps.

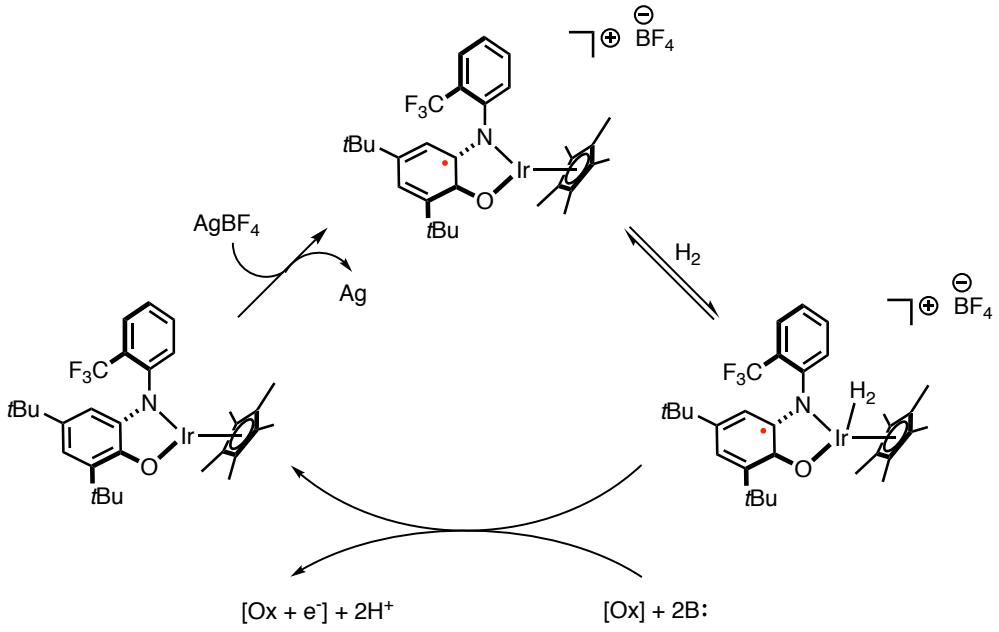

Scheme 1.2 Oxidation of H_2 by an Ir complex featuring a redox-active N^O ligand[39]

1.5.3 Non-Innocent Ligands for Iron-based Photosensitizers

As previously mentioned, non-innocent ligands are especially useful in photochemistry and allow for useful charge-transfer properties. One such example of a photochemical application is photosensitizers. Photosensitizers are molecules that can produce a chemical change in another molecule via light absorption.[37] One goal of using these types of ligands is to alleviate the need for precious metals in these complexes. Although Ru based dyes are useful and widely used today, several drawbacks exist including the inherent cost of Ru based starting materials. In addition to the sustainability aspect, typical Ru based dyes exhibit absorption spectra that attenuate at ~ 650 nm[42] (Figure 1.13, shaded in red), leaving half of the available solar incident photons unharvested (Figure 1.13. shaded in gray). Iron, an environmentally benign and sustainable metal, has long represented a key target as the central metal in coordination complexes useful for photochemical applications.[43]

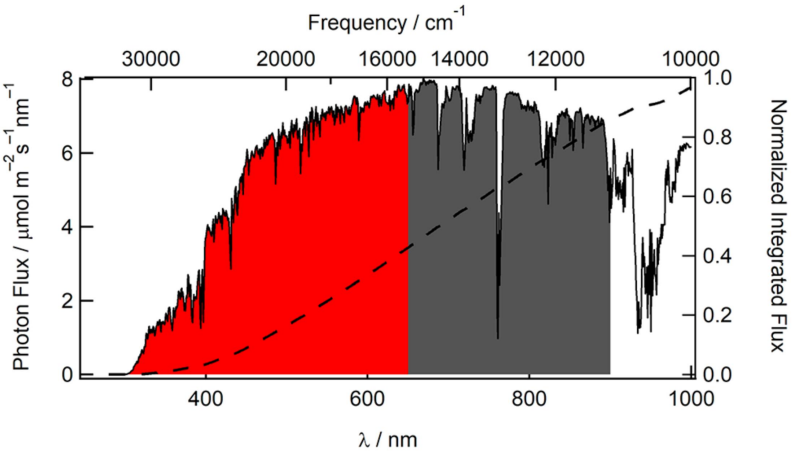

Figure 1.13 Solar flux as a function of wavelength[42]

This target, however, is problematic due to exceedingly short-lived charge-transfer excited-states in comparison to their Ru analogues.[44]

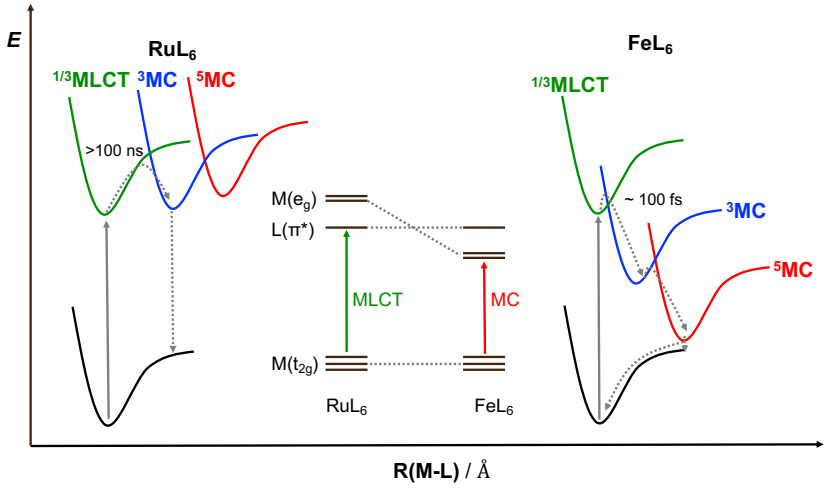

Figure 1.14 Schematic of potential energy surfaces of Ru(II)L_6 and Fe(II)L_6 complexes. Adapted from reference[44]

The Wärnmark group has made remarkable progress in the extension of excited-state lifetimes of Fe complexes by clever ligand design featuring strongly σ-donating carbenes (Figure 1.15).[38,45–47] By improving donor strength of the carbene, unproductive metal-centred states are

raised in energy (Figure 1.15, **D**), becoming less favourable and allowing for longer-lived charge-transfer excited-states. These lifetimes increase as a function of σ-donor strength increasing from a 9 ps MLCT for typical NHC supported complexes (Figure 1.15, **A**),[44] to 100 ps and 528 ps for the respective LMCT and MLCT of a *tris*-bidentate meso-ionic triazolyidene NHC supported complex (Figure 1.15, **B**),[38,46] to a 2 ns LMCT for an anionic borate NHC supported complex (Figure 1.15, **C**), exhibiting the first example of an Fe coordination complex with visible luminescence,[47] observable with the naked eye.

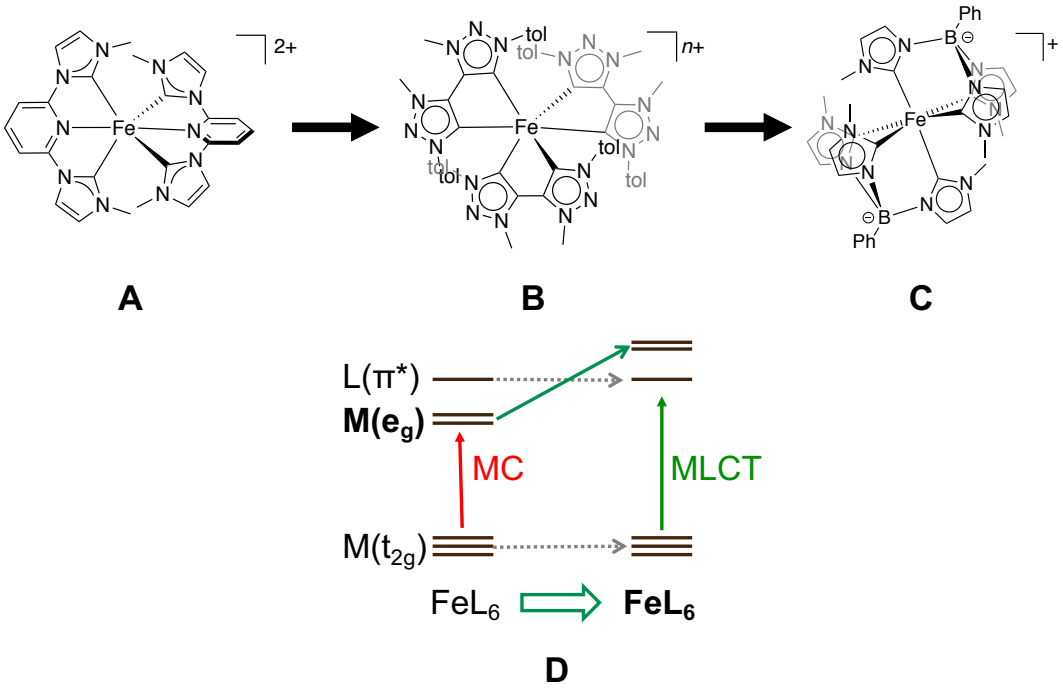

Figure 1.15 Increasing σ-donating strength of ligands and their influence on orbital energy.

As alluded to earlier, one important aspect of photosensitizer design in addition to long-lived excited states, is the ability to absorb strongly throughout the visible region of the electromagnetic spectrum. Ongoing research aims to extend the absorptive properties of iron complexes while still maintaining useable excited-state lifetimes. Progress in this area is described in detail in chapters 4 and 5.

1.5.4 Pyridine-Based Non-Innocent and Redox-Active Ligands

Among the classes of non-innocent and redox active ligands, pyridine-based ligands are quite common due to their cheap and derivitizable nature. They have also proven useful in numerous applications such as catalysis,[39] photosensitization,[37] organic light-emitting diodes (OLEDs)[48,49] and redox flow batteries (RFBs).[50,51] RFBs are scalable energy storage devices that facilitate the interconversion of electrical and chemical energy using solvated redox active species[50,51] and will be expanded on in chapter 2.

Chirik and coworkers have devoted significant effort into understanding the electronic structure of complexes of the redox active 2,6-diimine(pyridine) (DIP) ligand to further its use in the field of catalysis.[52] They have shown the exceptional redox-activity of the DIP ligands with base-metals including its triply reduced analogue with iron complexes (Figure 1.16).[53] The isolation and characterization of these structures is fundamental for the understanding of their role in catalytic mechanisms. The tunable nature and this ability for DIP ligands to form stable complexes throughout many oxidation states allows for impressive catalytic properties with base-metals that would otherwise not be possible.[54–57]

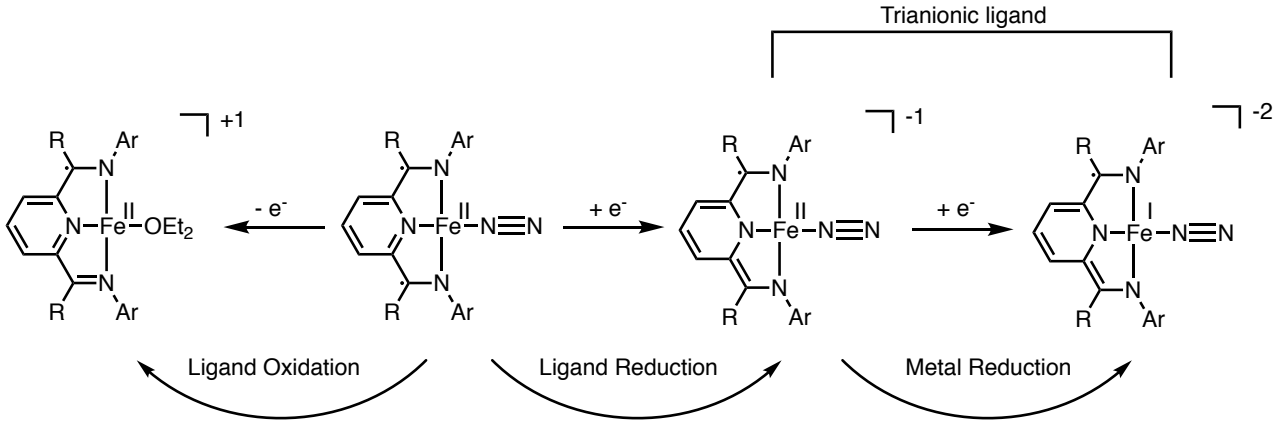

Figure 1.16 Electronic structure of iron complexes of the redox active DIP ligand[53]

The use of pyridine-based ligands and their complexes in luminescent materials have been investigated for several decades. OLEDs are a very widely used display technology that are comprised of an molecule that emits light in response to an electric current.[6] The development of electroluminescent materials has been a very crucial aspect in the advance of this technology. First developed in 1987, the first OLED devices utilized pseudo-octahedral Al complexes comprised of hydroxyquinoline ligands (Figure 1.17, **A**).[58] Since then, numerous MCCs have been developed as candidates for OLEDs included several Cu[59,60] (Figure 1.17, **B**) and Ir-based[61,62] (Figure 1.17, **C**) complexes. In all cases, the ligand is essential for the emission properties sought after in light-emitting technology.

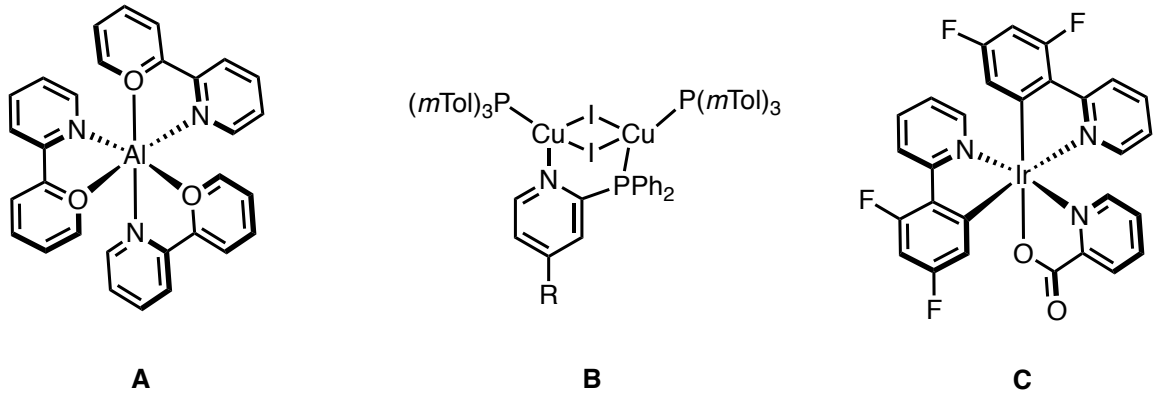

Figure 1.17 Examples of molecular photosensitizers for applications in OLED technology

1.6 Phenanthridine

1.6.1. Phenanthridine: An Introduction to its Structure and Properties

Phenanthridine is a conjugated organic molecule that has been well established in the literature.[63] The structure is analogous to phenanthrene with the exception of one carbon being replaced by a nitrogen atom (Figure 1.18) and can be considered a benzo-fused pyridine. It is the structural isomer of acridine and differs in the location of pyridine benzannulation.

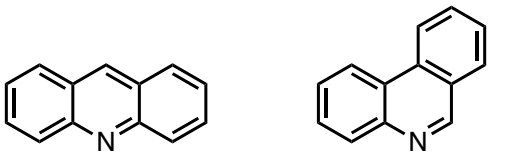

Acridine Phenanthridine

Figure 1.18 Structure of acridine and phenanthridine

Its discovery, dating back to 1891, has provided ample time to develop synthetic procedures to isolate and characterize it and its derivatives. Improvements in its synthesis were first established by Morgan and Walls in 1931,[64] however, it is mentioned that various substitution can hamper conversion. With the development of characterization techniques such as NMR and X-ray crystallography, a more complete picture of the structure of phenanthridine was established. In 1973, the first crystal structure was reported,[65] followed later by a more accurate description by use of better instrumentation.[66] The crystal structure provides insight into its insolubility, suggesting that π-stacking is prominent, at least in the solid-state.[66] In addition to this information, key bond angles and distances could now be extracted. What is interesting to note, is the C=N bond length (Figure 1.19). Unlike pyridine, quinoline and its structural isomer acridine, the C=N bond is much shorter, resembling imine-like character (Figure 1.19). Additionally, it can be seen that the lowest occupied molecular orbital (LUMO) can be manipulated through the site of benzannulation.

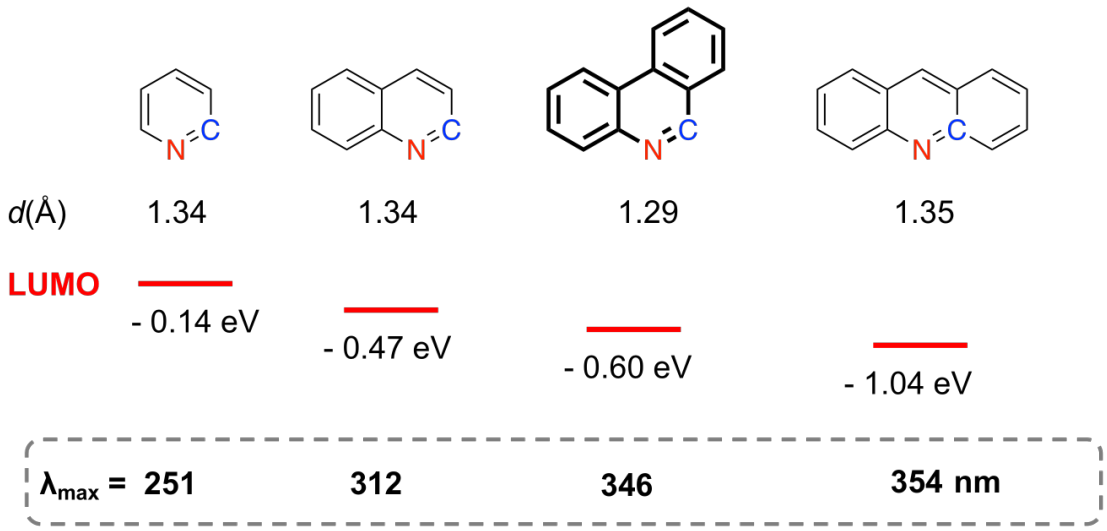

Figure 1.19 Imine bond length, LUMO energy and λ_{max} of pyridine, quinoline, phenanthridine and acridine[67,68]

1.6.2 Applications of Phenanthridine

Phenanthridine exhibits properties that lend itself useful in several applications. The imine-type character that phenanthridine exhibits has opened up the door for reactivity at this site. Several groups have shown that phenanthridine can act as a NADP(H) mimic to activate and transfer H_2 to organic substrates in the presence of a catalyst (Scheme 1.3).[69–71] The scope of the reaction shown in Scheme 1.3 is quite large and includes hydrogenation of benzoxazinones, benzoxazines, quinoxalines and quinolines under mild conditions and is useful in organic synthesis.[69]

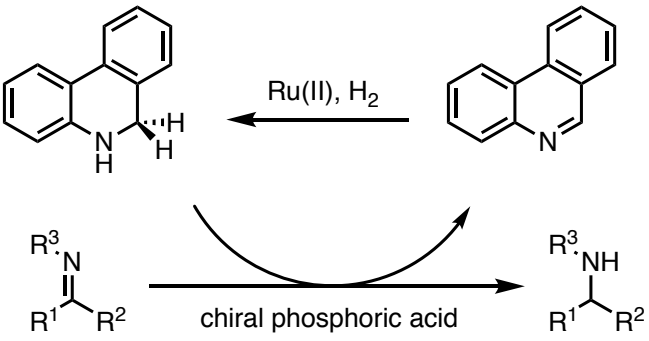

Scheme 1.3 Biomimetic hydrogenation involving phenanthridine

Using this study as motivation, our lab has recently reported the electrochemical hydrogenation of phenanthridine to obtain 1,2-dihydrophenanthridine in a solution containing a renewable acid.[72] At -1.23 V (vs. $FcH^{0/+}$), in the presence of formic acid (FA), phenanthridine could be hydrogenated to 1,2-dihydrophenanthridine which could then facilitate the transfer hydrogenation of benzoxazine (Scheme 1.4).[72] Following the hydrogenation of the organic substrate, phenanthridine would then again be generated. This method presents the first electrochemical hydrogenation of a benzannulated pyridine (phenanthridine in this case) to its corresponding dihydro analogue and illustrates how the phenanthridine molecule may not only be activated chemically, but also electrochemically.

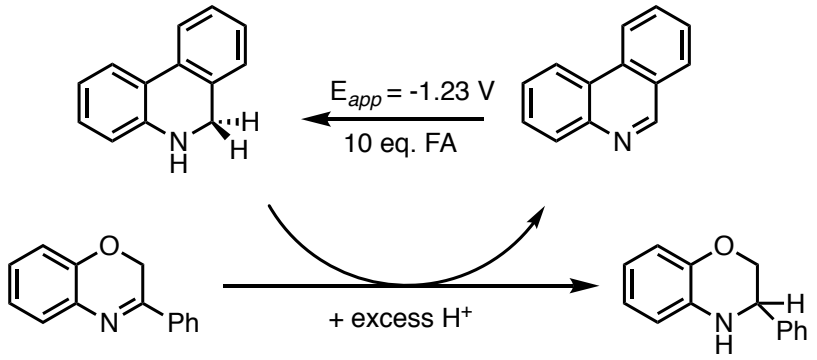

Scheme 1.4 Transfer hydrogenation of benzoxazine promoted by electrochemically generated 1,2-dihydrophenanthridine

Another use of phenanthridine is in the synthesis of the anti-cancer drug phenanthriplatin (Figure 1.20).[73] Replacement of a chloride ligand with phenanthridine in the commonly used cisplatin results in a much more cytotoxic anti-cancer agent. The increased efficacy of phenanthriplatin may be attributed to the larger, hydrophobic heterocyclic ligand in comparison to its cisplatin and pyriplatin analogues.[73]

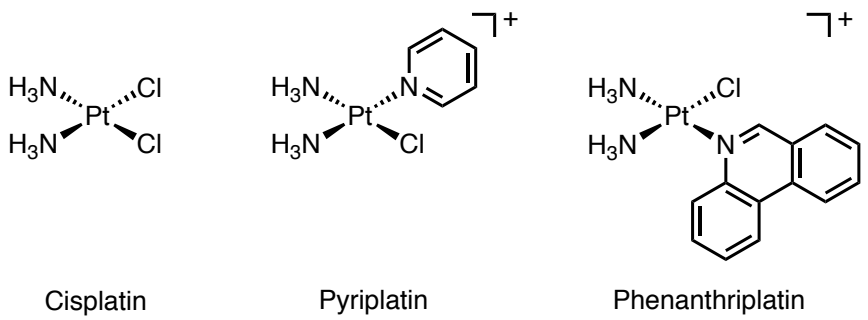

Figure 1.20 Structures of cisplatin, pyriplatin and phenanthriplatin

Additionally, phenanthridine has emissive properties that have been shown to be useful in a wide range of applications. Among these, phenanthridines ability to intercalate RNA and act as a fluorophore has been investigated and provides impressive cell imaging results.[74] Many groups have looked into exploiting the emissive properties of phenanthridine to make new MCCs of phenanthridine containing ligands and examine their properties. For example, Ir complexes of phenanthridine containing bidentate ligands have shown impressive red-shifted emission useful for the development of efficient near-infrared (NIR) phosphors in OLED technology.[75] The phenanthridine moiety contributes to the extended π-system that aids in this red-shifted emission.[75]

Our group is interested in developing multidentate non-innocent ligands that make use of the desirable properties of phenanthridine that have been highlighted in the previous sections. We have developed a new synthetic route to access substituted phenanthridines in good yields in such a way that leaves them amenable to inclusion in a ligand framework.[76] By introducing substituents, we were able to synthesize diarlyamido tridentate ligands and examine the influence of benzannulation and ligand substitution on the photophysical properties of a variety of MCCs (Figure 1.21). In contrast to the usual red-shift in emission upon benzannulation, we have found unusual trends in Pt complexes of these ligands that emit in the NIR, however, benzannulation appears to blue-shift emission, attributed to the rigid nature of the ligand.[77]

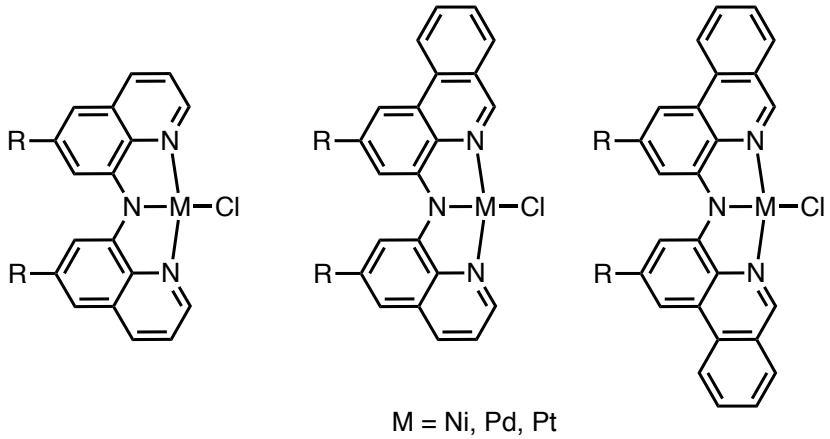

Figure 1.21 Incorporation of phenanthridine into diarlyamido N^N^N ligands and their group 10 complexes

Using the same methodology to synthesize substituted phenanthridines, our lab has also developed phenanthridine containing P^N and C^N ligands. In addition to dehydrogenative coupling catalysis performed by Ru complexes of the P^N ligands,[78] these ligands can also be used to construct Cu complexes with bright emission in both the solid and solution state (Figure 1.22).[79]

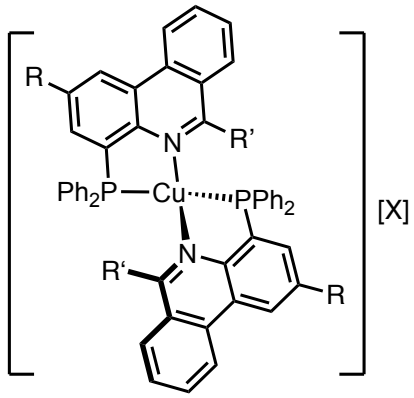

Figure 1.22 Cu complex of phenanthridine P^N ligand that exhibits solid and solution state emission

1.7 Description of Thesis and Acknowledgements

1.7.1 Description

This thesis aims to describe the synthesis, coordination chemistry and applications of coordination complexes of pyridine-based non-innocent ligands. Starting with well-known DIP ligands, pseudo-octahedral Fe complexes were synthesized and their performance as RFB anolytes was evaluated. Following this study, the incorporation of EWGs on the *para* position of the flanking aryl substituents was sought after. A new, Zn-templated ligand synthesis will be presented that affords these ligands in good yields and using remarkably mild conditions in comparison to what has previously been reported. Chapter 3 sticks with the theme of DIP ligands, however, *tert*-butyl substitution to the C=N carbon was invoked in order to pursue stable complexes of P(I) and P(III). Chapter 4 moves away from DIP ligands, however, a new pyridine-based tridentate ligand based on phenanthridine is presented. This ligand was designed to include a large π system with vacant low-energy orbitals, as well as high energy occupied ligand-based orbitals. This ligand framework and orbital manifold was explored in an attempt to broaden absorption profiles of their 3d complexes for possible applications in photosensitizer technologies. The optimized synthetic route to substituted phenanthridines and their associated ligands will be discussed. It also highlights iron complexes of these ligands. These complexes exhibit panchromatic absorption and exceptionally long, nanosecond charge-transfer excited state lifetimes that are attributed to a mixed-character HOMO and a low-energy phenanthridine-based LUMO. Chapter 5 looks at the change in the electronic structure when the iron metal centre is replaced with other 3d and main group metal centres. Chapter 6 will give a brief summary of the findings reported throughout the chapters as well as a look into some ongoing work and an outlook for the projects.

The format of this thesis is a sandwich thesis decided upon by myself, my supervisor and my committee, meaning tha each chapter is in the form of a published manuscript in a peer-reviewed scientific journal. Some additions and modifications to each chapter were made. Each draft was written by the author with input from the principle investigator and thesis committee.

1.7.2 Acknowledgments and Contributions of Authors

For all chapters, any cyclic voltammetry, differential pulse voltammetry, UV-vis/NIR spectroscopy, NMR spectroscopy and X-ray crystallography experiments were performed by the author. All Mössbauer and magnetometry experiments were carried out at the University of Manitoba Department of Physics with help from Dr. Johan van Lierop, Michael Shepit and Rachel Nickel. All mass spectrometry experiments were performed by Emy Komatsu.

Chapter 1: The introduction to the structure and bonding in coordination chemistry was inspired by Crabtree's '*The organometallic chemistry of the transition metals*, 5th ed.' Work by labmates Pavan Mandapati, Rajarshi Mondal, Patrick Giesbrecht and Dion Nemez also appears in the introduction.

Chapter 2: This chapter merges selections from two manuscripts featuring iron coordination complexes of DIP ligands for applications in RFBs {(1) Duarte, G. M.; Braun, J. D.; Giesbrecht, P. K.; Herbert, D. E. *Dalton Trans.* **2017**, *46* (47), 16439. (2) Braun. J. D.; Sidhu, B. K.; Gray, P. A.; Nemez. D. B.; Herbert. D. E. *Dalton Trans.* DOI: doi.org/10.1039/D0DT0000543F}. Electrochemical experiments were carried out by Gabriel Martins da Silva Almeida Duarte, Patrick Giesbrecht and Dion Nemez. Some synthetic experiments were performed by Baldeep Sidhu and

Dr. Paul Gray. Preliminary drafts of the manuscripts were prepared by myself and modified into its publication format by collaborators and my advisor.

Chapter 3: Selections from this chapter was reproduced from: Gray, P. A.; Braun, J. D.; Rahimi, N.; Budzelaar, P. H. M.; Herbert. D. E. *Eur. J. Inorg. Chem*. **2020**, 2105. Initial ligand design and synthesis was performed by Dr. Naser Rahimi and Dr. Peter Budzelaar. Subsequent ligand and complex synthesis were completed by Dr. Paul Gray and I along with all characterization data. All drafts of the manuscript were writing through a collaborative effort by Dr. Paul Gray, Dr. David Herbert and I.

Chapter 4: This chapter introduces phenanthridine-based tridentate ligands with selections reproduced with additional ligands and complexes from: Braun, J. D.; Lozada, I. B.; Kolodziej, Charles.; Burda, Clemens.; Newman, K.; van Lierop, J.; Davis, R. L.; Herbert, D. E. *Nat. Chem.* **2019**, *11* (12), 1144. Charles Kolodziej and Clemens Burda are thanked for their contribution of the transient absorption data. Bingqing Liu and Dr. Wengfang Sun are also thanked for their independent confirmation of photophysical data. Preliminary drafts of the manuscripts were prepared by myself and modified into its publication format by collaborators and my advisor.

Chapter 5: Chapter 5 investigates a series 3d and main group complexes of the phenanthridine-based ligands. All computational work was completed by Issiah Lozada. I am grateful for the instruction and use of the spectroelectrochemical apparatus from Dr. Viktor Nemykin and Dr. Yuriy Zatsikha. The initial draft of the manuscript was written by me, with contributions to subsequent drafts from Issiah Lozada and Dr. David Herbert.

References

(1) Crabtree, R. H. *The organometallic chemistry of the transition metals*, 5th ed.; Wiley: Hoboken, N.J, 2009.

(2) Schlenk, W.; Holtz, J. *Berichte der deutschen chemischen Gesellschaft* **1917**, *50* (1), 262.

(3) Grignard, V. *Compt. Rend. Hebd. Séances Acad. Sci.* **1900**, No. 86, 5344.

(4) Elsevier, C. J.; Reedijk, J.; Walton, P. H.; Ward, M. D. *Dalton Trans.* **2003**, No. 10, 1869.

(5) Lundgren, R. J.; Stradiotto, M. In *Ligand Design in Metal Chemistry*; Stradiotto, M., Lundgren, R. J., Eds.; John Wiley & Sons, Ltd: Chichester, UK, 2016; pp 1–14.

(6) Housecroft, C. E.; Sharpe, A. G. *Inorganic chemistry*, 4th ed.; Pearson: Harlow, England ; New York, 2012.

(7) Jutzi, P.; Burford, N. *Chem. Rev.* **1999**, *99* (4), 969.

(8) Wiacek, R. J.; Jones, J. N.; Macdonald, C. L.; Cowley, A. H. *Can. J. Chem.* **2002**, *80* (11), 1518.

(9) Green, M. L. H.; Parkin, G. *J. Chem. Ed.* **2014**, *91* (6), 807.

(10) Pearson, R. G. *J. Am. Chem. Soc.* **1963**, *85* (22), 3533.

(11) Pearson, R. G. *J. Chem. Ed.* **1968**, *45* (9), 581.

(12) Pearson, R. G. *J. Chem. Ed.* **1968**, *45* (10), 643.

(13) Shriver, D. F. and A., P. W. *Inorganic Chemistry.*; Oxford University Press, 2009.

(14) Smeltz, J. L.; Lilly, C. P.; Boyle, P. D.; Ison, E. A. *J. Am. Chem. Soc.* **2013**, *135* (25), 9433.

(15) Long, R. J.; Gibson, V. C.; White, A. J. P.; Williams, D. J. *Inorg. Chem.* **2006**, *45* (2), 511.

(16) Hartwig, J. F. *Organotransition metal chemistry: from bonding to catalysis*; University Science Books: Sausalito, Calif, 2010.

(17) Garrison, J. C.; Youngs, W. J. *Chem. Rev.* **2005**, *105* (11), 3978.

(18) Garçon, M.; Bakewell, C.; Sackman, G. A.; White, A. J. P.; Cooper, R. I.; Edwards, A. J.; Crimmin, M. R. *Nature* **2019**, *574* (7778), 390.

(19) Rosenzweig, M. W.; Heinemann, F. W.; Maron, L.; Meyer, K. *Inorg. Chem.* **2017**, *56* (5), 2792.

(20) Pascualini, M. E.; Di Russo, N. V.; Thuijs, A. E.; Ozarowski, A.; Stoian, S. A.; Abboud, K. A.; Christou, G.; Veige, A. S. *Chem. Sci.* **2015**, *6* (1), 608.

(21) Bethe, H. *Annalen der Physik* **1929**, *395* (2), 133.

(22) Van Vleck, J. H. *Physical Review* **1932**, *41* (2), 208.

(23) Griffith, J. S.; Orgel, L. E. *Q. Rev. Chem. Soc.* **1957**, *11* (4), 381.

(24) Shriver, D. F.; Atkins, P. W.; Langford, C. H. *Inorganic chemistry*; Oxford Univ. Press: Oxford, 1998.

(25) Tsuchida, R. *Bull. Chem. Soc. Jpn.* **1938**, *13* (5), 388.

(26) Xu, G.; Yano, J.; Sakai, S. *Environ. Sci. Technol.* **2019**, *53* (2), 733.

(27) Feng, Y.; Alonso-Vante, N. *Phys. Status Solidi B* **2008**, *245* (9), 1792.

(28) Jørgensen, Chr. K. *Coord. Chem. Rev.* **1966**, *1* (1–2), 164.

(29) van der Vlugt, J. I. *Chem. Eur. J.* **2019**, *25* (11), 2651.

(30) Gunanathan, C.; Milstein, D. *Acc. Chem. Res.* **2011**, *44* (8), 588.

(31) Vuzman, D.; Poverenov, E.; Shimon, L. J. W.; Diskin-Posner, Y.; Milstein, D. *Organometallics* **2008**, *27* (11), 2627.

(32) Ben-Ari, E.; Leitus, G.; Shimon, L. J. W.; Milstein, D. *J. Am. Chem. Soc.* **2006**, *128* (48), 15390.

(33) Chirik, P. J. *Inorg. Chem.* **2011**, *50* (20), 9737.

(34) Singh, B.; Indra, A. *Inorg. Chim. Acta.* **2020**, *506*, 119440.

(35) Ganguly, S.; Ghosh, A. *Acc. Chem. Res.* **2019**, *52* (7), 2003.

(36) Prier, C. K.; Rankic, D. A.; MacMillan, D. W. C. *Chem. Rev.* **2013**, *113* (7), 5322.

(37) Yuan, Y.-J.; Yu, Z.-T.; Chen, D.-Q.; Zou, Z.-G. *Chem. Soc. Rev.* **2017**, *46* (3), 603.

(38) Chábera, P.; Liu, Y.; Prakash, O.; Thyrhaug, E.; Nahhas, A. E.; Honarfar, A.; Essén, S.; Fredin, L. A.; Harlang, T. C. B.; Kjær, K. S.; Handrup, K.; Ericson, F.; Tatsuno, H.; Morgan, K.; Schnadt, J.; Häggström, L.; Ericsson, T.; Sobkowiak, A.; Lidin, S.; Huang, P.; Styring, S.; Uhlig, J.; Bendix, J.; Lomoth, R.; Sundström, V.; Persson, P.; Wärnmark, K. *Nature* **2017**, *543* (7647), 695.

(39) Lyaskovskyy, V.; de Bruin, Bas. *ACS Catal.* **2012**, *2* (2), 270.

(40) Small, B. L. *Acc. Chem. Res.* **2015**, *48* (9), 2599.

(41) Ringenberg, M. R.; Kokatam, S. L.; Heiden, Z. M.; Rauchfuss, T. B. *J. Am. Chem. Soc.* **2008**, *130* (3), 788.

(42) Whittemore, T. J.; Millet, A.; Sayre, H. J.; Xue, C.; Dolinar, B. S.; White, E. G.; Dunbar, K. R.; Turro, C. *J. Am. Chem. Soc.* **2018**, *140* (15), 5161.

(43) Galoppini, E. *Nat. Chem.* **2015**, *7* (11), 861.

(44) Liu, Y.; Persson, P.; Sundström, V.; Wärnmark, K. *Acc. Chem. Res.* **2016**, *49* (8), 1477.

(45) Liu, Y.; Harlang, T.; Canton, S. E.; Chábera, P.; Suárez-Alcántara, K.; Fleckhaus, A.; Vithanage, D. A.; Göransson, E.; Corani, A.; Lomoth, R.; Sundström, V.; Wärnmark, K. *Chem. Commun.* **2013**, *49* (57), 6412.

(46) Chábera, P.; Kjaer, K. S.; Prakash, O.; Honarfar, A.; Liu, Y.; Fredin, L. A.; Harlang, T. C. B.; Lidin, S.; Uhlig, J.; Sundström, V.; Lomoth, R.; Persson, P.; Wärnmark, K. *J. Phys. Chem. Lett.* **2018**, *9* (3), 459.

(47) Kjær, K. S.; Kaul, N.; Prakash, O.; Chábera, P.; Rosemann, N. W.; Honarfar, A.; Gordivska, O.; Fredin, L. A.; Bergquist, K.-E.; Häggström, L.; Ericsson, T.; Lindh, L.; Yartsev, A.; Styring, S.; Huang, P.; Uhlig, J.; Bendix, J.; Strand, D.; Sundström, V.; Persson, P.; Lomoth, R.; Wärnmark, K. *Science* **2019**, *363* (6424), 249.

(48) Rausch, A. F.; Thompson, M. E.; Yersin, H. *Chem. Phys. Lett.* **2009**, *468* (1–3), 46.

(49) Dumur, F. *Synth. Met.* **2014**, *195*, 241.

(50) Cabrera, P. J.; Yang, X.; Suttil, J. A.; Brooner, R. E. M.; Thompson, L. T.; Sanford, M. S. *Inorg. Chem.* **2015**, *54* (21), 10214.

(51) Duarte, G. M.; Braun, J. D.; Giesbrecht, P. K.; Herbert, D. E. *Dalton Trans.* **2017**, *46* (47), 16439.

(52) Obligacion, J. V.; Chirik, P. J. *Nat. Rev. Chem.* **2018**, *2* (5), 15.

(53) Tondreau, A. M.; Stieber, S. C. E.; Milsmann, C.; Lobkovsky, E.; Weyhermuller, T.; Semproni, S. P.; Chirik, P. J. *Inorg. Chem.* **2013**, *52* (2), 635.

(54) Bouwkamp, M. W.; Bowman, A. C.; Lobkovsky, E.; Chirik, P. J. *J. Am. Chem. Soc.* **2006**, *128* (41), 13340.

(55) Hoyt, J. M.; Sylvester, K. T.; Semproni, S. P.; Chirik, P. J. *J. Am. Chem. Soc.* **2013**, *135* (12), 4862.

(56) Schmidt, V. A.; Hoyt, J. M.; Margulieux, G. W.; Chirik, P. J. *J. Am. Chem. Soc.* **2015**, *137* (24), 7903.

(57) Hoyt, J. M.; Schmidt, V. A.; Tondreau, A. M.; Chirik, P. J. *Science* **2015**, *349* (6251), 960.

(58) Tang, C. W.; VanSlyke, S. A. *Appl. Phys. Lett.* **1987**, *51* (12), 913.

(59) Bizzarri, C.; Spuling, E.; Knoll, D. M.; Volz, D.; Bräse, S. *Coord. Chem. Rev.* **2018**, *373*, 49.

(60) Volz, D.; Wallesch, M.; Grage, S. L.; Göttlicher, J.; Steininger, R.; Batchelor, D.; Vitova, T.; Ulrich, A. S.; Heske, C.; Weinhardt, L.; Baumann, T.; Bräse, S. *Inorg. Chem.* **2014**, *53* (15), 7837.

(61) Shon, J.-H.; Teets, T. S. *ACS Energy Lett.* **2019**, *4* (2), 558.

(62) Baranoff, E.; Curchod, B. F. E. *Dalton Trans.* **2015**, *44* (18), 8318.

(63) Theobald, R. S.; Schofield, K. *Chem. Rev.* **1950**, *46* (1), 170.

(64) Morgan, G. T.; Walls, L. P. *J. Chem. Soc.* **1931**, *0* (0), 2447.

(65) Roychowdhury, P. *Acta Crystallogr., Sect. B.* **1973**, *29* (6), 1362.

(66) Brett, W. A.; Rademacher, P.; Boese, R. *Acta Crystallogr., Sect. C.* **1993**, *49* (9), 1564.

(67) Benmachiche, A.; Zendaoui, S.-M.; Bouaoud, S.-E.; Zouchoune, B. *Int. J. Quantum. Chem.* **2013**, *113* (7), 985.

(68) Katritzky, A. R. *Handbook of heterocyclic chemistry.*; Elsevier: Oxford, 2010.

(69) Chen, Q.-A.; Gao, K.; Duan, Y.; Ye, Z.-S.; Shi, L.; Yang, Y.; Zhou, Y.-G. *J. Am. Chem. Soc.* **2012**, *134* (4), 2442.

(70) Lu, L.-Q.; Li, Y.; Junge, K.; Beller, M. *Angew. Chem., Int. Ed.* **2013**, *52* (32), 8382.

(71) Lu, L.-Q.; Li, Y.; Junge, K.; Beller, M. *J. Am. Chem. Soc.* **2015**, *137* (7), 2763.

(72) Giesbrecht, P. K.; Nemez, D. B.; Herbert, D. E. *Chem. Commun.* **2018**, *54* (4), 338.

(73) Park, G. Y.; Wilson, J. J.; Song, Y.; Lippard, S. J. *Proc. Natl. Acad. Sci.* **2012**, *109* (30), 11987.

(74) Stevens, N.; O'Connor, N.; Vishwasrao, H.; Samaroo, D.; Kandel, E. R.; Akins, D. L.; Drain, C. M.; Turro, N. J. *J. Am. Chem. Soc.* **2008**, *130* (23), 7182.

(75) Jiang, B.; Gu, Y.; Qin, J.; Ning, X.; Gong, S.; Xie, G.; Yang, C. *J. Mater. Chem. C* **2016**, *4* (16), 3492.

(76) Mondal, R.; Giesbrecht, P. K.; Herbert, D. E. *Polyhedron* **2016**, *108*.

(77) Mandapati, P.; Braun, J. D.; Killeen, C.; Davis, R. L.; Williams, J. A. G.; Herbert, D. E. *Inorg. Chem.* **2019**, *58* (21), 14808.

(78) Mondal, R.; Herbert, D. E. *Organometallics* **2020**, *39* (8), 1310.

(79) Mondal, R.; Lozada, I. B.; Davis, R. L.; Williams, J. A. G.; Herbert, D. E. *J. Mater. Chem. C* **2019**, *7* (13), 3772.

Chapter 2

Redox Non-Innocent (2, 6-diimine-pyridine) ligands and Their Iron Complexes as Redox Flow Battery Anolytes

2.1 Abstract

Diiminepyridines (DIPs) are a well-known class of "non-innocent" ligands that impart additional redox activity to coordination complexes beyond metal-centred oxidation/reduction. Demonstrated here, metal coordination complexes (MCCs) of diiminepyridine ligands with iron are suitable anolytes for redox-flow battery applications, with enhanced capacitance and stability compared with bipyridine analogs. Accessible storage of up to 1.6 electron equivalents can be achieved using electron donating substituents on the 4-position of the flanking aryl substituents. Substitution of the ligand is shown to be a key factor in the cycling stability and performance of MCCs based on DIP ligands, and so DIP ligands featuring EWG were also explored via a new Zn-templated synthetic route. The findings suggest that ligands featuring arylhalides or pseudoarylhalides are not viable candidates as RFB anolytes, however, unsubstituted ligands perform significantly better, with storage of up to 1.9 electron equivalents and high efficiencies.

2.2 Introduction

The increasing portion of energy generation being devoted to renewable but intermittent sources such as solar, hydroelectric and wind has led to a resurgence of interest in flow batteries for scalable, inexpensive energy storage.[1,2] In redox flow batteries (RFBs), electrical energy is converted to chemical energy through electrochemical interconversion of a redox pair acting as the electrolyte, which in contrast to conventional batteries, are spatially separated from the

electrode.[3] If both the oxidized and reduced forms of the pairs are stable and soluble, RFBs offer promising options for long-term storage, where scalability in part will ultimately depend on the scarcity or abundance of the materials used as catholyte/anolyte.[4] Metal coordination complexes (MCCs) that can exhibit one or more accessible redox couples are commonly used in aqueous RFBs.[5] Water, however, exhibits a small potential window (~ 1.5 V), limiting its overall energy storage capacity and compatibility with alternative MCCs.[6] In employing an organic solvent such as acetonitrile with a larger voltage window (5.0 V), the challenge is to synthesize MCCs that can undergo multiple reversible electron transfers that occur past the water voltage window and are highly soluble in all oxidized and reduced forms. From this, a higher RFB energy storage capacity can be achieved, with a higher energy density output.[7,8]

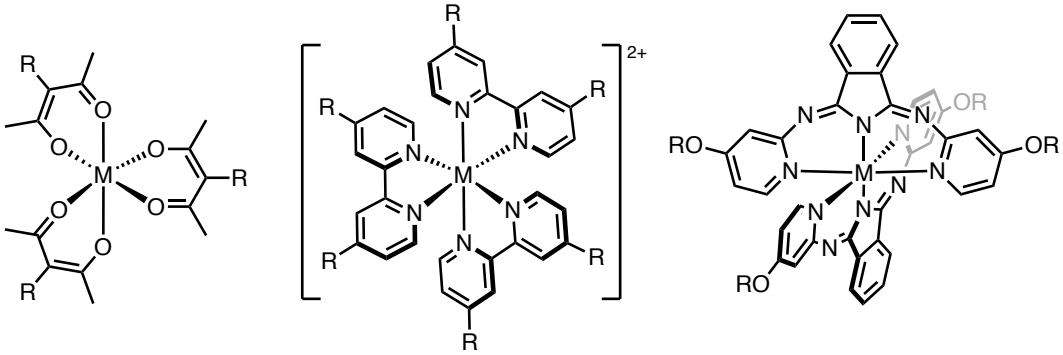

Figure 2.1 Selected examples of MCCs that have been evaluated for use in non-aqueous RFBs

While simple coordination complexes (e.g., Figure 1, **A**; acac = acetylacetonate) exhibit reversible reductions and oxidations that can enable use as both anolyte and catholyte in symmetric RFBs,[9] the introduction of redox 'non-innocent' ligands[10,11] can in principle augment the performance of MCCs in RFBs[12] by providing additional sites for electron-transfer. MCCs of redox non-innocent 2,2'-bipyridine (bpy; Figure 1, **B**)[13] and (bipyridylimino)isoindoline (BPI; Figure 1, **C**)[8] ligands, for example, have been shown to have properties favourable to RFB

applications including (for BPI MCCs) high solubility, long-term stability towards charge/discharge cycles (~200), multiple electron transfers per molecule and very little capacity fade.[8] For comparison, one of the more commercially promising systems is the all-vanadium flow battery, which utilizes four different oxidation state vanadium and oxyvanadium ions and shows impressive long-term cyclability of over 1000 stable cycles.[14] The high system costs comprised to a large extent of the cost of the redox-active material, however, still far exceed the U.S. Department of Energy's target.[15] In this context, the decision to explore the applicability of the prototypical redox non-innocent DIP[16] scaffold as a ligand in an MCC anolyte for RFBs was made. DIP ligands have been shown to act as electron reservoirs able to accommodate up to three additional electrons, and triply reduced DIP ligands have been identified in s-,[17] f-[18] and d-block[19] metal complexes.

In particular, the examination of two DIP proligands, differing in the presence of *tert*-butyl (**1a**) or methoxy substituents (**1b**) (Scheme 2.1) in the 4-positions of the imine-based aryl rings, and their octahedral [*bis*(DIP)$_2$Fe]$^{2+}$ coordination complexes was undertaken. While the use of organometallic iron complexes[20–24] and iron coordination complexes[25,26] has been demonstrated in aqueous and non-aqueous RFBs, the integration of redox-active ligands with the base metal iron has been considerably less explored.[6,8,27,28] Octahedral ligand environments for each iron supported by two DIP ligands were targeted to reduce ligand dissociation, with tridentate chelation anticipated to impart greater complex stability and higher cyclability compared with bidentate redox non-innocent ligand candidates such as diimines[29] or bipyridines.[27,30–33] 2,6-unsubstituted arenes were chosen as substituents at nitrogen to reduce steric congestion about the metal centre, as bulkier DIP ligands can induce ligand hemilability in reduced, octahedral [*bis*(DIP)$_2$Fe] complexes.[34]

2.3 Results and Discussion

2.3.1 Synthesis and Characterization of Coordination Complexes

Coordination complex **2a** and the previously reported **2b**[35] were prepared with hexafluorophosphate $[PF_6]^-$ counterions by reacting their respective proligands with $FeCl_2$ in methanol under an inert atmosphere to form dark purple solutions (Scheme 2.1). An excess of solid $NaPF_6$ was then added to provide non-coordinating counterions in common with the added electrolyte (nBu$_4$PF$_6$).

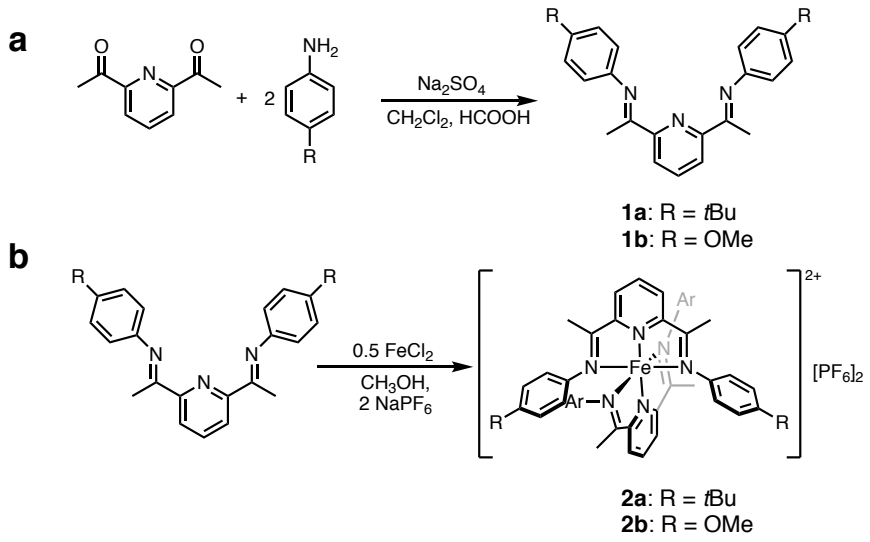

Scheme 2.1 Synthesis of (a) proligands (b) $[bis(DIP)_2Fe]_2+$ compounds

The MCCs show good solubility in polar organic solvents (solubility of **2a** > 0.13 M; **2b** > 0.26 M in CH_3CN) and were precipitated from dichloromethane (DCM) into pentane to give **2a** and **2b** as air and moisture-stable, deep purple solids in yields > 90 %. Complexes **2a** and **2b** were fully characterized in solution by multinuclear NMR, UV-Vis and Mössbauer spectroscopy, with spectroscopic data for **2b** compared to the literature.[35]

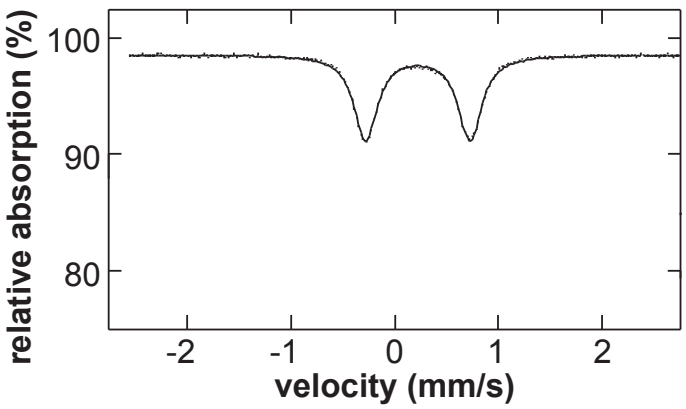

Figure 2.2 Mössbauer spectrum of **2a** at 10 K. Data collected using an α-Fe standard at 298 K

Mössbauer spectroscopic parameters for **2a** are very close to those reported for **2b**[35] (Table 2.1, Figure 2.2), with both isomer shifts and quadrupole splitting parameters consistent with low-spin Fe (II), and in line with parameters for related DIP supported Fe(II) centres.[34–36]

Table 2.1 Redox and Mössbauer parameters for **2a** and **2b**[35]

Compound	$E_{1/2}$/V	Δ_{ptp}/mV	i_{red}/i_{ox}	δ/mms^{-1}	Δ/ mms^{-1}
2a	-1.32	60	0.95	0.2237(6)[a]	1.002(1)[a]
	-1.59	60	1.04		
	0.90	69	0.97		
2b[35]	-1.30	61	0.99	0.235(8)[b]	1.081(5)[b]
	-1.60	75	0.97		
	0.86	77	0.97		

[a] Measured at 10 K. [b] Measured at 80 K; from reference [35].

To confirm an octahedral *bis*(DIP)$_2$ ligand environment, the solid-state structure of **2a** was determined by single-crystal X-ray diffraction (XRD). A representation of the cation of **2a** is shown in Figure 2.3 (right), and pertinent bond distances and angles for both **2a** and **2b** [35] included in Table 2.2. In the solid-state, the two neutral, tridentate ligands are bound to iron in a meridional fashion, with the pyridine nitrogens *trans* to each other [N_{pyr}-Fe-N_{pyr} 179.44(11)°]. The Fe atom

sits at the centre of a distorted octahedron, evidenced by N_{imine}-Fe-N_{imine} bond angles of ~160° for each ligand. This bond angle is nearly identical to those reported for sterically unencumbered, four-coordinate Fe(II) structures containing only a single DIP ligand, indicating that packing two DIP ligands around a single Fe atom does not introduce significant strain. When compared with the structure of **2b**,[35] incorporation of a bulkier *tert*-butyl aromatic substituent does not significantly influence the geometry around the Fe metal centre, consistent with their distant placement on the flanking *N*-phenyl rings.

Table 2.2 Selected bond distances (Å) and angles (°) for **2a** (this work) and **2b**[35]

	2a	**2b**
Fe – N_{pyr}		
Fe1 – N1	1.882(4)	1.8707(14)
Fe1 – N4	1.861(4)	1.8655(14)
Fe – N_{imine}		
Fe1 – N2	1.963(4)	1.974(2)
Fe1 – N3	1.986(4)	1.999(2)
Fe1 – N5	1.948(4)	1.9817(14)
Fe1 – N6	1.948(4)	1.9922(14)
N1 – Fe1 – N2	79.83(15)	79.81(6)
N1 – Fe1 – N3	80.42(15)	79.89(6)
N2 – Fe1 – N3	160.23(15)	159.69(6)
N1 – Fe1 – N4	177.84(16)	178.80(6)
N4 – Fe1 – N5	79.71(16)	79.86(6)
N4 – Fe1 – N6	79.81(16)	79.47(6)
N5 – Fe1 – N6	159.51(16)	159.09(6)
N1 – Fe1 – N5	99.78(16)	99.70(6)
N1 – Fe1 – N6	100.71(16)	101.03(6)
N2 – Fe1 – N4	98.08(15)	99.05(6)
N3 – Fe1 – N4	101.68(15)	101.25(6)

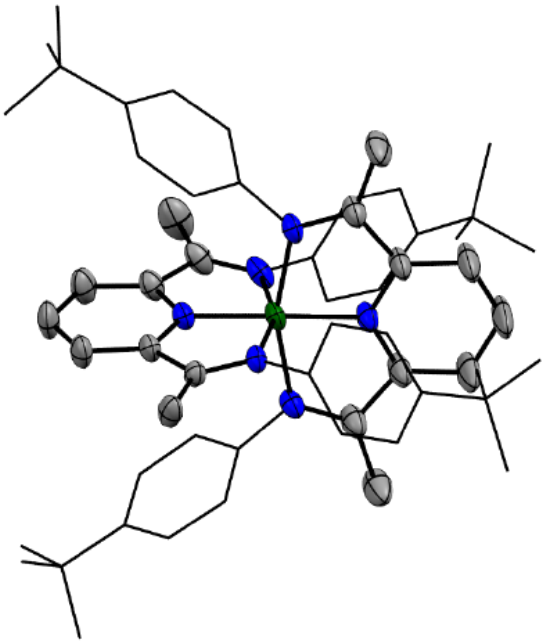

Figure 2.3 (Right) Crystal structure of **2a** with thermal ellipsoids shown at 50 % probability level. Solvent molecules, counterions and hydrogen atoms are omitted for clarity

Cyclic voltammetry (CV) and differential pulse voltammetry (DPV) analysis of **2a** and **2b** revealed nearly identical redox behaviour for both MCCs, with two reversible 1e$^-$ reductions evident at -1.3 V and -1.6 V, and one 1e$^-$ oxidation observed near +0.8 V vs. $FcH^{0/+}$ (Figure 2.4, left). The cathodic events are assigned as ligand-centred based on previous analysis of the redox behaviour of DIP complexes of Fe.[19,34,35] The oxidation peak is similarly assigned to a metal-centred oxidation process (Fe^{2+}/Fe^{3+}). Spectroelectrochemical oxidation of **2a** ($E_{applied}$ = -0.2 to 2.3 V; Figure 2.4a) shows conversion to a single new complex with clear isosbestic points corresponding to the reversible 1e$^-$ redox couple observed by CV at +0.8 V. Bulk reduction of **2a** in a spectroelectrochemical cell ($E_{applied}$ = -0.2 to -1.4 V) showed less well-defined isosbestic points (Figure 2.4b), but the appearance of a shoulder at ~ 800 nm is in line with previously reported spectra for electrochemically reduced **2b**,[35] and the appearance of a low energy band at 1420 nm is consistent with reduction to a single ligand-based radical.[37]

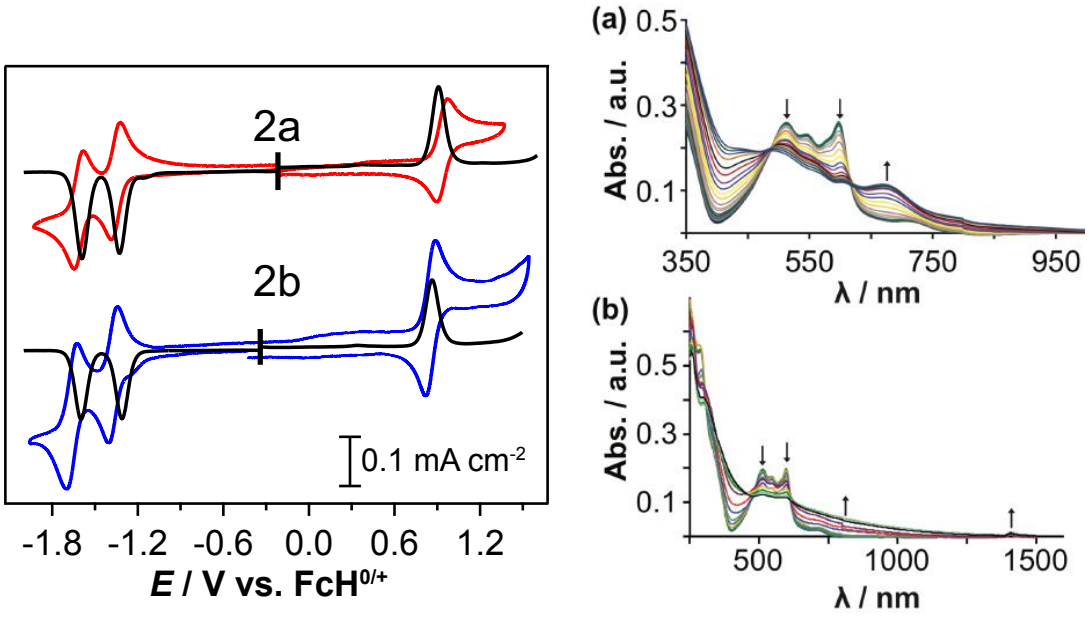

Figure 2.4 Left: CV and DPV of **2a** and **2b**, 0.6 mM of analyte, 0.1 M nBu$_4$PF$_6$ in CH$_3$CN; Right: UV-Vis/NIR spectroelectrochemistry of **2a**, 0.1 M nBu$_4$PF$_6$ in CH$_3$CN (a) oxidative potentials applied from -0.2 to 2.3 V (b) reductive potentials applied from -0.2 to -1.4 V

With respect to electrical energy storage, multiple electron transfers by a single complex offers the possibility of high storage capacity.[8] Furthermore, the potentials of the redox events demonstrated by the MCCs **2a** and **2b** surpass the voltage limits of water (ca. -1.2 V vs. $FcH^{0/+}$).[38] The two reduction events for both **2a** and **2b** are highly reversible by CV (Table 2.1). In particular, both show peak current ratios of close to unity and narrow peak separations, with a slightly larger separation (still close to the Nerstian limit of 59 mV) for the second reduction event.[39] Following electrochemical characterization, suitability of **2a** and **2b** as RFB anolytes was examined.

2.3.2 Charge/Discharge Measurements

Battery cycling at non-dilute concentrations in an H-type cell in the absence of flow were conducted to evaluate the shelf-life stability and potential efficacy of **2a** and **2b** as RFB anolytes. To avoid irreversible processes, potential cut-offs were set according to a wider voltammogram (see SI, Figure S5), which revealed two irreversible reductions at more negative voltages (< -2 V vs. $FcH^{0/+}$). Setting the negative potential cut-off to potentials that allowed for a third and fourth reductive event resulted in irreversible degradation of the MCC, with the colour of the solution changing from purple to brown and formation of a precipitate. In addition, the Coulombic efficiency (% CE) of the cell decreased dramatically after 14 cycles (Figures S2 and S3). For this reason, parameters were set at a cathodic range allowing only the first and second redox couples to be accessed (Figure 2.4 left), avoiding unwanted irreversible redox processes.

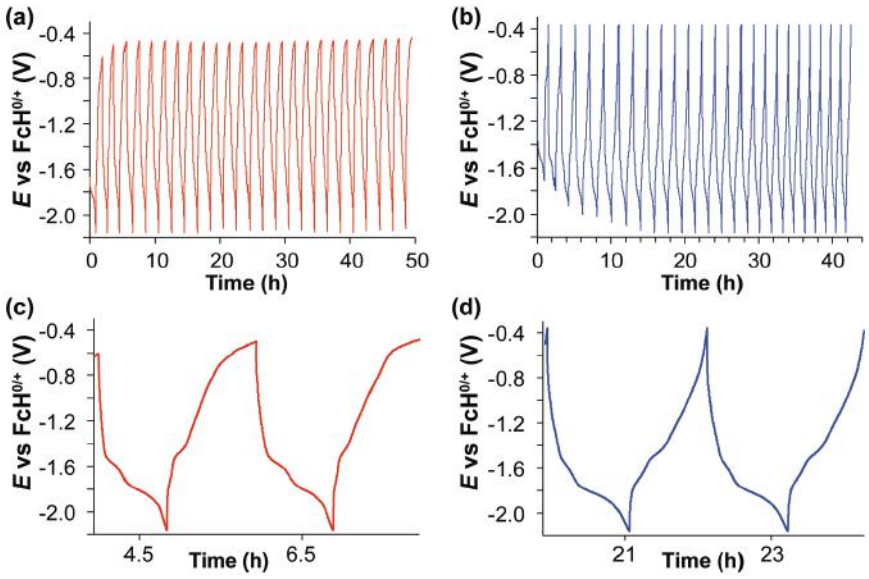

Figure 2.5 Total cell voltage (a and c) for **2a** and (b and d) for **2b**. Both traces with 1.1 mA cathodic/anodic current and charging rate of 1C.

Charge/discharge measurements were performed with MCCs **2a** and **2b** at charging rates of 0.5, 1, and 2 C. A charging rate of 1 C corresponds to a charge/discharge cycle of approximately 1 h, assuming that both 1e- reduction processes are being accessed during the electrolysis process. Charge/discharge cycling of **2a** and **2b** at 1 C (1.1 mA) are shown in Figure 2.5. During the charging segment of **2a**, two plateaus corresponding to the two redox couples seen by CV/DPV (Figure 2.4 left) are observed at -1.57 V and -1.78 V vs. $FcH^{0/+}$. Similarly, for **2b**, the potential was found to plateau at -1.53 V and -1.79 V vs. $FcH^{0/+}$, again agreeing with the results in Figure 2.4. After extended cycling, only one clear reduction plateau at ca. -1.73 V could be observed, with a corresponding oxidation plateau at -1.36 V. In the discharge segment, two plateaus are again observed for **2a** (-0.75 and -1.51 V). While they decrease in prominence after extended cycling, the number of electrons passed per molecule remains high (~ 1.6; Figure 2.6b). For **2b**, plateaus were observed at -1.49 and -0.91 V vs. $FcH^{0/+}$, but also fade away after two cycles. While both

compounds were able to perform the full 25 cycles, the time required for **2a** was slightly longer (49 hrs compared to 42 hrs) with retention of both reduction events, indicative of the higher stability of **2b** to electrochemical cycling.

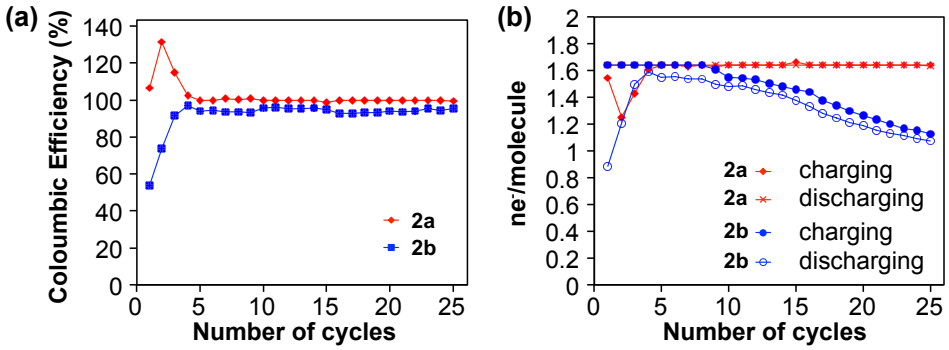

Figure 2.6 (a) Coulombic efficiency (% CE) for **2a** and **2b** at a 1C charging rate; (b) capacity retention for **2a** and **2b** at 1C charging rate

The long-term stability of RFB electrolytes is critical to their application. No decrease in charge capacity was observed for **2a** over extended charge/discharge cycles (Figure 2.6), where the number of electrons stored per molecule of **2a** is ca. 1.6, close to the expected value of 2. For **2b**, the charge capacity was found to drop from 1.6 electrons to 1 electron over 25 cycles (Figure 2.6b), suggesting that only one redox event is being accessed in later cycles. Quantifying the ratio of the charge passed in charging/discharging cycles (Coulombic Efficiency, % CE) for **2a** and **2b** shows that **2a** acts as a reversible anolyte with a high % CE of 99.9(4) % over cycles 5-25. While a reduction in capacity was observed over time, **2b** showed a stable but high % CE of 94(1) % for cycles 4-25. The performance of **2b** is in line with a related two electron anolyte candidate, *tris*(bpy)iron tetrafluoroborate (bpy = bipyridine), for which a decrease in capacitance from two electrons to one electron is similarly observed after 25 cycles,[6] while **2a** outperforms the bpy

analog in terms of stability. While **2a** and **2b** show less stable discharge capacities compared with MCC anolytes based on octahedral Fe^{2+} complexes of monoanionic bipyridylimino isoindoline (BPI) ligands,[8] the cationic nature of **2a** and **2b** does enable their application in common ion exchange RFBs.[6] The lower capacitance exhibited by **2b** could be due to a lower solubility of the reduced form of **2b**, though appreciable solid did not accumulate during battery cycling. Another possible explanation could originate in the slightly wider peak-to-peak separation (75 mV) observed by CV for the second cathodic redox couple of **2b** (Table 2.1). While still close to the Nernstian limit of 59 mV expected for a diffusion-controlled process,[39] the wider separation implies a lower level of electrochemical reversibility, which could over time lead to a decrease in capacitance for **2b** compared with **2a**. Optimal ligand substitution may thus help stabilize the reversibility of the redox couples of DIP MCCs, and increase capacitance in RFB applications. Despite **2a** demonstrating a higher capacitance relative to **2b**, the average number of electrons transferred (ca. 1.6) is still below the value of two expected from CV measurements due to the potential window utilized, which was selected to avoid irreversible reduction events. As the potential window was reached for these compounds at 1 C, the complexes were run at a lower charge rate (0.5 C) to determine if the full $2e^-$ capacity could be attained. Instead, a lower capacitance is observed over cycling, with 0.71 and 0.4 electrons passed for **2a** and **2b** respectively (Figure S9). Similar to the % CE at 1 C, the % CE at 0.5 C was found to reside around 90(4) % for **2a**, with a larger cycle-to-cycle variance observed for **2b** [% CE, 89(10), see Supporting Information].

Electrochemical decomposition appears unlikely due to the reversibility observed both on the CV and electrolysis timescale (% CE plots), with similar number of electrons being passed during charge/discharge cycles. Precipitation or surface adsorption of the reduced species could

reduce the reversibility of the redox processes and is the likely cause of the reduced capacitance. Furthermore, at the lower charging rate employed, crossover of the reduced species to the anode is more likely the cause for decrease in capacity of both **2a** and **2b**, given the longer period required for each cycle. Overall, **2a** presented higher % CE, number of electrons transferred per molecule, capacitance and stability relative to **2b** under the charge rates employed which is attributed to the solubilizing nature of the *t*Bu substituents of the DIP aryl substituents.

Noting the significant impact that the DIP aryl substituent had on the cycling stability, exploration into the impact electron-withdrawing groups (EWGs) might have on both the reduction potentials and cycling stability was proposed. Installation of *para*-EWGs on the flanking phenyl substituents in DIP frameworks, however, is potentially more problematic than electron-donating groups (EDGs). DIPs are typically prepared by condensation of 2,6-diacetylpyridine and the corresponding anilines as shown in Scheme 1.1. Substitution of anilines in the 4-position with EWGs can significantly reduce their nucleophilicity, hampering conversion.[40] For example, condensation syntheses of (*para*-fluoro)phenyl and (*para*-bromo)phenyl-substituted DIPs was achieved with isolated yields of only 24 % and 41 %, respectively, despite azeotropic removal of water.[40] Furthermore, the *para*-nitro analogue could only be isolated in similarly low yields despite a five day acid-catalyzed Dean-Stark reflux in high-boiling *p*-xylene.[41] In seeking to overcome these challenges, a report on the inclusion of EWGs on related ^{Ar}BIAN-type diimine ligands via a Zn-templated synthesis (^{Ar}BIAN = *bis*(aryl)acenaphthenequinonediimine) was considered.[42] Here, the application of this approach to the synthesis of DIP ligands with strong EWGs in relatively high yields under mild conditions is described. This methodology opens the chemical space for the synthesis of DIP ligands that incorporate strong EWGs and so may be useful for the many applications where these ligands are utilized.[43] Furthermore, a report on the synthesis and

electrochemical of properties of their pseudooctahedral Fe(II) complexes for potential use as anolytes in RFB applications is provided.

2.3.3 Synthesis and characterization of ligands and complexes with EWGs

DIP proligand synthesis is generally accomplished by the acid-catalyzed condensation of 2,6-diacetylpyridine with two equivalents of the appropriately substituted aniline. To avoid forcing conditions required for appreciable conversion using anilines substituted in the 4-position with electron-withdrawing groups (EWGs), a templated synthesis was employed. Templated ligand syntheses have long been used to overcome competing side reactions,[44] but can also be used to drive ligand formation reactions to completion that would otherwise suffer from less favourable thermodynamics in the absence of coordination to a templating metal ion.[45] The templated synthesis of imine-based ligands, for example, has enabled construction of complex scaffolds including chiral *P^N^N* and *P^N^N^P* multidentate architectures.[46] In comparison, reports of demetallation and subsequent use of the liberated proligands appear less often[47] than the targeted assembly of coordination complexes templated by a metal ion of choice. For imines, attempts to demetallate can lead to ligand hydrolysis. In the case of ^{Ar}BIAN ligands constructed around Zn^{2+} as a templating ion, the use of oxalate ($C_2O_4^{2-}$) as a displacing ligand produces insoluble ZnC_2O_4 and drives demetallation reactions to completion without any evidence of hydrolysis.[42]

Four (DIP)$ZnCl_2$ complexes (**3c-f,** Scheme 1.2) were prepared via the Zn^{2+}-templated condensation of two equivalents of aniline with 2,6-diacetylpyridine, broadly following the protocol for incorporating strong EWGs in ^{Ar}BIANs outlined by Ragaini.[42] Complex **3c** (R = H) has been previously reported.[48] Each of **3c-f** was prepared in this way by heating slightly more than two equivalents of the appropriate aniline (15 % excess) with 2,6-diacetylpyridine and excess

$ZnCl_2$ in CH_3OH (acetic acid for **3f**). Unlike complexes based on the acenaphthoquinone (^{Ar}BIAN) backbone,[42] using acetic acid as the solvent leads to full solubilization of the (DIP)$ZnCl_2$ fluoro- and bromo-derivatives, but partial solubilization of the cyano-derivative. Changing the reaction solvent to methanol, the crude (DIP)$ZnCl_2$ product precipitates as a yellow powder upon cooling to room temperature and can be filtered to easily separate **3c-f** from excess reactants. The (DIP)$ZnCl_2$ complexes can then be recrystallized by dissolving in hot acetonitrile solutions and slowly cooling to -20 °C. ^{1}H NMR spectra for **3c-f** show a single, pseudo C_{2v}-symmetric magnetic environment in solution for all Zn complexes. Diagnostic resonances for the formation of the imine arms can also be observed by $^{13}C\{^1H\}$ NMR at δ = ~165 ppm. The molecular formula for each compound was confirmed by high-resolution mass spectrometry (HR-MS).

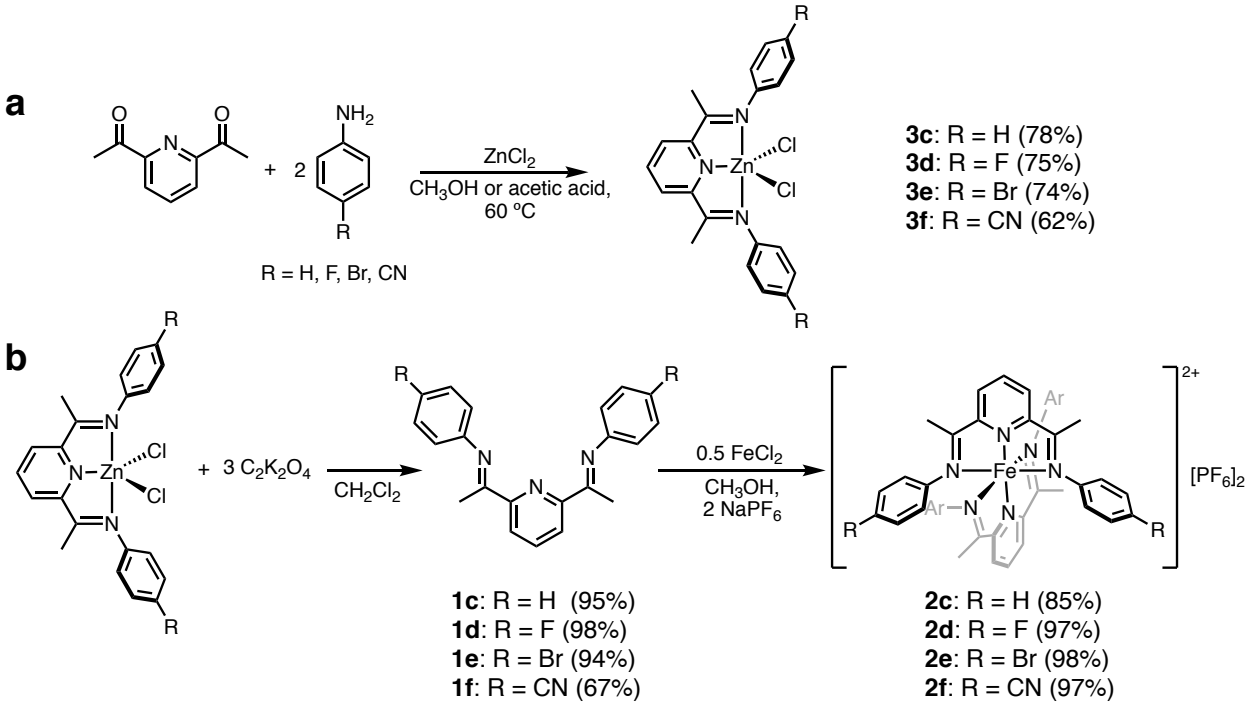

Scheme 2.2 Synthesis of (a) (DIP)$ZnCl_2$ complexes **3c-f**; (b) free proligands **1c-f** via de-zincation, and [*bis*(DIP)$_2$Fe][PF_6]$_2$ complexes **2c-f** with isolated yields in parentheses.

To confirm the structures of the (DIP)$ZnCl_2$ complexes suggested by solution NMR and HR-MS, solid-state structures of **3c-f** were also determined by single-crystal X-ray diffraction (XRD; Figure 2.7). In each case, a single DIP ligand is bound to Zn in a meridional, tridentate fashion and forms part of what is best described as a distorted square-based pyramid with τ_5 values[49] ranging from 0.30 (**3e**) to 0.40 (**3f**). This deviation from ideal geometry arises from different N_{pyr}-Zn-Cl angles. The two chlorides cant asymmetrically away from the pyridine ring, opening one N_{pyr}-Zn-Cl angle wider than the other. The relatively long Zn-N_{pyr} and Zn-N_{imine} distances, typical of (*N*-heterocycle/imine)-Zn^{2+} coordination,[50] are consistent across the series **3d-f** at ~2.08 Å and 2.21–2.26 Å, respectively. As a result, the N_{imine}-Zn-N_{imine} angles are quite pulled back (147-148°). The narrow range of bond distances and angles observed for the set of (DIP)$ZnCl_2$ complexes is consistent with the distal placement of the R groups on the ligand periphery.

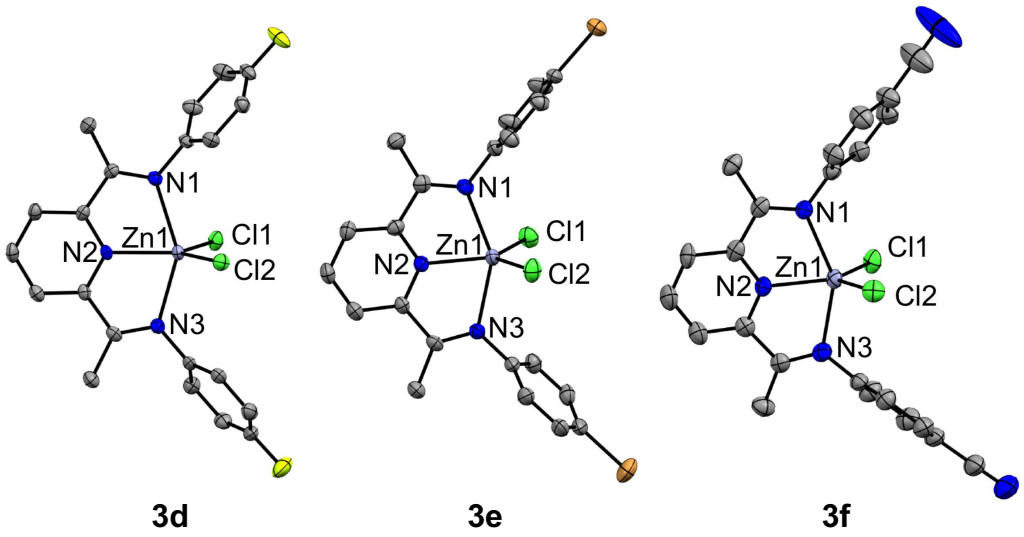

Figure 2.7 Crystal structures of **3d-f** with thermal ellipsoids shown at 50 % probability level. Hydrogen atoms and solvent molecules are omitted for clarity

The free proligands (**1c-f**) can be displaced from the $ZnCl_2$ unit and isolated in good to excellent yields (67-98 %) by mixing dichloromethane solutions of **3c-f** with aqueous solutions containing three equivalents of potassium oxalate, then extracting and drying the organic layer. The molecular composition of the resulting off-white/yellow solids as demetallated ligand was confirmed by multinuclear NMR, with shifts observed to all signals, including those attributed to the diagnostic imine carbon nuclei ($\delta_{C=N}$ = ~168 ppm). Iron MCCs **2c-f** were subsequently prepared by reaction of the desired proligand with 0.5 equivalents of anhydrous $FeCl_2$ and two equivalents of $NaPF_6$ in CH_3OH. These complexes were isolated as air and moisture-stable deep purple solids, with molecular formulae again confirmed by HR-MS. Multinuclear NMR suggests a symmetric environment around the Fe(II) centre with ^{13}C resonances for the diagnostic imine carbon centers shifted considerably downfield to $\delta_{C=N}$ ~180 ppm, with the most downfield resonance observed for **2f** ($\delta_{C=N}$ = 182 ppm), consisted with the most deshielded imine carbon. The dark purple colour of **2c-f** is reflected in strong and broad low energy features in the steady-state UV-Vis absorption spectra (Figure 2.8). These transitions are assigned as MLCT in character, as is typical of $[(DIP)_2Fe]^{2+}$ complexes.[35,51] Within the series, **2f** showed a marked hypsochromic absorption shift in the transitions observed beyond 400 nm, but otherwise, a consistent absorption profile is observed for all four complexes.

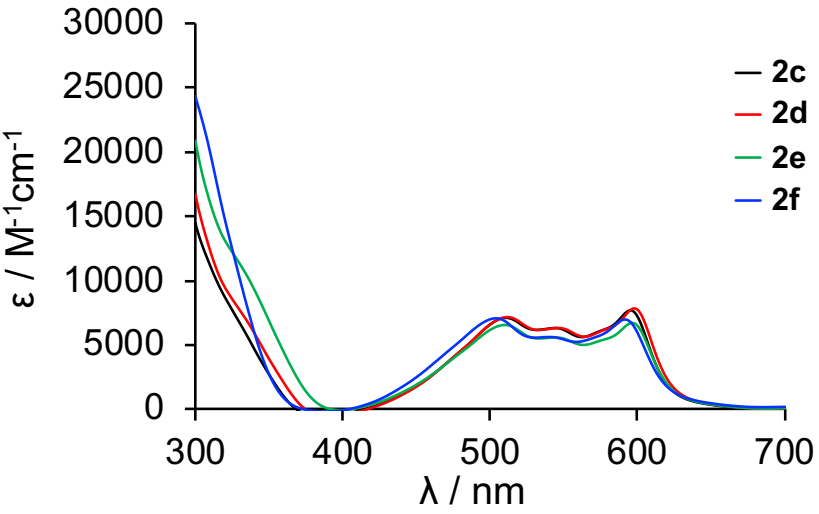

Figure 2.8 UV-vis absorption spectra of **2c-f** in CH_3CN

The pseudo-octahedral coordination environment around Fe was confirmed by XRD studies of **2e** and **2f** (Figure 2.9). A much tighter coordination environment can be seen with the Fe complexes compared with the Zn congeners (Tables 2.3 and S1), with closer M-N distances ranging from 1.86-1.87 Å for Fe-N_{pyr} and 1.96-2.00 Å for Fe-N_{imine}. As a result, the intraligand N_{imine}-Fe-N_{imine} angles are much larger at ~160°.

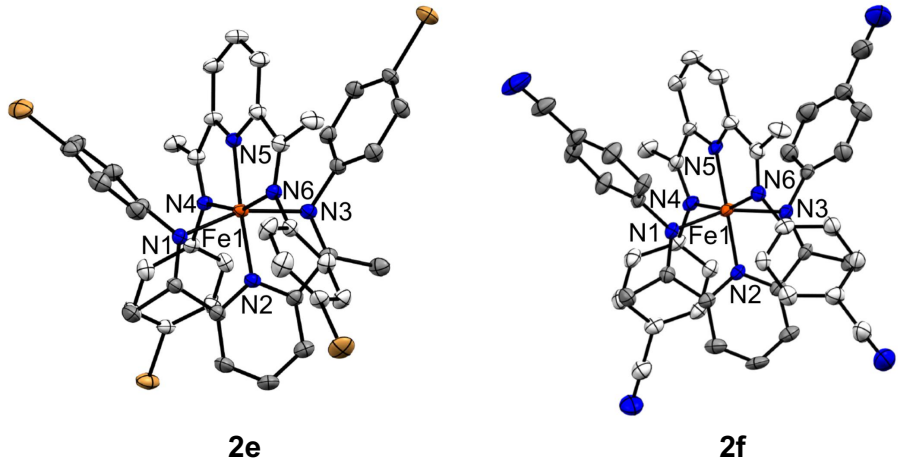

Figure 2.9 Crystal structures of **2e-f** with thermal ellipsoids shown at 50 % probability level. Hydrogen atoms and solvent molecules are omitted for clarity

Table 2.3 Selected bond distances (Å) for **3d-f** (Zn) and **2e-f** (Fe).

	3d	3e	3f	2e	2f
M – N$_{pyr}$					
M1 – N2	2.080(3)	2.081(4)	2.084(4)	1.870(3)	1.860(3)
M1 – N5(7) [a]	-	-	-	1.867(3)	1.865(3)
M – N$_{imine}$					
M1 – N1	2.210(3)	2.234(4)	2.245(4)	1.985(3)	1.981(3)
M1 – N3	2.258(3)	2.245(4)	2.240(4)	1.968(3)	1.963(3)
M1 – N4(6) [a]	-	-	-	1.998(3)	1.977(4)
M1 – N6(8) [a]	-	-	-	1.992(3)	1.980(4)
C$_{imine}$ – N$_{imine}$					
C1 – N1	1.273(5)	1.271(6)	1.280(6)	1.303(5)	1.305(5)
C8 – N3	1.281(5)	1.273(6)	1.281(6)	1.298(4)	1.302(5)
C22(23) – N4(6) [a]	-	-	-	1.299(5)	1.299(5)
C29(31) – N6(8) [a]	-	-	-	1.297(5)	1.299(5)
C$_{Ar}$ – N$_{imine}$					
C10 – N1	1.434(5)	1.422(7)	1.421(6)	1.433(3)	1.441(5)
C16(17) – N3 [a]	1.429(5)	1.420(7)	1.419(6)	1.435(5)	1.441(5)
C31(33) – N4(6) [a]	-	-	-	1.437(5)	1.442(5)
C37(40) – N6(8) [a]	-	-	-	1.439(5)	1.440(5)
Zn-Cl					
Zn1-Cl1	2.2570(10)	2.2439(14)	2.2437(11)	-	-
Zn1-Cl2	2.2375(10)	2.2324(13)	2.2316(13)	-	-
Zn2-Cl3	2.2433(10)	2.2337(14)	-	-	-
Zn2-Cl4	2.2526(10)	2.2300(14)	-	-	-

[a] Atom labels in parentheses are for cyano derivatives **3f** and **2f**

Cyclic voltammetry (CV) and differential pulse voltammetry (DPV; Figure 2.10, Table 2.4) revealed nearly identical redox behaviour for the series **2c-f**, with two reversible 1e$^-$ reductions evident between -1.0 and -2.0 V and a 1e$^-$ oxidation observed near +1.0 V vs FcH$^{0/+}$ (FcH = ferrocene). Based on the previous analysis of the redox behaviour of DIP complexes of Fe, the cathodic events are assigned as ligand centered.[35] The oxidation is attributed to a metal-centered Fe$^{2+/3+}$ couple. Each of the three redox events observed for **2c-f** are shifted anodically compared to those observed for [*bis*(DIP)$_2$Fe]$^{2+}$ analogs bearing electron releasing OMe (**2a**) or *t*Bu (**2b**) substituents.[51] This highlights the ability to tune redox potentials using distal substitution of the *N*-arene rings. In accordance with their Hammett parameters,[52] the largest anodic shift is observed

for R = CN, followed by R = Br and R = F consistent with the inductive removal of electron density from the imine-based LUMO.

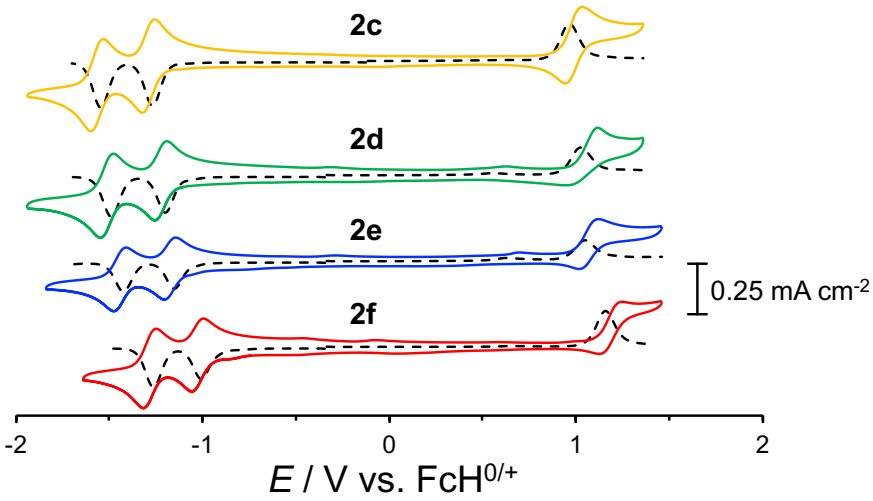

Figure 2.10 CV and DPV of **2c-f**, 0.6 mM of analyte, 0.1 M nBu$_4$PF$_6$ in CH$_3$CN

The reversibility of the ligand-based reductions as observed by CV does not seem to be as adversely affected by the introduction of EWGs as the $Fe^{2+/3+}$ couples, which are much more reversible for **2a-b** likely as a result of occurring at less positive potentials.[51] In particular, both cathodic events show peak current ratios near to unity and narrow peak-to-peak separations close to the Nernstian limit of 59 mV.[39] Moreover, the potentials surpass the voltage limits of water (*ca.* -1.2 V vs $FcH^{0/+}$)[38] and the multiple electron transfers possible with a single complex suggest the possibility of high energy storage capacity.[8] **2c-f** were therefore subject to evaluation of their suitability as RFB anolytes.

2.3.4 Charge/discharge measurements

Cycling measurements were performed on **2c-f** using a reticulated vitreous carbon (RVC) working electrode in a bulk electrolysis cell to examine the viability of these compounds as RFB anolytes. The maximum cathodic potentials were set according to the CV/DPV collected for each compound to ensure capture of the second reversible redox event without going so far as to irreversibly reduce the complexes.[51] The charge/discharge cycling experiments for **2c-f** are shown in Figure 2.11. While less pronounced than those observed for **2a-b**,[51] two plateaus corresponding to the two reduction events observed by CV/DPV can be seen in the charging segment. In the discharge segment, two plateaus corresponding to the reverse oxidation events can similarly be noted (Figure 2.11b). These decrease in prominence after extended cycling.

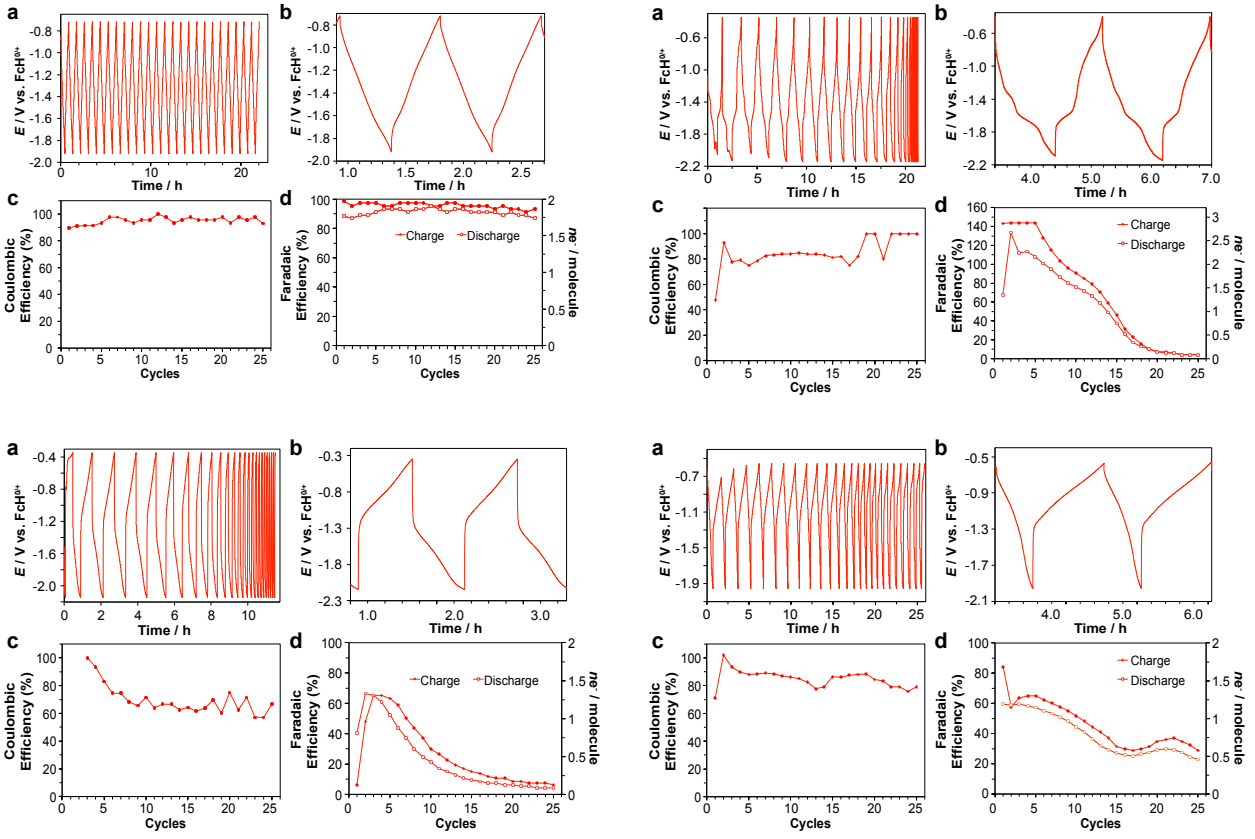

Figure 2.11 (a and b) Total cell voltage, (c) coulombic efficiency, and (d) capacity retention for **2c** (top left), **2d** (top right), **2e** (bottom left) and **2f** (bottom right). Anodic and cathodic current set to 7 mA with a charging rate of 1 C; in 0.3 M nBu_4PF_6 acetonitrile solution.

The cycling stability of RFB electrolytes is one of a number of key parameters for evaluating the potential for commercial application.[53] Through 25 cycles, **2c** exhibits a Coulombic efficiency (% CE) of 95.2 % (Figure 2.11c, top left), comparable to reported values for aqueous Li/I RFBs over 20 cycles,[54] but passing an average of ~1.9 electrons per molecule out of a theoretical maximum of 2 (Figure 2.11d, top left, Table 2.4). Zn-I flow batteries, in comparison have been reported to exhibit extended stability over 300 cycles, with a one-electron redox couple.[55] Compared to complexes bearing donating groups (**2a-b**),[51] **2c** surpasses the Faradaic efficiency (% FE) and number of electrons per molecule observed without any evidence of degradation. For **2d-f,** over the course of extended cycling, the cycles become narrower resulting in reduced, overall efficiency parameters (Table 2.4, Figure 2.11). It is noted that the potentials for reduction of organic aryl halides and nitriles[56] fall close to those observed for the reductions of **2a-f**. Over time, irreversible chemical reduction of these groups may contribute an underlying degradation pathway for the ligands that include these substituents. Indeed, slightly less Nernstian peak parameters are observed by CV for **2d-f** (Table 2.4).

Table 2.4 Electrochemical and RFB parameters for 2**a-f**.[a]

	$E_{1/2}$/V	Δ_{ptp}/mV	i_{red}/i_{ox}	CE/%	FE/%	e⁻ / mol.
2c	-1.55	67	0.88			
	-1.27	65	1.14	95.2	93.4	1.9
	0.97	82	0.86			
2d	-1.49	69	0.90			
	-1.20	66	1.16	84.8	61.2	1.2
	1.03	158	0.23			
2e	-1.43	65	0.86			
	-1.15	59	1.23	95.2	24.6	0.5
	1.05	103	0.68			
2f	-1.26	68	0.87			
	-1.01	62	1.31	85.0	42.6	0.9
	1.16	138	0.68			
2a[b]	-1.60	75	0.97			
	-1.30	61	0.99	94.3	70.0	1.4
	0.86	77	0.97			
2b[b]	-1.59	60	1.04			
	-1.32	60	0.95	>99.9	82.1	1.6
	0.90	69	0.97			

[a] Average Coulombic efficiency (CE), average Faradaic efficiency (FE) taken by averaging charging and discharging FE, and average number of electrons cycled taken by averaging number of electrons cycled upon charging and discharging. [b] Values taken from reference[51]

2.4 Conclusions

This work describes the utility of base metal coordination complexes supported by the well-known redox-active diiminepyridine (DIP) ligand scaffold in redox-flow battery applications. It also presents a facile synthetic route for the incorporation of strong EWGs into the *para* position of the flanking aryl substituents on DIP ligands. This Zn-templated methodology offers higher yields, shortened reaction times and requires considerably milder conditions than previously reported for analogous DIPs,[40,41] expanding the chemical scope available in the construction of these increasingly widely used ligands.[57] Isolation of DIP ligands bearing strong EWG has also enabled the high-yielding synthesis of new $[(DIP)_2Fe]^{2+}$ salts **2d-f**, along with novel, structurally

characterized examples of (DIP)$ZnCl_2$ complexes **3c-f**. The high solubility, reversible electrochemistry and multi-electron storage capability of the ligand and metal make these MCCs interesting candidates as RFB anolytes and catholytes. Regarding the potential application of **2a-f** in RFBs, **2a** and **2c** are shown to be viable candidates as an RFB anolytes, displaying long-term stability over extended cycling and access to multiple electrons equivalents per molecule (1.6-1.9) over this range, on par with the leading complexes in this area.[8] The use of halides or pseudohalides at the ligand periphery, however, was found to be detrimental to cycling performance. This observation should help guide future ligand designs for MCCs for RFB applications.

2.5 Experimental Section

Unless otherwise specified, all air sensitive manipulations were carried out either in a N_2 filled glove box or using standard Schlenk techniques under Ar. Proligand **1b** was prepared according to a literature procedure.[58] $FeCl_2$ (Acros), $NaPF_6$ (Alfa Aesar), $NaBPh_4$ (Sigma-Aldrich), $ZnCl_2$ (Alfa Aesar), 4-fluoroaniline (Combi Blocks), 4-bromoaniline (Acros Organics), aniline (Sigma Aldrich), 4-aminobenzonitrile (Combi Blocks), 2, 6-diacetylpyridine (Combi Blocks), $K_2[C_2O_4]$ (Alfa Aesar), $FeCl_2$ (Acros Organics), $NaPF_6$ (Alfa Aesar), acetic acid and methanol (Fisher Scientific) and $n$$Bu_4NPF_6$ (electrochemical grade, Sigma-Aldrich) were purchased and used without further purification. Organic solvents were dried and distilled using appropriate drying agents prior to use. 1- and 2D NMR spectra were recorded on Bruker Avance 300 MHz or Bruker Avance-III 500 MHz spectrometers. ^1H and $^{13}C\{^1H\}$ NMR spectra were referenced to residual solvent peaks. Electronic absorption spectra were recorded on an Agilent Technologies Cary 5000 Series UV-Vis-NIR spectrophotometer in dual beam mode (range: 230 – 1600 nm). Mössbauer experiments were performed in transmission geometry with a ^{57}Co in Rh

source and a WissEl constant acceleration drive. Spectra were collected at 10 K using a Janis SHI-850 closed-cycle refrigerator and are calibrated relative to α-Fe at room temperature.

2.5.1 Synthesis

Synthesis of proligand **1a**: A 100 mL Schlenk flask was charged with 2,6-diacetylpyridine (1.11 g, 6.80 mmol) and dissolved in dry dichloromethane (20 mL). To this solution, Na_2SO_4 (1.94 g, 13.6 mmol) was added. 4-*tert*-Butylanline (3.04 mL. 19.1 mmol) was added via syringe to the solution as well as 2 drops of formic acid. The solution was allowed to stir for 48 h at room temperature. The solvent was then removed and the residue redissolved in toluene and washed with a saturated solution of Na_2CO_3 (3 x 50 mL). The organic fraction was dried over Na_2SO_4 and filtered. The solvent was removed and the solid was stirred in cold ethanol (100 mL) and then filtered. Isolated yield: 2.30 g (79 %). The NMR matches the reported literature.[58]

Synthesis of **2a**: A 100 mL Schlenk flask was charged with $FeCl_2$ (0.022 g, 0.18 mmol) and **1a** (0.15 g, 0.35 mmol) under N_2. Degassed MeOH (30 mL) was added and the solution immediately turned dark purple. The reaction mixture was allowed to stir for 30 min at 22 °C. Solid $NaBPh_4$ (0.18 g, 0.53 mmol) was then added and the mixture stirred for an additional 30 min. The solvent was then removed and the purple solid dissolved in CH_2Cl_2 and filtered over Celite. The filtrate was concentrated and pentane added (100 mL) to precipitate the product as a purple solid. Isolated yield: 0.281 g (90 %). ^{1}H NMR (CD_3CN, 300 MHz, 25°C): δ 7.96 (m, 6H, C_{Ar}-*H*), 7.30 (ddd, 20H, J_{HH} = 8.0, 5.2, 2.5 Hz, [BPh_4] C_{Ar}-*H*), 7.19 – 7.14 (m, 8H, C_{Ar}-*H*), 6.99 (t, 20H, J_{HH} = 7.4 Hz, [BPh_4] C_{Ar}-*H*), 6.89 – 6.82 (m, 8H, C_{Ar}-*H*), 6.12 – 6.04 (m, 8H, C_{Ar}-*H*), 2.50 (s, 12H, C*H*$_3$), 1.21 ppm (s, 36H, *t*Bu). ^{13}C{^{1}H} NMR (CD_3CN, 75 MHz, 25°C): δ 178.8 (*C*=N), 165.8 – 163.8 (q,

1:1:1:1, J_{CB} = 49 Hz, C_{Ar}-B), 160.1 (CAr), 152.2 (C_{Ar}), 141.8 (C_{Ar}), 136.8 (C_{Ar}), 136.5 (C_{Ar}), 127.4 (C_{Ar}), 127.3 (C_{Ar}), 126.6 (dd, J_{CB} = 5.6, 2.7 Hz, C_{Ar}), 122.8 (C_{Ar}), 119.7 (C_{Ar}), 35.2 ($C(CH_3)_3$), 31.3 ($C(CH_3)_3$), 19.4 ppm (CH_3). Anal. Calcd for $C_{106}H_{110}B_2N_6Fe_1$: C, 82.38; H, 7.17. Found: C, 82.20; H, 7.16. Complex **2a** was synthesized with hexafluorophosphate counterion for battery tests: synthetic procedure as above using $FeCl_2$ (0.030 g, 0.23 mmol), **1a** (0.2 g, 0.5 mmol) and $NaPF_6$ (0.118 g, 0.70 mmol). Isolated yield: 0.281 g (94 %). ^{1}H NMR (CD_3CN, 300 MHz, 25 °C): δ 8.05 (s, 3H, C_{Ar}-*H*), 7.17 (d, 4 H, J_{HH} = 8.7 Hz, C_{Ar}-*H*), 6.11 (d, 4 H, J_{HH} = 8.7 Hz, C_{Ar}-*H*), 2.58 (s, 6 H, CH_3), 1.19 ppm (s, 18 H, *t*Bu). $^{13}C\{^1H\}$ NMR (CD_3CN, 75 MHz, 25 °C): δ 178.8 (*C*=N), 160.2 (C_{Ar}), 152.1 (C_{Ar}), 141.8 (C_{Ar}), 136.5 (C_{Ar}), 127.4 (C_{Ar}), 119.7 (CAr), 35.2 ($C(CH_3)_3$), 31.3 ($C(CH_3)_3$), 19.3 ppm (CH_3). UV-Vis (CH_3CN): λ (ε) 287 (25 190), 339 (sh), 513 (8 100), 545 (7 140), 598 nm (8 310 M^{-1} cm^{-1}).

Synthesis of **2b**: Complex **2b** has been previously published.[35] Here, **2b** was prepared using an identical procedure to **2a** using $FeCl_2$ (0.025 g, 0.20 mmol), **1b** (0.15 g, 0.40 mmol) and $NaPF_6$ (0.101 g, 0.60 mmol). Isolated yield: 0.199 g (91 %). Additional solution characterization data: ^{1}H NMR (CD_3CN, 300 MHz, 25 °C): δ 8.15 (s, 3H, C_{Ar}-*H*), 6.67 (d, 4 H, J_{HH} = 8.9 Hz, C_{Ar}-*H*), 6.10 (d, 4 H, J_{HH} = 8.9 Hz, C_{Ar}-*H*), 3.69 (s, 6 H, OCH_3), 2.56 ppm (s, 6 H, CH_3). $^{13}C\{^1H\}$ NMR (CD_3CN, 75 MHz, 25 °C): δ 179.24 (*C*=N), 160.34 (C_{Ar}), 159.80 (C_{Ar}), 137.77 (C_{Ar}), 136.62 (C_{Ar}), 127.76 (C_{Ar}), 121.83 (C_{Ar}), 115.65 (C_{Ar}), 56.29 (OCH_3), 19.44 ppm (CH_3). UV-Vis (CH_3CN): λ (ε) 291 (23 930), 343 (12 050), 518 (7 400), 549 (6 690), 603 nm (7,520 M^{-1} cm^{-1}).

Synthesis of **3c**: In a thick-walled flask, $ZnCl_2$ (0.250 g, 1.83 mmol) and 2,6-diacetylpyridine (0.102 g, 0.627 mmol) were combined with methanol (2.5 mL) giving a colourless precipitate.

This mixture was heated to 60 °C, and aniline (0.134 g, 1.43 mmol; 0.13 mL) added to the hot solution. The flask was then sealed with a Teflon stopper and heated to 90 °C for 4 h behind a blast shield. A yellow precipitate was formed upon cooling to room temperature and collected by filtration. The solid product was recrystallized from acetonitrile and washed with chloroform to give a light-yellow powder. Isolated yield: 0.220 g (78 %). ^{1}H NMR (CD_3CN, 500 MHz, 25 °C): δ 8.53 (m, 1H; PyrH_p), 8.41 (m, 2H; PyrH_m), 7.45 (m, 4H; Ar*H*), 7.29 (m, 2H; Ar*H*), 7.21 (m, 4H; Ar*H*), 2.46 ppm (s, 6H; N=C*Me*). ^{13}C{^{1}H} NMR (CD_3CN, 125 MHz, 25 °C): δ 164.9 (Me*C*=N), 149.7 (C_{Ar}), 147.6 (C_{Ar}), 144.9 (C_{Ar}), 129.6 (C_{Ar}), 128.1 (C_{Ar}), 126.9 (C_{Ar}), 122.8 (C_{Ar}), 17.4 ppm (CH_3). MS (ESI-TOF/MS, m/z) calcd for $C_{21}H_{19}ClN_3Zn$ $[M]^+$, 412.0553; found 412.0550.

Synthesis of **3d**: Procedure as for **3c** using: $ZnCl_2$ (0.250 g, 1.83 mmol), 2,6-diacetylpyridine (0.103 g, 0.631 mmol), methanol (2.5 mL), and 4-fluoroaniline (0.164 g, 1.48 mmol; 0.14 mL). Light-yellow powder. Isolated yield: 0.230 g (75 %). ^{1}H NMR (CD_3CN, 500 MHz, 25 °C): δ 8.54 (m, 1H; PyrH_p), 8.41 (m, 2H; PyrH_m), 7.25 (m, 4H; Ar*H*), 7.19 (m, 4H; Ar*H*), 2.47 ppm (s, 6H; N=C*Me*). ^{13}C{^{1}H} NMR (CD_3CN, 125 MHz, 25°C, ppm): δ 165.6 (Me*C*=N), 161.8 (d, J_{CF} = 241.3 Hz; C_{Ar}), 149.7 (C_{Ar}), 144.9 (C_{Ar}), 143.7 (d, J_{CF} = 3.75 Hz; C_{Ar}), 128.2 (C_{Ar}), 124.8 (d, J_{CF} = 7.5 Hz; C_{Ar}), 116.3 (d, J_{CF} = 23.8 Hz; C_{Ar}), 17.5 ppm (CH_3). ^{19}F{^{1}H} NMR (CD_3CN, 282 MHz, 25 °C): δ -118.9 ppm (s). MS (ESI-TOF/MS, m/z) calcd for $C_{21}H_{17}ClN_3ZnF_2$ $[M]^+$, 448.0365; found 448.0367.

Synthesis of **3e**: Procedure as for **3c** using: $ZnCl_2$ (1.00 g, 7.32 mmol), 2,6-diacetylpyridine (0.398 g, 2.44 mmol) methanol (8 mL) and 4-bromoaniline (0.880 g, 5.12 mmol). Light brown powder. Isolated yield: 1.10 g (74 %). ^{1}H NMR (CD_3CN, 300 MHz, 25 °C): δ 8.54 (m, 1H; PyrH_p), 8.42

(m, 2H; PyrH_m), 7.60 (m, 4H; Ar*H*), 7.15 (m, 4H; Ar*H*), 2.47 ppm (s, 6H; N=C*Me*). $^{13}C\{^1H\}$ NMR (CD_3CN, 125 MHz, 25 °C): δ 165.6 (Me*C*=N), 149.3 (C_{Ar}), 146.4 (C_{Ar}), 144.8 (C_{Ar}), 132.5 (C_{Ar}), 128.1 (C_{Ar}), 124.7 (C_{Ar}), 119.7 (C_{Ar}), 17.4 ppm (CH_3). MS (ESI-TOF/MS, m/z) calcd for $C_{21}H_{17}ClN_3ZnBr_2$ $[M]^+$, 567.8764; found 567.9041.

Synthesis of **3f**: In a thick-walled flask, $ZnCl_2$ (1.00 g, 7.34 mmol) and 2,6-diacetylpyridine (0.440 g, 2.70 mmol) were combined with acetic acid (8 mL) giving a colourless precipitate. This mixture was heated to 60 °C and 4-aminobenzonitrile (0.744 g, 6.3 mmol) added to the hot solution. The flask was then sealed with a Teflon stopper and heated to 130 °C for 3 h behind a blast shield. A yellow precipitate was formed upon cooling to room temperature and collected by filtration. The solid was suspended in diethyl ether and stirred for 10 min. This suspension was filtered and the collected solid washed with an additional 3 x 15 mL of diethyl ether, then dried *in vacuo*. Yellow solid. Isolated yield: 0.836 g (62 %). ^1H NMR (CD_3CN, 300 MHz, 25 °C): δ 8.60 (m, 1H; PyrH_p), 8.48 (m, 2H; PyrH_m), 7.81 (m, 4H; Ar*H*), 7.32 (m, 4H; Ar*H*), 2.46 ppm (s, 6H; N=C*Me*). $^{13}C\{^1H\}$ NMR (CD_3CN, 75 MHz, 25 °C): δ 167.4 (Me*C*=N), 151.0 (C_{Ar}), 149.0 (C_{Ar}), 145.5 (C_{Ar}), 134.1 (C_{Ar}), 128.8 (C_{Ar}), 123.6 (C_{Ar}), 119.4 (*C*≡N), 110.4 (C_{Ar}) 17.9 ppm (CH_3). MS (ESI-TOF/MS, m/z) calcd for $C_{23}H_{17}ClN_5Zn$ $[M]^+$, 462.0458; found 462.0447.

General Procedure for the Isolation of Decoordinated Proligands: Zn complexes **3c-f** (1 mmol) were each suspended in CH_2Cl_2 (50 mL) in a separatory funnel. An aqueous solution (20 mL) of potassium oxalate (3 mmol) was then added and the mixture was shaken for 5 min, giving a cloudy aqueous layer over a yellow organic layer. The organic layer was washed with an

additional 2 x 30 mL of water, stirred over Na_2SO_4, and the volatiles removed under reduced pressure.

Synthesis of proligand **1c**: Isolated yield: 0.298 g (95 %). ^{1}H NMR ($CDCl_3$, 300 MHz, 25 °C): δ 8.35 (d, 2H, J_{HH} = 7.8 Hz; PyrH_m), 7.88 (t, 1H, J_{HH} = 7.8 Hz; PyrH_p), 7.39 (t, 4H, J_{HH} = 7.9 Hz; Ar*H*), 7.13 (m, 2H; Ar*H*), 7.85 (m, 4H; Ar*H*), 2.41 ppm (s, 6H; N=C*Me*). ^{13}C{^{1}H} NMR ($CDCl_3$, 75 MHz, 25 °C): δ 167.5 (Me*C*=N), 155.6 (C_{Ar}), 151.4 (C_{Ar}), 137.0 (C_{Ar}), 129.2 (C_{Ar}), 123.8 (C_{Ar}), 122.4 (C_{Ar}), 119.4 (C_{Ar}), 16.4 ppm (CH_3).

Synthesis of proligand **1d**: Isolated yield: 0.342 g (98 %). ^{1}H NMR ($CDCl_3$, 300 MHz, 25 °C): δ 8.32 (d, 2H, J_{HH} = 7.8 Hz; PyrH_m), 7.88 (t, 1H, J_{HH} = 7.8 Hz; PyrH_p), 7.08 (m, 4H; Ar*H*), 6.81 (m, 4H; Ar*H*), 2.41 ppm (s, 6H; N=C*Me*). ^{13}C{^{1}H} NMR ($CDCl_3$, 75 MHz, 25 °C): δ 168.2 (Me*C*=N), 159.7 (d, J_{CF} = 241.2 Hz; F-C_{Ar}), 155.5 (C_{Ar}), 147.3 (d, J_{CF} = 2.8 Hz; C_{Ar}), 137.0 (C_{Ar}), 122.5 (C_{Ar}), 120.9 (d, J_{CF} = 7.9 Hz; C_{Ar}), 115.8 (d, J_{CF} = 22.5 Hz; C_{Ar}), 16.4 ppm (CH_3). ^{19}F{^{1}H} NMR ($CDCl_3$, 282 MHz, 25 °C): δ -120.5 ppm (s).

Synthesis of proligand **1e**: Isolated yield: 0.443 g (94 %). ^{1}H NMR ($CDCl_3$, 300 MHz, 25 °C): δ 8.32 (d, 2H, J_{HH} = 7.8 Hz; PyrH_m), 7.88 (t, 1H, J_{HH} = 7.8 Hz; PyrH_p), 7.49 (m, 4H; Ar*H*), 6.73 (m, 4H; Ar*H*), 2.39 ppm (s, 6H; N=C*Me*). ^{13}C{^{1}H} NMR ($CDCl_3$, 75 MHz, 25 °C): δ 168.1 (Me*C*=N), 155.3 (C_{Ar}), 150.3 (C_{Ar}), 137.1 (C_{Ar}), 132.2 (C_{Ar}), 122.7 (C_{Ar}), 121.3 (C_{Ar}), 116.8 (C_{Ar}), 16.4 ppm (CH_3).

Synthesis of proligand **1f**: Isolated yield: 0.243 g (67 %). ^{1}H NMR ($CDCl_3$, 300 MHz, 25 °C): δ 8.34 (d, 2H, J_{HH} = 9.0 Hz; PyrH_m), 7.93 (t, 1H, J_{HH} = 7.5 Hz; PyrH_p), 7.68 (d, 4H, J_{HH} = 6.0 Hz; Ar*H*), 6.92 (d, 4H, J_{HH} = 9.0 Hz; Ar*H*), 2.39 ppm (s, 6H; N=C*Me*). ^{13}C{^{1}H} NMR ($CDCl_3$, 75 MHz, 25 °C): δ 168.0 (Me*C*=N), 155.3 (C_{Ar}), 154.8 (C_{Ar}), 137.3 (C_{Ar}), 133.5 (C_{Ar}), 123.2 (C_{Ar}), 120.0 (C_{Ar}), 119.3 (*C*≡N), 107.2 (C_{Ar}), 16.7 ppm (CH_3).

Synthesis of Iron Complexes

Synthesis of **2c**: A 100 mL flask was charged with **1c** (0.125 g, 0.40 mmol) and $FeCl_2$ (0.25 g, 0.20 mmol) under N_2. Degassed methanol (30 mL) was added via cannula, immediately forming a dark purple solution. The solution was stirred for 30 min and solid $NaPF_6$ (0.101 g, 0.60 mmol) was added. The solution was stirred for an additional 30 min, and the volatiles were removed under reduced pressure. Water (20 mL) was added and the mixture was triturated, filtered, and washed with an addition 3 x 5 mL of water, leaving a dark purple solid. This solid was collected and dried *in vacuo*. Isolated yield: 0.165 g (85 %). ^{1}H NMR (CD_3CN, 300 MHz, 25 °C): δ 8.11 (m, 3H; PyrH_m and PyrH_p), 7.18 (m, 6H; Ar*H*), 6.21 (m, 4H; Ar*H*), 2.56 ppm (s, 6H; N=C*Me*). ^{13}C{^{1}H} NMR (CD_3CN, 75 MHz, 25 °C): δ 179.6 (Me*C*=N), 160.2 (C_{Ar}), 144.3 (C_{Ar}), 136.8 (C_{Ar}), 130.8 (C_{Ar}), 128.7 (C_{Ar}), 127.9 (C_{Ar}), 120.2 (C_{Ar}), 19.6 ppm (CH_3). ^{19}F NMR (CD_3CN, 282 MHz, 25 °C): δ -72.9 ppm (d, J_{PF} = 705.4 Hz; PF_6). ^{31}P{^{1}H} NMR (CD_3CN, 121 MHz, 25 °C): δ -144.7 (q, J_{FP} = 706.7 Hz; *P*F_6). Anal. calcd for $C_{42}H_{38}N_6F_{12}P_2Fe$: C, 51.87; H, 3.94. Found: C, 52.26; H, 4.02. MS (ESI-TOF/MS, m/z) calcd for $C_{42}H_{38}N_6Fe$ $[M+H]^+$, 681.2424; found 681.2439.

Synthesis of **2d**: Procedure as for **2c** using: **1d** (0.14 g, 0.40 mmol) and $FeCl_2$ (0.25 g, 0.20 mmol). Isolated yield: 0.203 g (97 %). ^{1}H NMR (CD_3CN, 300 MHz, 25 °C): δ 8.22 (m, 3H; PyrH_m and

PyrH_p), 6.92 (m, 4H; Ar*H*), 6.18 (m, 4H; Ar*H*), 2.58 ppm (s, 6H; N=C*Me*). $^{13}C\{^1H\}$ NMR (CD_3CN, 75 MHz, 25 °C): δ 180.5 (Me*C*=N), 162.1 (d, J_{CF} = 246.7 Hz; C_{Ar}), 160.0 (C_{Ar}), 140.3 (d, J_{CF} = 3.1 Hz; C_{Ar}), 137.2 (C_{Ar}), 128.6 (C_{Ar}), 122.5 (d, J_{CF} = 8.8 Hz; C_{Ar}), 117.5 (d, J_{CF} = 23.5 Hz; C_{Ar}), 19.8 ppm (CH_3). $^{19}F\{^1H\}$ NMR (CD_3CN, 282 MHz, 25 °C): δ -72.9 (d, J_{PF} = 707.0 Hz; PF_6), -114.5 (s; Ar-*F*). $^{31}P\{^1H\}$ NMR (CD_3CN, 121 MHz, 25 °C): δ -144.7 (q, J_{FP} = 707.1 Hz; *P*F_6). MS (ESI-TOF/MS, m/z) calcd for $C_{42}H_{34}F_4N_6Fe$ $[M+H]^+$, 753.2047; found 753.2069.

Synthesis of **2e**: Procedure as for **2c** using: **1e** (0.188 g, 0.40 mmol) and $FeCl_2$ (0.25 g, 0.20 mmol). Isolated yield: 0.252 g (98 %). ^1H NMR (CD_3CN, 300 MHz, 25 °C): δ 8.24 (m, 3H; PyrH_m and PyrH_p), 7.33 (m, 4H; Ar*H*), 6.07 (m, 4H; Ar*H*), 2.59 ppm (s, 6H; N=C*Me*). $^{13}C\{^1H\}$ NMR (CD_3CN, 75 MHz, 25 °C): δ 180.9 (Me*C*=N), 160.2 (C_{Ar}), 143.3 (C_{Ar}), 137.3 (C_{Ar}), 133.8 (C_{Ar}), 129.0 (C_{Ar}), 122.3 (C_{Ar}), 122.0 (C_{Ar}), 19.9 ppm (CH_3). ^{19}F NMR (CD_3CN, 282 MHz, 25 °C): δ -72.8 (d, J_{PF} = 706.4 Hz; PF_6). $^{31}P\{^1H\}$ NMR (CD_3CN, 121 MHz, 25 °C): δ -144.6 (q, J_{FP} = 706.8 Hz; *P*F_6). Anal. calcd for $C_{42}H_{34}N_6F_{12}P_2FeBr_4$: C, 39.16; H, 2.66. Found: C, 39.07; H, 2.79. MS (ESI-TOF/MS, m/z) calcd for $C_{42}H_{34}Br_4N_6Fe$ $[M+H]^+$, 992.8850; found 992.8894.

Synthesis of **2f**: Procedure as for **2c** using: **1f** (0.145 g, 0.40 mmol) and $FeCl_2$ (0.25 g, 0.20 mmol). Isolated yield: 0.208 g (97 %). ^1H NMR (CD_3CN, 300 MHz, 25 °C): δ 8.32 (m, 3H; PyrH_m and PyrH_p), 7.57 (d, 4H, J_{HH} = 8.4 Hz; Ar*H*), 6.31 (m, 4H, J_{HH} = 8.4 Hz; Ar*H*), 2.64 ppm (s, 6H; N=C*Me*). $^{13}C\{^1H\}$ NMR (CD_3CN, 75 MHz, 25°C): δ 182.0 (Me*C*=N), 160.0 (C_{Ar}), 147.2 (C_{Ar}), 138.1 (C_{Ar}), 135.2 (C_{Ar}), 129.9 (C_{Ar}), 121.6 (C_{Ar}), 118.4 (*C*≡N), 112.5 (C_{Ar}), 20.3 ppm (CH_3). ^{19}F NMR (CD_3CN, 282 MHz, 25 °C): δ -72.9 (d, J_{PF} = 706.7 Hz; PF_6). $^{31}P\{^1H\}$ NMR (CD_3CN, 121

MHz, 25 °C): δ -144.6 (q, J_{FP} = 706.5 Hz; PF_6). MS (ESI-TOF/MS, m/z) calcd for $C_{46}H_{34}N_{10}Fe$ $[M+H]^+$, 783.2391; found 783.2053.

2.5.2 X-ray data collection, solution and refinement

Crystal structure data was using collected from a multi-faceted crystal of suitable size and quality selected from a representative sample of crystals of the same habit using an optical microscope. Each crystal was mounted on a MiTiGen loop and data collection carried out in a cold stream of nitrogen (150 K; Bruker D8 QUEST ECO; Mo K_α radiation). All diffractometer manipulations were carried out using Bruker APEX3 software.[59] Structure solution and refinement was carried out in the OLEX2[60] program using XS, XT and XL software, embedded within the Bruker SHELXTL suite.[59] For each structure, the absence of additional symmetry was confirmed using ADDSYM incorporated in the PLATON program.[61]

Crystal structure parameters for **2a** (CCDC 1580534): X-ray quality single crystals were grown by layering a concentrated CH_2Cl_2 solution with Et_2O. Purple blocks; $C_{60}H_{74}Cl_4N_6F_{12}P_2Fe$ 1366.84 g/mol, monoclinic, space group $P2_1/c$; a = 18.5528(7) Å, b = 15.2508(5) Å, c = 24.3972(9) Å, $\alpha = \gamma = 90°$, β = 101.8756(13)°, V = 6755.3(4) Å^3; Z = 4, ρ_{calcd} = 1.344 g cm^{-3}; crystal dimensions 0.410 x 0.250 x 0.200 mm; $2\theta_{max}$ = 55.02°; 162896 reflections, 15595 independent (R_{int} = 0.0470, intrinsic phasing; absorption coeff (μ = 0.503 mm^{-1}), absorption correction semi-empirical from equivalents (SADABS); refinement (against F_o^2) with SHELXTL V6.1, 876 parameters, 132 restraints, R_1 = 0.0668 ($I > 2\sigma$) and wR_2 = 0.1967 (all data), Goof = 1.071, residual electron density 1.801/−1.024 Å^{-3}. Two disordered solvent molecules (CH_2Cl_2) were found co-crystallized within the unit cell and satisfactorily modelled, as was disorder in one of the *t*Bu groups.

Crystal structure data for **3d** (CCDC 1983239): X-ray quality single crystals were grown by cooling a concentrated CH_3CN solution to -20 °C overnight. Yellow plates, $C_{23}H_{20}Cl_2F_2N_4Zn$, 526.70 g/mol, triclinic, *P*-1; a = 8.8832(3) Å, b = 12.6990(5) Å, c = 21.7752(8) Å, α = 105.6760(10)°, β = 95.8720(10)°, γ = 94.3010(10)°, V = 2339.09(15) Å^3; Z = 4, ρ_{calcd} = 1.496 g cm^{-3}; crystal dimensions 0.27 × 0.24 × 0.07 mm; diffractometer Bruker D8 QUEST ECO CMOS; Mo K$_\alpha$ radiation, 150.0 K, $2\theta_{max}$ = 55.132°; 56870 reflections, 10800 independent (R_{int} = 0.0757), intrinsic phasing; absorption coeff (μ = 1.312 mm^{-1}), absorption correction semi-empirical from equivalents (SADABS); refinement (against F_o^2) with SHELXTL V6.1, 583 parameters, 0 restraints, R_1 = 0.0618 ($I > 2\sigma$) and wR_2 = 0.1038 all data), Goof = 1.111, residual electron density 0.63/−0.53 e Å^{-3}. Two CH_3CN solvent molecules were successfully modeled within the asymmetric unit.

Crystal structure parameters for **3e** (CCDC 1983241): X-ray quality single crystals were grown by cooling a concentrated CH_3CN/DMSO (10:1) solution to -20 °C overnight. Yellow rods, $C_{23}H_{18.5}Br_2Cl_2N_{3.5}Zn$, 627.99 g/mol, triclinic, space group *P*-1; a 12.9613(7) Å, b = 14.5938(6) Å, c = 15.1144(7) Å, α = 92.855(2)°, β = 110.335(2)°, γ = 102.818(2)°, V = 2588.7(2) Å^3; Z = 4, ρ_{calcd} = 1.611 g cm^{-3}; crystal dimensions 0.70 × 0.24 × 0.18 mm; diffractometer Bruker D8 QUEST ECO CMOS; Mo K$_\alpha$ radiation, 150.0 K, $2\theta_{max}$ = 61.442°; 34726 reflections, 15756 independent (R_{int} = 0.0702), intrinsic phasing; absorption coeff (μ = 4.257 mm^{-1}), absorption correction semi-empirical from equivalents (SADABS); refinement (against F_o^2) with SHELXTL V6.1, 555 parameters, 0 restraints, R_1 = 0.0708 ($I > 2\sigma$) and wR_2 = 0.1345 all data), Goof = 1.037, residual electron density 1.61/−1.16 e Å^{-3}. One CH_3CN solvent molecule was modeled successfully,

however due to difficulties modeling remaining solvents, the SQUEEZE protocol imbedded in PLATON[61] was used to remove a solvent void of 249 $Å^3$ containing 101 e^-.

Crystal structure parameters for **3f** (CCDC 1983240): X-ray quality single crystals were grown by layering a concentrated CH_3CN solution with Et_2O and cooling to -5 °C. Yellow blocks; $C_{25}H_{20}Cl_2N_6Zn$ 540.74 g/mol, monoclinic, space group $P2_1/c$; a = 7.7284(7) Å, b = 14.8601(13) Å, c = 22.4323(19) Å, $\alpha = \gamma = 90°$, β = 97.628(4)°, V = 2553.4(4) $Å^3$; Z = 4, ρ_{calcd} = 1.407g cm^{-3}; crystal dimensions 0.280 × 0.160 × 0.110 mm; $2\theta_{max}$ = 56.11°; 66904 reflections, 6121 independent (R_{int} = 0.0966, intrinsic phasing; absorption coeff (μ = 1.196 mm^{-1}), absorption correction semi-empirical from equivalents (SADABS); refinement (against F_o^2) with SHELXTL V6.1, 310 parameters, 0 restraints, R_1 = 0.0656 ($I > 2\sigma$) and wR_2 = 0.1495 (all data), Goof = 1.219, resid. electron density 0.85/−1.04 $Å^{-3}$.

Crystal structure parameters for **2e** (CCDC 1983242): X-ray quality single crystals were grown by layering isopropyl ether over an acetonitrile solution and placing it in the freezer. Purple blocks, $C_{44}H_{37}Br_4F_{12}FeN_7P_2$, 1329.23 g/mol, monoclinic, space group Cc; a 17.9244(7) Å, b = 17.5570(7) Å, c = 15.9880(6) Å, $\alpha = \gamma = 90°$, β = 102.194(2)°, V = 4917.9(3) $Å^3$; Z = 4, ρ_{calcd} = 1.795 g cm^{-3}; crystal dimensions 0.370 × 0.270 × 0.210 mm; diffractometer Bruker D8 QUEST ECO CMOS; Mo K_α radiation, 150.0 K, $2\theta_{max}$ = 61.234°; 79707 reflections, 14968 independent (R_{int} = 0.0501), intrinsic phasing; absorption coeff (μ = 3.708 mm^{-1}), absorption correction semi-empirical from equivalents (SADABS); refinement (against F_o^2) with SHELXTL V6.1, 637 parameters, 2 restraints, R_1 = 0.0356 ($I > 2\sigma$) and wR_2 = 0.0590 all data), Goof = 1.048, residual electron density

0.50/−0.51 e Å^{-3}. A CH_3CN solvent molecule was modeled successfully within the asymmetric unit.

Crystal structure parameters for **2f** (CCDC 1983243): X-ray quality single crystals were grown by layering isopropyl ether over an acetonitrile solution and placing it in the freezer. Purple plates. $C_{50}H_{40}N_{12}F_{12}P_2Fe$, 1154.73 g/mol, monoclinic, space group $P2_1/n$; a 11.5217(6) Å, b = 32.6571(16) Å, c = 13.8662(7) Å, $\alpha = \gamma = 90°$, β = 98.732(2)°, V = 5156.9(5) Å^3; Z = 4, ρ_{calcd} = 1.487 g cm^{-3}; crystal dimensions 0.23 × 0.22 × 0.07 mm; diffractometer Bruker D8 QUEST ECO CMOS; Mo K_α radiation, 150.0 K, $2\theta_{max}$ = 49.700°; 121300 reflections, 8890 independent (R_{int} = 0.1056), intrinsic phasing; absorption coeff (μ = 0.447 mm^{-1}), absorption correction semi-empirical from equivalents (SADABS); refinement (against F_o^2) with SHELXTL V6.1, 700 parameters, 0 restraints, R_1 = 0.0717 ($I > 2\sigma$) and wR_2 = 0.1611 (all data), Goof = 1.087, residual electron density 1.29/−0.97 e Å^{-3}. Two CH_3CN solvent molecules were modeled successfully within the asymmetric unit.

2.5.3 Electrochemical Methods

Cyclic voltammetry (CV) and differential pulse voltammetry (DPV) experiments were conducted using 0.6 mM of analyte dissolved in 15 mL dry CH_3CN containing 0.1 M (nBu$_4$N)PF$_6$ and purged with Ar for 20 minutes prior to analysis. A CHI 760c bipotentiostat was employed, using a 3 mm diameter glassy carbon working electrode, a Ag/Ag$^+$ quasi-non-aqueous reference electrode separated by a Vycor tip, and a Pt wire counter electrode. CV experiments were conducted using scan rates of 50-800 mV/s. DPV experiments were carried out using a 5 mV increment, 50 mV amplitude, 0.1 s pulse width, 0.0167 s sample width, and 0.5 s pulse period.

Following analysis, ferrocene (FcH) was added to each solution as an internal standard, and potentials are reported versus the $FcH^{0/+}$ redox couple.[62]

For battery tests of **2a** and **2b**, two 15 mL acetonitrile solutions were prepared, one with 2 mM 1 or 2 and 0.4 M nBu$_4$PF$_6$, and one constituted only of 0.4 M nBu$_4$PF$_6$. Battery tests were conducted in a custom-built air-tight H-cell (see SI), with the two chambers separated by a glass frit (fine porosity), and with two outputs for the working and reference electrodes in one chamber, and one output for the counter electrode in the other chamber. The solution containing **2a** or **2b** was placed in the working electrode chamber, with the electrolyte-only solution placed in the counter electrode chamber and the solutions stirred continuously throughout the experiments. Reticulated vitreous carbon (RVC) counter and working electrodes were used, with a non-aqueous Ag/Ag^+ quasi-reference electrode. Potential cutoffs, voltages at which the reversible couples start and finish, were set according to CV results. Cycling experiments were executed at a variety of anodic and cathodic currents (0.5, 1.1 and 2.2 mA) with different (dis)charge times (1800, 3600 or 7200 s), corresponding to 0.5, 1, and 2 C charging rates assuming a $2e^-$ reduction process, to examine the stability of the MCCs for RFB applications.

For battery tests of **2c**-**2f**, charging/discharging experiments were conducted via a chronopotentiometry protocol under an N_2 atmosphere using a reticulated vitreous carbon (RVC) working electrode (~700 cm^2) in a glass cylindrical chamber (85 mL) containing an acetonitrile solution of both analyte and nBu$_4$PF$_6$ (0.3 M), and a Teflon-coated stirbar. A graphite rod counter electrode immersed in a 0.3 M nBu$_4$PF$_6$ solution was placed in a fritted tube (10 mL) separating the working and counter electrode chambers, and a fritted Ag/AgCl quasi-reference electrode placed into the working electrode chamber. Potential cut-offs were set to voltages at which the reversible couples for each analyte was observed to start and finish, according to CV experiments.

Cycling experiments were executed at various anodic and cathodic currents, with a (dis)charge time of 3600 s, which corresponds to a 1C (dis)charging rate assuming a $2e^-$ reduction process.

2.6 References

(1) Kamat, P. V.; Schanze, K. S.; Buriak, J. M. *ACS Energy Lett.* **2017**, *2* (6), 1368.

(2) Winsberg, J.; Hagemann, T.; Janoschka, T.; Hager, M. D.; Schubert, U. S. *Angew. Chem., Int. Ed.* **2017**, *56* (3), 686.

(3) Wang, W.; Sprenkle, Vince. *Nat. Chem.* **2016**, *8* (3), 204.

(4) Shao, Y.; Cheng, Y.; Duan, W.; Wang, W.; Li, B.; Lin, Y.; Wang, Y.; Liu, Jun. *ACS Catal.* **2015**, *5* (12), 7288.

(5) Soloveichik, G. L. *Chem. Rev. (Washington, DC, U. S.)* **2015**, *115* (20), 11533.

(6) Laramie, S. M.; Milshtein, J. D.; Breault, T. M.; Brushett, F. R.; Thompson, L. T. *J. Power Sources* **2016**, *327* (Copyright (C) 2018 American Chemical Society (ACS). All Rights Reserved.), 681.

(7) Darling, R. M.; Gallagher, K. G.; Kowalski, J. A.; Ha, S.; Brushett, F. R. *Energy Environ. Sci.* **2014**, *7* (11), 3459.

(8) Sevov, C. S.; Fisher, S. L.; Thompson, L. T.; Sanford, M. S. *J. Am. Chem. Soc.* **2016**, *138* (47), 15378.

(9) Suttil, J. A.; Kucharyson, J. F.; Escalante-Garcia, I. L.; Cabrera, P. J.; James, B. R.; Savinell, R. F.; Sanford, M. S.; Thompson, L. T. *J. Mater. Chem. A* **2015**, *3* (15), 7929.

(10) van der Vlugt, J. I. *Chem. Eur. J.* **2019**, *25* (11), 2651.

(11) Storr, T.; Mukherjee, R. *Inorg. Chem.* **2018**, *57* (16), 9577.

(12) Cabrera, P. J.; Yang, X.; Suttil, J. A.; Hawthorne, K. L.; Brooner, R. E. M.; Sanford, M. S.; Thompson, L. T. *J. Phys. Chem. C* **2015**, *119* (28), 15882.

(13) Cabrera, P. J.; Yang, X.; Suttil, J. A.; Brooner, R. E. M.; Thompson, L. T.; Sanford, M. S. *Inorg. Chem.* **2015**, *54* (21), 10214.

(14) Ding, C.; Zhang, H.; Li, X.; Liu, T.; Xing, F. *J. Phys. Chem. Lett.* **2013**, *4* (8), 1281.

(15) Crawford, A.; Viswanathan, V.; Stephenson, D.; Wang, W.; Thomsen, E.; Reed, D.; Li, B.; Balducci, P.; Kintner-Meyer, M.; Sprenkle, V. *J. Power Sources* **2015**, *293*, 388.

(16) Gibson, V. C.; Redshaw, C.; Solan, G. A. *Chem. Rev. (Washington, DC, U. S.)* **2007**, *107* (5), 1745.

(17) Enright, D.; Gambarotta, S.; Yap, G. P. A.; Budzelaar, P. H. M. *Angew. Chem., Int. Ed.* **2002**, *41* (20), 3873.

(18) Kiernicki, J. J.; Fanwick, P. E.; Bart, S. C. *Chem. Commun.* **2014**, *50* (60), 8189.

(19) Tondreau, A. M.; Stieber, S. C. E.; Milsmann, C.; Lobkovsky, E.; Weyhermuller, T.; Semproni, S. P.; Chirik, P. J. *Inorg. Chem.* **2013**, *52* (2), 635.

(20) Park, K.; Cho, J. H.; Shanmuganathan, K.; Song, J.; Peng, J.; Gobet, M.; Greenbaum, S.; Ellison, C. J.; Goodenough, J. B. *J. Power Sources* **2014**, *263* (1), 52.

(21) Zhao, Y.; Ding, Y.; Song, J.; Li, G.; Dong, G.; Goodenough, J. B.; Yu, Guihua. *Angew. Chem., Int. Ed.* **2014**, *53* (41), 11036.

(22) Hwang, B.; Park, M.-S.; Kim, Ketack. *ChemSusChem* **2015**, *8* (2), 310.

(23) Beh, E. S.; De Porcellinis, D.; Gracia, R. L.; Xia, K. T.; Gordon, R. G.; Aziz, M. J. *ACS Energy Lett.* **2017**, *2* (3), 639.

(24) Hu, B.; DeBruler, C.; Rhodes, Z.; Liu, T. Leo. *J. Am. Chem. Soc.* **2017**, *139* (3), 1207.

(25) Gong, K.; Xu, F.; Grunewald, J. B.; Ma, X.; Zhao, Y.; Gu, S.; Yan, Yushan. *ACS Energy Lett.* **2016**, *1* (1), 89.

(26) Bamgbopa, M. O.; Shao-Horn, Y.; Almheiri, Saif. *J. Mater. Chem. A* **2017**, *5* (26), 13457.

(27) Mun, J.; Lee, M.-J.; Park, J.-W.; Oh, D.-J.; Lee, D.-Y.; Doo, S.-Gwang. *Electrochem. Solid-State Lett.* **2012**, *15*, A80.

(28) Anderson, T. M.; Anstey, M.; Tomson, N. C. Redox-active ligand-based transition metal complex flow batteries., August 28, 2014.

(29) Kaim, Wolfgang. *Eur. J. Inorg. Chem.* **2012**, *2012* (3), 343.

(30) Matsuda, Y.; Tanaka, K.; Okada, M.; Takasu, Y.; Morita, M.; Matsumura-Inoue, T. *J Appl. Electrochem.* **1988**, *18* (6), 909.

(31) Chakrabarti, M. H.; Dryfe, R. A. W.; Roberts, E. P. L. *Electrochim. Acta* **2007**, *52* (5), 2189.

(32) Park, M.-S.; Lee, N.-J.; Lee, S.-W.; Kim, K. J.; Oh, D.-J.; Kim, Y.-Jun. *ACS Appl. Mater. Interfaces* **2014**, *6* (13), 10729.

(33) Cabral, D. M.; Howlett, P. C.; MacFarlane, D. R. *Electrochim. Acta* **2016**, *220*, 347.

(34) Wile, B. M.; Trovitch, R. J.; Bart, S. C.; Tondreau, A. M.; Lobkovsky, E.; Milsmann, C.; Bill, E.; Wieghardt, K.; Chirik, P. J. *Inorg. Chem.* **2009**, *48* (9), 4190.

(35) De Bruin, B.; Bill, E.; Bothe, E.; Weyhermueller, T.; Wieghardt, Karl. *Inorg. Chem.* **2000**, *39* (13), 2936.

(36) Darmon, J. M.; Stieber, S. C. E.; Sylvester, K. T.; Fernandez, I.; Lobkovsky, E.; Semproni, S. P.; Bill, E.; Wieghardt, K.; DeBeer, S.; Chirik, P. J. *J. Am. Chem. Soc.* **2012**, *134* (41), 17125.

(37) Sun, D.-L.; Rosokha, S. V.; Lindeman, S. V.; Kochi, J. K. *J. Am. Chem. Soc.* **2003**, *125* (51), 15950.

(38) Noack, J.; Roznyatovskaya, N.; Herr, T.; Fischer, Peter. *Angew. Chem., Int. Ed.* **2015**, *54* (34), 9776.

(39) Bard, A. J.; Faulkner, L. R. *Electrochemical methods: fundamentals and applications*, 2nd ed.; Wiley: New York, 2001.

(40) Antonov, A. A.; Semikolenova, N. V.; Zakharov, V. A.; Zhang, W.; Wang, Y.; Sun, W.-H.; Talsi, E. P.; Bryliakov, K. P. *Organometallics* **2012**, *31* (3), 1143.

(41) Ionkin, A. S.; Marshall, W. J.; Adelman, D. J.; Shoe, A. L.; Spence, R. E.; Xie, T. *J. Polym. Sci. Pol. Chem.* **2006**, *44* (8), 2615.

(42) Gasperini, M.; Ragaini, F.; Cenini, S. *Organometallics* **2002**, *21* (14), 2950.

(43) Small, B. L. *Acc. Chem. Res.* **2015**, *48* (9), 2599.

(44) Thompson, M. C.; Busch, D. H. *J. Am. Chem. Soc.* **1962**, *84* (9), 1762.

(45) Busch, D. H.; Stephenson, N. A. *Coord. Chem. Rev.* **1990**, *100*, 119.

(46) Mikhailine, A. A.; Kim, E.; Dingels, C.; Lough, A. J.; Morris, R. H. *Inorg. Chem.* **2008**, *47* (15), 6587.

(47) Simler, T.; Danopoulos, A. A.; Braunstein, P. *Dalton Trans.* **2017**, *46* (18), 5955.

(48) Alyea, E. C.; Merrell, P. H. *Synth. React. Inorg. Met.-Org. Chem.* **1974**, *4* (6), 535.

(49) Addison, A. W.; Rao, T. N.; Reedijk, J.; van Rijn, J.; Verschoor, G. C. *J. Chem. Soc., Dalton Trans.* **1984**, No. 7, 1349.

(50) Lozada, I. B.; Murray, T.; Herbert, D. E. *Polyhedron* **2019**, *161*, 261.

(51) Duarte, G. M.; Braun, J. D.; Giesbrecht, P. K.; Herbert, D. E. *Dalton Trans.* **2017**, *46* (47), 16439.

(52) Hammett, L. P. *J. Am. Chem. Soc.* **1937**, *59* (1), 96.

(53) Wei, X.; Pan, W.; Duan, W.; Hollas, A.; Yang, Z.; Li, B.; Nie, Z.; Liu, J.; Reed, D.; Wang, W.; Sprenkle, V. *ACS Energy Lett.* **2017**, *2* (9), 2187.

(54) Zhao, Y.; Byon, H. R. *Adv. Energy. Mater.* **2013**, *3* (12), 1630.

(55) Xie, C.; Zhang, H.; Xu, W.; Wang, W.; Li, X. *Angew. Chem., Int. Ed.* **2018**, *57* (35), 11171.

(56) Roth, H.; Romero, N.; Nicewicz, D. *Synlett* **2015**, *27* (05), 714.

(57) Flisak, Z.; Sun, W.-H. *ACS Catal.* **2015**, *5* (8), 4713.

(58) Cetinkaya, B.; Cetinkaya, E.; Brookhart, M.; White, P. S. *J. Mol. Catal. A: Chem.* **1999**, *142* (2), 101.

(59) Sheldrick, G. M. *Acta Crystallogr., Sect. A: Found. Crystallogr.* **2008**, *64*, 112.

(60) Dolomanov, O. V.; Bourhis, L. J.; Gildea, R. J.; Howard, J. A. K.; Puschmann, H. *J. Appl. Crystallogr.* **2009**, *42* (2), 339.

(61) Spek, A. L. *Acta Crystallogr., Sect. D: Biol. Crystallogr.* **2009**, *65*, 148.

(62) Connelly, N. G.; Geiger, W. E. *Chem. Rev.* **1996**, *96* (2), 877.

Chapter 3

Synthesis and Characterization of P(I)/P(III) Complexes of Bulky Diimine-pyridine Ligands

3.1 Abstract

Diiminepyridines (DIP) are a popular class of redox "non-innocent" ligands with widespread application in late, first-row transition metal mediated catalysis and coordination chemistry. In this work, the isolation and characterization of a pair of phosphorus coordination complexes in the +1 and +3 oxidation states is reported. These complexes are supported by the same ligand framework bearing sterically imposing and electron-releasing *t*Bu substituents on the imine carbons of the DIP backbone. Electrochemical analysis experiments show that the DIP scaffold can retain its ability to serve as an electron reservoir when coordinated to reduced pnictogen centres, with a reversible reduction observed for the P(I) complex.

3.2 Introduction

Diiminepyridines (DIPs, Figure 3.1)[1] are amongst the most popular redox "non-innocent" ligands,[2–4] so-called because the ligand can serve as an additional site of redox events in metal coordination complexes.[5] In addition to widespread application in late, first-row transition metal mediated catalysis,[6] they are also useful for their ability to bind early transition metals,[7,8] rare earths,[9] and main-group elements in a pincer-like fashion.[4] With respect to the p-block, DIP complexes are known for Groups 13,[10–12] 14,[13,14] 15[15–18] and 16[19,20] centres. These complexes have found use, for example, in Lewis acid mediated catalysis including C-F bond allylation,[18] although

in such scenarios, hemi-lability (chemical non-innocence) of the supporting ligands rather than redox non-innocence can be prized.[21]

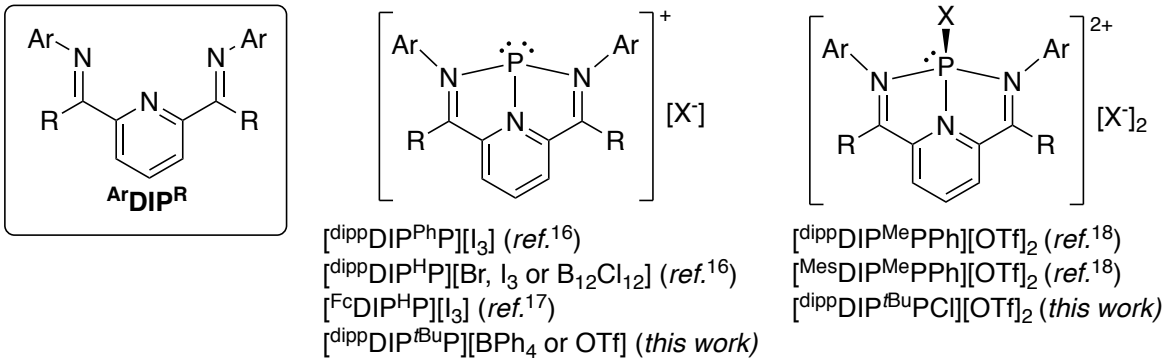

Figure 3.1 The diiminepyridine (DIP) scaffold, known P(I)[16,17] and P(III)[18] complexes of DIP ligands: dipp = 2,6-di(*iso*propyl)phenyl; Fc = ferrocenyl; Mes = 2,4,6-trimethylphenyl; and those described in this work.

A limited number of DIP complexes of phosphorus have been previously described in the literature. This includes select examples of complexes with P(I) oxidation states[16,17] and two examples of phenyl-substituted dicationic P(III) complexes.[18] In surveying known $[DIP(P)]^{n+}$ complexes, it is noted that pairs of P(I) and P(III) complexes supported by the same DIP ligand scaffold have not been reported. The redox chemistry of $[DIP(P)]^{n+}$ complexes is usually discussed in the context of their preparation. For example, one route to the generation of Pn(I) (Pn = pnictogen) congeners is to take advantage of spontaneous reduction of P(III) or As(III) halides via X_2 elimination upon coordination of a multidentate ligand.[22,23] This approach can be dependent on the nature of the chelating ligand: isolation of P(III) complexes without reductive X_2 elimination has been observed with related anionic diarylamido PNP ligands.[24] In comparison, α-diimine supported P(I) centres will spontaneously engage in electron transfer with more easily reduced α-diimine ligands, forming *N*-heterocyclic phosphenium P(III) cations supported by the resulting

formally dianionic ligand.[25] With respect to any discussion of the redox behavior of isolated DIP(P) complexes, the oxidative redox chemistry of the ferrocene-decorated [^{Fc}DIP^{H}P][I_3] has been described.[17] In that report, both ligand and phosphorus centred oxidation events could be discerned by comparison of cyclic voltammograms of [^{Fc}DIP^{H}P][I_3], [^{dipp}DIP^{H}P][I_3] and the proligand ^{Fc}DIP^{H}.

Given the widespread utility of DIP ligand-based electron storage (reduction) in transition metal bond activation and catalysis[26] and the increasingly successful exploitation of main-group element redox cycling[27–31] in expanding the chemistry of select main-group complexes to rival that of the transition metals,[32] a more in depth examination of the redox behaviour of phosphorus-based DIP complexes was performed. In particular, an investigation of a pair of cationic phosphorus complexes featuring P(I) and P(III) centres supported by a DIP ligand bearing *t*Bu substituents at its imine carbons is described. Despite report of the synthesis of this sterically bulky DIP ligand appearing over a decade ago,[33] its coordination chemistry has yet to be described beyond *in silico* modeling.[34]

3.3 Results and Discussion

3.3.1 Synthesis and Characterization of Proligand and Coordination Complexes

As noted above, combining phosphorus(III) halides PX_3 (X = Br, I) with multidentate ligands can enable formation of P(I) complexes upon elimination of X_2,[35,36] a route also observed with heavier chalcogen salts.[37] The liberated X_2 is typically either trapped by an appropriate halogen acceptor (e.g., cyclohexene for Br_2) or incorporated into the anion (e.g., formation of I_3^-).[23] Building on observations that tautomerization of Me-substituted DIP ligands can complicate their reactivity with main group centres,[16] a DIP variant with tertiary substitution at its α-carbons

was pursued. In addition to adding electron-releasing substituents that may help stabilize a higher valent P(III) analog, the chosen DIP scaffold with *tert*-butyl substituents presents the added benefit of increased solubility in common organic solvents,[33] and as noted above, its coordination chemistry has yet to be described.

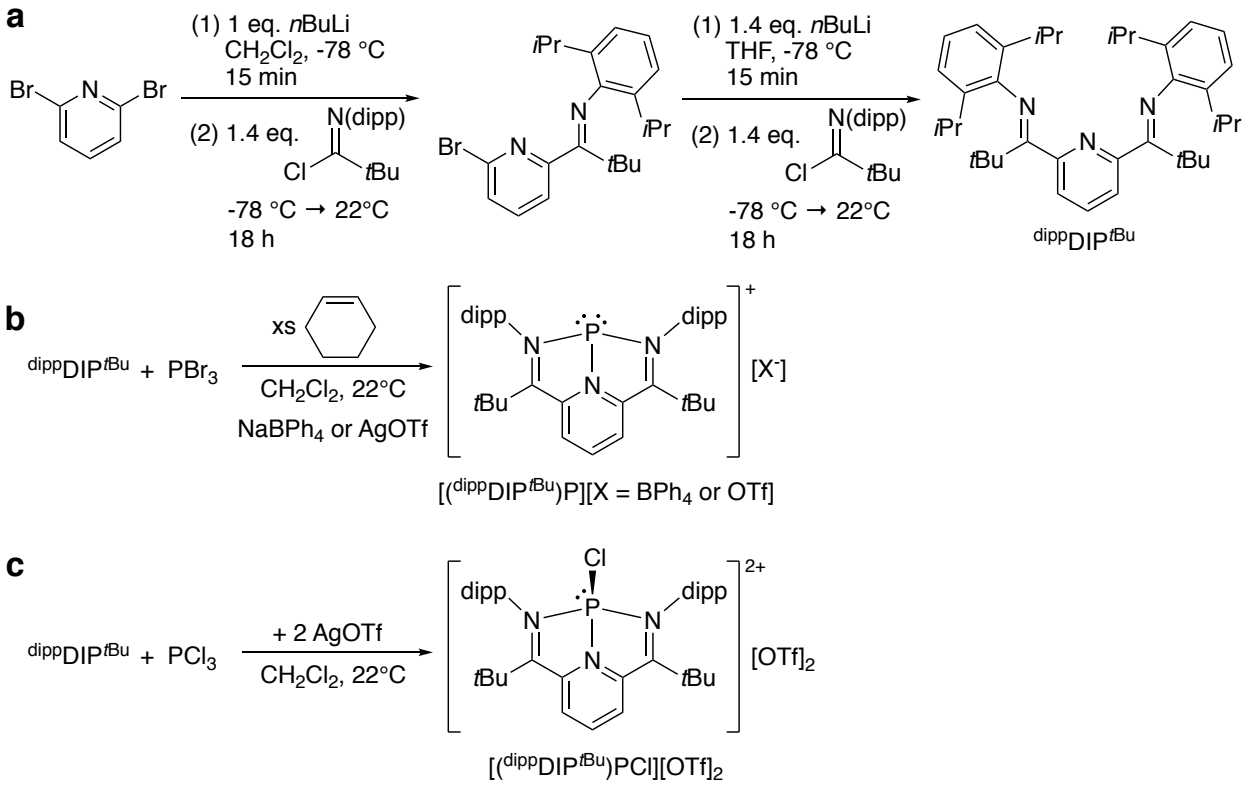

Scheme 3.1 Synthesis of **^{dipp}DIP^{tBu}** and its phosphorus complexes.

Synthesis of the proligand **^{dipp}DIP^{tBu}** was accomplished via a step-wise installation of the two imine arms by lithiation of 2,6-dibromopyridine with *n*BuLi and addition of *N*-(dipp) *tert*-butyl imidoyl chloride[38] [dipp = (2,6-diisopropyl)phenyl] in CH_2Cl_2/THF (Scheme 3.1), following the procedure reported for a closely related analog ^{Ar}DIP^{tBu} [Ar = (2,6-dimethyl)phenyl].[33] The **^{dipp}DIP^{tBu}** proligand was isolated in essentially quantitative yield (~99 % yield) as colourless

crystals following a CH_3CN washing. Multinuclear NMR spectroscopic analysis confirmed the liberation of the C_{2v} symmetric free ligand, with seven distinct signals observable by ^1H NMR: a set of overlapping doublets and a septet for magnetically equivalent *i*Pr substituents, as well as a doublet and triplet in the aromatic region, corresponding to the flanking aryl substituents, a singlet for the *t*Bu groups on the imine, and one doublet and triplet for the central pyridine moiety. The crystal structure that was obtained agrees with the NMR assignment (Figure 3.2).

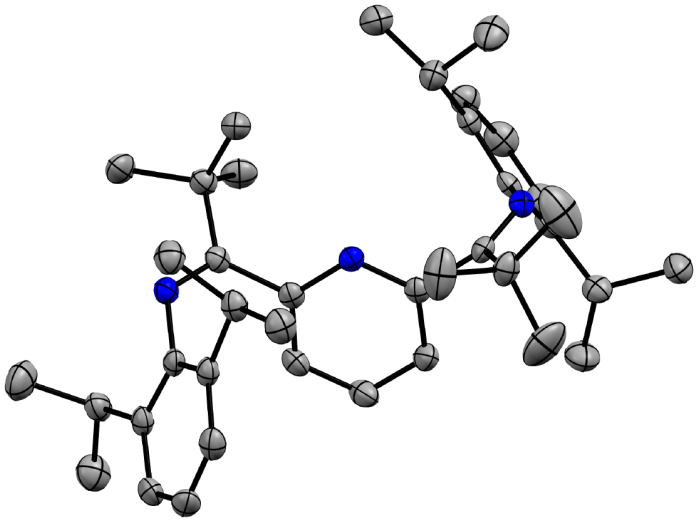

Figure 3.2 Crystal structure of $^{dipp}DIP^{tBu}$ proligand with thermal ellipsoids shown at 50 % probability level. Hydrogen atoms are omitted for clarity

Addition of PBr_3 to a CH_2Cl_2 solution of ^{dipp}**DIP**^{tBu} in the presence of excess cyclohexene at room temperature produced a yellow solution that changed to red over the course of two hours, in line with previously reported (DIP)P(I) complexes.[16] To minimize dynamic behaviour between bound and unbound halides in the oxidized species (*vide infra*), the bromide counterion was replaced with a weakly-coordinating anion by addition of either one equivalent of $NaBPh_4$ in CH_3CN or AgOTf (OTf = OSO_2CF_3; trifluoromethanesulfonate) in CH_2Cl_2. Salt metathesis was accompanied by the appearance of diagnostic resonances of the anion in the respective ^1H NMR

(BPh_4) or $^{19}F\{^1H\}$ NMR (OTf) spectra. Direct addition of the metathesis reagent at the beginning of the reaction does not appear to affect the course of the reaction or hamper conversion to the P(I) complexes.

Upon complexation, there is a marked change in the chemical shifts of the *meta* and *para* hydrogen nuclei of the DIP pyridine due to coordination to a cationic phosphorus centre.[16,18,20] Comparing the two salts, these signals are more shielded in **[(^{dipp}DIP^{tBu})P][BPh$_4$]** than for **[(^{dipp}DIP^{tBu})P][OTf]**, consistent with greater inter-ion separation for the bulkier borate counterion. Overall, the ^1H NMR spectra of both salts indicate a C_{2v}-symmetric structure in solution, with magnetically equivalent *i*Pr substituents and similar $^{31}P\{^1H\}$ chemical shifts **([(^{dipp}DIP^{tBu})P][BPh$_4$]**: δ_P = 149.9 ppm**; [(^{dipp}DIP^{tBu})P][OTf]**: δ_P = 149.7 ppm). Interestingly, both red solids appear to be stable in air. ^1H and $^{31}P\{^1H\}$ NMR spectroscopy show no evidence of hydrolysis or oxidation after two weeks in ambient atmosphere. Crystals of **[(^{dipp}DIP^{tBu})P][BPh$_4$]** suitable for X-ray diffraction were obtained by layering a saturated CH_2Cl_2 solution with pentane at room temperature overnight and used to confirm the molecular structure (Figure 3.3a). Table 3.1 highlights selected bond lengths and angles and compares them to the DFT optimized structures.

Table 3.1 Selected solid-state and optimized gas-phase bond lengths (Å) and angles (°) for **[(^{dipp}DIP^{tBu})P][BPh$_4$]** and **[(^{dipp}DIP^{tBu})PCl][OTf]$_2$**

	[(^{dipp}DIP^{tBu})P][BPh$_4$]		**[(^{dipp}DIP^{tBu})PCl][OTf]$_2$**	
	Solid-state	**DFT**	**Solid-state**	**DFT**
N1-P1	1.8933(19)	1.848	1.9989(19)	2.007
N2-P1	1.7111(17)	1.735	1.7752(18)	1.839
N3-P1	2.0055(18)	2.05	2.0009(19)	1.997
P1-Cl1	--	--	2.0192(8)	2.044
C1-N1	1.318(3)	1.323	1.285(3)	1.285
C11-N3	1.309(3)	1.294	1.294(3)	1.285
N1-P1-N3	162.75(8)	162.4	161.47(8)	160.4
N1-P1-N2	81.26(8)	82.9	81.36(8)	80.6
N2-P1-N3	80.49(8)	79.6	81.66(8)	80.5

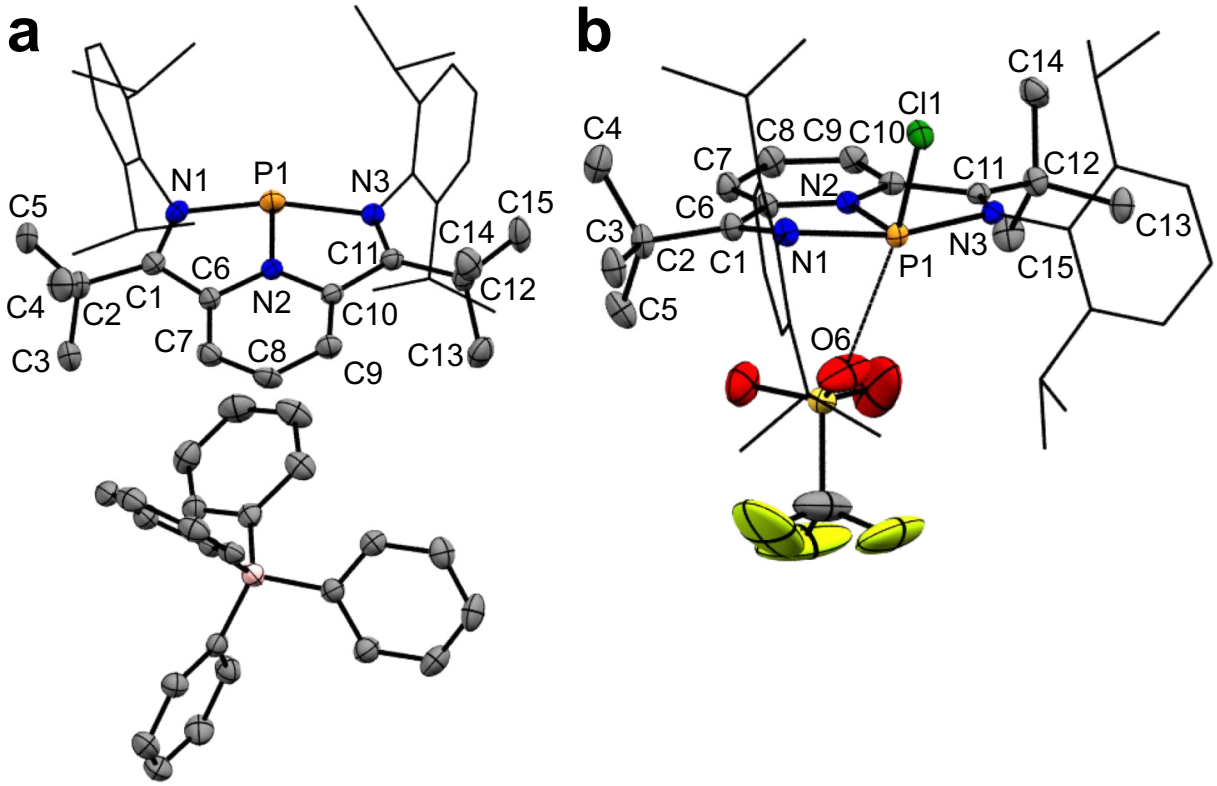

Figure 3.3 Molecular structures of (a) **[(^{dipp}DIP^{tBu})P][BPh$_4$]** and (b) **[(^{dipp}DIP^{tBu})PCl][OTf]$_2$** with thermal displacement parameters depicted at 50 % probability levels. Hydrogen atoms, select atom labels and the second triflate counterion (b) omitted for clarity

Coordination of the imine nitrogen donors to P occurs asymmetrically in the solid-state [N1-P1: 1.8933(19) Å; N3-P1: 2.0055(17) Å] of **[(^{dipp}DIP^{tBu})P][BPh$_4$]**. Both this asymmetry and the two P-N distances lie within the range of those previously reported.[16,18] The asymmetry in the solid-state contrasts with the symmetric coordination environment observed in solution, again consistent with literature (DIP)P(I) complexes, as is the closer bonding distance to the pyridine nitrogen [N2-P1: 1.7111(17) Å] compared to the imine arms. DFT optimization of the ground-state structure of **[(^{dipp}DIP^{tBu})P]$^+$** (M06/def2SVP level of theory; SMD: CH_2Cl_2) reproduces this asymmetry, with calculated N1-P1 and N3-P1 distances of 1.848 Å and 2.050 Å respectively (Table 3.1). The imine C=N distances are significantly longer (C1-N1: 1.318(3) Å and C11-N3: 1.309(3) Å) compared to the structure of the proligand ^{dipp}DIP^{tBu} (average d(C=N) = 1.27 Å], consistent with iminium and pyridinium charge delocalization character upon coordination to phosphorus. Hemilability of donor arms in phosphorus coordination complexes has been exploited to access masked Lewis acidic character for P(III) dications[18,21] and diimine-ligated phosphinidenes.[39] The P(I) centre has *pseudo*-T-shaped geometry, with a tied-back N1-P1-N3 angle of 162.75(8)° (DFT: 162.4°) and two lone pairs. The DIP ligand remains planar, with a negligible deviation [1.8(3)°] of the imine nitrogen atoms from the plane of the pyridine ring. The diisopropyl groups are nearly orthogonal to the plane of the ligand [89.1(3), 79.8(3)°] forming a steric pocket around the phosphorus centre, similar to what is observed with α-diimine ligand-metal complexes.[40] A somewhat close H---H distance between the *para*-H on the pyridine ring and *ortho*-proton on the BPh_4 moiety mirrors the interaction in solution indicated by the shielded ^{1}H NMR spectrum.

With a P(I) complex in hand, attention was turned towards a P(III) variant. As mentioned previously, only two (DIP)P(III) complex have been reported in the literature, with a phenyl

substituent installed at the phosphorus to limit reactivity,[18] and also, P(I) and P(III) centres supported by the same ligand have not been described, precluding precise comparison of the ligand environment in a pair of redox-related molecules. Combining a CH_2Cl_2 solution of PCl_3 and a light-yellow mixture of $^{dipp}DIP^{tBu}$ with two equivalents of AgOTf in the same solvent immediately produced an orange-red solution with precipitation of AgCl. The reaction was shown to be complete after 1 h, with conversion to a new single product peak in the $^{31}P\{^1H\}$ NMR spectrum (δ = 52.0 ppm), significantly upfield in comparison to **[(^{dipp}DIP^{tBu})P][BPh$_4$]**, (Figure 3.4) and also the complete consumption of PCl_3 (δ = 220 ppm) is noted. An orange solid was obtained in 81 % yield following filtration and precipitation with pentane. The ^1H NMR spectrum revealed a single DIP-containing environment for **[(^{dipp}DIP^{tBu})PCl][OTf]$_2$**.

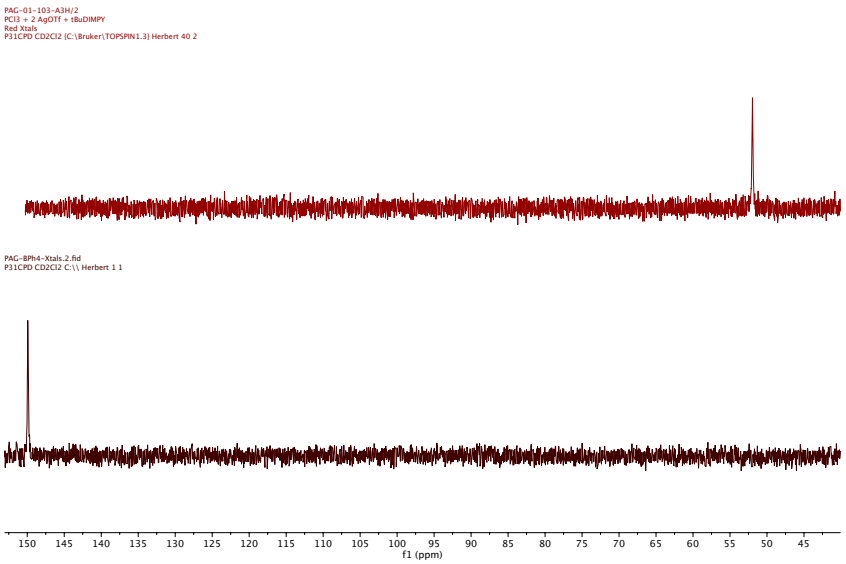

Figure 3.4 $^{31}P\{^1H\}$ NMR of **[(^{dipp}DIP^{tBu})P][BPh$_4$]** (top) and **[(^{dipp}DIP^{tBu})PCl][OTf]$_2$** (bottom)

Complexation to a P-Cl moiety produces a C_s-symmetric structure, with inequivalent methine protons of the *iso*propyl groups on the dipp substituents above and below the plane of the central DIP framework. Compared to the free ligand, shifts in the resonances assigned to the 3-

and 4-position of the pyridine ring are deshielded more so than in **[(^{dipp}DIP^{tBu})P[X]** (X = BPh_4, OTf), consistent with coordination to an increasingly cationic phosphorus centre. This correlates well with the emerging trend that decreased electron density at the ligated element centre results in a more deshielded H_p and H_m on the pyridine ring. In comparison, increased electron density at the central atom results in an opposite shielding effect in DIP complexes of Ge(0)[14] and Sn(0).[41] The higher cationic charge at the P(III) centre results in a lower energy non-bonding electron pair and as such is not as delocalized into the pyridine moiety. Instead, the build-up of positive charge at the phosphorus centre inductively withdraws electron density from the pyridine ring and contributes to the H_p and H_m deshielding. **[(^{dipp}DIP^{tBu})PCl][OTf]$_2$** is stable under inert atmosphere for upwards of 3 months but decomposes overnight on exposure of the solid compound to ambient atmosphere.

Crystals suitable for X-ray analysis (Figure 3.3b) were obtained by layering *n*-pentane over a concentrated CH_2Cl_2 solution with a few added drops of CH_3CN to fully solubilize the complex and storing at -30 °C. The crystal structure of the P(III) complex includes two triflate counter-ions, one of which was modelled successfully. The second triflate exhibited disorder and was best modelled over two positions, using appropriate constraints and restraints. In contrast to the P(I) structure, coordination of the imine nitrogen donors is symmetric, with statistically indistinguishable N1-P1 [2.0009(19) Å] and N3-P1 [1.9989(19) Å] distances. The pyridine N2-P1 distance is again shorter at 1.7752(18) Å, similar to in the two reported (DIP)P(III)Ph salts.[18] This distance is longer than in the P(I) complex, despite the increase in positive charge, ascribable to the increased coordination number of the P(III) centre. The ligand environment is close to planar around phosphorus (N1-P1-N3 angle: 161.47(8)°) while the dipp *i*Pr substituents on N1 and N3 are again twisted out of the plane at angles of 73.5° and 73.2°. The imine C=N bonds are noticeably

shorter (C1-N1: 1.285(3), C11-N3: 1.294(3)) than the corresponding distances in the P(I) complex (C1-N1 1.318(3), C11-N3 1.309(3)). This would be expected if electron density from the P(I) centre that delocalizes into C=N π* orbitals in the reduced congener is absent in the higher oxidation state P(III) complex. The P1-Cl1 distance at 2.0192(8) Å is significantly shorter than the sum of the P-Cl covalent radii (Σ_{CR} = 2.10 Å)[42] with the increased cationic charge of the P(III) centre causing contraction of the P-Cl bond. As is the case in **[(dippDIPtBu)P]**$^+$, the DFT-optimized structure of the dication reproduces the solid-state geometrical parameters in the dication well (Table 3.1), with an essentially symmetrical ligand coordination (N1-P1: 2.007 Å; N3-P1: 1.997 Å), as well as the shortened P-Cl bond (P1-Cl1: 2.044 Å) and C=N bonds (C1-N1: 1.285 Å; C11-N3: 1.285 Å). Additionally, close contact of a triflate counterion with a P---O contact distance of 2.980 Å is observed, with the second triflate being well outside of the sum of the van der Waals radii (2.32 Å).[43]

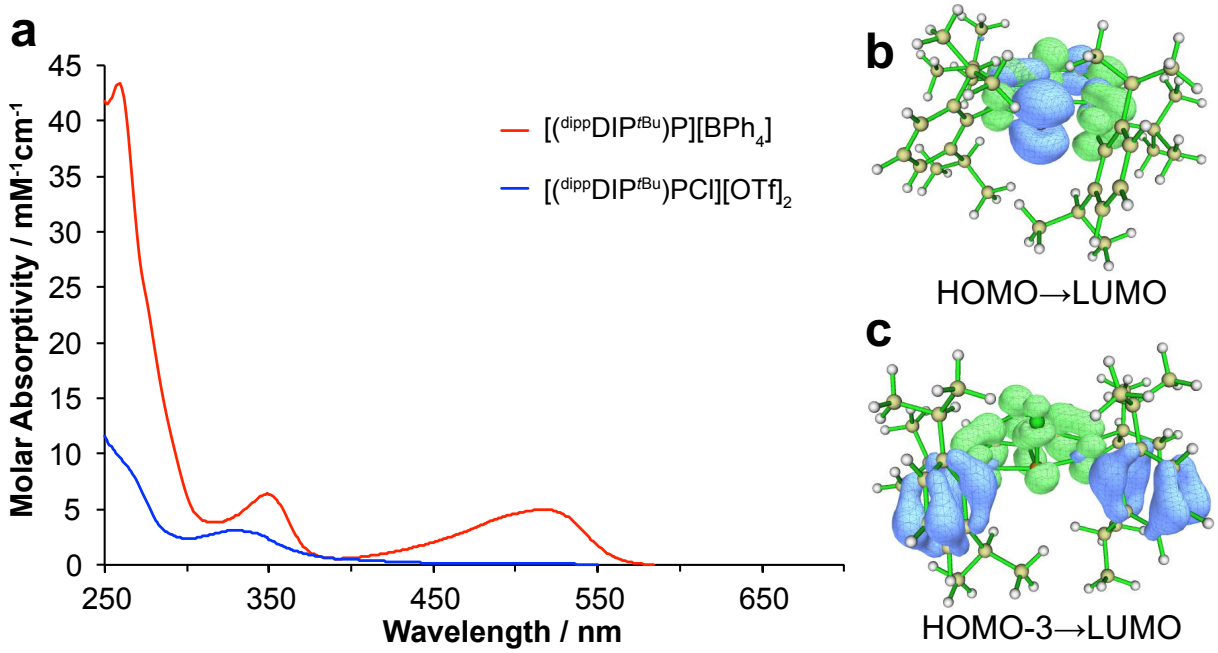

Figure 3.5 (a) UV-Vis absorption spectra of **[(dippDIPtBu)P][BPh$_4$] and [(dippDIPtBu)PCl][OTf]$_2$** in CH_2Cl_2; TD-DFT difference maps [M06/def2SVP] in CH_2Cl_2 showing electron density gain (green) and depletion (blue) distribution maps (isosurface = 0.003) illustrating the charge transfer

character of the lowest energy transition for (b) **[(^{dipp}DIP^{tBu})P][BPh$_4$]**: HOMO→LUMO and (c) **[(^{dipp}DIP^{tBu})PCl][OTf]$_2$**: HOMO-3→LUMO

In solution, the P(I) complex appears red whereas the P(III) more orange in colour. UV-Vis absorption spectra in CH_2Cl_2 accordingly contain a broad, low energy band (Figure 3.5a), with **[(^{dipp}DIP^{tBu})P][BPh$_4$]** absorbing considerably more strongly at longer wavelengths (λ_{max} = 517 nm, ε = 4990 M^{-1} cm^{-1}) than **[(^{dipp}DIP^{tBu})PCl][OTf]$_2$** (λ_{max} = 490 nm, 180 M^{-1} cm^{-1}). Higher energy bands (300-400 nm) attributable to ligand π-π* transitions are also evident, with a small bathochromic shift (20 nm) in these band maxima for the P(I) complex mirroring the red shift in the λ_{max}. DFT analysis indicates the P(I) centre bears a significant portion of the HOMO in the form of a *p*-type orbital containing a primarily non-bonding lone pair (Figure 3.6; see Figures S57 and S58 for expanded MO diagrams). The LUMO is localized largely on the pyridine ring with C=N π* contributions. The frontier orbitals in general are quite similar to those previously calculated for analogs [(^{H}DIP^{Me})P]$^+$ and [(^{H}DIP^{Me})As]$^+$, where aryl substituents were replaced with hydrogens for computational simplicity.[44]

In contrast, the HOMO-1 and HOMO of the P(III) complex are localized in the π-system of the DIP imine arms. The LUMO is pyridine-based, with a significant portion lying on the *para* carbon corroborating its deshielded ^{1}H NMR chemical shift, and also features P-Cl σ* character. The lowest energy absorption for the P(I) complex is accurately reproduced by time-dependent DFT (TD-DFT) and has largely HOMO→LUMO character. An electron-hole difference map showing the charge transfer involved in this transition is shown in Figure 3.5b. DFT predicts a larger HOMO-LUMO gap for the P(III) cation, however the lowest energy transition with a significant oscillator strength predicted by TD-DFT involves charge transfer from the HOMO-3→LUMO (electron-hole map, Figure 3.5c).

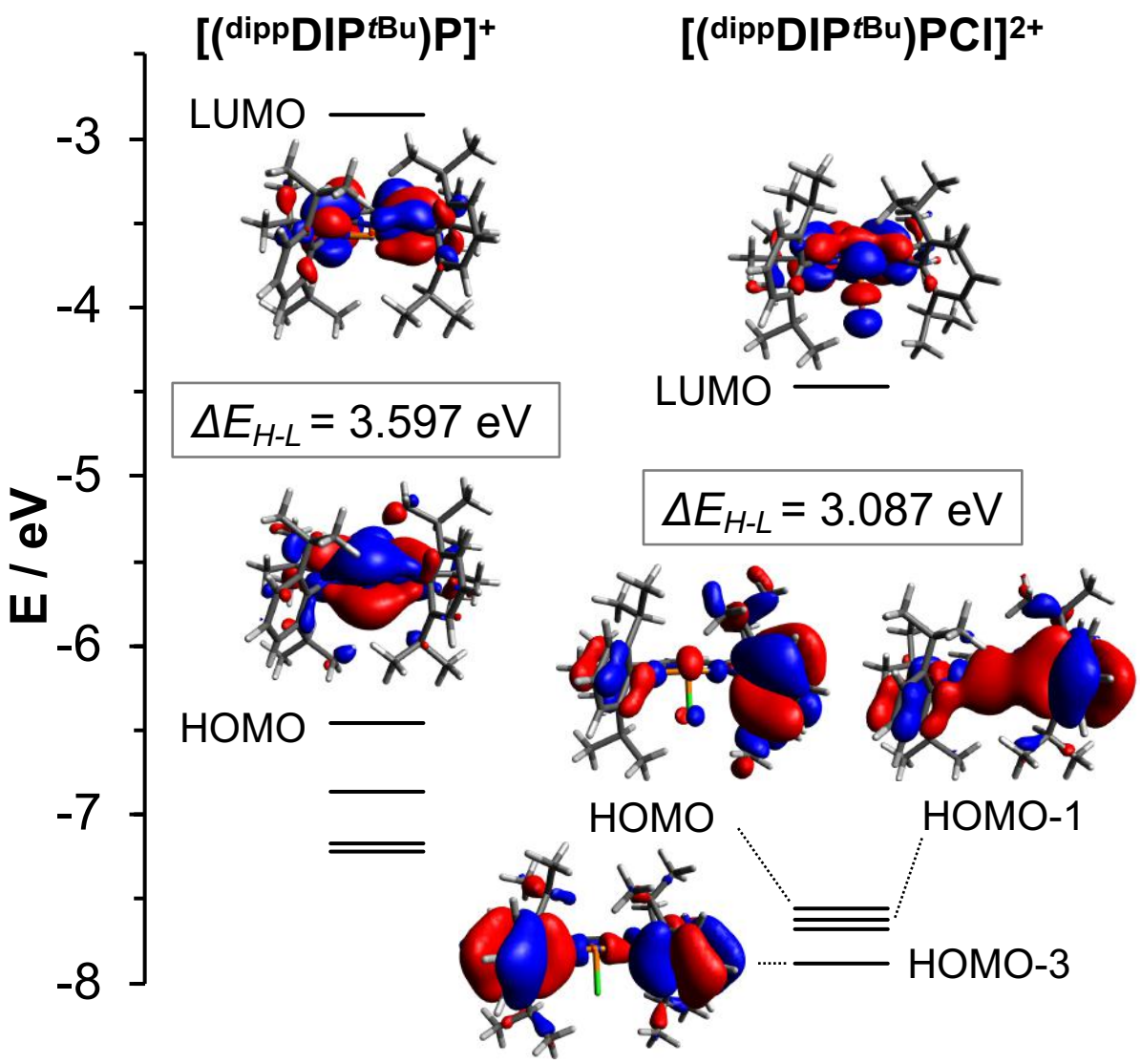

Figure 3.6 DFT optimized molecular orbital energy level diagrams and selected orbital isosurfaces (SMD-M06/def2SVP, CH_2Cl_2 solvent field) of **[(dippDIP*t*Bu)P]**$^+$ (left) and **[(dippDIP*t*Bu)PCl]**$^{2+}$ (right).

The rest of the lowest energy manifold of **[(dippDIP*t*Bu)P]**$^+$ is similarly attributed by TD-DFT to charge-transfer (CT) type transitions in which electron density is relocated from the P(I) lone pairs (HOMO, HOMO-1) to π^*-type orbitals on the DIP ligand (LUMO). Higher energy transitions are dominated by intraligand charge-transfer, with the flanking aryl rings (HOMO-2,

HOMO-3) acting as donor sites. For **[(^{dipp}DIP^{tBu})PCl]$^{2+}$**, the significantly weaker lower energy band accordingly has much smaller oscillator strengths predicted by TD-DFT. This band is ascribed primarily to a transition involving intraligand CT from the flanking aryl rings (HOMO-3), with a small contribution from phosphorus-based electron density (HOMO-2), to pyridine-based π^*-type acceptor MOs which also exhibit some P-Cl σ^* character (LUMO, LUMO+1).

As befits the ability to isolate both P(I) and P(III) congeners, (irreversible) oxidation of **[(^{dipp}DIP^{tBu})P][BPh$_4$]** is observed electrochemically at ~ +0.4 V vs FcH$^{0/+}$ (FcH = ferrocene; Figure 3.7). Interestingly, the complex also shows a reversible reduction at -1.38 V. This cathodic event is consistent with ligand-based reduction, common for diiminepyridine complexes of metals.[45,46] However, one could also postulate the reduction as forming a formally neutral P(0) complex with a monoanionic DIP ligand. The preparation of reduced, low-valent main group-DIP species has been examined previously with germanium[14] and tin.[41] These heavier main-group elements possess significantly more metal character than phosphorus, and as such, can accommodate electrons in lower energy orbitals, *vis-à-vis* the inert-pair effect. The increased s-character on the metal centre precludes the greater contributions from the triplet state, as shown by DFT calculations for the (DIP)Ge complex,[14] while in the case of phosphorus, one-electron reduction to a formal "P(0)" would form a radical. Attempts to isolate a chemically reduced species have thus far not yielded an isolable complex.

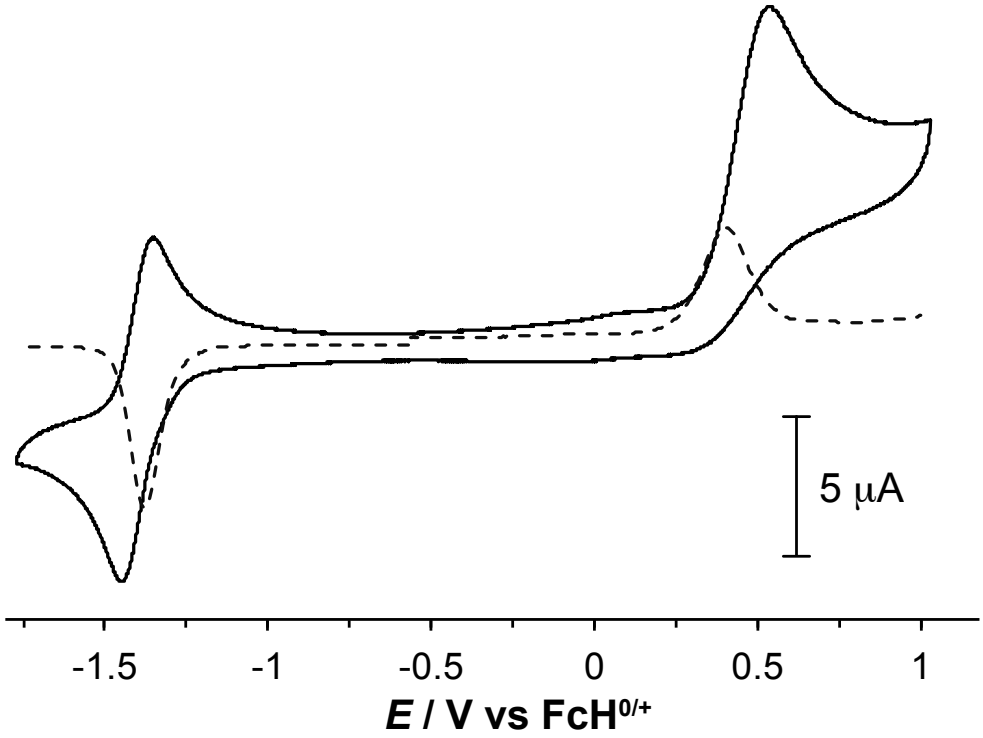

Figure 3.7 CV (—) and DPV (---) of **[(dippDIP^{t}Bu)P][BPh$_4$]** ([analyte] = 1.0 mM, 0.1 M nBu$_4$PF$_6$, CH_2Cl_2, glassy carbon working electrode, ν = 100 mV s^{-1})

3.4 Conclusion

In conclusion, a pair of cationic (^{dipp}DIP^{t}Bu)P(I) and (^{dipp}DIP^{t}Bu)P(III) complexes has been isolated and characterized, with the main group centre supported in each case by the same DIP ligand framework, enabling direct examination of differences in the ligand environment that arise from coordination to pnictogens in different oxidation states. This includes only the third reported example of a (DIP)P(III) complex and first with a halide substituent.[24] In addition, the reported complexes represent the first examples of coordination of a DIP ligand bearing sterically imposing *t*Bu substituents at the imine carbons. While this position is relatively remote from the site of ligation, previous attempts at metalation with both ferric and ferrous iron were reported to be unsuccessful[33] despite computational modeling suggesting coordination to late transition metals

should produce stable complexes.[34] Finally, the pair of complexes exhibit interesting electronic structures, with both "P to ligand" and intraligand CT character observed by UV-Vis absorption spectroscopy, as elucidated by TD-DFT. Electrochemical analysis reveals an electrochemically reversible reduction for the P(I) complex **[(^{dipp}DIP^{tBu})P][BPh$_4$]**, suggesting isolation of a reduced "P(0)" DIP complex may be feasible.

3.5 Experimental Section

Unless otherwise specified, all air sensitive manipulations were carried out either in a N_2-filled glove box or using standard Schlenk techniques under Ar. *N*-(2,6-diisopropyl-phenyl)-2,2-dimethyl-propionimidoyl chloride was prepared according to a literature procedure.[38] PCl_3 (Sigma Aldrich), PBr_3 (Sigma Aldrich) were purified by vacuum distillation prior to use. AgOTf (Alfa Aesar), $NaBPh_4$ (Sigma Aldrich), and nBu$_4$NPF$_6$ (electrochemical grade, Sigma Aldrich) were purchased and used without further purification. Organic solvents were dried and distilled using appropriate drying agents prior to use. NMR spectra were recorded on Bruker Avance 300 MHz or Bruker Avance-III 500 MHz spectrometers. ^{1}H and ^{13}C{^{1}H} NMR spectra were referenced to residual solvent peaks, while ^{31}P{^{1}H} (85% H_3PO_4 = 0 ppm) and ^{19}F{^{1}H}($CFCl_3$ = 0 ppm) spectra were referenced to external standards. Electronic absorption spectra were recorded on an Agilent Technologies Cary 5000 Series UV-Vis-NIR spectrophotometer in dual beam mode (range: 230–1600 nm). High-resolution mass spectra were recorded using a Bruker microOTOF-QIII. Computational methods are described in the supporting information (pg. 45).

3.5.1 Synthesis

Synthesis of **[1-(6-bromo-pyridin-2-yl)-2,2-dimethyl-propylidene]-(2,6-diisopropyl-phenyl)amine**: Prepared according to the procedure reported by Zubris and co-workers for the analogous reaction using *N*-(2,6-diisopropyl-phenyl)-2,2-dimethyl-propionimidoyl chloride.[33] A 100 mL Schlenk flask was charged with the 2,6-dibromopyridine (1.80 g, 7.60 mmol, 1.0 equiv.) and 30 mL of CH_2Cl_2. The mixture was subsequently cooled to -78 °C in a dry ice-acetone bath, following which a 1.6 M solution of *n*BuLi in hexanes (4.75 mL, 7.60 mmol, 1.0 equiv.) was added and the yellow solution was stirred at this temperature for 20 min. A solution of the imidoyl chloride (2.98 g, 10.64 mmol, 1.4 equiv.) in CH_2Cl_2 was subsequently added dropwise over the course of 15 min. The reaction was stirred for an additional 30 min at -78 °C, then allowed to warm to room temperature slowly overnight. The resulting slurry was filtered through a medium-porosity glass frit to give a light-yellow filtrate. The volatiles were removed under reduced pressure and the resulting residue was dried under vacuum for 4 hours to give a viscous semi-solid. This residue was dissolved in 2.5 % ethyl acetate-hexanes and passed through a 15 cm plug of silica. Removing the solvent and drying *in vacuo* gave the monoimine as a yellow solid (2.41 g, 79 %). ^{1}H NMR ($CDCl_3$, 300 MHz, 25 °C) δ: 7.21 (m, 2H, H_{Ar}), 6.87 (m, 3H, H_{Ar}), 6.63 (m, 1H, H_{Ar}), 2.90 (sept, 2H, J_{HH} = 6.8 Hz, C*H*$(CH_3)_2$), 1.37 (s, 9H, C(CH_3)$_3$), 1.11 (d, 6H, J_{HH} = 6.8 Hz, CH(CH_3)$_2$), 1.10 ppm(d, 6H, J_{HH} = 6.8 Hz, CH(CH_3)$_2$). ^{13}C{^{1}H} NMR (CD_3CN, 75 MHz, 25 °C): δ 173.7 (tBu*C*=N), 156.8 (C_{Ar}), 145.7 (C_{Ar}), 141.0 (C_{Ar}), 137.4 (C_{Ar}), 135.7 (C_{Ar}), 127.0 (C_{Ar}), 122.3 (C_{Ar}), 120.7 (C_{Ar}), 40.7 (*C*$(CH_3)_3$) 29.0 (C(*C*H_3)$_3$), 28.3 (*C*H$(CH_3)_2$), 23.7 (CH_3), 21.7 ppm (CH_3).

Synthesis of ^{dipp}**DIP**$^{t\mathbf{Bu}}$: Prepared using a modified literature procedure reported by Zubris and co-workers.[33] A 100 mL Schlenk flask was charged with [1-(6-bromo-pyridin-2-yl)-2,2-dimethyl-

propylidene]-(2,6-diisopropyl-phenyl)amine (0.50 g, 1.25 mmol, 1.0 equiv.) and anhydrous THF (20 mL) and subsequently cooled to -78 °C in a dry ice-acetone bath. A 1.6 M solution of *n*BuLi in hexanes (1.09 mL, 1.74 mmol, 1.4 equiv.) was then added dropwise over 15 min. The resulting yellow/brown mixture was stirred for 20 min before adding a solution of the imidoyl chloride (0.49 g, 1.74 mmol, 1.4 equiv.) in 10 mL of anhydrous THF, giving an orange/brown mixture. The reaction was stirred for an additional 30 min at -78 °C, then allowed to warm to room temperature slowly overnight. The solvent was then removed *in vacuo* to give an oily solid, to which 40 mL of CH_3CN was added. This mixture was isolated via vacuum filtration, yielding a colourless solid (0.70 g, 99 %). ^{1}H NMR ($CDCl_3$, 300 MHz, 25 °C) δ: 7.17 (t, 1H, J_{HH} = 7.9 Hz, PyrH_p), 6.88 (d, 4H, J_{HH} = 7.9 Hz, ArH_m), 6.81 (t, 2H, J_{HH} = 7.8 Hz ArH_p), 6.65 (d, 2H, J_{HH} = 7.9 Hz PyrH_m), 2.82 (sept, 4H, J_{HH} = 6.5 Hz, CH(CH_3)$_2$), 1.24 (s, 18H, C(CH_3)$_3$), 1.11 ppm (m (overlapping signals), 24H, CH(CH_3)$_2$). ^{13}C{^{1}H} NMR (CD_3CN, 75 MHz, 25 °C): δ 173.6 (tBu*C*=N), 155.0 (C_{Ar}), 146.2 (C_{Ar}), 134.8 (C_{Ar}), 134.1 (C_{Ar}), 122.6 (C_{Ar}), 122.2 (C_{Ar}), 121.4 (C_{Ar}), 40.8 (C(CH_3)$_3$) 29.1 (C(CH$_3$)$_3$), 28.4 (CH(CH_3)$_2$), 23.3 (CH_3), 21.5 ppm (CH_3). HRMS $C_{39}H_{55}N_3$ calcd (found): 566.4469 (566.4488).

Synthesis of **[(^{dipp}DIP^{tBu})P][OTf]**: A 20 mL glass scintillation vial was charged 5 mL of CH_2Cl_2, ^{dipp}DIP^{tBu} (141.5 mg, 0.25 mmol, 1.0 equiv.) and cyclohexene (123.2 mg, 1.5 mmol, 151 µL, 6.0 equiv.). PBr_3 (67.7 mg, 0.25 mmol, 23.8 µL, 1.0 equiv.) was then added, producing a red solution. The mixture was stirred for 30 min at room temperature. Solid AgOTf (64.3 mg, 0.25 mmol, 1 equiv.) was then added immediately forming a colourless precipitate of AgCl. The mixture was stirred for 30 min and the dark red solution isolated by filtration. The volatiles were removed *in vacuo* to give a dark red solid. Recrystallization from CH_2Cl_2 gave (^{dipp}DIP^{tBu})P[OTf] as dark red

crystals, which were washed twice with 2 mL of Et_2O and dried *in vacuo*. Crude yield: 0.147 g (79 %); Crystalline recovery: 0.0836 g (56 % recovery). ^{1}H NMR (CD_2Cl_2, 500 MHz, 25°C): δ 9.32 (d, 2H, J_{HH} = 8.3 Hz, PyrH_m), 8.34 (t, 1H, J_{HH} = 8.3 Hz PyrH_p), 7.40 (t, 2H, J_{HH} = 7.7 Hz, ArH_p), 7.24 (d, 4H, J_{HH} = 7.7 Hz, ArH_m), 2.32 (sept, 4H, J_{HH} = 6.7 Hz, CH(CH_3)$_2$), 1.58 (s, 18H, C(CH_3)$_3$), 1.22 (d, 12H, J_{HH} = 6.7 Hz, CH(CH_3)$_2$), 1.02 ppm (d, 12H, J_{HH} = 6.7 Hz, CH(CH_3)$_2$). ^{13}C{^{1}H} NMR (CD_2Cl_2, 125 MHz, 25 °C): δ 164.1 (d, J_{CP} = 6.2 Hz, tBuC=N), 143.4 (d, J_{CP} = 1.8z Hz, C_{Ar}), 136.8 (d, J_{CP} = 7.3 Hz, C_{Ar}), 134.4 (d, J_{CP} = 6.3 Hz, C_{Ar}), 131.3 (d, J_{CP} = 3.5 Hz, C_{Ar}), 129.8 (C_{Ar}), 125.7 (d, J_{CP} = 4.6 Hz, C_{Ar}), 124.2 (C_{Ar}) 41.0 (d, J_{CP} = 3.7 Hz, C(CH_3)$_3$) 32.7 (C(CH$_3$)$_3$), 29.2 (d, J_{CP} = 3.2 Hz, CH(CH_3)$_2$), 27.2 (d, J_{CP} = 3.6 Hz, CH(CH_3)$_2$), 23.6 ppm (CH_3). ^{31}P{^{1}H} NMR (CD_2Cl_2, 202 MHz, 25 °C): δ 149.7 ppm (s). ^{19}F NMR (CD_2Cl_2, 471 MHz, 25 °C): δ -78.9 ppm (s, SO_3CF_3). HRMS $C_{39}H_{55}N_3$ calcd (found): 596.4128 (596.4084).

Synthesis of **[(^{dipp}DIP^{tBu})P][BPh$_4$]**: A 20 mL glass scintillation vial was charged 5 mL of CH_2Cl_2 with ^{dipp}DIP^{tBu} (0.142 g, 0.250 mmol, 1.0 equiv.) and cyclohexene (0.123 g, 1.50 mmol, 151 µL, 6.0 equiv.). PBr_3 (0.068 g, 0.25 mmol, 23.8 µL, 1.0 equiv.) was added, resulting in the formation of a red solution. The mixture was stirred for 30 minutes at room temperature. To this solution was added $NaBPh_4$ (85.6 mg, 0.25 mmol, 1 eq) along with 1 mL of CH_3CN, resulting in the formation of colourless NaCl precipitate. The volatiles were removed *in vacuo* to give a red solid. The solid was redissolved in 3mL of CH_2Cl_2 and filtered again to give a dark red solution. The volatiles were removed *in vacuo* giving a dark red crystalline material. X-ray quality crystals were obtained by cooling a saturated CH_2Cl_2 solution in a -35 °C freezer overnight, giving [(^{dipp}DIP^{tBu})P][BPh$_4$] as dark red crystals. Crystals not selected for X-ray analysis were washed twice with 2mL of Et_2O and dried *in vacuo*. Crude yield: 0.187 g (82%); Crystalline recovery:

0.092 g (49% recovery). ^{1}H NMR (CD_2Cl_2, 500 MHz, 25°C): δ 8.96 (d, 2H, J_{HH} = 8.4 Hz PyrH_m), 7.75 (t, 1H, J_{HH} = 8.3 Hz PyrH_p), 7.41 (t, 2H, J_{HH} = 7.8 Hz, ArH_p), 7.35 (m, 8H, BPh_4), 7.24 (d, 4H, J_{HH} = 7.4 Hz, ArH_m), 7.02 (t, J_{HH} = 7.4 Hz, 8H, BPh_4), 6.87 (t, J_{HH} = 7.4 Hz, 4H, BPh_4), 2.30 (sept, 4H, J_{HH} = 6.8 Hz, CH(CH_3)$_2$), 1.53 (s, 18H, C(CH_3)$_3$), 1.22 (d, 12H, J_{HH} = 6.8 Hz, CH(CH_3)$_2$), 1.02 (d, 12H, J_{HH} = 6.8 Hz, , CH(CH_3)$_2$). ^{13}C NMR (CD_2Cl_2, 125 MHz, 25°C, ppm): δ 164.6 (q, J_{CB} = 49.3 Hz, BPh_4) 164.0 (d, J_{CP} = 3.7 Hz, tBuC=N), 143.3 (C_{Ar}), 136.5 (q, J_{CB} = 1.4 Hz, BPh_4), 134.4 (d, J_{CP} = 6.3 Hz, C_{Ar}), 130.7 (d, J_{CP} = 3.5 Hz, C_{Ar}),, 130.0 (C_{Ar}), 126.2 (q, J_{CB} = 2.7 Hz, BPh_4), 125.1 (d, J_{CP} = 4.3 Hz, C_{Ar}), 124.3 (C_{Ar}), 122.3 (BPh_4) 41.0 (dz, J_{CP} = 3.7 Hz, C(CH_3)$_3$) 32.7 (C(CH$_3$)$_3$), 29.2 (d, J_{CP} = 3.2 Hz, CH(CH_3)$_2$), 27.2 (d, J_{CP} = 3.7 Hz, CH(CH_3)$_2$), 22.9 (CH_3). Note: one aromatic signal was not observed due to overlap with BPh_4 signals at 136.5 ppm. ^{31}P{^{1}H} NMR (CD_2Cl_2, 202 MHz, 25°C, ppm): δ 149.9 (s). HRMS $C_{39}H_{55}N_3$ calcd (found): 596.4128 (596.4095). UV-Vis (CH_2Cl_2): λ (ε) 259 (43375 M^{-1} cm^{-1}) 349 (6400), 517 (4990).

Synthesis of **[(^{dipp}DIP^{tBu})PCl][OTf]$_2$**: A 20 mL glass scintillation vial was charged with ^{dipp}DIP^{tBu} (0.283 g, 0.5 mmol, 1.0 equiv), AgOTf (0.257 g, 1.0 mmol, 2 equiv.) and 5 mL of CH_2Cl_2. PCl_3 (0.069 g, 0.5 mmol, 43.7 µL) was added, resulting in the immediate formation of a dark red supernatant over a colourless precipitate. The mixture was stirred for 1 hour at room temperature in the dark and then filtered to give a red solution. The volatiles were removed *in vacuo* giving an orange solid. The solid was recrystallized from CH_3CN in a -30°C freezer to give red crystals of [(^{dipp}DIP^{tBu})PCl][OTf]$_2$, which were washed twice with 2 mL of Et_2O and 2 mL of *n*-pentane and dried *in vacuo*. Yield: 0.321 g, (69%). ^{1}H NMR (CD_2Cl_2, 300 MHz, 25°C): δ 9.60 (dd, 2H, J_{HH} = 8.3 Hz, J_{HP} = 2.5 Hz, PyrH_m), 9.38 (td, 1H, J_{HH} = 8.3 Hz, J_{HP} = 3.8 Hz, PyrH_p), 7.47 (m, 2H, ArH_p), 7.31 (m, 4H, ArH_m), 3.09 (sept, 4H, J_{HH} = 6.6 Hz, CH(CH_3)$_2$), 2.87 (sept, 4H, J_{HH} = 6.6 Hz,

C*H*(CH_3)$_2$), 1.64 (s, 18H, C(C*H*$_3$)$_3$), 1.22 (m (overlapping signals), 24H, CH(C*H*$_3$)$_2$). $^{31}P\{^1H\}$ NMR (CD_2Cl_2, 121MHz, 25°C, ppm): δ 52.0 (s). ^{19}F NMR (CD_2Cl_2, 282 MHz, 25°C, ppm): δ -78.7 (s, SO_3CF_3). HRMS $C_{39}H_{55}N_3$ calcd (found): 596.4128 (596.4149). UV-Vis (CH_2Cl_2): λ (ε) 329 (3109 M^{-1} cm^{-1}), 490 (182).

3.5.2 X-ray data collection, solution and refinement

Crystal structure data was using collected from multi-faceted crystals of suitable size and quality selected from a representative sample of crystals of the same habit using an optical microscope. In each case, crystals were mounted on MiTiGen loops with data collection carried out in a cold stream of nitrogen (150 K; Bruker D8 QUEST ECO). All diffractometer manipulations were carried out using Bruker APEX3 software.[47] Structure solution and refinement was carried out using XS, XT[48] and XL software, embedded within the Bruker SHELXTL suite.[49] For each structure, the absence of additional symmetry was confirmed using ADDSYM incorporated in the PLATON program.[50] Crystallographic data for the structures in this paper have been deposited with the Cambridge Crystallographic Data Centre, under CCDC deposition numbers 1981660 ([(^{dipp}DIP^{t}Bu)P][BPh_4].) and 1981661 ([(^{dipp}DIP^{t}Bu)PCl][$OTf]_2$).

Crystal structure parameters for **^{dipp}DIP^{t}Bu**: Crystals were grown by slow evaporation of a methanol solution. Colourless blocks; $C_{39}H_{55}N_3$ 565.86 g/mol, monoclinic, space group $P2_12_12_1$; a = 11.5846(5) Å, b = 15.1378(6) Å, c = 20.0063(8) Å, $\alpha = \beta = \gamma = 90°$, V = 3508.4(2) Å^3; Z = 4, ρ_{calcd} = 1.073 g cm^{-3}; crystal dimensions 0.400 x 0.260 x 0.180 mm; $2\theta_{max}$ = 55.018°; 56557 reflections, 8036 independent (R_{int} = 0.0668, intrinsic phasing; absorption coeff (μ = 0.062 mm^{-1}), absorption correction semi-empirical from equivalents (SADABS); refinement (against F_o^2) with

SHELXTL V6.1, 394 parameters, 0 restraints, R_1 = 0.0504 ($I > 2\sigma$) and wR_2 = 0.1057 (all data), Goof = 1.074, residual electron density 0.21/−0.23 Å^{-3}.

Crystal structure parameters for **[(^{dipp}DIP^{tBu})P][BPh$_4$]**: Crystals were grown by layering a saturated CH_2Cl_2 solution with pentane at room temperature overnight Orange blocks; $C_{63}H_{75}PN_3B$ 916.04 g/mol, triclinic, space group P-1 ; a = 11.1055(5) Å, b = 16.0253(7) Å, c = 17.3025(7) Å, α = 89.047(10)°, β = 77.2990(10)°, γ = 84.7880(10)°, V = 2991.5(2) Å^3; Z = 2, ρ_{calcd} = 1.017 g cm^{-3}; crystal dimensions 0.230 x 0.200 x 0.100 mm; $2\theta_{max}$ = 49.656°; 71070 reflections, 10284 independent (R_{int} = 0.0670, intrinsic phasing; absorption coeff (μ = 0.083 mm^{-1}), absorption correction semi-empirical from equivalents (SADABS); refinement (against F_o^2) with SHELXTL V6.1, 627 parameters, 0 restraints, R_1 = 0.0493 ($I > 2\sigma$) and wR_2 = 0.1217 (all data), Goof = 1.036, residual electron density 0.23/−0.24 Å^{-3}. The SQUEEZE function (spek 2009) was used through PLATON to remove two identical voids of 233 Å^3 and 87 electrons corresponding to two disordered dichloromethane molecules.

Crystal structure parameters for **[(^{dipp}DIP^{tBu})PCl][OTf]$_2$**: Crystals were obtained by layering *n*-pentane over a concentrated CH_2Cl_2 solution with a few added drops of CH_3CN to fully solubilize the complex and storing at -30 °C. Red blocks; $C_{41}H_{55}PN_3ClS_2O_6F_6$ 930.42 g/mol, monoclinic, space group $P2_1/n$; a = 12.0227(5) Å, b = 15.8372(6) Å, c = 23.6405(9) Å, $\alpha = \gamma$ = 90°, β = 98.638(2)°, V = 4450.2(3) Å^3; Z = 4, ρ_{calcd} = 1.389 g cm^{-3}; crystal dimensions 0.35 x 0.340 x 0.240 mm; $2\theta_{max}$ = 61.246°; 158336 reflections, 13673 independent (R_{int} = 0.0936, intrinsic phasing; absorption coeff (μ = 0.289 mm^{-1}), absorption correction semi-empirical from equivalents (SADABS); refinement (against F_o^2) with SHELXTL V6.1, 590 parameters, 24 restraints, R_1 =

0.0701 ($I > 2\sigma$) and wR_2 = 0.1683 (all data), Goof = 1.031, residual electron density 1.03/−0.87 $Å^{-3}$. The crystal structure includes two triflate counter-ions, one of which was modelled successfully. The second triflate exhibited disorder and was best modelled over two positions, using appropriate constraints and restraints. Specifically, each fluorine and sulfur atom was split over two positions and one of the three oxygen atoms were split over two positions.

3.5.3 Electrochemical Methods

For electrochemical analysis, 5-10 mg of the compound investigated was dissolved in 15 mL of 0.1 M [^{n}Bu$_4$N]PF$_6$ in CH_3CN and purged with Ar for 20 minutes prior to analysis. All electrochemical experiments were conducted under inert (Ar) atmosphere using a CHI 760c bipotentiostat, a 3 mm diameter glassy carbon working electrode, a Ag/Ag^+ non-aqueous quasi-reference electrode separated by a Vycor tip, and a Pt wire counter electrode. Cyclic voltammetric (CV) experiments were conducted using scan rates of 50-800 mV/s. Differential Pulse Voltammetry (DPV) experiments were also conducted, using a 5 mV increment, 50 mV amplitude, 0.1 s pulse width, 0.0167 s sample width, and 0.5 s pulse period. Upon completion of all CV and DPV analyses, ferrocene (FcH, [(η^5-C_5H_5)$_2$Fe)]) was added to the solution as an internal standard, with all potentials reported versus the $FcH^{0/+}$ redox couple.[51]

3.6 References

(1) Gibson, V. C.; Redshaw, C.; Solan, G. A. *Chem. Rev.* **2007**, *107* (5), 1745.

(2) Knijnenburg, Q.; Gambarotta, S.; Budzelaar, P. H. M. *Dalton Trans.* **2006**, No. 46, 5442.

(3) Zhu, D.; Thapa, I.; Korobkov, I.; Gambarotta, S.; Budzelaar, P. H. M. *Inorg. Chem.* **2011**, *50* (20), 9879.

(4) Römelt, C.; Weyhermüller, T.; Wieghardt, K. *Coord. Chem. Rev.* **2019**, *380*, 287.

(5) Lyaskovskyy, V.; de Bruin, Bas. *ACS Catal.* **2012**, *2* (2), 270.

(6) Flisak, Z.; Sun, W.-H. *ACS Catal.* **2015**, *5* (8), 4713.

(7) Rahimi, N.; Herbert, D. E.; Budzelaar, P. H. M. *Eur. J. Inorg. Chem.* **2018**, *45*, 4856.

(8) Rahimi, N.; Herbert, D. E.; Budzelaar, P. H. M. *Eur. J. Inorg. Chem.* **2019**, *6*,780.

(9) Galley, S. S.; Pattenaude, S. A.; Higgins, R. F.; Tatebe, C. J.; Stanley, D. A.; Fanwick, P. E.; Zeller, M.; Schelter, E. J.; Bart, S. C. *Dalton Trans.* **2019**, *48* (23), 8021.

(10) Scott, J.; Gambarotta, S.; Korobkov, I.; Knijnenburg, Q.; De Bruin, B.; Budzelaar, P. H. M. *J. Am. Chem. Soc.* **2005**, *127* (49), 17204.

(11) Jurca, T.; Lummiss, J.; Burchell, T. J.; Gorelsky, S. I.; Richeson, D. S. *J. Am. Chem. Soc.* **2009**, *131* (13), 4608.

(12) Jurca, T.; Dawson, K.; Mallov, I.; Burchell, T.; Yap, G. P. A.; Richeson, D. S. *Dalton Trans.* **2010**, *39* (5), 1266.

(13) Pedrido, R.; Romero, M. J.; Bermejo, M. R.; Gonzalez-Noya, A. M.; Maneiro, M.; Rodriguez, M. J.; Zaragoza, G. *Dalton Trans.* **2006**, No. 44, 5304.

(14) Chu, T.; Belding, L.; van der Est, A.; Dudding, T.; Korobkov, I.; Nikonov, G. I. *Angew. Chem., Int. Ed.* **2019**, *53* (10), 2711.

(15) Reeske, G.; Cowley, A. H. *Chem. Commun.* **2006**, No. 16, 1784.

(16) Martin, C. D.; Ragogna, P. J. *Dalton Trans.* **2011**, *40* (44), 11976.

(17) Magdzinski, E.; Gobbo, P.; Martin, C. D.; Workentin, M. S.; Ragogna, P. J. *Inorg. Chem.* **2012**, *51* (15), 8425.

(18) Chitnis, S. S.; LaFortune, J. H. W.; Cummings, H.; Liu, L. L.; Andrews, R.; Stephan, D. W. *Organometallics* **2018**, *37* (24), 4540.

(19) Martin, C. D.; Le, C. M.; Ragogna, P. J. *J. Am. Chem. Soc.* **2009**, *131* (42), 15126.

(20) Martin, C. D.; Ragogna, P. J. *Inorg. Chem.* **2012**, *51* (5), 2947.

(21) Andrews, R. J.; Chitnis, S. S.; Stephan, D. W. *Chem. Commun.* **2019**, *55* (39), 5599.

(22) Norton, E. L.; Szekely, K. L. S.; Dube, J. W.; Bomben, P. G.; Macdonald, C. L. B. *Inorg. Chem.* **2008**, *47* (3), 1196.

(23) Ellis, B. D.; Macdonald, C. L. B. *Coord. Chem. Rev.* **2007**, *251* (7+8), 936.

(24) Herbert, D. E.; Miller, A. D.; Ozerov, O. V. *Chem. Eur. J.* **2012**, *18* (25), 7696.

(25) Reeske, G.; Cowley, A. H. *Inorg. Chem.* **2007**, *46* (4), 1426.

(26) Chirik, P. J.; Wieghardt, K. *Science* **2010**, *327* (5967), 794.

(27) Dunn, N. L.; Ha, M.; Radosevich, A. T. *J. Am. Chem. Soc.* **2012**, *134* (28), 11330.

(28) Reichl, K. D.; Dunn, N. L.; Fastuca, N. J.; Radosevich, A. T. *J. Am. Chem. Soc.* **2015**, *137* (16), 5292.

(29) Zhao, W.; Yan, P. K.; Radosevich, A. T. *J. Am. Chem. Soc.* **2015**, *137* (2), 616.

(30) Nykaza, T. V.; Harrison, T. S.; Ghosh, A.; Putnik, R. A.; Radosevich, A. T. *J. Am. Chem. Soc.* **2017**, *139* (20), 6839.

(31) Ghosh, A.; Lecomte, M.; Kim-Lee, S.-H.; Radosevich, A. T. *Angew. Chem., Int. Ed.* **2019**, *58* (9), 2864.

(32) Power, P. P. *Nature* **2010**, *463* (7278), 171.

(33) Steves, J. E.; Kennedy, M. D.; Chiang, K. P.; Kassel, W. S.; Dougherty, W. G.; Dudley, T. J.; Zubris, D. L. *Dalton Trans.* **2009**, No. 7, 1214.

(34) Zhu, D.; Budzelaar, P. H. M. *Organometallics* **2008**, *27* (12), 2699.

(35) Ellis, B. D.; Carlesimo, M.; Macdonald, C. L. B. *Chem. Commun.* **2003**, No. 15, 1946.

(36) Ellis, B. D.; Macdonald, C. L. B. *Inorg. Chem.* **2006**, *45* (17), 6864.

(37) Dutton, J. L.; Sutrisno, A.; Schurko, R. W.; Ragogna, P. J. *Dalton Transactions* **2008**, No. 26, 3470.

(38) Cowley, R. E.; Chiang, K. P.; Holland, P. L.; Adhikari, D.; Zuno-Cruz, F. J.; Cabrera, G. S.; Mindiola, D. J. *Inorg. Synth.* **2010**, *35*, 13.

(39) Hyvl, J.; Yoshida, W. Y.; Rheingold, A. L.; Hughes, R. P.; Cain, M. F. *Chem. Eur. J.* **2020**, *22* (49), 17562.

(40) Soshnikov, I. E.; Bryliakov, K. P.; Antonov, A. A.; Sun, W.-H.; Talsi, E. P. *Dalton Trans.* **2019**, *48* (23), 7974.

(41) Flock, J.; Suljanovic, A.; Torvisco, A.; Schoefberger, W.; Gerke, B.; Pöttgen, R.; Fischer, R. C.; Flock, M. *Chem. Eur. J.* **2020**, *19* (46), 15504.

(42) Pyykkö, P.; Atsumi, M. *Chem. Eur. J.* **2009**, *15* (1), 186.

(43) Mantina, M.; Chamberlin, A. C.; Valero, R.; Cramer, C. J.; Truhlar, D. G. *J. Phys. Chem. A* **2009**, *113* (19), 5806.

(44) Ellis, B. D.; Macdonald, C. L. B. *Inorg. Chim. Acta.* **2007**, *360* (1), 329.

(45) Duarte, G. M.; Braun, J. D.; Giesbrecht, P. K.; Herbert, D. E. *Dalton Transactions* **2017**, *46* (47), 16439.

(46) Braun, J. D.; Gray, P. A.; Sidhu, B. K.; Nemez, D. B.; Herbert, D. E. *Dalton Transactions* **2020**, Ahead of Print.

(47) Bruker-AXS APEX3 v2016.1-0, Madison, Wisconsin, USA, 2016. .

(48) Sheldrick, G. M. *Acta Crystallogr., Sect. A: Found. Crystallogr.* **2015**, *71* (1), 3.

(49) Sheldrick, G. M. *Acta Crystallogr., Sect. A: Found. Crystallogr.* **2008**, *64*, 112.

(50) Spek, A. L. *Acta Crystallogr., Sect. D: Biol. Crystallogr.* **2009**, *65*, 148.

(51) Connelly, N. G.; Geiger, W. E. *Chem. Rev.* **1996**, *96* (2), 877.

Chapter 4

Iron Coordination Complexes with Nanosecond Charge-Transfer Excited-State Lifetimes

4.1 Abstract

Replacing current benchmark rare-element photosensitizers with ones based on abundant and low-cost metals such as iron would help facilitate the large-scale implementation of solar energy conversion. To do so, the ability to extend the lifetimes of photo-generated excited states of iron complexes is critical. A sensitizer design where iron is supported by frameworks containing benzannulated phenanthridine and quinoline heterocycles paired with amido donors is presented here. These complexes exhibit panchromatic absorption and nanosecond charge-transfer excited states, enabled by the combination of vacant, energetically accessible heterocycle-based acceptor orbitals and occupied molecular orbitals destabilized by strong mixing between amido nitrogen atoms and iron. These findings show how ligand design can extend MLCT-type charge-transfer excited-state lifetimes of iron(II) complexes into the nanosecond regime and expand the range of potential applications for iron-based photosensitizers.

4.2 Introduction

Despite solar energy's potential for mitigating the environmental impacts of powering our planet,[1] the cost of light-harvesting materials still presents a considerable barrier to widespread adoption.[2] In this respect, sensitizing wide band-gap semiconductors by anchoring light-absorbing molecules to their surfaces[3] offers appealing advantages in constructing practical devices from

inexpensive, abundant semiconductor materials with low fabrication costs.[4] But designing materials for the global market requires that high-performing sensitizers are also based on abundant and affordable elements.[5] This is likewise true of increasing the sustainability of materials used for solar fuel-forming catalysis[6] and photochemical synthesis.[7] To do so, coordination complexes must ideally be engineered to broadly absorb visible light and exhibit sufficiently long-lived charge-transfer (CT) excited states essential to efficient charge injection[8] or to building up sufficient concentrations of reactive excited states for synthesis.[9]

Precious metal photosensitizers tend to fulfill these criteria effectively, and photochemical/photovoltaic applications are presently dominated by the use of complexes of Ru and Ir,[10,11] though inventive ligand designs are imbuing complexes of Cu,[11,12] Zr,[13] Co,[14] Cr,[15,16] and W[17] with properties that are favourable for photosensitizer applications.[18] With respect to abundant and benign metals, iron has long represented a target in sustainable photosensitizer design.[19] Compared with benchmark precious metal photosensitizers such as $[Ru(bpy)_3]^{2+}$ (bpy = 2,2'-bipyridine), iron coordination complexes typically suffer from rapid, sub-picosecond (ps) relaxation of metal-to-ligand charge transfer (MLCT) states into low-lying metal-centred (MC) states.[20] Strategies to extend CT lifetimes by tuning ligand fields through strengthening metal-ligand bonds have pushed the boundary of accessible charge-transfer excited state lifetimes from ~10 ps[21] to ~20 ps[22] for complexes of strongly σ-donating, cyclometallated carbene[23] or cyanide ligands. This has enabled much higher yields of electron injection into dye-sensitized TiO_2 photoelectrodes compared to from polypyridyl analogs.[24,25] Further extending this strategy to incorporate six triazolylidene carbenes in an octahedral arrangement about Fe, led to a remarkably long-lived ligand-to-metal charge transfer (^{2}LMCT) excited state (~100 ps) and the first example of room-temperature photoluminescence from a low-spin Fe(III) complex,[26] with a record ^{3}MLCT

lifetime of 528 ps for the reduced Fe(II) analog.[27] Weakening the ligand field by enhancing interligand repulsion can also extend CT excited state lifetimes generated from high-spin ground state Fe(II) compounds, with lifetimes of ~17 ps reported for *bis*-homoleptic Fe(II) complexes of 6,6"-halogenated terpyridines.[28] These design strategies, however, are conceivably limited by either the saturation of an octahedral ligand field with a maximum of six, strong σ-donors[29] or the reduced stability of metal-ligand complexes in the weak field limit,[28] and neither offers an obvious mechanism for combining extended CT excited-state lifetimes and panchromatic absorption.

A distinct design approach is to increase mixing between filled metal t_{2g} orbitals and filled ligand molecular orbitals. Thereby, the character of the highest occupied molecular orbital (HOMO) of an octahedral Fe(II) complex is transformed from being metal-centred to ligand-centred ('HOMO inversion'[30]). This has been predicted computationally to produce dramatic changes in light absorption, including increased molar extinction coefficients and broad absorptive cross-sections across the visible wavelength region.[30] Installing orthogonal, tridentate diarylamido pincer-type ligands on Fe to give octahedral d^6 complexes conceptually fits this design motif: two filled amido N(2p) orbitals would have the appropriate symmetry to mix with orthogonal occupied metal d orbitals resulting in a destabilization of the HOMO and HOMO-1 that would take on anti-bonding (π*(p+d)) character, provided orbital energies match and overlap is significant (Figure 4.1).[31] Combined with moieties that incorporate energetically accessible, vacant orbitals elsewhere on the molecular scaffold, such designs should conceivably also exhibit enhanced charge-transfer character in their excited states.[32]

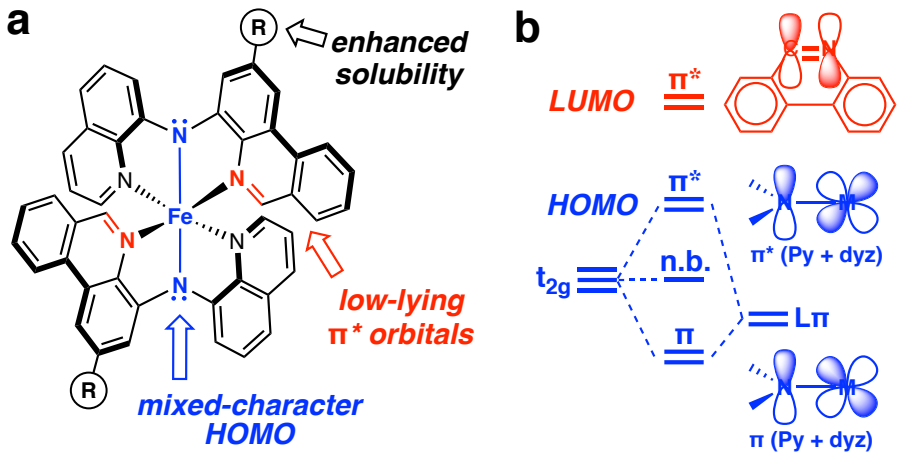

Figure 4.1 (a) [Fe{(phenanthridine-4-yl(quinoline-8-yl)amido}$_2$] complexes (b) Schematic showing design principles of the work

The synthesis and characterization of Fe complexes of benzannulated amido pincer-like ligands (Figure 4.1a) is reported and an investigation into their electronic absorption and photophysics is described below.

4.3 Results and Discussion

4.3.1 Synthesis and Characterization of Ligands and Coordination Complexes

Bis(8-quinolinyl)amido (BQA) ligands are particularly robust examples of chelating diarylamido motifs and pseudo-octahedral iron(II) complexes have been previously reported;[31] however, poor solubility precluded thorough investigation of their photophysical properties. To remedy this and target improved CT character, incorporation of ancillary substituents and further benzannulation in the form of phenanthridine units was employed. Compared with quinoline, phenanthridines present more accessible unoccupied orbitals (lower energy, π*-based LUMO), as the dominant resonance contributor is an 'imine-bridged, biphenyl' that maximizes the number of aromatic subunits.[33] The LUMO is thus localized at the C=N, lending phenanthridines

conceptually similar electron-accepting character to the prototypical redox non-innocent scaffold (2,6-diimine)pyridine (DIP).[34]

Following a strategy developed for constructing bidentate analogs,[35] 4-halo/4-nitro/4-amino substituted phenanthridines (**4a-e**) were prepared and coupled with 8-aminoquinoline/8-bromoquinoline to access proligands **5a-c** in yields >90% (Scheme 4.1).

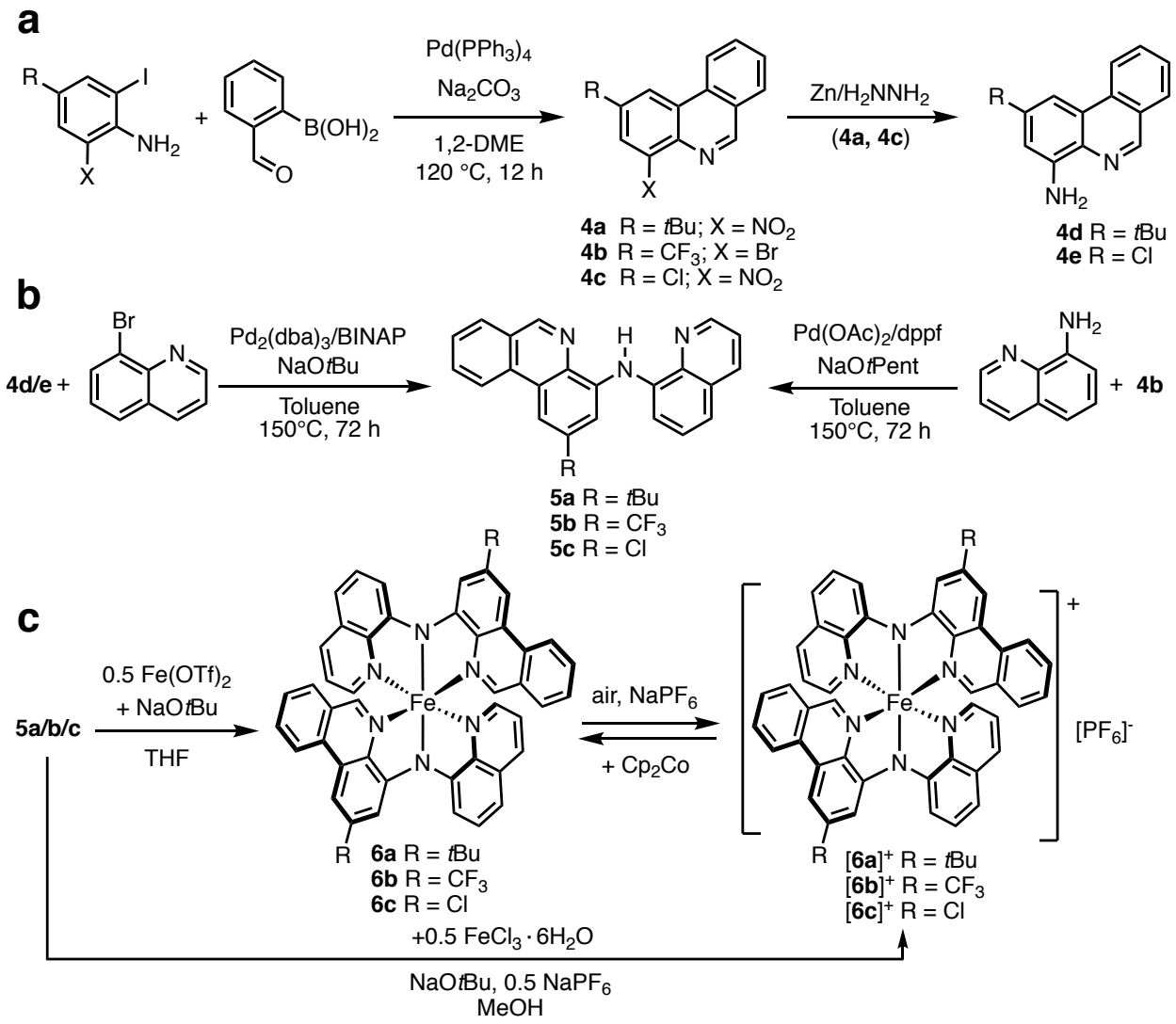

Scheme 4.1 Synthesis of (a) substituted phenanthridines (b) ligands (c) pseudo-octahedral neutral and cationic iron complexes.

The formation of **5a-c** was confirmed by multinuclear NMR by the appearance of a downfield N-H resonance at ~10.5 – 10.8 ppm and in the case of **5a**, single-crystal X-ray diffraction (Figure 4.2).

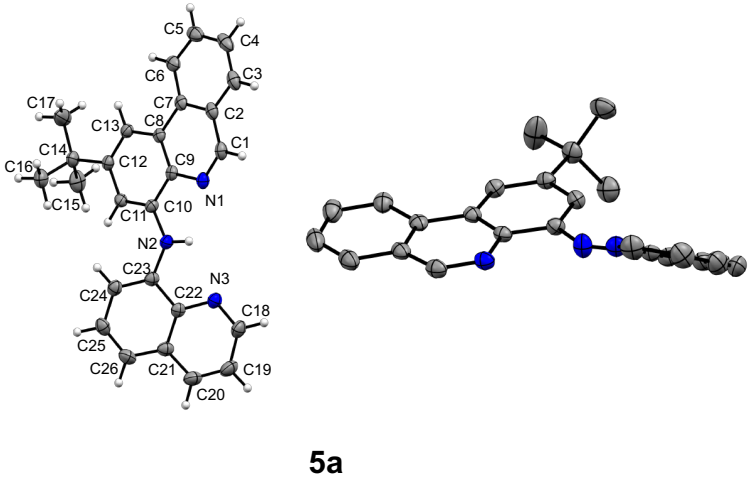

5a

Figure 4.2 Crystal structure of **5a** with thermal ellipsoids shown at 50 % probability level

Addition of base to solutions of the proligands produced a deep purple colour, which changed to green upon combining with ferrous iron. **6a-c** were isolated as dark green solids following recrystallization. One-electron oxidized species [**6a-b**]$^{+}$ could in turn be isolated as PF_6^- salts via oxidation in air in the presence of $NaPF_6$, however, **6c** did not seem to oxidize. The cationic complexes could also be synthesized directly via metallation of **5a-c** with $FeCl_3$•$6H_2O$. Voltammetric analysis of [**6a-c**]PF_6 revealed two additional (quasi)reversible oxidation events (Figure 4.8) for [**6a-b**]PF_6 and one for [**6c**]PF_6 (Figure S167) and overlapping reductions below -2 V that are likely phenanthridine-based, as similar cathodic events are not observed for the smaller π-system of $Fe(BQA)_2$.[31]

4.3.2 Solid-State and Electronic Structures

The solid-state structures of [**6a-c**]$^{0/+}$ were determined by single-crystal X-ray diffraction (Figures 4.3 and 4.4). In all six complexes, Fe is in a distorted octahedral geometry, with trans-disposed amido nitrogens (N_{amido}-Fe-N_{amido} 178-180°; Table 4.1) and drawn-back intraligand N_{phen}–Fe–N_{quin} angles (~166°). While heterocycle $N_{phen/quin}$-Fe bond distances are similar, a slightly shorter distance is observed for each anionic N_{amido}-Fe interaction. Changing the substituent in the 2-position of the phenanthridinyl unit does not significantly impact the coordination environment around Fe.

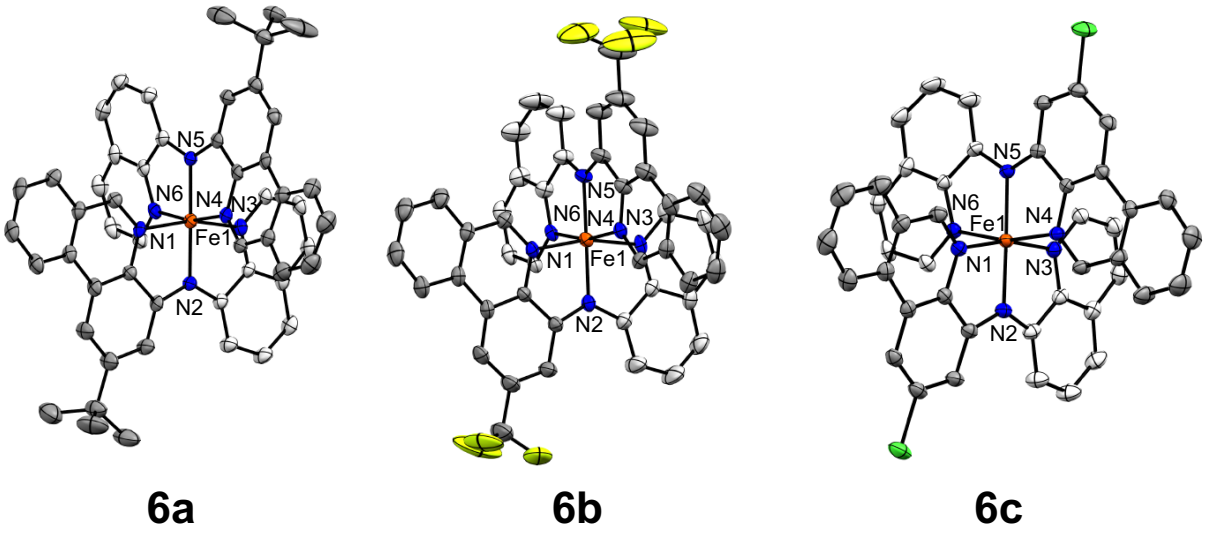

Figure 4.3 Crystal structure of **6a-c** with thermal ellipsoids shown at 50 % probability level. Solvent molecules and hydrogen atoms are omitted for clarity

Comparing neutral and cationic compounds, the most pronounced difference is shorter N_{amido}-Fe bonds in [**6a-c**]$^{+}$, which contract by an average of 0.04 Å. The $N_{phen/quin}$-Fe distances do not change significantly. In related pseudo-octahedral complexes of diarylamido ligands, redox-induced changes to N_{amido}-metal distances were found to be sensitive to the degree of mixing between filled metal orbitals and N(2p) lone pairs. For example, statistically insignificant changes

in N_{amido}-metal distances were observed on oxidation of Ni(II) complexes supported by *bis*(pyrazolyl)amido ligands.[36] Despite the presence of a redox-active Ni(II), the orbital from which oxidation occurred was largely localized on nitrogen with only weak mixing with Ni; the weaker ligand field precluded substantial (p+d) π interactions.

Table 4.1 Selected bond distances (Å) and angles (°) for [**6a-c**]$^{0/+}$

	6a	**6b**	**6c**	[**6a**]PF_6	[**6b**]PF_6	[**6c**]PF_6
Fe – N_{phen}						
Fe1 – N1	1.941(3)	1.945(2)	1.9407(13)	1.946(2)	1.957(4)	1.953(8)
Fe1 – N4	1.945(3)	1.955(2)	1.9410(13)	1.966(2)	1.958(4)	1.953(8)
Fe – N_{amido}						
Fe1 – N2	1.934(3)	1.924(3)	1.9294(14)	1.885(2)	1.881(4)	1.884(6)
Fe1 – N5	1.936(3)	1.932(2)	1.9330(14)	1.905(2)	1.906(4)	1.884(6)
Fe – N_{quin}						
Fe1 – N3	1.943(3)	1.946(2)	1.9389(14)	1.945(2)	1.959(4)	1.930(7)
Fe1 – N6	1.947(3)	1.956(2)	1.9468(14)	1.964(2)	1.965(4)	1.930(7)
N_{phen} – C[a]						
N1 – C1	1.309(5)	1.306(4)	1.315(2)	1.306(4)	1.298(6)	1.295(11)
N4 – C23	1.312(4)	1.309(4)	1.311(2)	1.306(3)	1.307(6)	1.295(11)
N4 – C24						
N4 – C27						
Intraligand angles						
N1 – Fe1 – N3	165.77(12)	166.46(11)	166.23(6)	167.08(10)	166.76(18)	166.4(3)
N1 – Fe1 – N2	82.85(12)	82.77(10)	82.94(5)	83.80(10)	83.64(17)	83.5(3)
N2 – Fe1 – N3	82.91(12)	83.69(10)	83.31(6)	83.41(10)	83.18(17)	82.9(3)
N4 – Fe1 – N6	166.11(12)	165.92(10)	166.26(6)	164.87(10)	166.97(17)	166.4(3)
N4 – Fe1 – N5	83.10(11)	82.89(10)	83.27(6)	82.58(10)	83.12(17)	83.5(3)
N5 – Fe1 – N6	83.03 (11)	83.03(10)	83.14(6)	82.33(10)	83.87(18)	82.9(3)
Interligand angles						
N2 – Fe1 – N5	179.23(12)	179.65(11)	178.72(6)	178.16(11)	179.7(2)	179.8(4)
N1 – Fe1 – N6	92.18(11)	89.85(9)	92.34(5)	93.24(10)	91.39(17)	93.1(3)
N2 – Fe1 – N4	96.39(11)	97.12(10)	97.99(6)	98.72(10)	96.74(17)	96.3(3)
N2 – Fe1 – N6	97.47(11)	96.96(10)	95.61(6)	96.39(10)	96.27(18)	97.3(3)
N1 – Fe1 – N5	97.72(12)	96.88(11)	96.84(6)	94.93(10)	96.66(17)	96.3(3)
N3 – Fe1 – N5	96.51(12)	96.66(11)	96.93(6)	97.81(10)	96.52(17)	97.3(3)
N3 – Fe1 – N4	91.02(11)	90.22(9)	89.84(6)	94.57(10)	93.48(17)	93.1(3)

[a] "Imine-like" (C=N) carbon adjacent to N(4) in the phenanthridine arm, labeled C27 in **6a**/[**6a**]$^+$, C24 in **6b**/[**6b**]$^+$ and C23 in **6c**/[**6c**]PF_6

In comparison, constriction of the N_{amido}-Fe distance following oxidation of **6a-c** is attributable to depopulation of a HOMO with substantial N-Fe π-antibonding character (Figure 4.1b). Density functional theory (DFT) calculations reinforce this interpretation. The two highest energy occupied orbitals (HOMO, HOMO-1) of **6a-c** represent π anti-bonding overlap between the amido nitrogens and the metal centre (π*(p+d)). The HOMO-2 presents substantial non-bonding character and is localized at iron (~67%), while the next two highest energy MOs contain the corresponding π-bonding overlap.

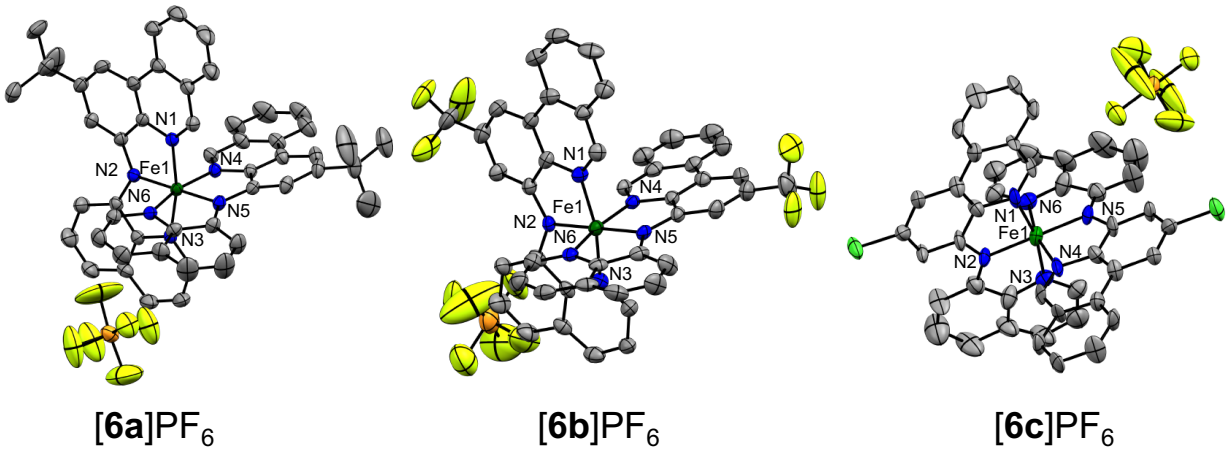

Figure 4.4 Crystal structure of [**6a-c**]$^{+}$ with thermal ellipsoids shown at 50 % probability level. Solvent molecules and hydrogen atoms are omitted for clarity

Therefore, **6a-c** represent intermediate cases of the 'HOMO inversion' model.[30] Accordingly, the distorted coordination about the Fe ions is clearly identified by the presence of non-zero electric field gradients, quantified by ^{57}Fe Mössbauer spectral doublets for **6a-b** (Figure 4.5, Table 4.2) that exhibit much larger splitting (**6a**: quadrupolar splitting Δ = 1.442(1) mm s^{-1} and isomer shift δ = 0.2911(6) mm s^{-1}; **6b**: Δ = 1.425(1) mm s^{-1}, δ = 0.2863(5) mm s^{-1}) than Fe(smif)$_2$[37] (Δ = 0.62(1) mm s^{-1}, δ = 0.30(1) mm s^{-1}) that is a neutral pseudooctahedral Fe(II) complex of tridentate azaallyl ligands (smif = [(2-pyridinyl-CH)$_2$N]$^{-}$), with *trans* central N donors,

flanking pyridyl donors, and very similar N_{py}-Fe-N_{py} bond angles and central Fe-N distances to **6a-b**. $Fe(smif)_2$ is an example of full HOMO inversion, with carbon-based azaallyl HOMO and HOMO-1 MOs that do not significantly mix with Fe-based d-orbitals as a result of the presence of a node at the N bound to Fe.[37] Nor are the isomer shifts and quadrupole splittings as affected by oxidation (i.e., for [**6a-b**]$^{0/+}$) as for other polypyridyl Fe complexes (Table 4.2).

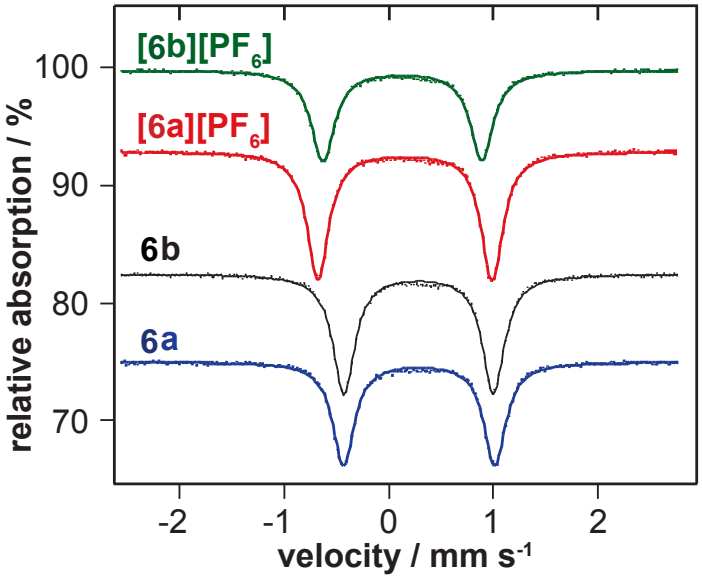

Figure 4.5 Mössbauer spectra (10 K) of **6a-b** and [**6a-b**]PF_6

Table 4.2 Hyperfine parameters for **6a-b** and [**6a-b**]PF_6 and related compounds

Compound	δ / mm s^{-1}	Δ / mm s^{-1}
6a[a]	0.2911(6)	1.442(1)
6b[a]	0.2863(5)	1.425(1)
$[Fe(terpy)_2][ClO_4]_2$[38]	0.238	1.14
$[Fe(bpy)_3][ClO_4]_2$[b39]	0.325	0.39
[Fe(2-arylazo-phenanthroline)$_2$][ClO_4]$_2$[b40]	0.22	1.80
$Fe((2\text{-pyridyl-CH})_2N)_2$[b37]	0.30(1)	0.62(1)
[**3a**]PF_6[a]	0.1563(5)	1.661(1)
[**3b**]PF_6[a]	0.1307(6)	1.513(1)
$[Fe(terpy)_2][ClO_4]_3$[b41]	0.07	3.43

[a] 10 K [b] 80 K

Focusing on trends within the two separate pairs of molecules, oxidation of $[Fe(terpy)_2]^{2+}$ to $[Fe(terpy)_2]^{3+}$,[41] for example, resulted in larger relative changes in δ and Δ compared with [**6a-**

b]$^{0/+}$, suggesting that oxidation more strongly perturbs the electronic environment about Fe in [Fe(terpy)$_2$]$^{2+/3+}$ compared to [**6a-b**]$^{0/+}$, with a more symmetric electric field about the nucleus in the latter compound as evidenced by the significantly smaller value of Δ.

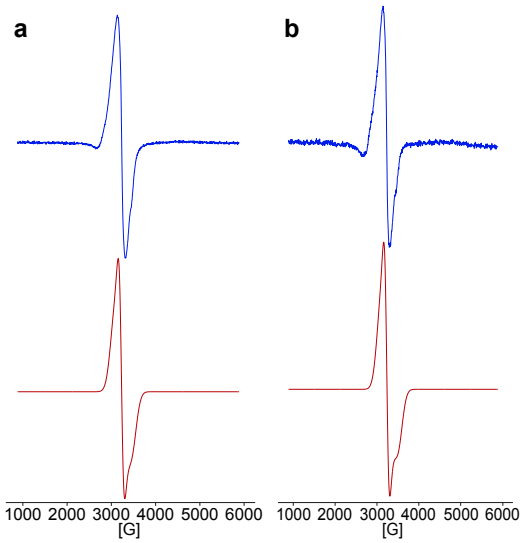

Figure 4.6 X-band EPR spectrum (top) and simulations (bottom) in frozen CH_2Cl_2 glass at 20 K of (a) [**6a**]PF_6 and (b) [**6b**]PF_6

Indeed, the EPR spectra of [**6a-b**]PF_6 collected at 20 K in CH_2Cl_2 glass contain asymmetric, broad resonances best modeled with slightly inequivalent *g* tensors (Figures 4.6, S86), unlike the rhombic signal observed for [Fe(BQA)$_2$]$^+$.[31] This is inconsistent with localization of the unpaired electron at the metal, though resolved ^{14}N hyperfine coupling was not observed.

The lowest energy unoccupied MOs (LUMO, LUMO+1) have limited contributions from Fe and are instead largely comprised of the π* system of the phenanthridinyl arms (**6a**: LUMO: 77 %, LUMO+1: 52 %; **6b**: LUMO: 86 %, LUMO+1: 70 %; **6c**: LUMO: 52 %, LUMO+1: 75 %). The quinolinyl π* systems contribute as well, to a lesser but still significant extent, and more strongly to the LUMO+2 (**6a**: 60 %; **6b**: 63 %; **6c**: 44 %) and LUMO+3 (**6a**: 50 %; **6b**: 75 %; **6c**: 64 %). Exchanging electron-releasing *t*Bu groups in **6a** for electron-withdrawing CF_3 substituents

in the 2-positions of the phenanthridinyl arms of **6b** increases the phenanthridine contributions to the two lowest energy unoccupied MOs over those from quinoline, slightly stabilizing the LUMO and LUMO+1 and shifting the edge of the lowest energy absorption manifold to lower energy (Figure 4.7; calculated HOMO-LUMO gap: **6a** 1.43 eV, **6b** 1.38 eV).

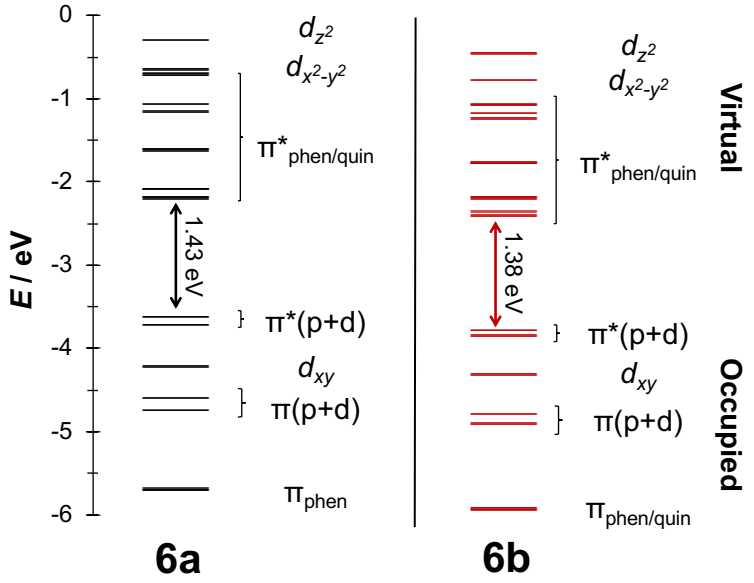

Figure 4.7 Relative energies of the molecular orbitals calculated for **6a** and **6b** [SMD-M06L/6-31+G(d,p)//SMD-O3LYP/6-31+G(d,p)]

Indeed, the potential for the reduction of [**6b**]$^{0/-}$ (-2.20 V vs FcH$^{0/+}$) is shifted anodically by 230 mV compared to that of [**6a**]$^{0/-}$ (-2.43 V) and 80 mV to that of [**6c**]$^{0/-}$ (-2.26 V vs FcH$^{0/+}$) (Figures 4.8 and S167), consistent with a lower energy LUMO (DFT-calculated LUMO energies: **6a** = -2.20 eV; **6b** -2.40 eV; **6c** -2.30 eV). This substituent effect is mirrored in the first oxidation event, with the [**6a**]$^{0/+}$ redox couple accessed at a more negative potential (-0.77 V vs. FcH$^{0/+}$) than [**6b**]$^{0/+}$ (-0.61 V) and [**6c**]$^{0/+}$ (-0.63 V). MOs comprised of the remaining two Fe d orbitals that present metal-ligand σ-anti-bonding character (i.e., the e_g states of a symmetric octahedral complex) are significantly destabilized (LUMO+10, LUMO+11).

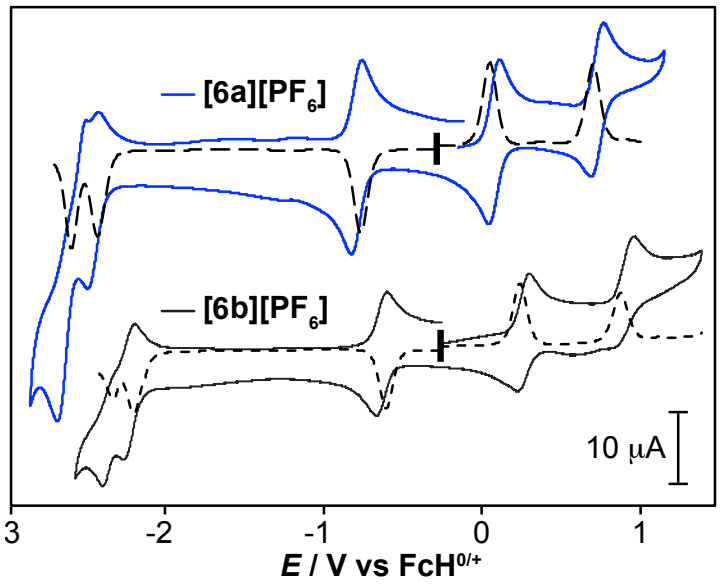

Figure 4.8 Cyclic voltammograms (—) and differential pulse voltammograms (---) of [**6a**]PF_6 (top) and [**6b**]PF_6 (bottom) in CH_3CN with 0.10 M [^{n}Bu$_4$N]PF_6 as the supporting electrolyte

The ligand field of our phenanthridinyl/quinolinyl amido ligands therefore induces considerable N(2p)-Fe(3d) mixing, raising the energy of the two mixed-character HOMOs, with the phenanthridinyl moieties dominating the lower energy unoccupied orbital manifolds and destabilizing metal-centred (MC) excited states in favour of charge-transfer ones.

4.3.3 Steady-State and Transient Absorption (TA) Spectroscopy

Steady-state UV-Vis spectra showed **6a-c** absorb strongly across the visible spectrum (Figures 4.9 and S88). The high molar absorptivities (ε ~ 10-30 $mM^{-1}cm^{-1}$) for broad peaks at ~450, 600 and 730 nm that tail off at ~850 nm are consistent with CT character to transitions throughout this region. Time-dependent DFT (TD-DFT) simulations support this assignment: the lowest energy spectral bands (650-900 nm) of **6a-c** are dominated by five key transitions with similar CT character in which electron density is relocated from occupied π*(p+d) N_{amido}-Fe anti-

bonding orbitals (HOMO, HOMO-1) to *N*-heterocycle ligand-based π* acceptor MOs (LUMO-LUMO+3) in transitions that can be described as '$\pi_{anti\text{-}bonding}$-to-ligand charge transfer' (PALCT).[42] Metal-to-ligand charge transfer (MLCT) transitions involving the Fe-localized HOMO-2 occur at higher energy [**6a**: 500-590 nm; **6b**: 556-613; **6c**: 554-590 nm] while the corresponding PBLCT ('$\pi_{bonding}$-to-ligand charge transfer') transitions involving the two MOs with π(p+d) N_{amido}-Fe bonding character (HOMO-3, HOMO-4) are found at slightly higher energy (**6a**: 475-510 nm, **6b**: 430-515 nm, **6c**: 434-498 nm; Tables S13-S15).

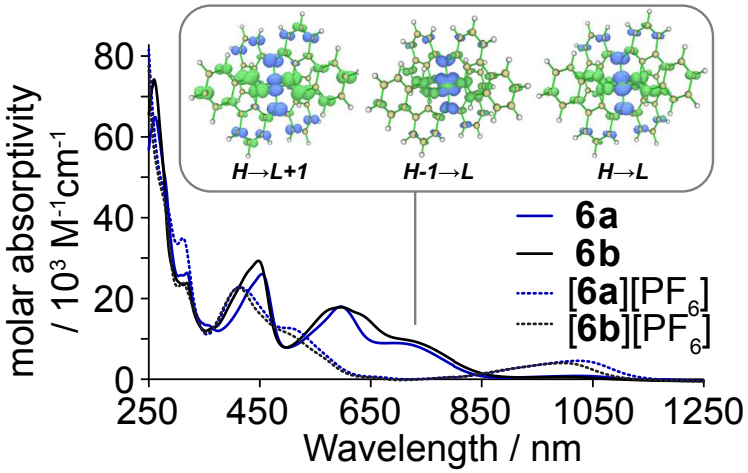

Figure 4.9 Steady-state UV/Vis absorption spectra of **6a-b** and [**6a-b**]PF_6 in CH_3CN. [**6c**]$^{0/+}$ are omitted for clarity but found in Figures S88 and S89. Inset: TD-DFT calculated electron density gain (green) and depletion (blue) distribution maps (isosurface = 0.002) for **6b**

Noting the correlation between the spacing of the first one-electron oxidation and reduction potentials and MLCT energies,[43] the $\Delta E_{1/2}$ calculated for **6a-b** (**6a**: 1.66 V; **6b**: 1.59 V; **6b**: 1.63 V) are ~0.75 V lower than for $[Fe(tpy)_2]^{2+}$ (2.36 V),[44] consistent with the significant red-shift to the lowest energy absorptions of the benzannulated complexes. In the one-electron oxidized complexes ([**6a-c**]PF_6), most of the absorptive cross-section was attenuated between 600-800 nm, in agreement with loss of low-energy PALCT transitions, while broad, strong absorptions (ε ~ 10-

20 mM^{-1} cm^{-1}) were evident at ~410 and 510 nm. TD-DFT (for [**6a-b**]$^{+}$) assigns these bands to CT transitions involving ligand π* acceptor orbitals (Figures S106-109 and Tables S18-19). LMCT/$\pi_{anti\text{-}bonding}$-to-metal CT-type transitions involving the singly occupied MO of [**6a-b**]$^{+}$ as the acceptor orbital appear at very low energy (λ_{max} ~ 1000 nm). All features of the steady-state spectra of [**6a-c**]$^{0/+}$ were reproduced by spectroelectrochemistry (Figure S90).

Transient differential pump-probe spectra were collected to investigate the excited state dynamics of **6a-c**. Solutions were excited into the lower energy end of the broad charge-transfer manifold ($\lambda_{excitation}$ = 780 nm) and probed with broadband white light (see Supporting Information for full experimental details). Similar features were observed for both **6a-c**, and so **6a-b** is described in detail here (see SI for discussion of **6c**). At early delay times of < 1 ps, an excited-state absorption (ESA) band centred at ~ 480 nm (**6a**: 486 nm, **6b**: 472 nm) is initially observed, followed by a slight red-shift to the ESA and establishment of the ground-state bleach (GSB) which reaches maximum intensity at 1.98 ps for **6b** (0.34 ps for **6a**). The steady-state UV-Vis spectrum shows three main features at wavelengths greater than 400 nm; these are the broad transient bleaching features observed in the time-resolved spectra (Figure 4.10). The broad GSB at 600 nm overlaps somewhat with the sharp ESA feature at 485 nm. From 0.34 ps to 3 ns (**6a**) and 1.98 ps to 3 ns (**6b**), the ESA broadens slightly, which is attributet to the GSB weakening over this same period.

To assign the nature of the excited states responsible for both the ESA and the GSB, the experimental transient spectra can be compared to the spectra of the corresponding oxidized or reduced complexes.[45] The potentials necessary to reduce **6a-c** were quite negative (**6a**: -2.4 V; **6b**: -2.2 V; **6c**: -2.26 V vs $FcH^{0/+}$) and overlapped with a second, irreversible reduction (Figures 4.8 and S167). As such, electrochemically generated spectra of the reduced species [**6a-c**]$^{-}$ could not

be obtained. Nevertheless, the oxidized species [**6a-c**]$^{+}$ presented distinctive optical markers with which charge-transfer states may be distinguished from non-redox, ligand field ones.[45] Notably, the well-defined ESA feature at ~480 nm faithfully reproduced the absorption peak observed for [**6a-c**]$^{+}$ assigned to PALCT transitions in a region of reduced absorptive cross-section for **6a-c** (Figure 4.10a). This feature can confidently be attributed to the redox nature of a charge-transfer state.[28] Similarly, the strong bleach observed between 550-750 nm coincides with the loss of broad, panchromatic absorptive cross-section from **6a-c** upon oxidation; [**6a-c**]$^{+}$ does not absorb at all over this spectral range (Figures 4.9, S88 and S89). In comparison, the bleach of features close to 450 nm was not as pronounced, indicative of a trade-off in spectral intensity in this region upon oxidation, with the growth of a peak in this region for [**6a-c**]$^{+}$ compensating for reduction of an absorption near 450 nm in **6a-c**. Experimental limitations prevented acquisition of data in the region of the low energy absorption at 1000 nm.

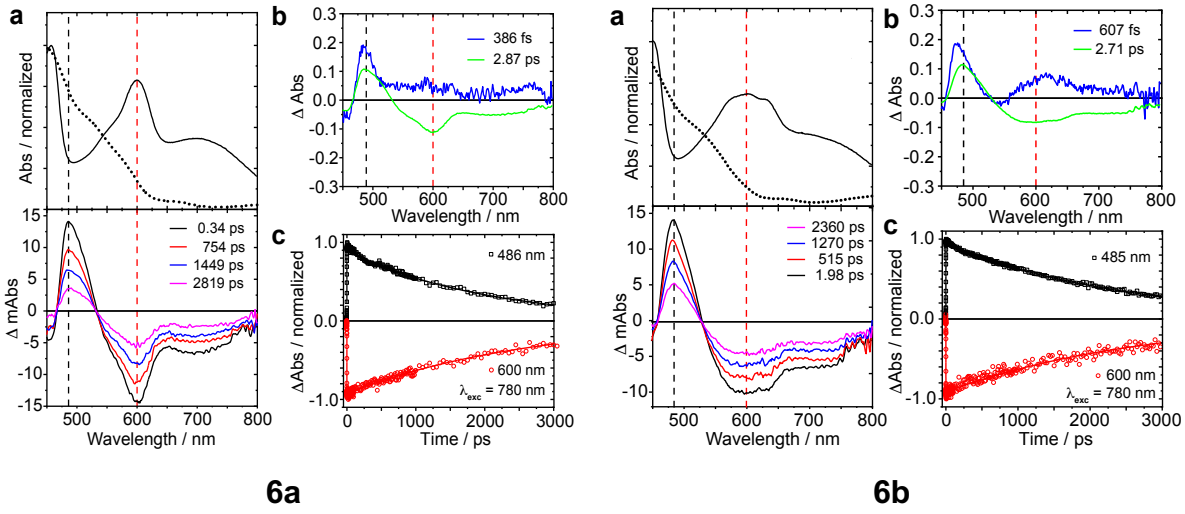

Figure 4.10 (a) Steady-state absorption spectrum of [**6a-b**]$^{0/+}$ (top) and transient absorption spectra (bottom) of **6a-b** in toluene at indicated time delays. (b) Global fit analysis principle components constructed from TA data. The two shown components model the main spectral changes: a red shift of the initial 450 nm absorption and formation of the transient bleaching. (c) Kinetic traces at indicated wavelengths (see legend) and exponential fits

The ESA and GSB fit equally well to single exponent rise and decay functions (Figures 4.10c and S110-113). The rise of the ESA was faster than the instrument response time of 150 fs, consistent with rapid formation of a ^{1}MLCT-like state and subsequent population of a ^{3}MLCT-type one.[46] Intersystem crossing to a ^{3}MLCT state within tens of femtoseconds of population of a ^{1}MLCT state has been established for a range of Fe(II) polypyridyl complexes, including $[Fe(bpy)]_3^{2+}$.[47] Global fit analysis identified two principle components in the TA spectra, which resemble the characteristic spectra at 386 fs and 2.87 ps for **6a** and 607 fs and 2.71 ps for **6b** (Figure 4.10b). An initial ESA is centred at ~470 nm without a GSB, and at 2.87 ps (**6a**) the ESA has started to decay with the GSB fully established at 600 nm by that time. Decay of both the ESA and bleaching indicate a long-lived CT excited state with a surprising lifetime of 2-3 ns for **6a-c** (Table 4.3). This is well beyond the recently reported longest charge-transfer excited-state lifetime accessible for LMCT[26,29] in an Fe(III) complex or the corresponding MLCT for its Fe(II) analog.[27]

Table 4.3 Time constants obtained from kinetic traces in toluene shown in Figures 4.10 and S110-113 at the indicated wavelengths by the fit to single-exponential decay functions

Compound	λ_{obs} (nm)	τ_{decay} (ps)
6a	486	2041 ± 23
	600	2625 ± 35
6b	485	2454 ± 13
	600	2669 ± 41
6c	472	3280 ± 118
	602	2965 ± 110

Changing the solvent has only a small impact on the measured lifetimes, with τ_{decay} reaching 3.3 ns for the ESA feature of **6c** in toluene (Table S21). Solvent polarity does not therefore appear to play a role in how the compounds relax. As can be seen in the calculated electron-hole maps and NTOs (Figures S95-96, 98-99), a consequence of the symmetry of **6a-c** is that PALCT-type charge-transfer does not reorganize electron density in a strictly linear fashion. Accordingly,

large changes in dipole moments are not expected and there is little solvent dependence to the CT lifetimes.[48]

Recent theoretical and experimental work has shown that the excited state landscape of Fe(II) coordination complexes can be complex, as a high density of states and unexpectedly large spin-orbit coupling can enable spin-forbidden channels and render different competitive deactivation pathways.[49,50] In a simplified picture, ^{3}MLCT states of Fe(II) coordination complexes are usually considered to decay via ^{3}MLCT$\rightarrow$^{3}MC$\rightarrow$^{5}MC pathways,[20] though the extent of participation of the typically highly distorted quintet state can depend on the ligand field.[27] Here, DFT revealed the minimum energies of the lowest-lying triplet (^{3}MC) and quintet (^{5}MC) states, both of metal-centred character (Table S20), are destabilized with respect to the ground-state minimum (Figure 4.11). The lowest-lying triplet excited state at the ground state geometry is calculated to have substantial charge-transfer character, with diminished spin density at Fe. The increased energies of the lowest-lying MC excited states suggests that the nanosecond CT lifetimes are attributable to an increase in the activation barrier for the decay of the MLCT-type state (here, ^{3}PALCT) to ^{3}MC and lower-lying ^{5}MC states, respectively.

Experimentally, the strong ESA features observed in the time-resolved spectra of **6a-c** are also inconsistent with long-lived metal-centred triplets or quintets. ^{3}MC states for Fe systems are typically spectroscopically elusive.[27] Similarly, formation of a metal-centred quintet state tends to result in significant attenuation of optical density ($\Delta\varepsilon \sim 10^3$ M^{-1} cm^{-1}) as σ-anti-bonding e_g-type orbitals are populated.[51] For example, in $[Fe(terpy)_2]^{2+}$ and $[Fe(bpy)_3]^{2+}$, excited-state thermalization increases Fe-N distances by ~0.2 Å which in turn decreases metal-ligand overlap, reducing MLCT peak intensity.[45] For $[Fe(terpy)_2]^{2+}$, the rapid formation and decay of a charge-transfer state into a ligand-field state was also established using TA, with assignment of CT

character similarly made by correlating excited state features with electrochemically-generated ones.[45] In that case, the diagnostic marker of a charge-separated species (a reduced terpy$^-$ signal) rapidly decayed within the first picosecond of the evolution of the excited state. For **6a-c**, the ESA at ~480 nm persists for nanoseconds.

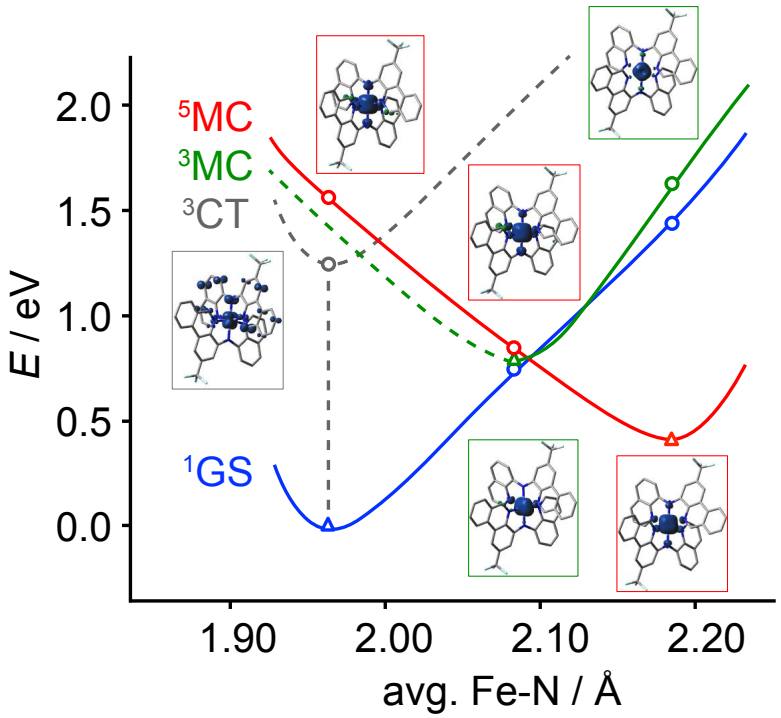

Figure 4.11 Potential energies and average Fe-N equilibrium bond lengths for relevant electronic states of **6b** (triangles) and potential surfaces (lines) drawn through the energy of each state at the geometry of the two other states (circles). Spin density maps (isosurface = 0.004; see Supplementary Table 14) are overlaid next to the relevant data points

The quintet state predicted by DFT presents long average Fe-N distances compared with the ground state. As a result of this strong distortion, such states do not appear to play a significant role in the decay cascade, despite lying at relatively low energy.[50] In comparison, the contraction of Fe-N_{amido} distances in **6a-c** upon oxidation should also be replicated in charge-transfer excited states, maintaining close contacts with the chelating ligands and explaining the intensity of CT

peaks observed by TA. This also portends greater photostability, as contrary to ligand-field and MLCT excited states (with depopulation of MOs with non-bonding character), metal-ligand interactions largely strengthen upon excitation as orbitals with anti-bonding character are depopulated. In addition, π-extended phenanthridine based ligands have been shown to increase the rigidity of photoexcited Cu(I) complexes, leading to blue-shifted emission compared with smaller quinoline congeners.[52] The exceptionally long, nanosecond excited-state CT lifetimes observed for **6a-c** may also benefit from reduced conformational freedom, inhibiting dynamic processes leading to intersystem crossing that would otherwise lead to faster relaxation.[28] Consistent with long-lived excited states, absorption spectra of solutions of **6c** in wet toluene remained unchanged in the dark, however, exposure to visible light ultimately led to decomposition (Figure S168).

4.4 Conclusion

In summary, it is shown that panchromatic absorption and nanosecond lifetimes of MLCT-type charge-transfer excited states are accessible for coordination complexes of Fe composed of ligands combining HOMO inversion design principles[30] with benzannulated *N*-heterocycle acceptor units (Figure 4.1). Notably, complete inversion of HOMO character from solely metal-based to fully ligand-centred is not critical, but 'HOMO raising' in combination with judicious acceptor ligand choice can yield low-energy CT states with exceptionally long lifetimes. Moreover, an absorption profile with high absorptive cross section covering the spectrum from the UV to the edge of the visible (~850 nm) means a greater proportion of the solar spectrum may be harvested with sustainable sensitizers constructed using this ligand design, and the MLCT-type nature of the excited state is well-suited for electron injection into n-type semiconductors,

compared with recently reported sustainable sensitizers with long-lived LMCT excited states.[13,14,26,29] These findings demonstrate how Fe complexes can be constructed to compete with sensitizers based on less abundant[53] or benign metals.[15,16]

4.5 Experimental Section

Unless otherwise specified, all air sensitive manipulations were carried out either in a N_2 filled glove box or using standard Schlenk techniques under Ar. 2-Formylphenyl boronic acid (AK Scientific), 4-*tert*-butylaniline (Sigma Aldrich), 2-nitro-4-(trifluoromethyl)aniline (Sigma Aldrich), 4-chloro-2-nitroaniline (Combi Blocks), *N*-iodosuccinimide (AK Scientific), *N*-bromosuccinimide (Alpha Aesar), $Pd(PPh_3)_4$ (Sigma Aldrich), $Pd_2(dba)_3$ (Sigma Aldrich), $Pd(OAc)_2$ (Sigma Aldrich), (1,1'-diphenylphosphino)ferrocene (dppf, Sigma Aldrich), (±)-2,2'-bis(diphenyphosphino)-1,1'-binapthalene (*rac*-BINAP, Sigma Aldrich), Na_2CO_3 (Alfa Aesar), trifluoroacetic acid (Sigma Aldrich), sodium *tert*-pentoxide (NaO*t*Pen, Sigma Aldrich), sodium *tert*-butoxide (NaO^{t}Bu, Sigma Aldrich), hydrazine hydrate (Sigma Aldrich), formic acid (Alfa Aesar), 8-bromoquinoline (Matrix Scientific), 8-aminoquinoline (Alfa Aesar), $Fe(OTf)_2$ (Sigma Aldrich), $FeCl_3 \cdot 6H_2O$ (Fisher Scientific), $NaPF_6$ (Alfa Aesar), and methanol (Sigma Aldrich) were purchased and used without any further purification. Organic solvents were dried and distilled using appropriate drying agents prior to use. 1- and 2D NMR spectra were recorded on Bruker Avance 300 MHz or Bruker Avance – III 500 MHz spectrometers. ^1H and $^{13}C\{^1H\}$ NMR spectra were referenced to residual solvent peaks. Elemental analyses were performed by Microanalytical Service Ltd., Delta, BC (Canada), and at the University of Manitoba using a Perkin Elmer 2400 Series II CHNS/O Elemental Analyzer. A complete description of the Mössbauer experiment can be found in the supporting information (pg. 72). A description of the computational details for the

calculations included in this chapter is provided in the supporting information (pg. 77-78). 2-nitro-4-*tert*-butylaniline[54] and 2-iodo-6-nitro-4-*tert*-butylaniline[55] were synthesized from 4-*tert*-butylaniline according to literature procedures. 2-iodo-6-bromo-4-trifluoromethylaniline was synthesized according to a patent.[56]

4.5.1 Synthesis

Synthesis of **2-iodo-4-chloro-6-nitroaniline**: N-iodosuccinimide (6.26 g, 27.8 mmol) and 2-nitro-4-chloroaniline (3.00 g, 17.4 mmol) were mixed in a 250 mL round bottom flask and dissolved in 50 mL glacial acetic acid. This mixture was stirred at 60 °C for 24 h. The mixture was poured into a 0 °C water bath. A solid precipitated out and the mixture was filtered over celite. The solid was brought through the filter with dichloromethane and washed with water (3 x 100 mL). The organic layer was separated and pumped to dryness. Isolated yield = 3.97 g (76 %) ^{1}H NMR ($CDCl_3$, 300 MHz, 25 °C): δ 8.18 (d, 1H, J_{HH}=2.4 Hz, C_{Ar}), 7.90 (d, 1H, 2.4 Hz, C_{Ar}), 6.66 ppm (s, 2H, NH_2).

Synthesis of **4-nitro-2-tert-butylphenanthridine** (**4a**): A 500 mL Teflon-stoppered flask was charged with $Pd(PPh_3)_4$ (1.03 g, 0.89 mmol), and 50 mL of DME. After stirring briefly to mix, 2-iodo-6-nitro-4-*tert*-butylaniline (5.73 g, 17.91 mmol), 2-formylphenylboronic acid (2.96 g, 19.70 mmol) and an additional 70 mL of DME were added, followed by Na_2CO_3 (5.69 g, 53.73 mmol) dissolved in 100 mL of degassed water. The flask was then sealed and the mixture stirred vigorously for 6 h in an oil bath (130 °C). The flask was then allowed to cool, charged with 130 mL of 2M HCl, and refluxed for additional 2 h. The reaction mixture was cooled, neutralized with NaOH, and pumped to dryness. The residue was then taken up in dichloromethane (100 mL) and washed with brine (3 x 100 mL). The organic layer was separated, dried over Na_2SO_4 and volatiles

removed. Column chromatography on silica gave a pale yellow solid (R_f = 0.42; 20% EtOAc/hexane). Isolated yield = 5.54 g (96 %). ^{1}H NMR ($CDCl_3$, 300 MHz, 25 ºC): δ 9.50 (s, 1H, $C_{Ar}H$), 8.78 (d, 1H, J_{HH} = 2.1 Hz, $C_{Ar}H$), 8.70 (d, 1H, J_{HH} = 8.3 Hz, $C_{Ar}H$), 8.23-8.13 (overlapped m, 2H, $C_{Ar}H$), 8.03 (m, 1H, J_{HH} =8.4, 7.1 Hz, $C_{Ar}H$), 7.86 (m, 1H, J_{HH} = 8.1, 7.1 Hz; $C_{Ar}H$), 1.53 ppm (s, 9H, ^{t}Bu). $^{13}C\{^1H\}$ NMR ($CDCl_3$, 75 MHz, 25 °C): δ 155.0 (C_{Ar}), 149.8 (C_{Ar}), 149.2 (C_{Ar}), 134.0 (C_{Ar}), 131.8 (C_{Ar}), 131.3 (C_{Ar}), 129.1 (C_{Ar}), 128.6 (C_{Ar}), 126.4 (C_{Ar}), 124.9 (C_{Ar}), 121.9 (C_{Ar}), 121.4 (C_{Ar}), 120.5 (C_{Ar}), 35.6 (CC_{Me}), 31.3 ppm (CH_3).

Synthesis of **4-bromo-2-trifluoromethylphenanthridine** (**4b**): A 500 mL Teflon-stoppered flask was charged with $Pd(PPh_3)_4$ (1.92 g, 1.67 mmol), and 50 mL of DME. After stirring briefly to mix, 2-bromo-6-iodo-4-(trifluoromethyl)aniline (15.24 g, 41.67 mmol), 2-formylphenylboronic acid (6.87 g, 45.83 mmol) and an additional 70 mL of DME were added, followed by Na_2CO_3 (13.25 g, 125.0 mmol) dissolved in 100 mL of degassed water. The flask was then sealed and the mixture stirred vigorously for 6 h in an oil bath (130 °C). The flask was then allowed to cool, charged with 130 mL of 2M HCl, and refluxed for additional 2 h. The reaction mixture was cooled, neutralized with NaOH, and pumped to dryness. The residue was then taken up in dichloromethane (100 mL) and washed with brine (3 x 100 mL). The organic layer was separated, dried over Na_2SO_4 and volatiles removed. Column chromatography on silica gave a pale yellow solid (R_f = 0.50; 20% EtOAc/hexane). Isolated yield = 14.93 g (98 %). ^{1}H NMR ($CDCl_3$, 300 MHz, 25 ºC): δ 9.35 (s, 1H, $C_{Ar}H$), 8.68 (s, 1H, $C_{Ar}H$), 8.49 (d, 1H, J_{HH} = 8.3 Hz, $C_{Ar}H$), 8.18 (d, 1H, J_{HH} = 1.7, $C_{Ar}H$), 8.05 (d, 1H, J_{HH} = 8.0 Hz; $C_{Ar}H$), 7.94-7.85 (m, 1H, $C_{Ar}H$), 7.76 ppm (app t, 1H, J_{HH} = 7.9 Hz, $C_{Ar}H$). $^{13}C\{^1H\}$ NMR ($CDCl_3$, 75 MHz, 25 °C): δ 156.3 (C_{Ar}), 143.1 (C_{Ar}), 132.3 (C_{Ar}), 131.9

(C_{Ar}), 129.2 (q, C_{Ar}), 128.5 (C_{Ar}), 126.7 (C_{Ar}), 126.5 (C_{Ar}), 125.3 (C_{Ar}), 125.2 (C_{Ar}), 122.1 (C_{Ar}), 121.7 (C_{Ar}), 117.6 ppm (q, C_{Ar}). $^{19}F\{^{1}H\}$ NMR ($CDCl_3$, 470 MHz, 25 °C): δ -62.0 ppm.

Synthesis of **4-nitro-2-chlorophenanthridine** (**4c**): Sodium carbonate (1.60 g, 15.09 mmol), 2-formylphenylboronic acid (0.829 g, 5.53 mmol), and 2-nitro-4-chloro-6-iodoaniline (1.5 g, 5.03 mmol) were added to a 250 mL Teflon-stoppered flask which was evacuated and filled with nitrogen gas. DME and water were degassed in sealed round bottom flasks. The Teflon-stoppered flask was charged with 0.29 g $Pd(PPh_3)_4$ catalyst. 30 mL DME and 25 mL H_2O were added to the flask and the mixture was stirred for 24 h at 130°C. The solution was cooled and filtered over celite. The solvents were pumped off and the solid re-dissolved in dichloromethane. It was then washed with water (3x100 mL). The dichloromethane was pumped off and the resulting solid was re-dissolved in toluene. 4.76 g $MgCl_2$ was added and the new mixture was stirred overnight. This was filtered over celite and washed with cold pentane (3x75 mL). Solvent was pumped off. Isolated yield = 0.747 g (57.4%). ^{1}H NMR ($CDCl_3$, 300 MHz, 25°C): δ 9.35 (s, 1H, $C_{Ar}H$), 8.68 (d, 1H, J_{HH}=2.2 Hz, $C_{Ar}H$), 8.53 (d, 1H, J_{HH}=8.2 Hz, $C_{Ar}H$), 8.13 (d, 1H, J_{HH}=8.0 Hz, $C_{Ar}H$), 7.98 (m, 1H, $C_{Ar}H$), 7.93 (d, 1H, J_{HH}=2.2 Hz, $C_{Ar}H$), 7.86 ppm (m, 1H, $C_{Ar}H$). $^{13}C\{^{1}H\}$ NMR ($CDCl_3$, 75 MHz, 25°C): δ 155.94 (C_{Ar}), 149.56 (C_{Ar}), 134.38 (C_{Ar}), 132.45 (C_{Ar}), 132.15 (C_{Ar}) 131.94 (C_{Ar}), 130.36 (C_{Ar}), 129.59 (C_{Ar}), 129.37 (C_{Ar}), 126.66 (C_{Ar}), 125.23 (C_{Ar}), 122.74 (C_{Ar}), 122.12 ppm (C_{Ar}).

Synthesis of **4-amino-2-*tert*-butylphenanthridine (4d)**: To a stirred solution of 4-nitro-2-*tert*-butylphenanthridine (4.5 g, 16.1 mmol) in methanol (100 mL), Zn dust (2.1 g, 32.2 mmol), and hydrazinium monoformate solution (54 mL; prepared by slowly neutralizing equal molar amounts of hydrazine hydrate (50 mL) with 85% formic acid (4 mL) in an ice-water bath) were added, and

stirred vigorously at 60 °C. The resulting green suspension was cooled and filtered using celite. The filtrate was pumped dry, the residue dissolved in dichloromethane (100 mL), and washed with brine (3 x 60 mL). The organic layer was separated, dried over Na_2SO_4 and dried to leave a green-brown solid, which was purified using column chromatography (silica, R_f = 0.29; 20% EtOAc/hexane). Isolated yield = 3.74 g (86 %). ^{1}H NMR ($CDCl_3$, 300 MHz, 25 °C): δ 9.10 (s, 1H, $C_{Ar}H$), 8.61 (dd, 1H, J_{HH} = 8.5, 1.1 Hz; $C_{Ar}H$), 8.00 (dd, 1H, J_{HH} = 7.9, 1.5 Hz; $C_{Ar}H$), 7.93 (d, 1H, J_{HH} = 1.9, $C_{Ar}H$), 7.81 (app td, 1H, J_{HH} = 8.4, 7.0, 1.4 Hz; $C_{Ar}H$), 7.65 (app dt, 1H, J_{HH} = 8.0, 7.0, 1.1 Hz; $C_{Ar}H$), 7.14 (d, 1H, J_{HH} = 1.9 Hz; $C_{Ar}H$), 5.01 (s, 2H, NH_2), 1.48 ppm (s, 9H, ^{t}Bu). $^{13}C\{^1H\}$ NMR ($CDCl_3$, 75 MHz, 25 °C): δ 150.9 (C_{Ar}), 149.8 (C_{Ar}), 144.3 (C_{Ar}), 133.1 (C_{Ar}), 132.1 (C_{Ar}), 130.5 (C_{Ar}), 128.7 (C_{Ar}), 127.1 (C_{Ar}), 126.9 (C_{Ar}), 124.2 (C_{Ar}), 122.4 (C_{Ar}), 110.1 (C_{Ar}), 107.1 (C_{Ar}), 35.3 (CC_{Me}), 31.6 ppm (CH_3).

Synthesis of **4-amino-2-chlorophenanthridine** (**4e**): Zinc metal (0.379 g, 5.80 mmol), and 4-nitro-2-chlorophenanthridine (0.747 g, 2.90 mmol), were added to a 250 mL Teflon-stoppered flask and dissolved in methanol (100 mL). A 7.44 mL hydrazinium monoformate solution (prepared by slowly neutralizing 6.86 mL hydrazine monohydrate with 0.58 mL formic acid at 0 °C) was added and the mixture was stirred for 24 h at 60 °C. The suspension was cooled and filtered over celite. The solvent and volatiles were pumped off and the remaining solid was re-dissolved in dichloromethane. This solution was washed with water (3x100 mL) and the organic layer was separated. Dichloromethane was pumped off leaving a beige solid. Isolated yield = 0.58 g (87 %). ^{1}H NMR ($CDCl_3$, 300 MHz, 25 °C): δ 9.07 (s, 1H, $C_{Ar}H$), 8.42 (d, 1H, J_{HH}=8.4 Hz, $C_{Ar}H$), 8.00 (d, 1H, J_{HH}=7.8 Hz, $C_{Ar}H$), 7.81 (m, 1H, $C_{Ar}H$), 7.78 (d, 1H, J_{HH}=2.0 Hz, $C_{Ar}H$), 7.69 (m, 1H, $C_{Ar}H$), 6.94 (d, 1H, J_{HH}= 2.1 Hz, $C_{Ar}H$), 5.13 ppm (s, 2H, NH_2). $^{13}C\{^1H\}$ NMR ($CDCl_3$,

75 MHz, 25 °C): δ 150.14 (C_{Ar}), 145.87 (C_{Ar}), 133.68 (C_{Ar}), 131.84 (C_{Ar}), 131.76 (C_{Ar}), 130.83 (C_{Ar}), 128.60 (C_{Ar}), 127.78 (C_{Ar}), 126.90 (C_{Ar}), 125.53 (C_{Ar}), 122.36 (C_{Ar}), 111.08 (C_{Ar}), 110.09 ppm (C_{Ar}).

Synthesis of $^{t\text{Bu-Phen}}$**NN(H)N**$^{\text{Quin}}$ (**5a**): A 500 mL Teflon-stoppered flask was charged with $Pd_2(dba)_3$ (0.26 g, 0.30 mmol), BINAP (0.42 g, 0.70 mmol) and toluene (30 mL). After stirring for 5 min, 8-bromoquinoline (2.0 g, 10.1 mmol), 4-amino-2-*tert*-butylphenanthridine (2.5 g, 10.1 mmol), and an additional 20 mL of toluene were added, followed by sodium *tert*-butoxide (NaO^{t}Bu; 1.4 g, 15.1 mmol). The reaction mixture was stirred and subject to reflux in an oil bath at 150 °C for 72 h. After cooling the flask, the volatiles were removed and the residue was taken up in dichloromethane. The suspension was then filtered over a silica plug and the solvent was removed to leave a brown solid. Isolated yield = 3.8 g (> 99 %). ^{1}H NMR ($CDCl_3$, 300 MHz, 25 °C): δ 10.53 (s, 1H, N_2-H), 9.29 (s, 1H, C_1-H), 8.98 (dd, 1H, J_{HH} = 4.2, 1.7 Hz, C_{18}-H), 8.68 (d, 1H, J_{HH} = 8.4 Hz, C_3-H), 8.21- 8.04 (m, 4H, C_6-H, C_{13}-H, C_{20}-H, C_{26}-H), 7.90 – 7.84 (m, 2H, C_{11}-H, C_{25}-H), 7.71 (ddd, 1H, J_{HH} = 8.0, 7.0 1.1 Hz, C_4-H), 7.55 (t, 1H, C_5-H), 7.47 (dd, 1H, J_{HH} = 8.2, 4.2 Hz, C_{19}-H), 7.32 (dd, 1H, J_{HH} = 8.2, 1.2 Hz, C_{24}-H), 1.55 ppm (s, 9H, ^{t}Bu). ^{1}H NMR (C_6D_6, 500 MHz, 25 °C): δ 11.58 (s, 1H, N_2-H), 9.10 (s, 1H, C_1-H), 8.73 (dd, 1H, J_{HH} = 4.3, 1.6 Hz, C_{18}-H), 8.40 (d, 1H, J_{HH} = 8.3 Hz, C_3-H), 8.32 (s, 1H, C_{13}-H), 8.12-8.05 (m, 2H, C_{11}-H, C_{26}-H), 7.59 (dd, 1H, J_{HH} = 8.2, 1.6 Hz, C_{20}-H), 7.44 (d, 1H, J_{HH} = 7.9 Hz, C_6-H), 7.39 (m, 2H, C_4-H, C_{25}-H), 7.20 (t, 1H, J_{HH} = 7.4 Hz, C_5-H), 7.06 (d, 1H, J_{HH} = 8.2 Hz, C_{24}-H), 6.83 (dd, 1H, J_{HH} = 8.2, 4.1 Hz, C_{19}-H), 1.46 ppm (s, 9H, ^{t}Bu). ^{13}C{^{1}H} NMR ($CDCl_3$, 75 MHz, 25 °C): δ 150.6 (C_1), 150.5 (C_{12}), 148.1 (C_{18}), 140.2 ($C_{21, 22 \text{ or } 23}$), 139.5 ($C_{10 \text{ or } 23}$), 139.2 ($C_{10 \text{ or } 23}$), 134.0 ($C_{20}$), 133.1 ($C_{7 \text{ or } 8}$), 130.7 ($C_{8 \text{ or } 9}$), 129.2 ($C_4$), 129.1 ($C_{21, 22 \text{ or } 23}$), 128.9 ($C_6$), 128.3 ($C_{25}$), 127.3 ($C_{2 \text{ or } 7}$), 127.3 ($C_5$),

124.3 ($C_{2\text{ or }7}$), 122.3 (C_3), 121.7 (C_{19}), 117.5 (C_{24}), 110.6 (C_{13}), 109.2 (C_{11}), 108.9 (C_{26}), 35.7 (C_{14}), 31.7 ppm ($C_{15,16,17}$). $^{13}C\{^1H\}$ NMR (C_6D_6, 125 MHz, 25 °C): δ 150.5 (C_1), 150.5 (C_{12}), 148.0 (C_{18}), 140.8 ($C_{21,\ 22\text{ or }23}$),), 140.2 ($C_{10\text{ or }23}$),140.0 ($C_{10\text{ or }23}$), 135.9 (C_{20}), 134.6 ($C_{7\text{ or }8}$), 133.3 ($C_{8\text{ or }9}$), 130.5 (C_4), 129.5 ($C_{21,\ 22\text{ or }23}$), 129.0 (C_6), 127.5 (C_{25}), 127.3 ($C_{2\text{ or }7}$), 127.1 (C_5), 124.7 ($C_{2\text{ or }7}$), 122.4 (C_3), 121.8 (C_{19}), 117.6 (C_{24}), 110.3 (C_{13}), 109.3 (C_{11}), 108.9 (C_{26}), 35.6 (C_{14}), 31.7 ppm ($C_{15,16,17}$). UV-Vis (CH_3CN): λ (ε) 306 (9 680), 388 nm (12 270 M^{-1} cm^{-1}).

Synthesis of $^{\text{CF3-Phen}}$**NN(H)N**$^{\text{Quin}}$ (**5b**): A 500 mL Teflon-stoppered flask was charged with $Pd(OAc)_2$ (0.04 g, 0.18 mmol), dppf (0.057 g, 0.20 mmol) and toluene (30 mL). After stirring for 5 minutes, 4-bromo-2-trifluoromethylphenanthridine (1.0 g, 3.06 mmol), 8-aminoquinoline (0.42 g, 2.92 mmol), and an additional 20 mL of toluene were added, followed by sodium *tert*-pentoxide (NaO^tPent; 0.48 g, 4.38 mmol). The reaction mixture was stirred and subjected to reflux in an oil bath set at 150 °C for 72 h. After cooling the flask, the volatiles were removed and the residue was taken up in dichloromethane. The suspension was then filtered over a silica plug and the solvent was removed to leave a brown solid. Isolated yield = 0.742 g (66 %). ^1H NMR ($CDCl_3$, 500 MHz, 25 °C): δ 10.80 (s, 1H, N-H), 9.38 (s, 1H, C1-H), 8.98 (dd, 1H, J_{HH} = 4.2, 1.7 Hz, C_{15}-H), 8.58 (d, 1H, J_{HH} = 7.5 Hz, C_3-H), 8.27 (s, 1H, C_{13}-H), 8.16 (dd, 1H, J_{HH} = 8.3, 1.7 Hz, C_{17}-H), 8.10 (m, 2H, C_{11}-H, C_{23}-H), 7.89 (m, 2H, C_4-H, C_6-H), 7.75 (td, 1H, J_{HH} =7.5, 6.9, 1.0 Hz C_{22}-H), 7.57 (t, 1H, J_{HH} = 8.0 Hz, C_5-H), 7.48 (dd, 1H, J_{HH} = 8.2, 4.2 Hz, C_{16}-H), 7.39 ppm (dd, 1H, J_{HH} = 8.2, 1.1 Hz, C_{21}-H). $^{13}C\{^1H\}$ NMR ($CDCl_3$, 125 MHz, 25 °C): 152.9 (C_1), 148.4 (C_{15}), 140.6 (C_{10}), 140.3 (C_{20}), 138.2 ($C_{2\text{ or }7}$), 136.3 (C_{17}), 136.3 (C_{14}), 132.8 ($C_{2\text{ or }7}$), 131.6 (C_4), 129.1 ($C_{18\text{ or }19}$), 129.1 (C_{23}), 128.3 (C_{22}), 127.2 (C_5), 127.0 ($C_{18\text{ or }19}$), 125.8 ($C_{8\text{ or }9}$), 124.4 (C_{12}), 123.7 ($C_{8\text{ or }9}$), 122.5 (C_3),

121.9 (C_{16}), 119.0 (C_{21}), 110.8 (C_6), 109.6 (q, C_{13}), 105.9 ppm (q, C_{11}). $^{19}F\{^1H\}$ NMR ($CDCl_3$, 470 MHz, 25 °C): δ -62.2 ppm. UV-Vis (CH_3CN): λ (ε) 305 (7 070), 379 nm (12 090 M^{-1} cm^{-1}).

Synthesis of **$^{CF3\text{-}Phen}$NN(H)N^{Quin}** (**5c**): A 500 mL Teflon-stoppered flask was charged with $Pd_2(dba)_3$ (0.12 g, 0.13 mmol), dppf (0.17 g, 0.31 mmol) and toluene (30 mL). After stirring for 5 min, 8-bromoquinoline (0.91 g, 4.37 mmol), 4-amino-2-chlorophenanthridine (1.0 g, 4.37 mmol), and an additional 20 mL of toluene were added, followed by sodium *tert*-butoxide (NaO^{t}Bu; 0.63 g, 6.56 mmol). The reaction mixture was stirred and subject to reflux in an oil bath at 150 °C for 72 h. After cooling the flask, the volatiles were removed and the residue was taken up in dichloromethane. The suspension was then filtered over a silica plug and the solvent was removed to leave a brown solid. Isolated yield = 1.40 g (90 %). ^1H NMR ($CDCl_3$, 300 MHz, 25 °C): δ 10.75 (s, 1H, N_2-H), 9.27 (s, 1H, C_1-H), 8.97 (dd, 1H, J_{HH} = 4.2, 1.7 Hz, C_{14}-H), 8.46 (d, 1H, J_{HH} = 8.3 Hz, C_3-H), 8.15 (dd, 1H, J_{HH} = 8.2, 1.7 Hz, C_{16}-H), 8.05 (dd, 1H, J_{HH} = 8.2, 1.7 Hz, C_6-H), 7.95 (d, 1H, J_{HH} = 2.1 Hz, C_{13}-H), 7.90-7.87 (m, 2H, C_{11}-H, C_{22}-H), 7.82 (ddd, 1H, J_{HH} = 8.2, 4.2, 1.3 Hz, C_4-H), 7.70 (ddd, 1H, J_{HH} = 8.0, 7.0, 1.1 Hz, C_5-H), 7.55 (t, 1H, J_{HH} = 7.9 Hz, C_{21}-H), 7.47 (dd, 1H, J_{HH} = 8.2, 4.2 Hz, C_{15}-H), 7.37 ppm (dd, 1H, J_{HH} = 8.2, 1.1 Hz, C_{20}-H). $^{13}C\{^1H\}$ NMR ($CDCl_3$, 75 MHz, 25 °C): δ 150.9 (C_1), 148.4 (C_{14}), 140.8 ($C_{10 \text{ or } 19}$), 140.2 ($C_{10 \text{ or } 19}$), 138.2 ($C_{17 \text{ or } 18}$), 136.3 (C_{16}), 133.9 ($C_{17 \text{ or } 18}$), 133.6 (C_2) 132.0 (C_9), 131.1 (C_4), 129.1 (C_7), 128.9 (C_6), 128.0 (C_5), 127.2 (C_{21}), 127.1 (C_{12}), 125.7 (C_8), 122.5 (C_3), 121.8 (C_{15}), 118.8 (C_{20}), 111.8 (C_{13}), 110.9 ($C_{11 \text{ or } 22}$), 110.7 ppm ($C_{11 \text{ or } 22}$).

Synthesis **of Fe(**$^{t\text{Bu-Phen}}$**NNN**^{Quin}**)$_2$** (**6a**): $Fe(OTf)_2$ (0.02 g. 0.06 mmol), **5a** (0.047 g, 0.12 mmol), NaO^{t}Bu (0.01 g, 0.13 mmol) were combined in a 20 mL scintillation vial and dissolved in THF

(10 mL). The purple solution was stirred under inert conditions for 72 h over which time the solution turned a deep green. The solvent was removed and the product was washed with pentane (3 x 10 mL), and extracted with toluene. Isolated yield = 0.039 g (78 %). ^{1}H NMR (C_6D_6, 300 MHz, 25 °C): δ 8.86 (s, 2H, C_{13}-H), 8.63, (d, 2H, J_{HH} = 8.0 Hz, C_{26}-H), 8.54 (s, 2H, C_1-H), 8.06 (m, 4H, C_3-H, C_{18}-H), 7.73 (s, 2H, C_{11}-H), 7.62 (t, 2H, J_{HH} = 8.0 Hz, C_{25}-H), 6.95 (m, 4H, C_4-H, C_{20}-H), 6.72 (d, 2H, J_{HH} = 8.0 Hz, C_{24}-H), 6.63 (t, 2H, J_{HH} = 7.5 Hz, C_5-H), 6.43 (d, 2H, J_{HH} = 8.1 Hz, C_6-H), 5.85 (dd, 2H, J_{HH} = 8.2, 4.9 Hz, C_{19}-H), 1.68 ppm (s, 18 H, ^{t}Bu). ^{13}C{^{1}H} NMR (C_6D_6, 125 MHz, 25 °C): 153.1 (C_{23}), 152.6 (C_1), 151.1 (C_{12}), 149.9 (C_{18}), 145.0 (C_{10}), 132.3 (C_4), 131.8 (C_9), 131.3 ($C_{21\text{ or }22}$), 128.9 (C_{20}), 128.7 (C_{25}), 126.9 (C_5), 126.8 (C_6), 125.5 ($C_{2,\ 7,\text{ or }8}$), 122.1 (C_3), 121.7 (C_{19}), 112.8 (C_{26}), 112.6 (C_{24}), 112.1 (C_{13}), 105.8 (C_{11}), 35.8 (C_{14}), 32.2 ppm ($C_{15,16,17}$); note: 3 peaks are not observed due to solvent overlap ($C_{2,\ 7,\ 8,\ 21,\text{ or }22}$). UV-Vis ($CH_3CN$): λ (ε) 262 (64 890), 319 (sh), 454 (26 030), 596 nm (17 990), 724 (8 510 M^{-1} cm^{-1}). Anal. Calcd for $FeC_{52}H_{44}N_6$: C, 77.48; H, 5.96. Found: C, 77.28; H, 6.11.

Synthesis of **Fe(**$^{\mathbf{CF3\text{-}Phen}}$**NNN**$^{\mathbf{Quin}}$**)$_2$** (**6b**): $Fe(OTf)_2$ (0.013 g. 0.04 mmol), **5b** (0.03 g, 0.077 mmol), NaO^{t}Bu (0.007 g, 0.08 mmol) were combined in a 20 mL scintillation vial and dissolved in THF (10 mL). The purple solution was stirred under inert conditions for 72 h over which time the solution turned a deep green. The solvent was removed and the product was washed with pentane (3 x 10 mL), and extracted with THF. Isolated yield = 0.021 g (67 %). ^{1}H NMR (C_6D_6, 500 MHz, 25 °C): δ 8.96 (s, 2H, C_{13}-H), 8.52 (d, 2H, J_{HH} = 8.0 Hz, C_{23}-H), 8.44 (s, 2H, C_1-H), 7.97 (dd, 2H, J_{HH} = 5.0, 1.4 Hz, C_{15}-H), 7.81 (s, 2H, C_{11}-H), 7.54 (d, 2H, J_{HH} = 8.3 Hz, C_3-H), 7.41 (t, 2H, J_{HH} = 8.0 Hz, C_{22}-H), 6.92 (m, 2H, C_{17}-H), 6.82 (t, 2H, J_{HH} = 7.4 Hz C_4-H), 6.76 (d, 2H, J_{HH} = 8.0 Hz, C_{21}-H), 6.57 (t, 2H, J_{HH} = 7.5 Hz C_5-H), 6.40 (d, 2H, J_{HH} = 8.1 Hz, C_6-H), 5.90 ppm (dd, 2H, J_{HH}

= 8.2, 5.0 Hz, C_{16}-H). ^{13}C {^{1}H} NMR (C_6D_6, 125 MHz): 154.4 (C_1), 153.7 (C_{14}), 152.3 (C_{20}), 151.9 (C_{19}), 150.4 (C_{15}), 147.3 (C_{10}), 133.1 (C_{17}), 131.2 (C_7), 131.0 (C_{18}), 129.8 (C_4), 128.9 (C_{22}), 126.7 (C_6), 126.4 ($C_{2, 8, 9, \text{or } 12}$), 125.7 ($C_{2, 8, 9, \text{or } 12}$), 122.4 ($C_3$), 121.8 ($C_{16}$), 114.7 ($C_{21}$), 114.0 ($C_{23}$), 108.7 ($C_{13}$), 105.6 ppm ($C_{11}$); note: 3 peaks are missing due to solvent overlap ($C_{2, 5, 8, 9, \text{or } 12}$). ^{19}F {^{1}H} NMR ($CDCl_3$, 470 MHz, 25 °C): δ -61.3 ppm. UV-Vis (CH_3CN): λ (ε) 259 (74 180), 319 (sh), 448 (29 300), 596 nm (17 800), 728 (9 370 M^{-1} cm^{-1}). Anal. Calcd for $FeC_{46}H_{26}N_6F_6$: C, 66.36; H, 3.15. Found: C, 66.25; H, 3.32.

Synthesis **of Fe($^{\text{Cl-Phen}}$NNN$^{\text{Quin}}$)$_2$** (**6c**): $Fe(OTf)_2$ (0.025 g. 0.07 mmol), **5c** (0.05 g, 0.14 mmol), NaO^tBu (0.014 g, 0.14 mmol), and THF (10 mL) were added to a vial. The purple solution was stirred under inert conditions for 48 h over which time the solution turned a deep green. The solvent was removed and the product was washed with pentane (3 x 10 mL), and extracted with toluene. Isolated yield = 0.045 g (84 %). ^{1}H NMR (C_6D_6, 300 MHz, 25 °C): δ 8.66 (s, 2H, J_{HH} = 2.0 Hz, C_{13}-H), 8.37, (s, 2H, C_1-H), 8.32 (d, 2H, J_{HH} = 8.0 Hz, C_{22}-H), 7.97 (dd, 2H, J_{HH} = 4.9, 1.4 Hz, C_{14}-H), 7.55 (s, 2H, C_{11}-H), 7.51 (t, 2H, J_{HH} = 8.2 Hz, C_6-H), 7.41 (t, 2H, J_{HH} = 8.0 Hz, C_{21}-H), 6.93 (dd, 2H, J_{HH} = 8.2, 1.4 Hz, C_{16}-H), 6.81 (ddd, 2H, J_{HH} = 8.3, 6.9, 1.3 Hz, C_5-H), 6.75 (d, 2H, J_{HH} = 8.0 Hz, C_{20}-H), 6.57 (t, 2H, J_{HH} = 7.5 Hz, C_4-H), 6.43 (d, 2H, J_{HH} = 8.1 Hz, C_3-H), 5.94 (dd, 2H, J_{HH} = 8.2, 5.0 Hz, C_{15}-H). $^{13}C\{^{1}H\}$ NMR (C_6D_6, 125 MHz, 25 °C): 153.8 (C_{10}), 152.8 (C_1), 152.4 (C_{12}), 151.9 (C_{19}), 150.3 (C_{10}), 145.0 (C_9), 136.1 (C_8), 132.8 (C_{16}), 130.9 (C_{18}), 130.5 (C_7), 129.4 (C_5), 128.7 (C_2), 128.6 (C_{21}), 127.6 (C_4), 126.8 (C_{17}), 126.6 (C_3), 122.4 (C_6), 121.8 (C_{15}), 114.4 (C_{20}), 113.9 (C_{22}), 113.87 (C_{13}), 108.3 ppm (C_{11}). UV-Vis (CH_3CN): λ (ε) 318 (17 192), 445 (23 833), 592 (15 337), 703 nm (8 205 M^{-1} cm^{-1}). Two molecules found in the asymmetric

unit with one molecule of pentane and benzene. Anal. Calcd for $Fe_2C_{99}H_{70}N_{12}Cl_4$: C, 70.73; H, 4.20. Found: C, 70.33; H, 4.42.

Synthesis of **[Fe($^{t\text{Bu-Phen}}$NNN$^{\text{Quin}}$)$_2$]PF$_6$** (**[6a]PF$_6$**): A 250 mL round-bottom flask was charged with $FeCl_3 \cdot 6H_2O$ (52 mg, 0.19 mmol), **5a** (150 mg, 0.40 mmol), $NaPF_6$ (33 mg, 0.19 mmol), and NaO^{t}Bu (38 mg, 0.40 mmol). MeOH (50 mL) was added and the flask was stirred and refluxed at 100 °C overnight. The flask was then cooled to room temperature and stirred for 1 h where a brown precipitate formed. The mixture was then filtered over celite and extracted with dichloromethane. The filtrate was concentrated and placed in the freezer overnight. The resulting precipitate was subject to the same treatment. Isolated yield = 0.135 g (73 %). ^{1}H NMR ($CDCl_3$, 300 MHz, 25 °C): δ 30.5 (br), 20.1 (br), 11.2 (s), 10.4 (s), 3.00 (s), -10.0 (br), -30.6 (br), -32.3 (br), -49.3 (br), -54.8 (br), -66.8 (v br), -68.8 ppm (v br). UV-Vis/NIR (CH_3CN): λ (ε) 311 (sh), 414, (22 810), 512, (12 430), 1024 nm (4 560 M^{-1} cm^{-1}). μ_{eff} (Evans method) = 1.66 μ_B. Anal. Calcd for $FeC_{52}H_{44}N_6PF_6$: C, 65.48; H, 4.65. Found: C, 65.70; H, 4.79.

Synthesis of **[Fe($^{\text{CF3-Phen}}$NNN$^{\text{Quin}}$)$_2$]PF$_6$** (**[6b]PF$_6$**): A 250 mL round-bottom flask was charged with $FeCl_3 \cdot 6H_2O$ (0.07 mg, 0.26 mmol), **5b** (0.200 g, 0.52 mmol), $NaPF_6$ (0.043 g, 0.26 mmol), and NaO^{t}Bu (0.050 g, 0.52 mmol). MeOH (50 mL) was added and the flask was stirred and refluxed at 100 °C overnight. The flask was then cooled to room temperature and the solvent removed. The brown solid was dissolved in minimal CH_2Cl_2 and added slowly to 100 mL of pentane to precipitate the compound. The mixture was then filtered and the solid collected. Isolated yield = 0.180 g (72 %). ^{1}H NMR ($CDCl_3$, 300 MHz, 25 °C): δ 29.0 (br), 19.3 (br), 11.1 (s), 10.6 (s), 3.1 (s), 2.9 (s), -8.9 (br), -29.6 (br), -31.9 (br), -49.9 (br), -56.5 (br), -61.4 (v br), -64.7 ppm (v

br). ^{19}F NMR ($CDCl_3$, 282 MHz, 25 °C): δ -70.6 (d, 6F, J = 712.8 Hz, PF_6), -82.0 ppm (s, 3F, CF_3). UV-Vis (CH_3CN): λ (ε) 312 (sh), 412 (22 627), 505 (11 102), 996 nm (4 000 M^{-1} cm^{-1}). μ_{eff} (Evans method) = 1.72 μ_B. Anal. Calcd for $FeC_{46}H_{26}N_6F_{12}P$: C, 56.52; H, 2.68. Found: C, 56.57; H, 2.66.

Synthesis **of [Fe($^{Cl\text{-}Phen}$NNN^{Quin})$_2$]PF_6 ([6b]PF_6)**: A 250 mL round-bottom flask was charged with $FeCl_3 \cdot 6H_2O$ (0.019 mg, 0.070 mmol), 2a (50 mg, 0.14 mmol), $NaPF_6$ (12 mg, 0.070 mmol), and NaO^{t}Bu (14 mg, 0.14 mmol). MeOH (20 mL) was added and the flask was stirred and refluxed at 100 °C overnight. The flask was then cooled to room temperature and the solvent removed. The brown solid was dissolved in minimal CH_2Cl_2 and added slowly to 100 mL of pentane to precipitate the compound. The mixture was then filtered and the solid collected. Isolated yield = 55 mg (86 %). ^{1}H NMR ($CDCl_3$, 300 MHz, 25 °C): δ 29.2 (br), 19.5 (br), 11.0 (s), 10.6 (s), 2.8 (s), 2.7 (s), -9.1 (br), -29.8 (br), -33.7 (br), -50.5 (br), -56.9 (v br), -61.9 (v br), -65.5 ppm (v br). UV-Vis/NIR (CH_3CN): λ (ε) 312 (sh), 410, (19 225), 495, (11 310), 1004 nm (3 335 M^{-1} cm^{-1}).

4.5.2 X-ray data collection, solution and refinement

Crystal structure data was using collected from multi-faceted crystals of suitable size and quality selected from a representative sample of crystals of the same habit using an optical microscope. In each case, crystals were mounted on MiTiGen loops with data collection carried out in a cold stream of nitrogen (150 K; Bruker D8 QUEST ECO). All diffractometer manipulations were carried out using Bruker APEX3 software.[57] Structure solution and refinement was carried out using XS, XT[58] and XL software, embedded within the Bruker SHELXTL suite.[59] For each structure, the absence of additional symmetry was confirmed using ADDSYM

incorporated in the PLATON program.[60] Crystallographic data for some of the structures have also been deposited at the Cambridge Crystallographic Data Centre, under deposition numbers 1589420 (**5a**), 1589421 (**6a**), 1589422 (**6b**), 1589423 ([**6a**]PF_6) and 1589424 ([**6b**]PF_6).

Crystal structure parameters for **5a** (CCDC number 1589420): X-ray quality crystals were grown by evaporation of an EtOAc/hexanes solution. Crystal structure parameters: $C_{26}H_{23}N_3$, 377.47 g/mol, monoclinic, space group $P2_1/c$; a = 9.1993(2) Å, b = 13.7461(3) Å, c = 15.8350(4) Å, $\alpha = \gamma = 90°$, β = 92.2660(10)°, V = 2000.84(8) Å^3; Z = 4, ρ_{calcd} = 1.253 g cm^{-3}; crystal dimensions 0.340 x 0.300 x 0.180 mm; diffractometer Bruker D8 QUEST ECO CMOS; Mo K$_\alpha$ radiation, 150(2) K, θ_{max} = 30.540°; 112931 reflections, 6123 independent (R_{int} = 0.0840), direct methods; absorption coeff (μ = 0.074 mm^{-1}), absorption correction semi-empirical from equivalents (SADABS); refinement (against F_o^2) with SHELXTL V6.1, 265 parameters, 0 restraints, R_1 = 0.0584 ($I > 2\sigma$) and wR_2 = 0.1607 (all data), Goof = 1.023, residual electron density 0.426/−0.243 e Å^{-3}.

Crystal structure parameters for **6a** (CCDC number 1589421): X-ray quality crystals were grown as a pentane solvate from a benzene solution at -35 °C. A disordered pentane molecule could be successfully modeled and is included in the final structure. A disordered ^{t}Bu was modeled using the appropriate restraints. Crystal structure parameters: $C_{54.50}H_{49.50}FeN_6$, 844.35 g/mol, triclinic, space group P-1; a = 11.8116(11) Å, b = 11.8288(11) Å, c = 15.8752(15) Å, α = 95.132(5)°, β = 92.310(5)°, γ = 102.631(5)°, V = 2151.6(4) Å^3; Z = 2, ρ_{calcd} = 1.303 g cm^{-3}; crystal dimensions 0.200 × 0.200 × 0.100 mm; diffractometer Bruker D8 QUEST ECO CMOS; Mo K$_\alpha$ radiation, 150(2) K, θ_{max} = 30.963°; 962193 reflections, 13227 independent (R_{int} = 0.0957), intrinsic phasing; absorption coeff (μ = 0.396 mm^{-1}), absorption correction semi-empirical from

equivalents (SADABS); refinement (against F_o^2) with SHELXTL V6.1, 597 parameters, 30 restraints, $R_1 = 0.0872$ ($I > 2\sigma$) and $wR_2 = 0.2125$ (all data), Goof = 1.141, residual electron density 2.31/−1.22 e Å^{-3}.

Crystal structure parameters for **6b** (CCDC number 1589422): X-ray quality crystals were grown as fluorobenzene solvate from a pentane solution at room temperature. Disordered CF_3 groups were modeled with the use of appropriate restraints. One solvent molecule could be successfully modeled; however residual electron density (1402 e^-) assigned to two additional co-crystallized fluorobenzene molecules was found in a solvent accessible void (5799 Å^3). These additional solvent molecules could seen in the initial structure and by solution NMR analysis of the crystals, but not successfully refined, and so were dealt with using the SQUEEZE protocol included in the PLATON program.[60] The results from the SQUEEZE protocol are appended to the end of the .cif, included as supporting information. Crystal structure parameters: $C_{52}H_{26}F_7FeN_6$, 923.64 g/mol, orthorhombic, space group $I4_1/a$; $a = b = 19.4851(11)$ Å, $c = 54.499(3)$ Å, $\alpha = \beta = \gamma = 90°$, V = 206941(3) Å^3; Z = 16, $\rho_{calcd} = 1.186$ g cm^{-3}; crystal dimensions 0.300 × 0.200 × 0.200 mm; diffractometer Bruker D8 QUEST ECO CMOS; Mo K_α radiation, 150(2) K, $\theta_{max} = 30.585°$; 325859 reflections, 15793 independent ($R_{int} = 0.0685$), direct methods; absorption coeff ($\mu = 0.354$ mm^{-1}), absorption correction semi-empirical from equivalents (SADABS); refinement (against F_o^2) with SHELXTL V6.1, 627 parameters, 184 restraints, $R_1 = 0.0828$ ($I > 2\sigma$) and $wR_2 = 0.2356$ (all data), Goof = 0.982, residual electron density 0.765/−0.711 e Å^{-3}.

Crystal structure parameters for **6c**: X-ray quality crystals were grown as benzene solvate from a pentane solution at room temperature. Disordered solvent molecules were modelled

successfully. Crystal structure parameters: $C_{49.5}H_{35}Cl_2FeN_6$, 840.58 g/mol, triclinic, space group P-1; a = 12.5698(5) Å, b = 17.9561(6) Å, c = 18.7664(6) Å, α = 82.3000(10)º, β = 75.4080(10)º, γ = 75.1090(10)°, V = 3950.5(2) Å^3; Z = 4, ρ_{calcd} = 1.413 g cm^{-3}; crystal dimensions 0.440 × 0.230 × 0.200 mm; diffractometer Bruker D8 QUEST ECO CMOS; Mo K$_\alpha$ radiation, 150(2) K, θ_{max} = 38.508°; 180195 reflections, 41675 independent (R_{int} = 0.0625), direct methods; absorption coeff (μ = 0.562mm^{-1}), absorption correction semi-empirical from equivalents (SADABS); refinement (against F_o^2) with SHELXTL V6.1, 1072 parameters, 48 restraints, R_1 = 0.0601 ($I > 2\sigma$) and wR_2 = 0.1643 (all data), Goof = 1.020, residual electron density 1.500/−1.004 e Å^{-3}.

Crystal structure parameters for [**6a**]PF_6 (CCDC number 1589423): X-ray quality crystals were grown as a fluorobenzene solvate from a pentane solution at room temperature. One fluorobenzene solvent molecule could be successfully modeled and is included in the final structure. Electron density (135 e$^-$) corresponding to 1.5 additional solvent molecules per asymmetric unit was found in a solvent accessible void (549 Å^3) and removed using the SQUEEZE protocol included in the PLATON program.[60] The results from the SQUEEZE protocol are appended to the end of the .cif, included as supporting information. Crystal structure parameters: $C_{58}H_{49}F_7FeN_6P$, 1049.85 g/mol, triclinic, space group *P*-1; a = 13.2396(6) Å, b = 14.5753(6) Å, c = 16.2281(7) Å, α = 95.6490(10)°, β = 107.6880(10)°, γ = 103.7250(10)°, V = 2848.7(2) Å^3; Z = 2, ρ_{calcd} = 1.224 g cm^{-3}; crystal dimensions 0.520 × 0.100 × 0.030 mm; diffractometer Bruker D8 QUEST ECO CMOS; Mo K$_\alpha$ radiation, 150(2) K, θ_{max} = 24.732°; 65313 reflections, 9702 independent (R_{int} = 0.0536), intrinsic phasing; absorption coeff (μ = 0.356 mm^{-1}), absorption correction semi-empirical from equivalents (SADABS); refinement (against F_o^2) with SHELXTL

V6.1, 652 parameters, 0 restraints, R_1 = 0.0548 ($I > 2\sigma$) and wR_2 = 0.1479 (all data), Goof = 1.019, residual electron density 0.90/−0.44 e Å^{-3}.

Crystal structure parameters for [**6b**]PF_6 (CCDC number 1589424): X-ray quality crystals were grown as a fluorobenzene solvate from a pentane solution at room temperature. Electron density (264 e^-) corresponding to a co-crystallized fluorobenzene solvent molecule, whose presence was corroborated by NMR spectra of the crystallized compound, was found in a solvent accessible void (752 Å^3) and could not be successfully refined, and so was removed using the SQUEEZE protocol included in the PLATON program,[60] with the results from the SQUEEZE protocol appended to the end of the CIF. Crystal structure parameters: $C_{46}H_{26}F_{12}FeN_6P$, 977.55 g/mol, monoclinic, space group $P2_1/n$; a = 11.1843(7) Å, b = 25.0821(15) Å, c = 16.3728(10) Å, $\alpha = \gamma = 90°$, β = 101.949(4)°, V = 4493.5(5) Å^3; Z = 4, ρ_{calcd} = 1.445 g cm^{-3}; crystal dimensions 0.200 x 0.050 x 0.050 mm; diffractometer Bruker D8 QUEST ECO CMOS; Mo K_α radiation, 150(2) K, θ_{max} = 24.823°; 114141 reflections, 7692 independent (R_{int} = 0.1111), direct methods; absorption coeff (μ = 0.461 mm^{-1}), absorption correction semi-empirical from equivalents (SADABS); refinement (against F_o^2) with SHELXTL V6.1, 595 parameters, 0 restraints, R_1 = 0.0879 ($I > 2\sigma$) and wR_2 = 0.2368 (all data), Goof = 1.541, residual electron density 0.752/−0.528 e Å^{-3}.

Crystal structure parameters for [**6b**]PF_6: X-ray quality crystals were grown as a pentane solvate from a fluorobenzene solution. Crystal structure parameters: $C_{44}H_{26}Cl_2F_6FeN_6P$, 910.43 g/mol, hexagonal, space group $P6_122$; $a = b$ = 11.9344(7) Å, c = 52.414(3) Å, $\alpha = \beta = 90°$, $\gamma = 120°$, V = 6465.2(8) Å^3; Z = 6, ρ_{calcd} = 1.403 g cm^{-3}; crystal dimensions 0.600 × 0.120 × 0.100 mm;

diffractometer Bruker D8 QUEST ECO CMOS; Mo K_α radiation, 150(2) K, $2\theta_{max}$ = 49.362°; 41641 reflections, 3647 independent (R_{int} = 0.0800), direct methods; absorption coeff (μ = 0.576 mm^{-1}), absorption correction semi-empirical from equivalents (SADABS); refinement (against F_o^2) with SHELXTL V6.1, 273 parameters, 0 restraints, R_1 = 0.0812 ($I > 2\sigma$) and wR_2 = 0.1477 (all data), Goof = 1.038, residual electron density 0.44/−0.33 e $Å^{-3}$.

4.5.3 Electrochemical Methods

For electrochemical analysis, 5-10 mg of the compound investigated was dissolved in 15 mL of 0.1 M [^{n}Bu$_4$N]PF$_6$ in CH_3CN and purged with Ar for 20 minutes prior to analysis. All electrochemical experiments were conducted under inert (Ar) atmosphere using a CHI 760c bipotentiostat, a 3 mm diameter glassy carbon working electrode, a Ag/Ag^+ non-aqueous quasi-reference electrode separated by a Vycor tip, and a Pt wire counter electrode. Cyclic voltammetric (CV) experiments were conducted using scan rates of 50-800 mV/s. Differential Pulse Voltammetry (DPV) experiments were also conducted, using a 5 mV increment, 50 mV amplitude, 0.1 s pulse width, 0.0167 s sample width, and 0.5 s pulse period. Upon completion of all CV and DPV analyses, ferrocene (FcH, [(η^5-C_5H_5)$_2$Fe)]) was added to the solution as an internal standard, with all potentials reported versus the $FcH^{0/+}$ redox couple.[61]

4.6 References

(1) Lewis, N. S.; Nocera, D. G. *Proc. Natl Acad. Sci. USA* **2006**, *103* (43), 15729.

(2) Haegel, N. M.; Margolis, R.; Buonassisi, T.; Feldman, D.; Froitzheim, A.; Garabedian, R.; Green, M.; Glunz, S.; Henning, H.-M.; Holder, B.; Kaizuka, I.; Kroposki, B.; Matsubara, K.; Niki, S.; Sakurai, K.; Schindler, R. A.; Tumas, W.; Weber, E. R.; Wilson, G.; Woodhouse, M.; Kurtz, S. *Science* **2017**, *356* (6334), 141.

(3) O'Regan, B.; Graetzel, M. *Nature* **1991**, *353*.

(4) Hagfeldt, A.; Boschloo, G.; Sun, L.; Kloo, L.; Pettersson, H. *Chem. Rev.* **2010**, *110* (11), 6595.

(5) Bozic-Weber, B.; Constable, E. C.; Housecroft, C. E. *Coord. Chem. Rev.* **2013**, *257* (21–22), 3089.

(6) Ardo, S.; Fernandez Rivas, D.; Modestino, M. A.; Schulze Greiving, V.; Abdi, F. F.; Alarcon Llado, E.; Artero, V.; Ayers, K.; Battaglia, C.; Becker, J.-P.; Bederak, D.; Berger, A.; Buda, F.; Chinello, E.; Dam, B.; Di Palma, V.; Edvinsson, T.; Fujii, K.; Gardeniers, H.; Geerlings, H.; H. Hashemi, S. M.; Haussener, S.; Houle, F.; Huskens, J.; James, B. D.; Konrad, K.; Kudo, A.; Kunturu, P. P.; Lohse, D.; Mei, B.; Miller, E. L.; Moore, G. F.; Muller, J.; Orchard, K. L.; Rosser, T. E.; Saadi, F. H.; Schüttauf, J.-W.; Seger, B.; Sheehan, S. W.; Smith, W. A.; Spurgeon, J.; Tang, M. H.; van de Krol, R.; Vesborg, P. C. K.; Westerik, P. *Energy Environ. Sci.* **2018**, *11* (10), 2768.

(7) Larsen, C. B.; Wenger, O. S. *Chem. Eur. J.* **2018**, *24* (9), 2039.

(8) Ponseca, C. S.; Chábera, P.; Uhlig, J.; Persson, P.; Sundström, V. *Chem. Rev.* **2017**, *117* (16), 10940.

(9) Schultz, D. M.; Yoon, T. P. *Science* **2014**, *343* (6174), 1239176.

(10) Robertson, N. *Angew. Chem., Int. Ed.* **2006**, *45* (15), 2338.

(11) Prier, C. K.; Rankic, D. A.; MacMillan, D. W. C. *Chem. Rev.* **2013**, *113* (7), 5322.

(12) Housecroft, C. E.; Constable, E. C. *Chem. Soc. Rev.* **2015**, *44* (23), 8386.

(13) Zhang, Y.; Lee, T. S.; Petersen, J. L.; Milsmann, C. *J. Am. Chem. Soc.* **2018**, *140* (18), 5934.

(14) Pal, A. K.; Li, C.; Hanan, G. S.; Zysman-Colman, E. *Angew. Chem., Int. Ed.* **2018**, *57* (27), 8027.

(15) Büldt, L. A.; Wenger, O. S. *Angew. Chem., Int. Ed.* **2017**, *56* (21), 5676.

(16) Otto, S.; Grabolle, M.; Förster, C.; Kreitner, C.; Resch-Genger, U.; Heinze, K. *Angew. Chem., Int. Ed.* **2015**, *54* (39), 11572.

(17) Sattler, W.; Henling, L. M.; Winkler, J. R.; Gray, H. B. *J. Am. Chem. Soc.* **2015**, *137* (3), 1198.

(18) Wenger, O. S. *J. Am. Chem. Soc.* **2018**, *140* (42), 13522.

(19) Galoppini, E. *Nat. Chem.* **2015**, *7* (11), 861.

(20) Juban, E. A.; Smeigh, A. L.; Monat, J. E.; McCusker, J. K. *Coord. Chem. Rev.* **2006**, *250*.

(21) Liu, Y.; Harlang, T.; Canton, S. E.; Chábera, P.; Suárez-Alcántara, K.; Fleckhaus, A.; Vithanage, D. A.; Göransson, E.; Corani, A.; Lomoth, R.; Sundström, V.; Wärnmark, K. *Chem. Commun.* **2013**, *49* (57), 6412.

(22) Liu, L.; Duchanois, T.; Etienne, T.; Monari, A.; Beley, M.; Assfeld, X.; Haacke, S.; Gros, P. C. *Phys. Chem. Chem. Phys.* **2016**, *18* (18), 12550.

(23) Liu, Y.; Wärnmark, K.; Liu, Y.; Sundstrom, V.; Persson, P. *Acc. Chem. Res.* **2016**, *49* (8), 1477.

(24) Duchanois, T.; Etienne, T.; Cebrián, C.; Liu, L.; Monari, A.; Beley, M.; Assfeld, X.; Haacke, S.; Gros, P. C. *Eur. J. Inorg. Chem.* **2015**, *2015* (14), 2469.

(25) Harlang, T. C. B.; Liu, Y.; Gordivska, O.; Fredin, L. A.; Ponseca, C. S.; Huang, P.; Chábera, P.; Kjaer, K. S.; Mateos, H.; Uhlig, J.; Lomoth, R.; Wallenberg, R.; Styring, S.; Persson, P.; Sundström, V.; Wärnmark, K. *Nat. Chem.* **2015**, *7* (11), 883.

(26) Chábera, P.; Liu, Y.; Prakash, O.; Thyrhaug, E.; Nahhas, A. E.; Honarfar, A.; Essén, S.; Fredin, L. A.; Harlang, T. C. B.; Kjær, K. S.; Handrup, K.; Ericson, F.; Tatsuno, H.; Morgan, K.; Schnadt, J.; Häggström, L.; Ericsson, T.; Sobkowiak, A.; Lidin, S.; Huang, P.; Styring, S.; Uhlig, J.; Bendix, J.; Lomoth, R.; Sundström, V.; Persson, P.; Wärnmark, K. *Nature* **2017**, *543* (7647), 695.

(27) Chábera, P.; Kjaer, K. S.; Prakash, O.; Honarfar, A.; Liu, Y.; Fredin, L. A.; Harlang, T. C. B.; Lidin, S.; Uhlig, J.; Sundström, V.; Lomoth, R.; Persson, P.; Wärnmark, K. *J. Phys. Chem. Lett.* **2018**, *9* (3), 459.

(28) Fatur, S. M.; Shepard, S. G.; Higgins, R. F.; Shores, M. P.; Damrauer, N. H. *J. Am. Chem. Soc.* **2017**, *139* (12), 4493.

(29) Kjær, K. S.; Kaul, N.; Prakash, O.; Chábera, P.; Rosemann, N. W.; Honarfar, A.; Gordivska, O.; Fredin, L. A.; Bergquist, K.-E.; Häggström, L.; Ericsson, T.; Lindh, L.; Yartsev, A.; Styring, S.; Huang, P.; Uhlig, J.; Bendix, J.; Strand, D.; Sundström, V.; Persson, P.; Lomoth, R.; Wärnmark, K. *Science* **2019**, *363* (6424), 249.

(30) Mukherjee, S.; Torres, D. E.; Jakubikova, E. *Chem. Sci.* **2017**, *8* (12), 8115.

(31) Betley, T. A.; Qian, B. A.; Peters, J. C. *Inorg. Chem.* **2008**, *47* (24), 11570.

(32) Mengel, A. K. C.; Förster, C.; Breivogel, A.; Mack, K.; Ochsmann, J. R.; Laquai, F.; Ksenofontov, V.; Heinze, K. *Chem. Eur. J.* **2015**, *21* (2), 704.

(33) Maksić, Z. B.; Barić, D.; Müller, T. *J. Phys. Chem. A* **2006**, *110* (33), 10135.

(34) Gibson, V. C.; Redshaw, C.; Solan, G. A. *Chem. Rev.* **2007**, *107* (5), 1745.

(35) Mondal, R.; Giesbrecht, P. K.; Herbert, D. E. *Polyhedron* **2016**, *108*, 156.

(36) Hewage, J. S.; Wanniarachchi, S.; Morin, T. J.; Liddle, B. J.; Banaszynski, M.; Lindeman, S. V.; Bennett, B.; Gardinier, J. R. *Inorg. Chem.* **2014**, *53* (19), 10070.

(37) Frazier, B. A.; Wolczanski, P. T.; Lobkovsky, E. B.; Cundari, T. R. *J. Am. Chem. Soc.* **2009**, *131* (10), 3428.

(38) Epstein, L. M. *J. Chem. Phys.* **1964**, *40* (2), 435.

(39) Collins, R. L.; Pettit, R.; Baker, W. A. *J. Inorg. Nucl. Chem.* **1966**, *28* (4), 1001.

(40) Sinha, S.; Das, S.; Sikari, R.; Parua, S.; Brandaõ, P.; Demeshko, S.; Meyer, F.; Paul, N. D. *Inorg. Chem.* **2017**, *56* (22), 14084.

(41) Reiff, W. M.; Baker, W. A.; Erickson, N. E. *J. Am. Chem. Soc.* **1968**, *90* (18), 4794.

(42) Dixon, I. M.; Khan, S.; Alary, F.; Boggio-Pasqua, M.; Heully, J.-L. *Dalton Trans.* **2014**, *43* (42), 15898.

(43) Lever, A. B. P. *Inorg. Chem.* **1990**, *29* (6), 1271.

(44) Braterman, P. S.; Song, J. I.; Peacock, R. D. *Inorg. Chem.* **1992**, *31* (4), 555.

(45) Brown, A. M.; McCusker, C. E.; McCusker, J. K. *Dalton Trans.* **2014**, *43* (47), 17635.

(46) Auböck, G.; Chergui, M. *Nat. Chem.* **2015**, *7* (8), 629.

(47) Gawelda, W. *J. Am. Chem. Soc.* **2007**, *129* (26), 8199.

(48) Lever, A. B. P. in Inorganic Electronic Spectroscopy 2nd edn, 208–209 (Elsevier, 1986). .

(49) Ashley, D. C.; Jakubikova, E. *Coord. Chem. Rev.* **2017**, *337*, 97.

(50) Francés-Monerris, A.; Magra, K.; Darari, M.; Cebrián, C.; Beley, M.; Domenichini, E.; Haacke, S.; Pastore, M.; Assfeld, X.; Gros, P. C.; Monari, A. *Inorg. Chem.* **2018**, *57* (16), 10431.

(51) Smeigh, A. L.; Creelman, M.; Mathies, R. A.; McCusker, J. K. *J. Am. Chem. Soc.* **2008**, *130* (43), 14105.

(52) Mondal, R.; Lozada, I. B.; Davis, R. L.; Williams, J. A. G.; Herbert, D. E. *Inorg. Chem.* **2018**, *57* (9), 4966.

(53) Wenger, O. S. *Chem. Eur. J.* **2019**, *25* (24), 6043.

(54) Lee, J.-Y.; Lee, M.-H.; Jeong, K.-S. *Supramolecular Chemistry* **2007**, *19* (4–5), 257.

(55) Mandapati, P.; Giesbrecht, P. K.; Davis, R. L.; Herbert, D. E. *Inorg. Chem.* **2017**, *56* (6), 3674.

(56) Conte-Mayweg, A.; Kuehne, H.; Luebbers, T.; Maugeais, C.; Mueller, W.; Pflieger, P. Preparation of indole, indazole or indoline derivatives as cholesterol ester-exchanging protein inhibitors. WO2006013048A1, 2006.

(57) Bruker-AXS APEX3 v2016.1-0, Madison,Wisconsin, USA, 2016. .

(58) Sheldrick, G. M. *Acta Crystallogr., Sect. A: Found. Crystallogr.* **2015**, *71* (1), 3.

(59) Sheldrick, G. M. *Acta Crystallogr., Sect. A: Found. Crystallogr.* **2008**, *64*, 112.

(60) Spek, A. L. *Acta Crystallogr., Sect. D: Biol. Crystallogr.* **2009**, *65*, 148.

(61) Connelly, N. G.; Geiger, W. E. *Chem. Rev.* **1996**, *96* (2), 877.

Chapter 5

Targeting Low-Energy Absorption in Monometallic Coordination Complexes of Diarylamido Ligands

5.1 Abstract

The ability to broadly absorb light across the incident solar spectrum is an important design target in the development of photosensitizers. The 'HOMO inversion' model predicts that for $Fe(tpy)_2$ (tpy = 2,2':6',2''-terpyridine) comounds, adjusting the character of the highest occupied molecular orbital (HOMO) from metal-centred to ligand-centred can drastically improve photophysical properties by broadening absoprtion in the visible and increasing molar extinction coefficients. In an effort to experimentally realize strong, panchromatic absorption, a tridentate *N^N-^N* diarylamido ligand bearing flanking benzannulated *N*-heterocyclic donors (**5a**$^-$) was used to prepare deeply coloured, pseudo-octahedral coordination complexes of a range of first-row transition and main-group metals ([**6a-10a**]$^{0/+}$; 6 = Fe, 7 = Co, 8 = Ni, 9 = Zn, 10 = Ga). While the Fe(II) congener exhibits the sought-after broad absorption, isostructural and isoelectronic complexes of other transition and main-group metals show vastly different absorption and redox properties. Density functional theory (DFT) calculations point towards the relative energies of the metal *d*-orbitals and ligand orbitals as the source of major changes in electronic structure, experimentally confirming aspects of the computational 'HOMO inversion' model with implications for the design of transition-metal sensitizers with broad, panchromatic absorptive properties.

5.2 Introduction

The development of molecular photosensitizers that can efficiently harvest incident solar radiation is critical to the widespread application of sustainable energy capture and light-driven synthesis including in dye-sensitized solar cells (DSSCs),[1,2] photoredox catalysis[3] and the on-site production of solar fuels.[4] To facilitate the electron-transfer required for such applications, photosensitizers must exhibit sufficiently long-lived charge-transfer (CT) lifetimes to enable electron transfer,[5] but also ideally be engineered to strongly absorb as much of the solar spectrum as possible.[6] Late transition metal coordination complexes (MCCs) supported by highly conjugated ligands successfully fulfill the first of these criteria. Accordingly, many of the most widely used sensitizers are MCCs based on Ru(II) and Ir(III) centres supported by *N*-heterocyclic or related conjugated, chelating ligands,[7–9] though creative ligand design has led to development of mid- and early-metal photosensitizer candidates with potentially useful properties.[10–12] A limitation of many of these dyes, including recently reported examples based on abundant metals such as Zr,[10] Fe,[13] and Co,[14] is the absence of low-energy visible and near-infrared (NIR) light absorption that precludes exploitation of a significant portion of available solar photons and contributes to low incident photon-to-current efficiencies[15] (Table 5.1).

Table 5.1 Selected optical properties of abundant metal-based sensitizer candidates

Compound[a]	λ_{max} (nm)	ε (M^{-1} cm^{-1})	FWHM (nm)[b]
Zr(^{Me}PDP^{Ph})$_2$[10]	525	21 570	80
[V(ddpd)$_2$][PF_6]$_3$[12]	597	1 945	120
[Fe(btz)$_3$][PF_6]$_2$[16]	688	2 200[b]	300[c]
[Fe(btz)$_3$][PF_6]$_3$[16]	541[d]	1 500	95
[Fe(phtmeimb)$_2$][PF_6][13]	502	2 950	120
6a[17]	724	8 510	130
6b[17]	728	9 370	140
[Co(dgpy)$_2$][BF_4]$_3$[14]	325	14 800	60
[Co(dgpz)$_2$][BF_4]$_3$[14]	360	15 100	80

[a] btz = 3,3′-dimethyl- 1,1′-bis(*p*-tolyl)-4,4′-bis(1,2,3-triazol-5-ylidene); phtmeimb = {phenyl[tris(3-methylimidazol-1-ylidene)] borate}$^-$; ^{Me}PDP^{Ph} = [2,6-bis(5-(2,4,6-trimethylphenyl)-3-phenyl-1*H*-pyrrol-2-yl)pyridine]; dgpy = 2,6-diguanidylpyridine; dgpz = 2,6-diguanidylpyrazine; ddpd = *N*,*N*'-dimethyl-*N*,*N*'-dipyridine-2-ylpyridine-2,6-diamine.

[b] Estimated from peak width at half-max of ε for lowest-energy absorption peak

[c] Estimated by doubling half-width, half-max, as peak does not attenuate at higher energy edge

[d] Average of two shoulder peaks

A variety of approaches to extending the wavelength range over which MCCs can strongly absorb have been reported. Some of the more successful examples include the use of ligands comprised of large, extended π systems[18] and/or multi-metallic assemblies.[19] For example, bimetallic Rh complexes supported by bridging 1,8-naphthyridine and formamidinate ligands have broad light-absorption profiles and long-lived charge-transfer states capable of facilitating electron-transfer reactivity.[15,20,21] Exchanging napththyridine for a bridging benzo[*c*]cinnoline ligand furthermore leads to panchromatic absorbing molecules that can photochemically catalyze H_2 evolution using low-energy light.[22] In these systems, the bridging ligands help maximize symmetric overlap between the Rh_2 δ* and *N*-heterocyclic ligand π* orbitals, boosting the oscillator strength of transitions involving these orbitals, while also ensuring a short Rh−Rh bond that raises the energy of the Rh_2 σ* orbital and thereby destabilizes metal-centred excited states in favour of charge-transfer ones.

Bimetallic complexes with no metal-metal interaction can also show intense, low energy absorptions when paired with appropriately conjugated binucleating ligands. *Bis*-iron(II) and *bis*-ruthenium(II) complexes of cyclam-derived macrocyclic ligands with a tetraiminoethylene core

(Figure 5.1, **A**), for example, exhibit strong, low energy metal-to-ligand charge transfer (MLCT) absorptions for both Fe_2 (λ = 874 nm, ε = 24 600 M^{-1} cm^{-1})[23] and Ru_2 (λ = 910 nm, ε = 19 000 M^{-1} cm^{-1})[24] analogues. Upon oxidation, the mixed valent Ru(II)/Ru(III) analogue displays an even larger absorptive cross-section at slightly higher energy (λ = 805 nm, ε = 68 000 M^{-1} cm^{-1}), though the band is quite narrow (FWHM = ~ 50 nm).

MCCs supported by porphyrin ligands represent another strategy, owing to their intense absorption in the UV-visible region conferred by the conjugated macrocyclic ligand.[25] Solubility of these highly planar complexes can present challenges,[26] though appending peripheral tethers to the porphyrin framework (Figure 5.1, **B**) has been shown to encourage solubility in common organic solvents with retention of favourable absorption properties.[27] For example, despite narrow absorption bands, substituted Zn-based porphyrins have been used as dyes in prototype DSSCs, enabling up to 7% power conversion efficiencies (η).[28] Absorption by metal-porphyrins, however, typically attenuates beyond 500-600 nm, and this deficiency has been implicated in the relatively low η-values in comparison to DSSCs based on Ru-based MCC dyes.[27] Efforts to extend the absorption into the NIR by means of extended π-conjugation[29] or introduction of a push-pull system were found to be moderately successful, resulting in η-values of up to 13% for Zn porphyrins featuring a (2',4'-*bis*(hexyloxy)-[1,1'-biphenyl]-4-yl)amine donor.[30] Despite these advances, MCCs exhibiting strong and broad, panchromatic absorption remain quite rare, especially for mononuclear analogs based on abundant, first-row metals.

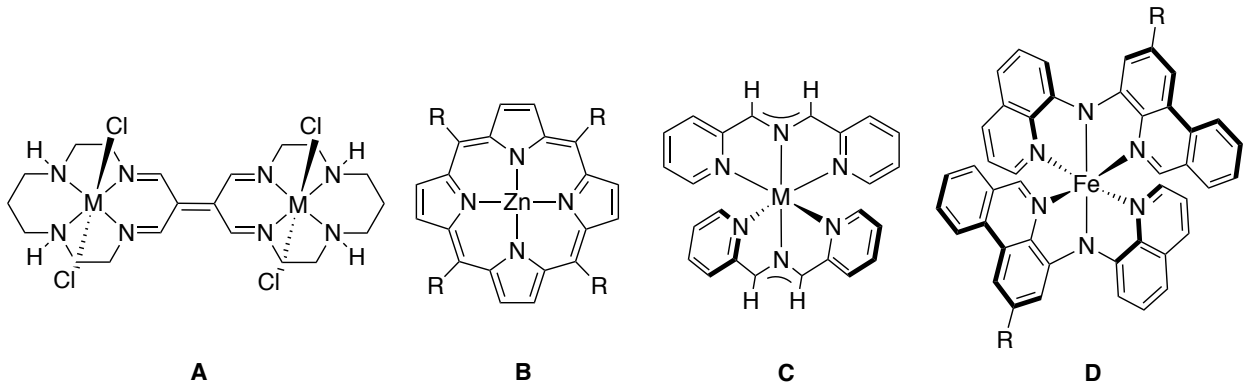

Figure 5.1 Selected design motifs for complexes that exhibit strong, low-energy absorption. Ranges of strong absorption ($\varepsilon > 5\ 000\ cm^{-1}\ M^{-1}$): **A** (M = Fe: < 400 nm, 650 – 1000 nm,[23] M = Ru: < 450 nm, 750 – 1100 nm, upon single oxidation: < 450 nm, 720 – 900 nm[24]); **B** < 600 nm, depending on R group[27]; **C** (M = V: < 600 nm, M = Cr: < 825 nm, M = Mn: < 625 nm, M = Fe: < 650 nm, M = Co: < 650 nm, M = Ni: < 600 nm)[31]; **D** R = *t*Bu < 780 nm, R = CF_3 < 795 nm[17]

In seeking to outline a design strategy for iron-based sensitizers with improved optical properties, Jakubikova and coworkers zeroed in on the impact of altering the π-donor properties of 2,2':6',2"-terpyridine (tpy) ligands in pseudooctahedral $[bis(tpy)_2Fe]^{2+}$ complexes of Fe(II).[32] By computationally probing the energy match between occupied ligand orbitals of π-symmetry and the filled t_{2g} set on the d^6 metal, a model was developed in which better energy matching leads to stronger metal-ligand π-type interactions, increasing the energy of the highest occupied molecular orbital (HOMO) and fostering multiple mixed metal-to-ligand and intraligand charge transfer (MLCT/ILCT) transitions in the calculated spectrum. Further stabilization of ligand π-orbitals through appending π-extension to the tpy ligands was predicted to lead to full 'HOMO inversion' in which the HOMO becomes wholly ligand centred. An experimental realization of this extreme that predated the computational study can be found in $(smif)_2Fe$[33] (Figure 5.1, **C**), where 'smif' is a azaallyl ligand *bis*[1,3-di(2-pyridyl)-2-azapropenide], first reported formed by the thermolysis of methylzinc *bis*(2-pyridylmemyl)amide.[34] For $(smif)_2Fe$, the HOMO and HOMO-1 are both ligand-centred, localized in the carbon nonbonding orbitals of the azaallyl

moiety. As a result, very strong (ε = 40 000 – 60 000 M^{-1} cm^{-1}) interligand charge-tranfer (ILCT) transitions from these orbitals to π^* orbitals on the smif pyridine arms are observed,[31] reminiscent of those observed in complexes of dipyrromethane and related ligands.[35] These IL transitions extend the absorption spectra out to ~750 nm for $(smif)_2Fe$ and even further (~850 nm) for $(smif)_2Cr$ with strong absorptivity (ε = 6000 $M^{-1}cm^{-1}$) from 650 – 850 nm.[31]

The construction of pseudo-octahedral iron complexes, $(^{R}\mathbf{L})_2Fe$ (R = *t*Bu, CF_3), where $^{R}\mathbf{L}$ is a benzannulated (4-phenanthridinyl)(8-quinolinyl)amido ligand (Figure 5.1, **D**) were recently reported.[17] These complexes exhibit nanosecond charge-transfer (CT) excited-state lifetimes and have broad absorptive cross-sections across the visible spectrum (ε > 5000 from λ = 250 – 795 nm). The absorption properties are attributed to a combination of a π-extended ligand with strong acceptor properties and 'HOMO raising'. In this intermediate case of HOMO inversion, the energies of the HOMO through to HOMO-4 are increased by strong mixing between Fe d and amido-based 2p orbitals.[36] Given recent exciting findings reported on sensitizer designs based on abundant transition elements beyond Group 8,[37,38] an investigation as to how the identity of the metal centre (M = Fe, Co, Ni, Zn and Ga) affects the redox chemistry and absorption profiles of complexes of $^{R}\mathbf{L}$ through changes to the dπ-pπ interaction induced by metal element selection and oxidation state was envisioned. An increased degree of mixing between ligand and metal-based orbitals should encourage intramolecular electronic communication across the metal bridges, and should be evidenced by the appearance low-energy charge-transfer (CT) bands in the absorption spectra where an increase in delocalization often favours strong, red-shifted absorption.[39]

Here, the synthesis, characterization and electronic properties of a series of metal coordination complexes (MCCs) of ligand **5a** is reported. It can be observed that increasing the atomic number of the chelated metal ion to greater than that of Fe, the energies of filled dπ orbitals

fall below those of filled ligand-based orbitals of similar symmetry, rendering these complexes susceptible to N_{amido}-based oxidation. Spectroelectrochemical experiments indicate a degree of mixed-valency not seen with the Fe(II) congeners, with significantly strong and broad low-energy absorption. This should have implication for the use of HOMO inversion design principles in the construction of panchromatic absorbing sensitizers using metals beyond iron.

5.3 Results and Discussion

5.3.1 Synthesis of Ligands and Coordination Complexes

In selecting metal ions for the series, first-row transition metals with *d*-electron counts [d^6: Fe(II), Co(III); d^8: Ni(II)] that favour metal-to-ligand type charge transfer transitions that typically form the basis of sensitization using MCCs[40] were selected. To round out these selections, two d^{10} metal ions were included, Zn(II) and Ga(III), to probe how a templating ion might facilitate solely intra- or inter-ligand transitions in the absence of energetically accessible *d* electrons. The synthesis of the benzannulated, phenanthridine-based diarylamido pincer-type ligand (**5a**) and its neutral Fe(II) and cationic complexes [**6a**] and [**6a**]PF_6 has been described.[17] Pseudooctahedral complexes of $\mathbf{5a}^-$ with Ni(II), Zn(II) and Co(III) were prepared by the addition of two equivalents of the *N^N(H)^N* proligand **5a** to the appropriate metal salt in refluxing methanol (Scheme 1). The Ga(III) salt was similarly prepared using dry THF at reflux. Where necessary, an exogenous Brønsted base was also present.

In all cases, the formation of the desired compounds was followed by the appearance of a strongly coloured solution and the loss of the amine N-*H* proligand peak in the ^{1}H NMR spectra. Paramagnetism was observed for **8a** and reaction progress was therefore determined by loss of peaks attributed to free proligand in the diamagnetic range of the ^{1}H NMR spectrum. ^{1}H and ^{13}C

NMR spectra of each diamagnetic complex showed a single ligand environment, suggesting magnetic equivalence in solution on the NMR timescale. A downfield ^{1}H shift of the proton nucleus in the 6-position of the phenanthridinyl arm (*ortho* to the N donor atom) was found to be diagnostic of compound identity [δ / ppm = 8.54 **6a**; 8.66, [**7a**]PF_6; 8.57, [9a]; 8.72 [**10a**]PF_6. Combustion analysis of the isolated products confirmed the purity of each bulk sample in the solid state.

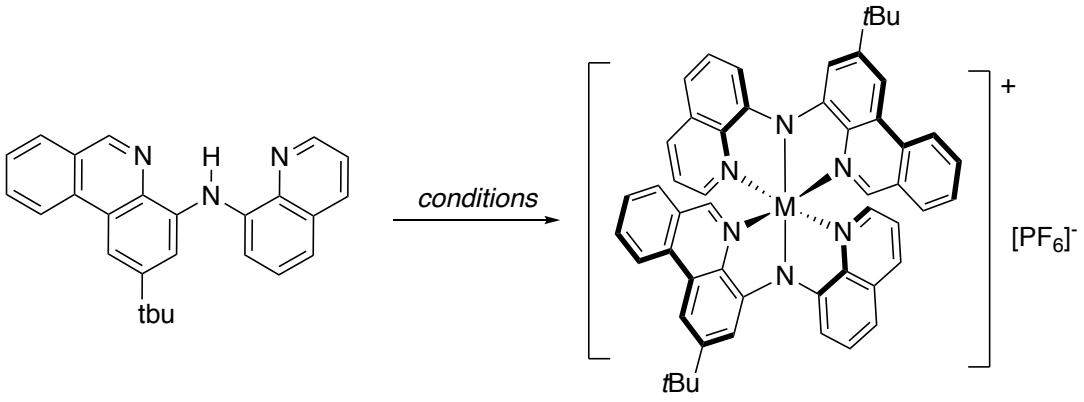

Scheme 5.1 Synthesis of homoleptic metal coordination complexes described in this work. Conditions: M = Co, *n* = 1: $Co(acac)_3$, $NaPF_6$, CH_3OH, 100 °C, 16 h; M = Ni, *n* = 0: $NiCl_2{\cdot}6H_2O$, NaO*t*Bu, CH_3OH, 100 °C, 16 h; M = Zn, *n* = 0: $Zn(NO_3)_2{\cdot}6H_2O$, NaO*t*Bu, CH_3OH, 100 °C, 16 h; M = Ga, *n* = 1: $GaCl_3$, NaO*t*Bu, $NaPF_6$, THF, 100 °C, 16 h. For conditions for (M = Fe, *n* = 0, 1), see reference [17].

5.3.2 Solid-State Structures of [(6-10)a]$^{0/+}$

The solid-state structures of the MCCs were determined using single crystal X-ray diffraction (Figure 5.2). In each case, the metal is arranged in a pseudo-octahedral coordination environment, with amido nitrogen (N_{amido}) atoms located *trans* to one another. Bond distances and angles are summarized in Table S22. A significantly larger coordination sphere is observed for the Ni and Ga complexes in comparison to earlier transition metal analogues, as seen through the length of all M-N bond distances. The gallium and nickel complexes exhibit similar bond distances

between the metal and neutral nitrogen donors (~2.07 Å), but the anionic Ga-N_{amido} [1.958(3) Å] separations are smaller compared to Ni-N_{amido} [2.0168(13), 2.0161(13) Å]. This is consistent with the increased positive charge at the higher oxidation state Ga(III) centre. In general, the M-N_{amido} distance is the shortest M-N contact within each molecule and is significantly shorter yet for the Group 8/9 transition metal analogues following the trend Fe ≈ Co < Ga < Ni. The two d^6 congeners, **6a** and [**7a**]PF_6, show only minor differences in bond lengths to the central metal, with a tighter coordination environment seen with Co, befitting the larger positive charge on Co(III). The coordination sphere observed for these molecules correlate strongly with trends of ionic radii.[41] The rigid nature of the ligand enforces the smaller ligand bite angles observed for complexes of the larger metal ions[42] (~160º for Ga/Ni, ~166° for Fe, ~170° for Co).

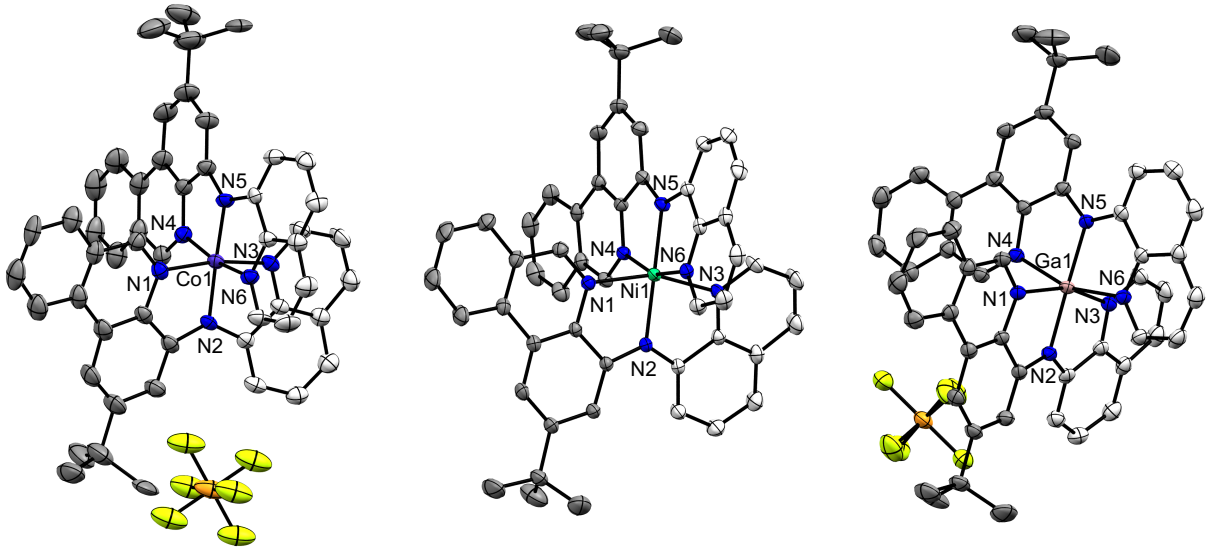

[**7a**]PF_6 **8a** [**10a**]PF_6

Figure 5.2 Crystal structures of [**7a**]PF_6, **8a** and [**10a**]PF_6 with thermal ellipsoids shown at 50% probability levels. Hydrogen atoms, select atom labels and co-crystallized solvent molecules are omitted for clarity.

5.3.3 Electronic Structure of [(6-10)a]$^{0/+}$

While the solid-state structures of [(**6-10**)**a**]$^{n+}$[PF_6]$_n$ do not vary significantly, the complexes show interesting differences in their colours and therefore in their electronic absorption spectra. All deeply coloured thanks to the benzannulated ligand framework, but the metal identity strongly influences absorption profile. When the central metal is Co(III), Ni(II) or Zn(II), the resultant [(**6-10**)**a**]$^{n+}$[PF_6]$_n$ complexes are dark red both as amorphous powders and crystalline solids. In acetonitrile solution, the compounds all show high molar absorptivities (ε; ~20 000-30 000 M^{-1} cm^{-1}) for transitions in the visible range (~480-540 nm, Figure 5.3 and Table S23). The lowest energy absorptions for [**7a**]PF_6, **8a** and **9a** are all relatively narrow bands (FWHM = ~ 90 nm), with maxima at ~ 500 nm. In comparison, λ_{max} for [**10a**]PF_6 is slightly blue-shifted (λ_{max} = 472 nm, ε = 17 220 M^{-1} cm^{-1}) and the complex is accordingly a lighter orange to the eye. In contrast, **6a** is deep green showing true panchromatic absorption with a broad and large absorptive cross-section spanning across the visible.[17] Integration of the solar spectra to 900 nm represents a doubling in both the number of harvestable photons and the theoretical incident photon-to-current efficiencies when compared to dyes with absorption that attenuates at ~650 nm,[15] underscoring the motivation to design such complexes.

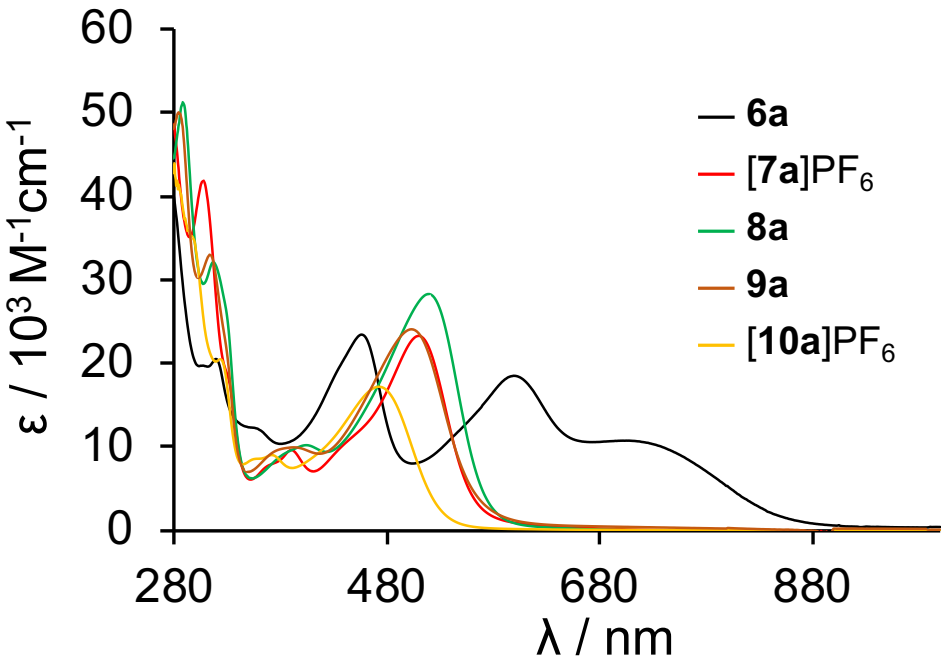

Figure 5.3 UV-Vis/NIR absorption spectra of $[(\mathbf{6\text{-}10})\mathbf{a}]^{n+}[PF_6]_n$ in CH_3CN

To explain the stark difference in the electronic absorption spectra, density functional theory (DFT) modeling of $[\mathbf{7a}]^+$, **8a** and $[\mathbf{10a}]^+$ was undertaken in order to compare with the electronic structure of $[\mathbf{6a}]^{n+}$.[17] The Zn congener was omitted in favour of the isoelectronic, d^{10} Ga(III) complex for ease of comparison of the optimized structure with the experimentally determined structure from X-ray diffraction (See Table S24 for a comparison of selected bond distances determined experimentally and theoretically). The ground-state orbital energies and HOMO isosurfaces [SOMO for **8a**] are shown in Figure 5.4 (see Figure S169 for frontier orbitals of $[\mathbf{7a}]^+$, **8a** and $[\mathbf{10a}]^+$). In all the complexes, low-lying, vacant ligand-based π* orbitals are present, and in each case are comprised of significant contributions from the $(H)C{=}N_{phen}$ subunit of the phenanthridinyl ligand arm (Table 5.2; see also Supporting Information, Tables S25-27). The strong electron density acceptor character of the benzannulated diarylamido ligand **5a** thanks to

the presence of phenanthridine (3,4-benzoquinoline) heterocyclic unit is thus retained across the series.

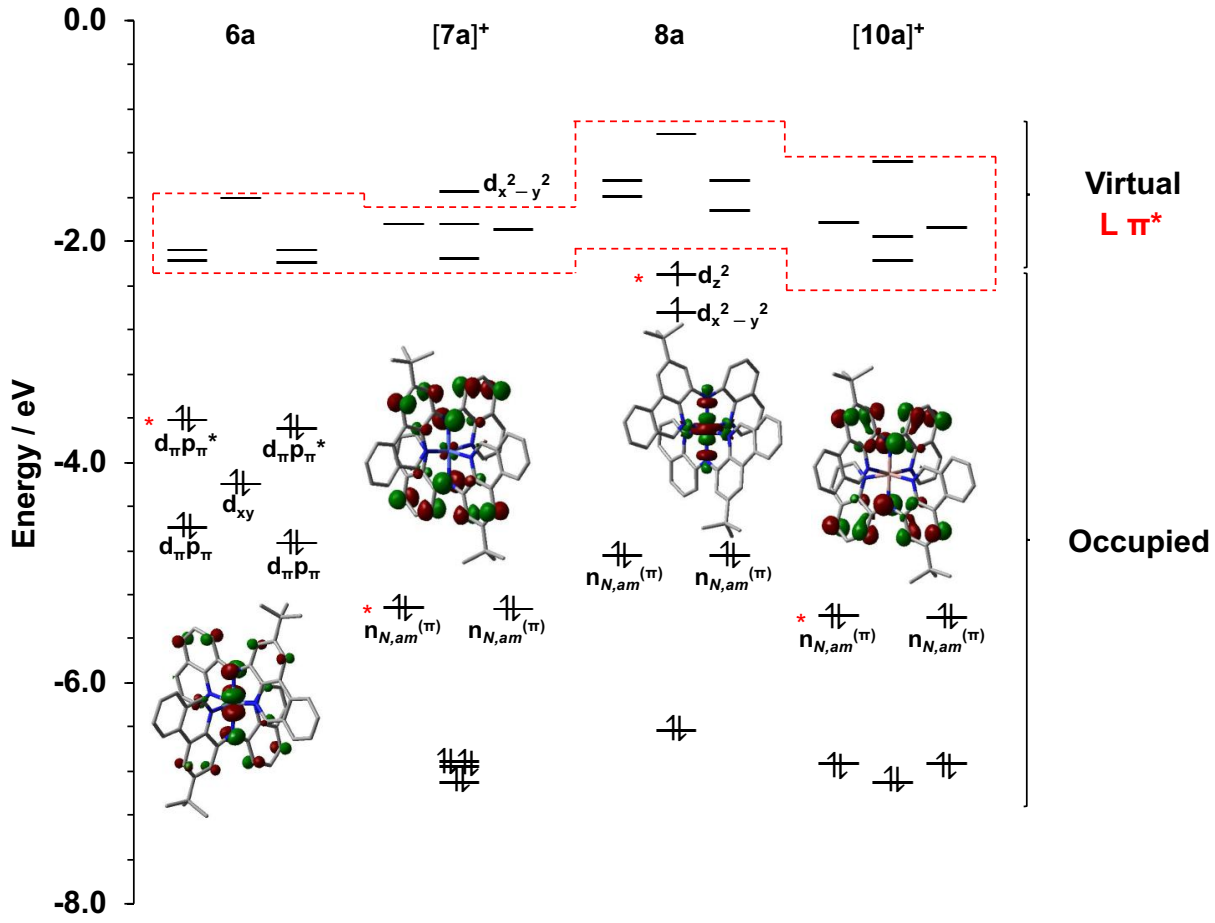

Figure 5.4 Selections from the ground-state MO diagrams of [(**6-10**)**a**]$^{n+}$ comparing the relative energies of the *d*-orbitals, N_{amido} lone pairs, and ligand-based π* orbitals. Isosurfaces are shown for the highest energy (partially) occupied MOs marked with a red asterisk. Vacant, acceptor ligand-based π* orbitals are outlined in red.

In the ferrous complex **6a**, the two highest-energy occupied orbitals (HOMO, HOMO–1) represent π-anti-bonding overlap between the amido nitrogens and the metal centre [π*(p + d)]. Population analysis reports 10% N_{amido} character in both the HOMO and HOMO-1 with significant metal contributions (~50%; Table 5.2). The HOMO–2 in contrast is localized on the iron (~67%) and has predominantly non-bonding character, while the HOMO-3 and HOMO-4 present the

corresponding π-bonding overlap.[17] Thus, **6a** can be described as an intermediate case of the 'HOMO inversion' model, attributable to significant mixing between the N(2p) and Fe(3d) orbitals of appropriate symmetry. This results in the *d*-orbital manifold covering a broader spread of energy levels, causing a significant contraction of the HOMO-LUMO gap and additional transitions in the visible responsible for the observed broad, panchromatic absorption. In the isoelectronic $3d^6$ complex [**7a**]PF_6, on the other hand, the lower energy *d*-π orbitals do not mix as strongly with the N_{amido} orbitals due to the greater disparity in energies. The HOMO and HOMO-1 of [**7a**]PF_6 are each comprised of only 3% metal character with stronger contributions from the N_{amido} orbitals (~20%), consistent with a ligand-based HOMO and HOMO-1 and a more complete case of 'HOMO inversion'. When the central metal is replaced with a $3d^{10}$ Ga(III) cation, the occupied *d* orbitals of [**10a**]$^+$ are now all stabilized to the extent where the highest occupied orbitals, the HOMO and HOMO-1 have even more negligible contributions from the metal centre (~1%) and are again largely comprised of N_{amido} lone pair character (19%) with significant contributions as well from the C_6 rings directly attached to the amide donors (~36% per ring). A similar electronic structure was reported for related pseudooctahedral Ga(III) complexes of *bis*(pyrazolyl)amido ligands.[43]

Table 5.2 Fragment contributions to the frontier molecular orbitals (MOs)

	MO	M	N_{amide}	$HC{=}N_{phen}$	$HC{=}N_{quin}$	Ar_{phen}	Ar_{quin}
6a[17]	**LUMO+1**	11	1	19	9	33	22
	LUMO	3	1	28	6	49	14
	HOMO	48	10	4	4	15	18
	HOMO-1	56	10	4	4	12	14
[**7a**]$^+$	**LUMO+1**	1	1	33	2	56	6
	LUMO	3	1	19	14	31	31
	HOMO	3	19	4	3	34	36
	HOMO-1	3	20	4	3	34	36
8a[a]	**LUMO+1**	1	1	28	4	51	14
	LUMO	2	1	22	10	38	26
	SOMO 1	80	9	3	3	2	2
	SOMO 2	84	0	6	6	1	1
[**10a**]$^+$	**LUMO+1**	1	1	36	1	58	1
	LUMO	1	1	21	13	34	29
	HOMO	1	19	3	3	35	37
	HOMO-1	1	19	3	3	35	37

[a] Restricted open-shell Kohn-Sham (ROKS) MOs.

While the fully occupied *d*-orbitals of [**8a**] are also lower in energy than the N_{amido} lone pairs, single point calculations at the optimized triplet ground state geometry using the restricted open-shell Kohn-Sham (ROKS) formalism reveals that the nearly degenerate d_z^2 (80%) and d_x^2-$_y^2$ (84%) in the d^8 Ni(II) structure contribute very strongly to the singly occupied molecular orbitals (SOMOs; Figure 5.4 and Figure S170). Consistent with this, a triplet ground state is also observed by Evans' method with two unpaired electrons and a $\mu_{eff} = 2.90\ \mu_B$. A calculated spin density map isolates the majority of this spin to the Ni metal centre (Figure S171). In comparison, square-planar Ni complexes of dithiolene ligands bearing protonated pyrazine moieties show strong d-π hybridization, which only diminishes when the 3*d* metal is replaced by a heavier elements such as Pt.[44] In that case, the modulation of the HOMO energy level in the Ni(II) complex is sufficient to

control proton-electron coupling in protonation reactions. Here, the energies of the filled π-type orbitals of diarylamido fragments do not closely enough match those of the appropriate symmetry within the Ni(II) ion's 3*d* manifold to engender substantial mixing.

Simulations of the absorption spectra using time-dependent DFT (TD-DFT; see Experimental Section for details) for each compound were found to give good agreement with experimental data (see Supporting Information, Figures S172-179). For [**7a**]$^+$, **8a** and [**10a**]$^+$case, the prominent absorption bands in the visible region of the spectra can be assigned to electronic excitations largely involving the degenerate HOMO and HOMO-1 (Tables S28-30). Fragment contribution analysis of these MOs [Table 5.2, Table S26 for **8a**] indicate a significant contribution from the N_{amido} lone pairs ([**7a**]$^+$ = 19%, **8a** = 20%, [**10a**]$^+$ = 19%). In agreement with ground-state DFT calculations, the π*-orbitals of the phenanthridine arms serve as the acceptor orbitals for transitions at lower energies (λ > 460 nm). Higher energy excitations (λ < 460 nm) populate orbitals that are largely localized on the quinoline arms of the ligand (Table S28-30), consistent with phenanthridine offering more energetically accessible acceptor orbitals. Altogether, the majority of absorptions observed in the visible region of the spectra of [**7a**]$^+$, **8a** and [**10a**]$^+$ are mainly comprised of ligand-to-ligand charge-transfer character (LLCT) consistent with the experimentally observed strong ε values.

One way of explaining the similarities in both the absorption profile and redox behaviour (*vide infra*) of **8a** compared to those of [**7a**]$^+$ and [**10a**]$^+$ despite the presence of nearly degenerate metal-based SOMOs, is to consider *non*-Aufbau behaviour upon electromagnetic excitation or reduction/oxidation,[45] as has been observed for vanadium complexes supported by porphyrinate and phthalocyanine ligands.[46] In these cases, a decrease in electron-electron repulsion promotes both removal and excitation of an electron from a doubly occupied (ligand-based) orbital versus

from the metal-based SOMOs, and population of ligand-based orbitals before the metal-based SOMOs. Another possible description is that, electronically, the complex behaves as an isolated Ni(II) ion within an pseudooctahedral NiN_6 coordination environment that only weakly interacts with the ligand π-system, as has been invoked for related Ni(II) complexes of diarylamido ligands with flanking pyrazolyl donors.[47]

Accordingly, [**7a**]PF_6, **8a**, **9a** and [**10a**]PF_6 show similar anodic redox behaviour, with two closely spaced quasi-reversible or irreversible oxidation events observed at ~ -0.05 V vs $FcH^{0/+}$ (FcH = ferrocene) for the neutral parent species and +0.3-0.6 V for the monocations (Figure 5.5). Metal-N_{amido} (d+p)π mixing stabilizes the radicals formed by these oxidations, and the events observed for [**7a**]PF_6 and **6a** are the most reversible within the series, consistent with the lowest degree of 'naked' aminyl radical character.[48] For the Co(III) species, an electrochemically reversible reduction is observed at -1.30 V. Ligand-based reduction events are also observed for all complexes close to the edge of the solvent window (~ -2.5 V), consistent with the relatively constant calculated LUMO energies and characters.

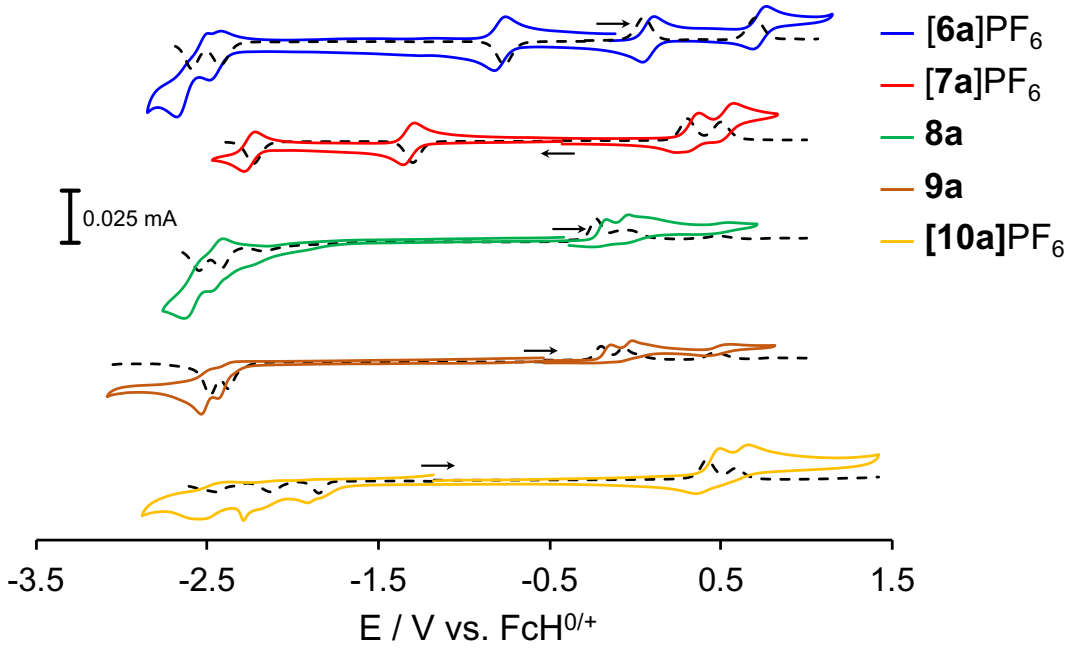

Figure 5.5 Cyclic voltammograms (–) and corresponding differential pulse voltammograms (---) of [(**6-10**)**a**]$^{n+}$[PF_6]$_n$ in CH_3CN with 0.10 M [$n$$Bu_4N$]$PF_6$ as the supporting electrolyte, glassy carbon electrode. CV scan rates were 100 mV/s. Potentials are listed vs. the $FcH^{0/+}$ redox couple (FcH = ferrocene)

The similar redox chemistry between the complexes where M = Co, Ni, Zn and Ga encouraged us to investigate oxidation of these compounds in a spectroelectrochemical cell. Each compound was dissolved in a CH_3CN solution containing [$n$$Bu_4N$]$PF_6$ electrolyte, and subjected to increasingly anodic potentials while absorbance spectra were collected (Figure 5.6).

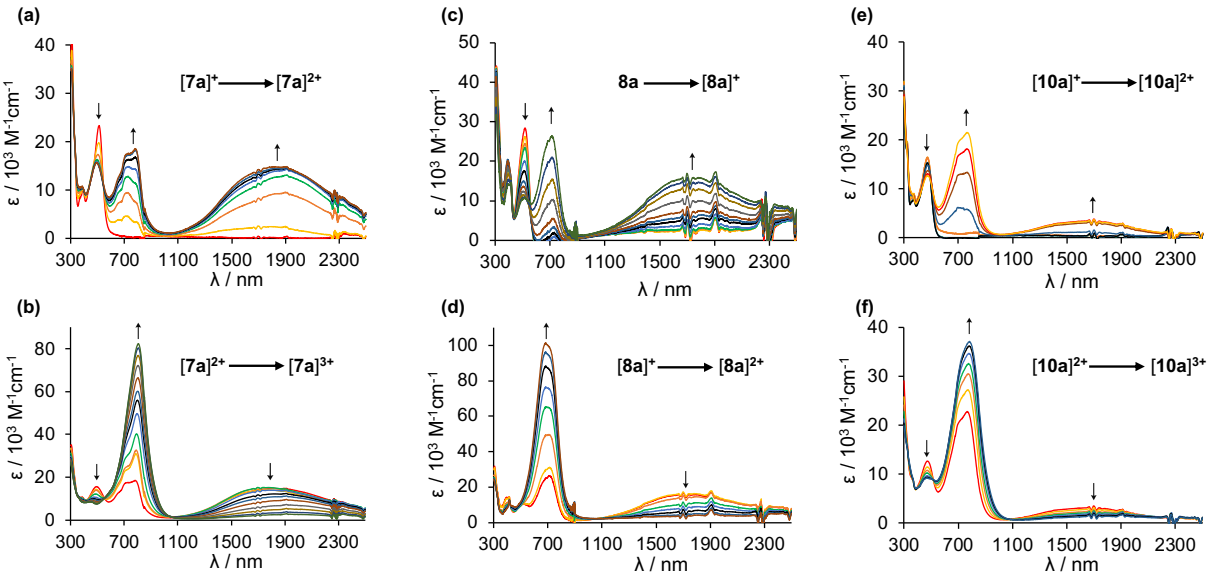

Figure 5.6 UV-Vis/NIR absorption spectra of [(**6-10**)**a**]$^{n+}$ in 0.3 M [nBu$_4$N]PF$_6$ CH$_3$CN solution: (a) M = Co, oxidative potentials applied from -0.1 to 0.8 V; (b) M = Co, oxidative potentials applied from 0.8 to 1.3 V; (c) M = Ni, oxidative potentials applied from -0.1 to 0.35 V; (d) M = Ni, oxidative potentials applied from 0.35 to 0.8 V; (e) M = Ga, oxidative potentials applied from -0.1 to 1.0 V; (f) M = Ga, oxidative potentials applied from 1.0 to 1.8 V

Under these conditions, **9a** suffered from rapid ligand dissociation and was not further investigated. In contrast, similar features were seen upon oxidation of the series to [**7a**]$^{2+}$, [**8a**]$^{+}$ and [**10a**]$^{2+}$. Application of mildly oxidative potentials led to the disappearance of the lowest energy band, supporting the TD-DFT assignments of HOMO/HOMO-1 involvement in these transitions. In addition, a new band appeared at ~700 nm alongside an even lower energy band [**7a**]$^{2+}$ = 1824 nm; [**8a**]$^{+}$ = 1769 nm; [**10a**]$^{2+}$ = 1666 nm; Figure 5.6, top row). TD-DFT simulations of the spectra observed for [**7a**]$^{2+}$ are in good agreement with experiment (Figures S180-182, Tables S31-32). The lowest-energy peak (λ_{max} = 1824 nm) can be assigned largely to a HOMO(β)→LUMO(β) excitation, in which the HOMO(β) is comprised of the doubly-occupied N_{amido} lone pair orbital and the LUMO(β) is the opposing phase oxidized aminyl radical (SOMO; Figure 5.7). The

delocalization observed in the electron hole map is consistent with the calculated spin density map, which shows delocalized aminyl radical character with minimal contributions from Co (Figure S183). The character of this transition can therefore be assigned as intervalence charge-transfer (IVCT) transitions, between one N_{amido} to another, across the metal bridge. The absorption band at ~700 nm (~1.5-1.7 eV) is dominated by two states (Table S31) where electrons from π-orbitals of the phenanthridine and quinoline fragments (Figure S182 and Table S32), HOMO-3(β) and HOMO-4(β), populate the SOMO.

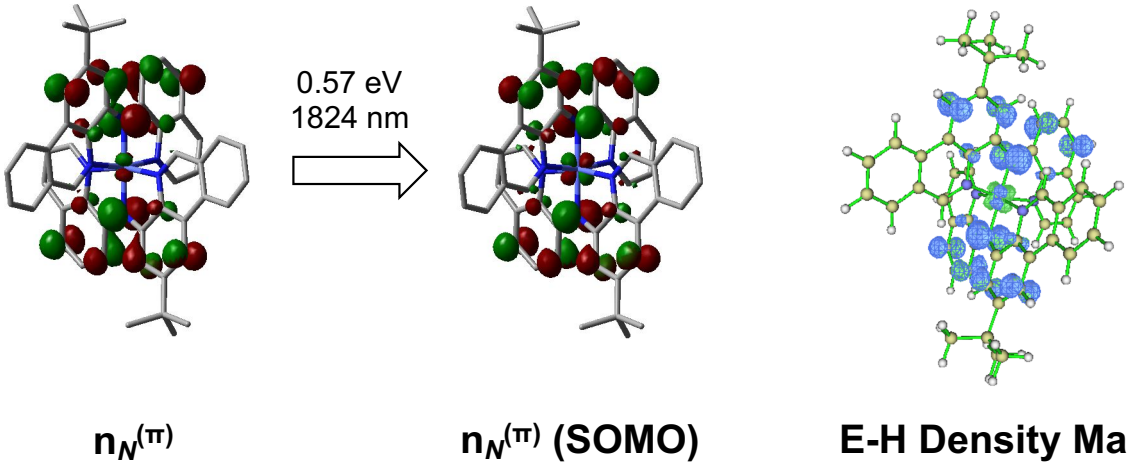

Figure 5.7 Frontier orbitals of [**7a**]$^{2+}$ with the calculated (eV) and observed (nm) energies for the IVCT. TD-DFT difference maps calculated in acetonitrile showing electron density gain (green) and depletion (blue).

Upon further oxidation of all complexes, the peak at ~700 nm continues to grow, while the lowest energy peaks begin to diminish. When the spectra had stopped changing with the increasing applied potential, the peaks ~700 nm had significantly large ε values and the lowest energy peaks had completely disappeared (Figure 5.6, bottom row) indicative of a now symmetric molecule with two aminyl radicals. This observation is consistent with the electrochemical data acquired that displays two oxidations at similar potentials. While the peak positions of the oxidized complexes

are similar, the intensities of the absorption bands depend significantly with the metal identity in the order $[\mathbf{8a}]^{+} \geq [\mathbf{7a}]^{2+} > [\mathbf{10a}]^{2+}$.

Together, the spectroelectrochemical and electrochemical data reveal electronic communication between the N_{amido} fragments in $[\mathbf{7a}]^{2+}$, $[\mathbf{8a}]^{+}$ and $[\mathbf{10a}]^{2+}$, modulated by the metal centre. Instead of overlapping one-electron oxidation waves for the two N_{amido} lone pairs, the second oxidation is shifted slightly anodically from the first, implying either Coulombic effects[47] or electronic communication; the appearance of an IVCT band supports the latter. Studies of homoleptic Ga complexes of di(2-3R-pyrazolyl)-p-arylamine ligands show similar low-energy absorption properties as a result of electronic communication between the N-amido fragments of the ligands upon oxidation of the complex.[43] Upon exchanging Ga with Ni, the communication between the amido fragments strengthens[47] owing to strengthened dπ-pπ interactions between Ni d orbitals and amido p orbitals albeit still relatively weak. Using classical Marcus[49] theory along with Hush[50] relations, (see Supplementary Information) the degree of communication between these electroactive N_{amido} centres can be calculated. Comproportionation constants (K_{com}) obtained from the electrochemical data suggest that $[\mathbf{10a}]^{2+}$ exhibits Robin-Day Class I, nearing Class II behaviour,[51] while spectroelectrochemical data supports a Class IIA assignment. As for the transition metal analogs, **8a** and $[\mathbf{7a}]PF_6$ show very similar behaviour to each other, as well as to $[\mathbf{10a}]PF_6$. The oxidations are slightly more resolved resulting in a $K_{com} = 1760$ for both complexes. They exhibit much stronger ε values (~15 000 – 20 000 $M^{-1}\,cm^{-1}$) for the low-energy IVCT band upon single oxidation, and very strong ε values (~ 80 000 – 100 000 $M^{-1}cm^{-1}$) for the UV/NIR peak (~700 nm) upon subsequent oxidation. This, together with the electrochemical data indicate Robin-Day Class IIB and Class II-III limit behaviour for $[\mathbf{8a}]^{+}$ and $[\mathbf{7a}]^{2+}$ respectively. In comparison to the homoleptic Ga and Ni complexes of pyrazolyl diarlyamido ligands mentioned

above,[43,47] this series exhibit ε values nearing 20 times greater in the NIR region of the absorption spectra.

In comparison, the significant orbital overlap between metal and N_{amido} lone pair in **6a** gives rise to completely different optical and electronic properties. Unlike the rest of the series, all redox events are well separated. Upon oxidation of the neutral ferrous complex, the spectroelectrochemically generated spectrum of [**6a**]$^{+}$ exhibits a loss in panchromatic absorption and appearance of a low-energy absorption peak (~1000 nm) in the NIR region.[17] Upon further oxidation (Figure 5.8), this NIR absorption decreases while a small peak at 674 nm and an intense peak (ε = 8 910 $M^{-1}cm^{-1}$) at 1273 nm grow in (Figure 5.8b). Due to the strong (d+p) π mixing, the character of the low-energy peaks for [**6a**]$^{+}$ and [**6a**]$^{2+}$ cannot be described as IVCT and therefore the Robin-Day classification is not appropriate. Instead, the low-energy peak for [**6a**]$^{2+}$ is assigned as predominantly π(p+d)-to-π*(p+d) (N_{amido}-Fe) (Table S33, Figures S184-185) consistent with the spin density plot that shows significant radical character evenly distributed across both N_{amido} atoms as well as significant metal character (Figure S186).

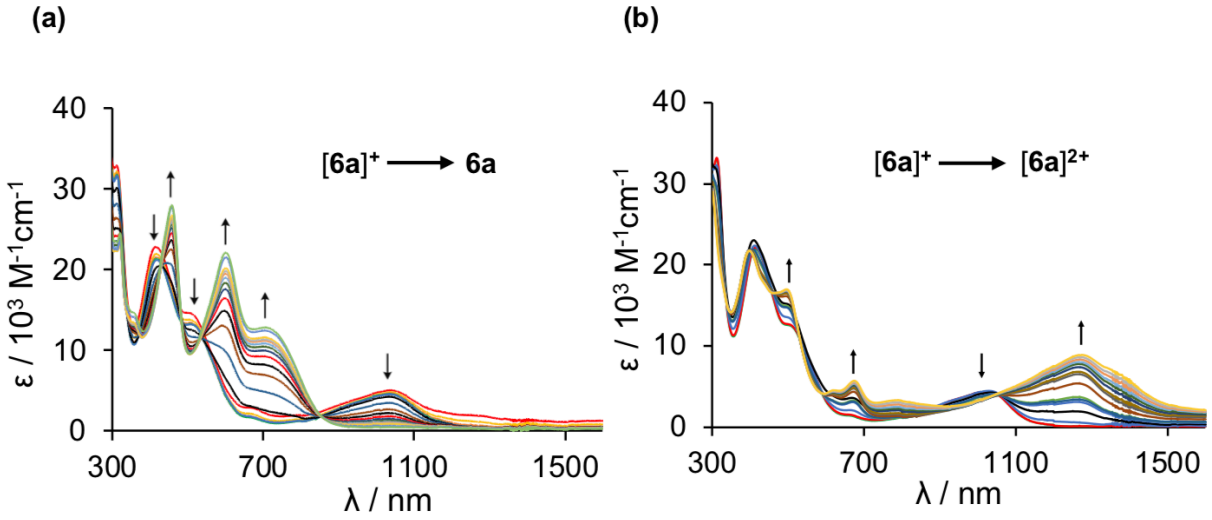

Figure 5.8 UV-Vis/NIR absorption spectra of [**6a**]$^{+}$ in 0.3 M [nBu$_4$N]PF$_6$ CH_3CN solution: (a) reductive potentials applied from -0.3 to -1.8 V; (b) oxidative potentials applied from -0.2 to 1.0 V.

In addition to using ligand modification, the 'HOMO inversion'[32] design principle can therefore be exploited by tuning metal *d* orbital energies. Although this yields strong absorptive cross-sections, the analogs studied here with full inversion of HOMO character from metal to ligand-centred have absorption profiles that attenuate at ~550 nm in their parent oxidation states, similar to what is observed in first row transition metal complexes of the 'smif' ligand ligand with metals other than Fe.[31] This contrasts the mixed-character HOMO observed for **6a**, in which balanced ligand and metal-based orbital energies lead to destabilized HOMOs. Low-lying acceptor orbitals paired with an increased energy in the HOMOs facilitate not only low energy absorption, but also panchromatic absorption enabled by a wider energetic spread of electronic transitions in the visible.

5.4 Conclusion

A series of pseudo-octahedral complexes of a tridentate *N*^*N*-^*N* diarylamido ligand bearing flanking benzannulated *N*-heterocyclic donors (**5a**$^-$) was used to prepare deeply coloured, pseudo-octahedral coordination complexes of a range of first-row transition and main-group metals ([**6a-10a**]$^{0/+}$. Changing the identity of the ligated transition metal enables access to either a gradient of 'HOMO inversion'. In particular, the different energies of the metal *d*-orbitals significantly alters the electronic structure, engendering different photophysical properties. Changing the transition metal ion to incorporate high-energy filled ligand orbitals, the accessibility of ligand-based redox chemistry enables monometallic mixed-valent Co, Ni and Ga complexes that show very broad, low-energy absorption that is dependent of the metal; in contrast, **6a** is an intermediate case of the 'HOMO inversion' model and results in dramatic changes in light absorption. In addition, sequential oxidations significantly change the absorptive properties, where the dication absorbs

throughout the visible range and attenuates at ~1500 nm. In each complex, low-lying acceptor orbitals within the ligand π-system help to stabilize ligand-based radicals and facilitate these strong transitions. This study demonstrates how the relationship between ligand design and the imposed electronic structure of an MCC will continue to guide the development of photosensitizers.[52] Here, the use of multiple strategies for enhancing strong low-energy absorption were used together producing a redox series of several metal complexes that are good candidates for light-harvesting applications.

5.5 Experimental section

Unless otherwise specified, all air sensitive manipulations were carried either in an N_2-filled glove box or using standard Schlenk techniques under Ar. $NiCl_2 \cdot 6H_2O$ (Alpha Aesar), Co(acetylacetonate)$_3$ ($Co(acac)_3$, Sigma Aldrich) and $Zn(NO_3)_2 \cdot 6H_2O$ (Fisher Scientific), were purchased and used without any further purification. Organic solvents were dried and distilled using appropriate drying agents prior to use. $^{t\text{Bu-Phen}}NN(H)N^{Quin}$ (**5a**), **6a** and **[6a]**PF_6 were synthesized according to literature procedures.[17] For electrochemical analysis, 5-10 mg of each compound investigated was dissolved in 15 mL of 0.1 M (nBu$_4$N)PF_6 in CH_3CN, and purged with Ar for 20 minutes before analysis. All electrochemical experiments were conducted under inert (Ar) atmosphere using a CHI 760c bipotentiostat, a 3 mm diameter glassy carbon working electrode, a Ag/Ag^+ quasi-non-aqueous reference electrode separated by a Vycor tip, and a Pt wire counter electrode. Cyclic voltammetric (CV) experiments were conducted using scan rates of 50-800 mV/s. Differential Pulse Voltammetry (DPV) experiments were also conducted, using a 5 mV increment, 50 mV amplitude, 0.1 s pulse width, 0.0167 s sample width, and 0.5 s pulse period. Upon completion of all CV and DPV analyses, ferrocene (FcH) was added to the solution as an internal standard, with all potentials reported versus the $FcH^{0/+}$ redox couple. 1- and 2D NMR

spectra were recorded on Bruker Avance 300 MHz or Bruker Avance – III 500 MHz spectrometers. ^{1}H and $^{13}C\{^{1}H\}$ NMR spectra were referenced to residual solvent peaks. Elemental analysis was performed at the University of Manitoba using a Perkin Elmer 2400 Series II CHNS/O Elemental Analyzer. Electronic absorption spectra were recorded on an Agilent Technologies Cary 5000 Series UV-Vis-NIR spectrophotometer in dual beam mode (range: 230–1600 nm). Spectroelectrochemical experiments were performed using a Jasco-V770 spectrophotometer using a CHI-620 C electrochemical analyzer and a custom-made cell. A three-electrode system of platinum working, auxiliary and Ag/Ag^{+} reference electrodes was used. The computational methods utilized in this chapter are described in the supporting information (pg. 141-142).

5.5.1 Synthesis

Synthesis of **[7a]**PF_6: A 250 mL round-bottom flask was charged with $Co(acac)_3$ (0.069 g, 0.19 mmol), **5a** (0.15 g, 0.40 mmol), and $NaPF_6$ (0.033 g, 0.19 mmol). MeOH (50 mL) was added and the flask was stirred and refluxed at 100 °C overnight. The flask was then cooled to room temperature and stirred for 1 h. The solution was then concentrated and added dropwise to a stirring solution of pentane (100 mL). The red precipitate was then filtered and washed with Et_2O (3 x 20 mL). Isolated yield = 0.167 g (90 %). ^{1}H NMR ($CDCl_3$, 500 MHz): δ 8.66 (d, 2H, J_{HH} = 1.5 Hz, C_{13}-H), 8.50 (d, 2H, J_{HH} = 8.3 Hz, C_3-H), 8.48 (d, 2H, J_{HH} = 8.1 Hz, C_{26}-H), 8.35 (s, 2H, C_1-H), 8.10-8.03 (m, 4H, C_{18}-H, C_{20}-H), 7.93 (s, 2H, C_{11}-H), 7.89 (t, 2H, J_{HH} = 8.1 Hz, C_{25}-H), 7.80 (ddd, 2H, J_{HH} = 8.3, 6.9, 1.3 Hz, C_4-H), 7.63 (dd, 2H, J_{HH} = 8.2, 1.3 Hz, C_6-H), 7.53 (ddd, 2H, J_{HH} = 8.0, 6.8, 0.9 Hz, C_5-H), 7.25 (d, 2H, J_{HH} = 7.8 Hz, C_{24}-H), 7.16 (dd, 2H, J_{HH} = 8.2, 5.3 Hz, C_{19}-H), 1.74 ppm (s, 18H, $C_{15, 16, 17}$-H). $^{13}C\{^{1}H\}$ NMR ($CDCl_3$, 125 MHz): δ 154.9 (C_{12}), 151.8 (C_1), 148.3 (C_{20}), 148.0 (C_{10}), 147.7 (C_{23}), 147.5 (C_{22}), 139.5 (C_9), 139.2 (C_{18}), 133.5 (C_4), 132.9 (C_7), 131.4

(C_{21}), 130.8 (C_{25}), 129.5 (C_6), 128.4 (C_5), 127.0 (C_3), 126.9 (C_8), 123.4 (C_{19}), 122.5 (C_3), 116.3 (C_{24}), 114.9 (C_{26}), 113.2 (C_{13}), 108.6 (C_{11}), 36.2 (C_{14}), 32.0 ppm ($C_{15,16,17}$). UV-vis (CH_3CN): λ (ε) 308 (41 880), 390 (9 670), 510 nm (23 310 M^{-1} cm^{-1}). Anal. Calcd for $CoC_{52}H_{44}N_6PF_6$: C, 65.27; H, 4.64. Found: C, 65.13; H, 4.64.

Synthesis of **8a**: A 250 mL round-bottom flask was charged with $NiCl_2 \cdot 6H_2O$ (0.06 g, 0.25 mmol), **5a** (0.200 g, 0.53 mmol), and NaO*t*Bu (0.051 g, 0.53 mmol). MeOH (50 mL) was added and the flask was stirred and refluxed at 100 °C overnight. The flask was then cooled to room temperature and stirred for 1 h. The solvent was then removed and the red compound was dissolved again in minimal CH_2Cl_2 (5 mL) and precipitated from cold pentane. The solution was filtered and the filter washed off with CH_2Cl_2 and dried to leave a bright red solid. Isolated yield = 0.160 g (78 %). ^1H NMR ($CDCl_3$, 300 MHz): δ 43.0 (br), 32.4 (br), 29.3 (br), 19.8 (br), 17.3 (br), 12.9 (s), 12.0 (br), 10.3 (s), 5.7 (br), 2.0 ppm (s). UV-vis (CH_3CN): λ (ε) 289 (51 330), 318 (32 190), 405 (10 280), 519 nm (28 370 M^{-1} cm^{-1}). μ_{eff} (Evans method) = 2.90 μ_B. Anal. Calcd for $NiC_{52}H_{44}N_6$: C, 76.95; H, 5.46. Found: C, 77.07; H, 5.47.

Synthesis of **9a**: A 250 mL round-bottom flask was charged with $Zn(NO_3)_2 \cdot 6H_2O$ (0.077 g, 0.26 mmol), **5a** (0.200 g, 0.53 mmol), and NaO*t*Bu (0.051 g, 0.53 mmol). MeOH (50 mL) was added and the flask was stirred and refluxed at 100 °C overnight. The flask was then cooled to room temperature and stirred for 1 h where a red precipitate formed. The mixture was then filtered over celite and extracted with dichloromethane. The filtrate was concentrated and put in the freezer overnight. The resulting precipitate was subject to the same treatment. Isolated yield = 0.191 g (91 %). ^1H NMR ($CDCl_3$, 300 MHz): δ 8.57 (s, 2H, C_{13}-H), 8.52 (d, 2H, J_{HH} = 8.4 Hz, C_3-H), 8.46 (s.

2H, C_1-H), 8.26 (d, 2H, J_{HH} = 7.9 Hz, C_{26}-H), 8.06 (dd, 2H, J_{HH} = 4.4, 1.7 Hz, C_{18}-H), 7.90 (dd, 2H, J_{HH} = 8.2, 1.7 Hz, C_{20}-H), 7.77 (d, 2H. J_{HH} = 1.8 Hz, C_{11}-H), 7.69-7.61 (m, 4H, C_4-H, C_{25}-H), 7.58-7.54 (m, 2H, C_6-H), 7.40 (t, 2H, J_{HH} = 7.6 Hz, C_5-H), 6.94 (dd, 4H, J_{HH} = 8.1, 4.1 Hz, C_{19}-H, C_{24}-H) 1.66 ppm (s, 18H, $C_{15, 16, 17}$-H). ^{13}C {^1H} NMR ($CDCl_3$, 125 MHz): δ 151.8 (C_{12}), 147.3 (C_{10}), 147.3 (C_{23}), 146.7 (C_1), 144.2 (C_{18}), 141.2 (C_{22}), 137.0 (C_{20}), 134.3 (C_9), 133.8 (C_7), 130.8 (C_4), 130.3 (C_{21}), 129.2 (C_{25}), 129.1 (C_6), 126.6 (C_5), 126.5 (C_2), 125.0 (C_8), 122.3 (C_3), 121.2 (C_{19}), 111.2 (C_{24}), 109.5 (C_{13}), 108.7 (C_{26}), 103.6 (C_{11}), 36.0 (C_{14}), 32.0 ppm ($C_{15, 16, 17}$). UV-vis (CH_3CN): λ (ε) 314 (33 000), 393 (19 880), 503 nm (24 040 M^{-1} cm^{-1}). $ZnC_{52}H_{44}N_6$: C, 76.32; H, 5.42. Found: C, 76.18; H, 5.39.

Synthesis of **[10a]**PF_6: A 100 mL Teflon stoppered flask was charged with $GaCl_3$ (0.023 g, 0.13 mmol), **5a** (0.1 g, 0.26 mmol), NaO*t*Bu (0.025 g, 0.26 mmol), $NaPF_6$ (0.22 g, 0.13 mmol), and THF (20 mL). The flask was placed in an oil bath at 100 °C and stirred overnight. The solvent was the removed and the orange solid dissolved in CH_2Cl_2 (20 mL), filtered over a pad of celite, and pumped dry leaving a bright orange solid. Isolated yield = 0.112 g (88 %). ^1H NMR (CD_2Cl_2, 500 MHz): δ 8.72 (d, 2H, J_{HH} = 1.7 Hz, C_{13}-H), 8.66 (d, 2H, J_{HH} = 8.4 Hz, C_3-H), 8.58 (s, 2H, C_1-H), 8.52 (d, 2H, J_{HH} = 8.0 Hz, C_{26}-H), 8.32 (dd, 2H, J_{HH} = 8.3, 1.6 Hz, C_{20}-H), 8.20 (dd, 2H, J_{HH} = 4.8, 1.6 Hz, C_{18}-H), 8.11 (d, 2H, J_{HH} = 1.7 Hz, C_{11}-H), 7.98 – 7.83 (m, 4H, C_4-H, C_{25}-H), 7.76 (d, 2H, J_{HH} = 8.0 Hz, C_6-H), 7.61 (t, 2H, J_{HH} = 7.5 Hz, C_5-H), 7.40 (d, 2H, J_{HH} = 8.3 Hz, C_{24}-H), 7.27 (dd, 2H, J_{HH} = 8.2, 4.8 Hz, C_{19}-H) 1.74 ppm (s, 18H, $C_{15, 16, 17}$). ^{13}C {^1H} NMR (CD_2Cl_2, 125 MHz): δ 154.6 (C_{12}), 146.9 (C_1), 143.6 (C_{18}), 141.9 (C_{23}), 141.6 (C_{10}), 141.3 (C_{20}), 137.1 (C_{21}), 134.6 (C_9), 133.9 (C_4), 130.9 (C_{25}), 130.6 (C_{22}), 130.4 (C_6), 129.9 (C_7), 128.7 (C_5), 126.3 (C_2), 126.2 (C_8), 122.9 (C_3), 122.6 (C_{19}), 116.0 (C_{24}), 111.8 (C_{26}), 110.9 (C_{13}), 108.1 (C_{11}), 36.6 (C_{14}),

31.9 ppm ($C_{15, 16, 17}$). UV-vis (CH_3CN): λ (ε) 280 (42 710), 324 (20 510), 359 (8 610), 372 (9 050), 472 nm (17 220 M^{-1} cm^{-1}). Anal. Calcd for $GaC_{52}H_{44}N_6PF_6$ (CH_2Cl_2 x 1): C, 60.48; H, 4.40. Found: C, 60.29; H, 4.29.

5.5.2 X-ray data collection, solution and refinement

X-ray crystal structure data was using collected from a multi-faceted crystal of suitable size and quality selected from a representative sample of crystals of the same habit using an optical microscope. The crystal was mounted on MiTiGen loops with data collection carried out in a cold stream of nitrogen (150 K; Bruker D8 QUEST ECO; Mo K_α radiation). All diffractometer manipulations were carried out using Bruker APEX3 software.[53] Structure solution and refinement was carried out using XS, XT and XL software, embedded within the Bruker SHELXTL suite.[54] For each structure, the absence of additional symmetry was confirmed using ADDSYM incorporated in the PLATON program.[55]

Crystal structure data for **[7a]**PF_6: Crystals were grown by slow diffusion of pentane into a saturated solution of fluorobenzene. Red blocks; $C_{52}H_{44}N_6F_6PCo$ 956.83 g/mol, monoclinic, space group C2/c; a = 24.9037(13) Å, b = 11.5317(7) Å, c = 19.7403(11) Å, $\alpha = \gamma = 90°$, β = 93.041(3), V = 5661.1(6) $Å^3$; Z = 4, ρ_{calcd} = 1.123 g cm^{-3}; crystal dimensions 0.200 x 0.100 x 0.070 mm; $2\theta_{max}$ = 58.158°; 39165 reflections, 6523 independent (R_{int} = 0.0782), intrinsic phasing; absorption coeff (μ = 0.387 mm^{-1}), absorption correction semi-empirical from equivalents (SADABS); refinement (against F_o^2) with SHELXTL V6.1, 328 parameters, 0 restraints, R_1 = 0.0673 ($I > 2\sigma$) and wR_2 = 0.1705 (all data), Goof = 1.143, residual electron density 0.36/−0.45$Å^{-3}$. Residual solvent molecules were not able to be modelled successfully. Two solvent voids of 839 $Å^3$ each

containing an electron density of 180 e was dealt with using the SQUEEZE protocol included in the PLATON program.

Crystal structure data for [**8a**]: Crystals were grown by slow evaporation of a saturated pentane solution. Red blocks; $C_{52}H_{44}N_6Ni$ 811.64 g/mol, triclinic, space group P-1; a = 11.7853(4) Å, b = 11.9157(4) Å, c = 16.3161(5) Å, α = 85.686(2)º, β = 85.655(2)º, γ = 74.584(2)°, V = 2198.87(13) Å^3; Z = 2, ρ_{calcd} = 1.226 g cm^{-3}; crystal dimensions 0.300 x 0.250 x 0.150 mm; $2\theta_{max}$ = 66.538°; 141096 reflections, 16881 independent (R_{int} = 0.0503), intrinsic phasing; absorption coeff (μ = 0.483 mm^{-1}), absorption correction semi-empirical from equivalents (SADABS); refinement (against F_o^2) with SHELXTL V6.1, 538 parameters, 0 restraints, R_1 = 0.0509 ($I > 2\sigma$) and wR_2 = 0.1305 (all data), Goof = 1.028, residual electron density 1.05 /−0.57Å^{-3}. Residual solvent molecules were not able to be modelled successfully. A solvent void of 252 Å^3 containing an electron density of 49 e was dealt with using the SQUEEZE protocol included in the PLATON program.

Crystal structure data for **[10a]**PF_6: Crystals were grown by slow evaporation of diethyl ether into a saturated dichloromethane solution. Orange blocks; $C_{52}H_{44}N_6F_6PGa$ 967.63 g/mol, monoclinic, space group C2/c; a = 18.29(2) Å, b = 16.66(2) Å, c = 16.81(2) Å, $\alpha = \gamma$ = 90°, β = 99.338(18)º, V = 5055(12) Å^3; Z = 4, ρ_{calcd} = 1.226 g cm^{-3}; crystal dimensions 0.170 x 0.080 x 0.030 mm; $2\theta_{max}$ = 55.29°; 63854 reflections, 5863 independent (R_{int} = 0.1402), intrinsic phasing; absorption coeff (μ = 0.855 mm^{-1}), absorption correction semi-empirical from equivalents (SADABS); refinement (against F_o^2) with SHELXTL V6.1, 330 parameters, 0 restraints, R_1 = 0.0533 ($I > 2\sigma$) and wR_2 = 0.1242 (all data), Goof = 1.059, residual electron density 0.75 /−0.65 Å^{-3}.

5.6 References

(1) Hagfeldt, A.; Boschloo, G.; Sun, L.; Kloo, L.; Pettersson, H. *Chem. Rev.* **2010**, *110* (11), 6595.

(2) O'Regan, B.; Grätzel, M. *Nature* **1991**, *353* (6346), 737.

(3) Strieth-Kalthoff, F.; James, M. J.; Teders, M.; Pitzer, L.; Glorius, F. *Chem. Soc. Rev.* **2018**, *47* (19), 7190.

(4) Gust, D.; Moore, T. A.; Moore, A. L. *Acc. Chem. Res.* **2009**, *42* (12), 1890.

(5) Ponseca, C. S.; Chábera, P.; Uhlig, J.; Persson, P.; Sundström, V. *Chem. Rev.* **2017**, *117* (16), 10940.

(6) Pashaei, B.; Shahroosvand, H.; Graetzel, M.; Nazeeruddin, M. K. *Chem. Rev.* **2016**, *116* (16), 9485.

(7) Robertson, N. *Angew. Chem., Int. Ed.* **2006**, *45* (15), 2338.

(8) Prier, C. K.; Rankic, D. A.; MacMillan, D. W. C. *Chem. Rev.* **2013**, *113* (7), 5322.

(9) Wang, P.; Klein, C.; Humphry-Baker, R.; Zakeeruddin, S. M.; Grätzel, M. *J. Am. Chem. Soc.* **2005**, *127* (3), 808.

(10) Zhang, Y.; Lee, T. S.; Favale, J. M.; Leary, D. C.; Petersen, J. L.; Scholes, G. D.; Castellano, F. N.; Milsmann, C. *Nat. Chem.* **2020**.

(11) Baslon, V.; Harris, J. P.; Reber, C.; Colmer, H. E.; Jackson, T. A.; Forshaw, A. P.; Smith, J. M.; Kinney, R. A.; Telser, J. *Can. J. Chem.* **2017**, *95* (5), 547.

(12) Dorn, M.; Kalmbach, J.; Boden, P.; Päpcke, A.; Gómez, S.; Förster, C.; Kuczelinis, F.; Carrella, L. M.; Büldt, L. A.; Bings, N. H.; Rentschler, E.; Lochbrunner, S.; González, L.; Gerhards, M.; Seitz, M.; Heinze, K. *J. Am. Chem. Soc.* **2020**, *142* (17), 7947.

(13) Kjær, K. S.; Kaul, N.; Prakash, O.; Chábera, P.; Rosemann, N. W.; Honarfar, A.; Gordivska, O.; Fredin, L. A.; Bergquist, K.-E.; Häggström, L.; Ericsson, T.; Lindh, L.; Yartsev, A.; Styring, S.; Huang, P.; Uhlig, J.; Bendix, J.; Strand, D.; Sundström, V.; Persson, P.; Lomoth, R.; Wärnmark, K. *Science* **2019**, *363* (6424), 249.

(14) Pal, A. K.; Li, C.; Hanan, G. S.; Zysman-Colman, E. *Angew. Chem. Int. Ed.* **2018**, *57*.

(15) Whittemore, T. J.; Millet, A.; Sayre, H. J.; Xue, C.; Dolinar, B. S.; White, E. G.; Dunbar, K. R.; Turro, C. *J. Am. Chem. Soc.* **2018**, *140* (15), 5161.

(16) Chábera, P.; Liu, Y.; Prakash, O.; Thyrhaug, E.; Nahhas, A. E.; Honarfar, A.; Essén, S.; Fredin, L. A.; Harlang, T. C. B.; Kjær, K. S.; Handrup, K.; Ericson, F.; Tatsuno, H.; Morgan, K.; Schnadt, J.; Häggström, L.; Ericsson, T.; Sobkowiak, A.; Lidin, S.; Huang, P.; Styring, S.; Uhlig, J.; Bendix, J.; Lomoth, R.; Sundström, V.; Persson, P.; Wärnmark, K. *Nature* **2017**, *543* (7647), 695.

(17) Braun, J. D.; Lozada, I. B.; Kolodziej, C.; Burda, C.; Newman, K. M. E.; van Lierop, J.; Davis, R. L.; Herbert, D. E. *Nat. Chem.* **2019**, *11* (12), 1144.

(18) He, M.; Ji, Z.; Huang, Z.; Wu, Y. *J. Phys. Chem. C* **2014**, *118* (30), 16518.

(19) Kaim, W. *Coord. Chem. Rev.* **2011**, *255* (21–22), 2503.

(20) Li, Z.; Leed, N. A.; Dickson-Karn, N. M.; Dunbar, K. R.; Turro, C. *Chem. Sci.* **2014**, *5* (2), 727.

(21) Whittemore, T. J.; Sayre, H. J.; Xue, C.; White, T. A.; Gallucci, J. C.; Turro, C. *J. Am. Chem. Soc.* **2017**, *139* (41), 14724.

(22) Whittemore, T. J.; Xue, C.; Huang, J.; Gallucci, J. C.; Turro, C. *Nat. Chem.* **2020**, *12* (2), 180.

(23) Mountford, H. S.; Spreer, L. O.; Otvos, J. W.; Calvin, M.; Brewer, K. J.; Richter, M.; Scott, B. *Inorg. Chem.* **1992**, *31* (5), 717.

(24) Spreer, L. O.; Allan, C. B.; MacQueen, D. B.; Otvos, J. W.; Calvin, M. *J. Am. Chem. Soc.* **1994**, *116* (5), 2187.

(25) Campbell, W. M.; Burrell, A. K.; Officer, D. L.; Jolley, K. W. *Coord. Chem. Rev.* **2004**, *248* (13–14), 1363.

(26) Boyle, N. M.; Rochford, J.; Pryce, M. T. *Coord. Chem. Rev.* **2010**, *254* (1–2), 77.

(27) Higashino, T.; Imahori, H. *Dalton Trans.* **2015**, *44* (2), 448.

(28) Campbell, W. M.; Jolley, K. W.; Wagner, P.; Wagner, K.; Walsh, P. J.; Gordon, K. C.; Schmidt-Mende, L.; Nazeeruddin, M. K.; Wang, Q.; Grätzel, M.; Officer, D. L. *J. Phys. Chem. C* **2007**, *111* (32), 11760.

(29) Tanaka, M.; Hayashi, S.; Eu, S.; Umeyama, T.; Matano, Y.; Imahori, H. *Chem. Commun.* **2007**, No. 20, 2069.

(30) Mathew, S.; Yella, A.; Gao, P.; Humphry-Baker, R.; Curchod, B. F. E.; Ashari-Astani, N.; Tavernelli, I.; Rothlisberger, U.; Nazeeruddin, Md. K.; Grätzel, M. *Nat. Chem.* **2014**, *6* (3), 242.

(31) Frazier, B. A.; Bartholomew, E. R.; Wolczanski, P. T.; DeBeer, S.; Santiago-Berrios, M.; Abruña, H. D.; Lobkovsky, E. B.; Bart, S. C.; Mossin, S.; Meyer, K.; Cundari, T. R. *Inorg. Chem.* **2011**, *50* (24), 12414.

(32) Mukherjee, S.; Torres, D. E.; Jakubikova, E. *Chem. Sci.* **2017**, *8* (12), 8115.

(33) Frazier, B. A.; Wolczanski, P. T.; Lobkovsky, E. B.; Cundari, T. R. *J. Am. Chem. Soc.* **2009**, *131* (10), 3428.

(34) Westerhausen, M.; Kneifel, A. N. *Inorg. Chem. Commun.* **2004**, *7* (6), 763.

(35) Sazama, G. T.; Betley, T. A. *Inorg. Chem.* **2010**, *49* (5), 2512.

(36) Betley, T. A.; Qian, B. A.; Peters, J. C. *Inorg. Chem.* **2008**, *47* (24), 11570.

(37) Glaser, F.; Wenger, O. S. *Coord. Chem. Rev.* **2020**, *405*, 213129.

(38) Wenger, O. S. *Nat. Chem.* **2020**, *12* (4), 323.

(39) Whittemore, T. J.; White, T. A.; Turro, C. *J. Am. Chem. Soc.* **2018**, *140* (1), 229.

(40) Wenger, O. S. *J. Am. Chem. Soc.* **2018**, *140* (42), 13522.

(41) Wells, A. F. *Structural inorganic chemistry*, 5th ed.; Clarendon Press ; Oxford University Press: Oxford [Oxfordshire] : New York, 1984.

(42) Alvarez, S. *Chem. Rev* **2015**, *115* (24), 13447.

(43) Liddle, B. J.; Wanniarachchi, S.; Hewage, J. S.; Lindeman, S. V.; Bennett, B.; Gardinier, J. R. *Inorg. Chem.* **2012**, *51* (23), 12720.

(44) Hayashi, M.; Takahashi, Y.; Yoshida, Y.; Sugimoto, K.; Kitagawa, H. *J. Am. Chem. Soc.* **2019**, *141* (29), 11686.

(45) Gryn'ova, G.; Coote, M. L.; Corminboeuf, C. *Wiley Interdisciplinary Reviews: Computational Molecular Science* **2015**, *5* (6), 440.

(46) Westcott, B. L.; Gruhn, N. E.; Michelsen, L. J.; Lichtenberger, D. L. *J. Am. Chem. Soc.* **2000**, *122* (33), 8083.

(47) Hewage, J. S.; Wanniarachchi, S.; Morin, T. J.; Liddle, B. J.; Banaszynski, M.; Lindeman, S. V.; Bennett, B.; Gardinier, J. R. *Inorg. Chem.* **2014**, *53* (19), 10070.

(48) Kaim, W. *Inorg. Chem.* **2011**, *50* (20), 9752.

(49) Marcus, R. A.; Sutin, N. *Biochimica et Biophysica Acta (BBA) - Reviews on Bioenergetics* **1985**, *811* (3), 265.

(50) Hush, N.S. *Prog. Inorg. Chem.* No. 8, 391.

(51) In *Inorganic Electrochemistry*; Royal Society of Chemistry: Cambridge, 2007; pp 159–216.

(52) Shon, J.-H.; Teets, T. S. *ACS Energy Lett.* **2019**, *4* (2), 558.

(53) Sheldrick, G. M. *Acta Crystallogr., Sect. A: Found. Crystallogr.* **2008**, *64*, 112.

(54) Dolomanov, O. V.; Bourhis, L. J.; Gildea, R. J.; Howard, J. A. K.; Puschmann, H. *J. Appl. Crystallogr.* **2009**, *42* (2), 339.

(55) Spek, A. L. *Acta Crystallogr., Sect. D: Biol. Crystallogr.* **2009**, *65*, 148.

Chapter 6

Conclusion

6.1 Summary

This thesis describes the design and synthesis of pyridine-containing N^N^N tridentate pincer ligands and their coordination to various transition and main group elements.

Chapter 2: This chapter dives into an exploration of the reductive electrochemistry of iron complexes bearing well-known diiminepyridine (DIP) ligands and their applicability to redox flow batteries (RFBs). Additionally, the incorporation of electron-withdrawing groups (EWGs) on the *para* position of the flanking aryl groups was realized through a Zn-templated synthesis, giving rise to new DIP analogues, potentially useful in the many fields of chemistry where these ligands are utilized. It was found that ligands bearing EWGs were susceptible to degradation over extended cycling periods and were therefore not appropriate RFB candidates, however, unsubstituted or *tert*-butyl substituted analogues showed exceptional stability and performance efficiencies that make them viable candidates for RFB anolytes.

Chapter 3: The synthesis of cationic P(I) and P(III) complexes supported by the same, bulky DIP ligand was accomplished. These complexes were studied via a full suite of experimental characterization tools including X-ray crystallography, multinuclear NMR, UV-Vis, DFT/TDDFT and electrochemistry. Interestingly, reversible electrochemistry is observed for the P(I) complex, however, chemical reduction has not yet been achieved.

Chapter 4: In this chapter, the design and synthesis of tridentate, phenanthridine-containing ligands was achieved. HOMO inversion design principles[1] combined with accessible acceptor units provided panchromatic absorption and nanosecond charge-transfer excited state lifetimes,

potentially useful for photochemical applications. A combination of transient absorption spectroscopy and theoretical work suggest these excited-states are MLCT-type in nature.

Chapter 5: Using the ligand framework described in chapter 4, a series of complexes were synthesized based on first-row transition metals and main group elements. By altering the central metal, a gradient of HOMO inversion is observed resulting in dramatic changes in light absorption. Solely N_{amido}-based redox chemistry is much more prevalent in complexes based on metals heavier than iron as evidenced by electrochemical experiments and theoretical calculations. Sequential oxidations of all complexes led to very low energy absorption of the mixed-valent compounds that varied with metal identity, illustrating how the relationship between ligand design and metal choice plays a significant role in the pursuit of complexes with desired properties.

6.2 Conclusion and Outlook

The design and synthesis of multidentate ligand architectures has led to a myriad of coordination complexes available to chemists for a variety of applications including chemical synthesis and in the green energy sector. The ability to tailor ligands to engender desirable properties has been of significant interest to organometallic/inorganic chemists and continues to be a driving force in the synthesis of new materials. In this thesis, the design and synthesis of pyridine-containing multidentate ligand architectures have been described. Taking inspiration from the widespread literature on diimine-pyridine (DIP) and N-heterocyclic ligands, I was able to devise iron coordination complexes for completely different applications made possible by ligand design. The redox-active nature of the DIP ligand has attracted significant attention in the past few decades and make for great candidates for RFB applications with benign metals and had so far not been explored. The use of these redox-active ligands can be further envisioned within

the realm of RFBs by synthesizing new derivatives that may be more stable towards redox cycling, and in addition, have manipulatable redox potentials. Future work in this project includes synthesizing ligand derivatives that are substituted nearer to the imine-based[2] LUMO and evaluating their Fe complexes for RFB applications.

Focusing further on the derivatization of DIP ligands, a new bulky DIP ligand featuring *tert*-butyl groups substituents located of the imine carbon were synthesized. Subsequently, these ligands could be bound to P(I) and P(III) centres, producing the first example of a single DIP ligand that is able to stabilize these redox pairs. In agreement with the reversible reductions seen in DIP ligands in chapter 2, the P(I) complex shows a reversible ligand-based reduction that will be the focus of future work on this project. Inclusion of a once reduced complex will result in a redox series that can be studied further. In recent literature, phosphorus complexes comprised of tridentate pyridine-containing ligands have been shown to facilitate hydrosilylation of olefins and ketones[3] and therefore, the reactivity of these redox congeners will be explored.

The redox activity and non-innocent behaviour of pyridine-containing tridentate ligands is evident in the literature and further demonstrated in chapters 2 and 3. With this information in hand, the idea of including pyridine moieties to enhance electron transfer properties within ligands with extended π systems was formulated. The diarlyamido motif with flanking N-heterocyclic donor arms was envisioned as previous reports of similar structures demonstrated rich photochemical and electrochemical properties.[4] The incorporation of phenanthridine into this ligand framework offers a derivitizable backbone that ultimately leads to much better solubility than similar structures[4] and the potential to synthesize a wide variety of analogues to fine tune the properties of its complexes. As explained thoroughly in chapter 4, the Fe complexes of these ligands exhibit panchromatic absorption and long-lived excited-state lifetimes best described as

charge-transfer in nature. An intermediate case of the 'HOMO inversion'[1] model is observed, effectively raising the energy of the HOMO which is comprised of a π*(p+d) orbital. This in combination with low-lying π* acceptor orbitals significantly localized to the C=N bond in phenanthridine are responsible for these desirable properties. Further work aims to shed more light on the nature of these excited states and orbital arrangement by using various X-ray spectroscopic methods including XAS, XES and RIXS. This study provides insight as to how photosensitizers based on sustainable metals may be constructed.[5,6] Additional future work involves derivatizing the ligand to make the complexes amenable to tethering to a surface.[7] Figure 6.1 highlights some of the possibilities for anchoring groups that have been previously shown to work with TiO_2 surfaces.[7] These anchoring groups would allow for electron transfer studies from the complex to a surface and eventually the construction of devices such as DSSCs.

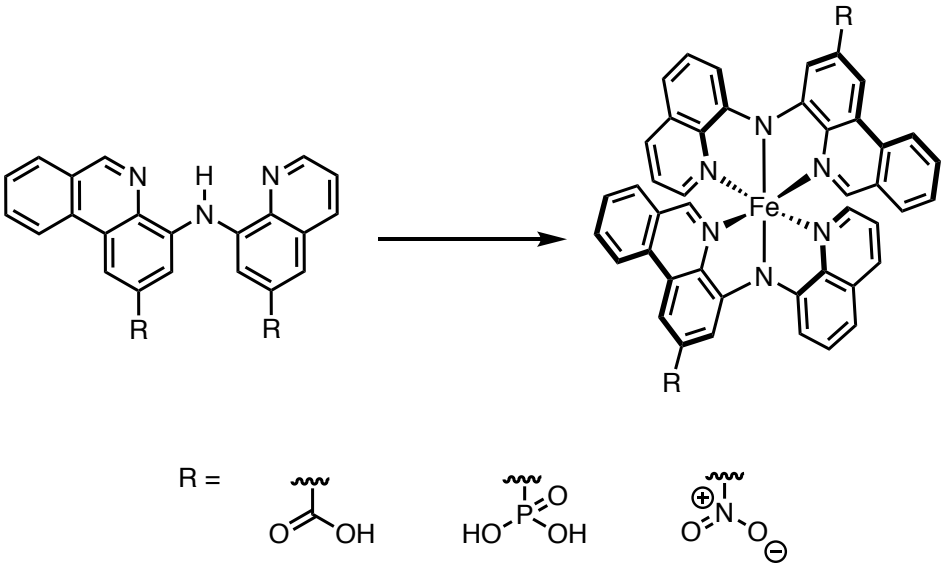

Figure 6.1 Potential anchoring groups suitable for tethering to a TiO_2 surface

With the exciting results observed with the Fe complexes of the ligands described in chapter 4, the central metal was exchanged using 3d and main group elements to examine how the

electronic properties change with metal identity. Manipulating the energy of the dπ orbitals results in drastic changes in the absorption and electrochemical properties resulting in absorption features with very low energy with intensity dependant on metal identity. Although not yielding the sought-after panchromatic absorption seen in the Fe complexes, studying these complexes in the context of the same ligand should help guide the design of photosensitizers based on abundant and sustainable metals. Future work will aim to look at complexes with d-electron counts of less than d^6. These complexes should lie on the other side of the HOMO inversion continuum, whereby the HOMO should likely be comprised of metal-based orbitals, and again drastic changes in absorption and electrochemical properties are to be expected.

This thesis highlights the design and synthesis of pyridine-based tridentate ligands that play a crucial role in the properties of their complexes. The chemical space opened up by the design of these ligands offers a wide variety of possibilities for new and exciting complexes of different metals using various ligand derivatives. Their complexes have and will continue to show promise in green energy and photochemical applications.

6.3 References

(1) Mukherjee, S.; Torres, D. E.; Jakubikova, E. *Chem. Sci.* **2017**, *8* (12), 8115.

(2) Gray, P. A.; Braun, J. D.; Rahimi, N.; Herbert, D. E. *Eur. J. Inorg. Chem.* **2020**, *2020* (21), 2105.

(3) Andrews, R. J.; Chitnis, S. S.; Stephan, D. W. *Chem. Commun.* **2019**, *55* (39), 5599.

(4) Betley, T. A.; Qian, B. A.; Peters, J. C. *Inorg. Chem.* **2008**, *47* (24), 11570.

(5) Buldt, L. A.; Wenger, O. S. *Angew. Chem. Int. Ed.* **2017**, *56*.

(6) Otto, S. *Angew. Chem. Int. Ed.* **2015**, *54*.

(7) Zhang, L.; Cole, J. M. *ACS Appl. Mater. Interfaces* **2015**, *7* (6), 3427.